Macromolecules at Interfaces:

From Pure Protein Bilayers to the Adhesion of Cells

Dissertation

zur Erlangung des Grades
des Doktors der Naturwissenschaften
der Naturwissenschaftlich-Technischen Fakultät
der Universität des Saarlandes

von

Friederike Nolle

Saarbrücken

2023

Tag des Kolloquiums:	29.09.2023
Dekan:	Prof. Dr. Ludger Santen
Berichterstatter:	Prof. Dr. Karin Jacobs
	Prof. Dr. Markus Bischoff
Vorsitz:	Prof. Dr. Albrecht Ott
Akad. Mitarbeiter:	Dr. Alexis Darras

Abstract

Macromolecules in cell membranes and cell walls are essential for many cell functions. The use of macromolecules as possible replacements for lipids in membranes and the role of cell wall macromolecules in adhesion have not been fully explored. In this work, HFBI bilayers were shown to have extremely low water permeability while maintaining high stability to osmotic pressure. Disruption of protein order increases water permeability. The methodology of HFBI vesicle preparation was further developed, especially in terms of reproducibility and control. Also, the incorporation of HFBI into lipid membranes has been shown to stabilize the formation of pores. The role of macromolecules in *Staphylococcus aureus* adhesion was investigated by varying the surfaces used and using knock-out mutants. For adhesion on nano-rough surfaces, the contact area between the macromolecule and the surface is crucial. While many macromolecules, especially cell wall proteins, adhere weakly to hydrophobic surfaces, only a few cell wall macromolecules adhere strongly to hydrophilic surfaces. Electrostatic interactions play a crucial role on hydrophilic surfaces. Furthermore, it has been shown that in human retinal pigment epithelial cells, adhesion weakens as the size of focal adhesions decreases.

Kurzzusammenfassung

Makromoleküle in Zellmembranen und Zellwänden sind für viele Zellfunktionen von entscheidender Bedeutung. Die Verwendung von Makromolekülen als möglicher Ersatz für Lipide in Membranen, aber auch die Rolle von Zellwandmakromolekülen bei der Adhäsion sind noch nicht vollständig erforscht. In dieser Arbeit wurde gezeigt, dass HFBI-Doppelschichten eine sehr geringe Wasserpermeabilität bei gleichzeitig hoher Stabilität gegenüber osmotischem Druck aufweisen. Durch Störung der Proteinordnung steigt die Wasserpermeabilität. Die Methodik der HFBI-Vesikelherstellung wurde insbesondere hinsichtlich Reproduzierbarkeit und Kontrolle weiterentwickelt. Ebenso wurde durch den Einbau von HFBI in Lipidmembranen eine Stabilisierung der gebildeten Poren festgestellt. Die Rolle der Makromoleküle bei der Adhäsion von Staphylococcus aureus wurde durch Variation der verwendeten Oberflächen und die Nutzung von Knock-out-Mutanten untersucht. Für die Adhäsion auf nanorauen Oberflächen ist die Kontaktfläche Makromolekül/Oberfläche entscheidend. Während auf hydrophoben Oberflächen viele Makromoleküle, insbesondere Zellwandproteine, schwach haften, tun dies nur wenige Zellwandmakromoleküle stark auf hydrophilen Oberflächen. Elektrostatische Wechselwirkungen spielen dabei auf hydrophilen Oberflächen eine entscheidende Rolle. Weiterhin konnte gezeigt werden, dass sich bei humanen retinalen Pigmentepithelzellen die Adhäsion mit abnehmender Größe der Fokalkontakte abschwächt.

Contents

List of Abbreviations

AFM – atomic force microscopy

CBD – cellulose binding domain

ClfA, ClfB – clumping factor A, clumping factor B

CWA – cell wall anchored

DIB – droplet interface bilayer

DNA – deoxyribonucleic acid

DOPC – 1,2-Di-(9Z-octadecenoyl)-*sn*-glycero-3-phosphocholin

E. coli – *Escherichia coli*

Eap – extracellular adherence protein

ECM – extracellular matrix

EDTA – ethylenediaminetetraacetic acid

Emp – extracellular matrix protein

FnBPA, FnBPB – fibronectin binding protein A, fibronectin binding protein B

HAp – hydroxyapatite

HFBI-dCBM – HFBI-double cellulose binding molecule

HPLC – high-performance liquid chromatography

IEP – isoelectric point

IsdA – iron-regulated surface protein A

LTA – lipoteichoic acid

MC simulations – Monte-Carlo simulations

MD simulations – molecular dynamics simulations

MiuA – miuraenamide A

Monoolein – 1-Oleoyl-*rac*-glycerol

MRSA – methicillin-resistant *Staphylococcus aureus*

MSCRAMM – microbial surface components recognizing adhesive matrix molecule

NaAc – sodium acetate

NEAT – near iron transporter

OTS – octadecyltrichlorosilane

P. aeruginosa – *Pseudomonas aeruginosa*

PBS – phosphate buffered saline

PDB – Protein Data Bank

PDMS – polydimethylsiloxane

RMS – root mean square

RPE – retinal pigment epithelium

S. aureus – *Staphylococcus aureus*

SA113 – *Staphylococcus aureus* SA113

SasG – surface protein G

SCFS – single-cell force spectroscopy

SDS-PAGE – sodium dodecylsulfate polyacrylamide gel electrophoresis

SERAM – secretable expanded repertoir adhesive molecule

SiO_2 – silicon dioxide

SpA – Protein A

SraP – serine-rich adhesin of platelets

SrtA – sortase A

TSB – tryptic soy broth

WCA – water contact angle

WTA – wall teichoic acid

1 Introduction

Cell membranes and cell walls perform many different functions in nature [1]. They separate two areas from each other and thus have a protective, stabilizing function. But they are also there to interact with their environment, both by exchanging molecules with the environment (permeability) and by establishing contact with other surfaces (adhesion). To accomplish all these functions, macromolecules play a major role as an important component of cell membranes/walls [2].

A cell membrane is mainly composed of phospholipids arranged in bilayers. Due to their amphiphilic nature, lipids form these bilayers with their hydrophobic tails attracting each other in water through hydrophobic interactions. In addition to being a major component of cell membranes, lipids also play a role in the production of lipid bilayers and liposomes for technical applications such as desalination or drug delivery [3, 4]. To achieve a greater variety of properties in these bilayers and vesicles, the lipid composition can be varied and other components, including proteins, can be added [5–9]. There are also other amphiphilic molecules: (block co-)polymers [10], proteins [11] and peptides [12] that can be used to create artificial membranes and tune the properties of these bilayers. Bilayers formed by the natural amphiphilic protein HFBI (pronounced HFB-"one"), from *Trichoderma reesei*, are an alternative to lipid bilayers, since it is also possible to form vesicles composed entirely of HFBI [13]. These bilayers are of great interest because of their high stability against lateral tension [14] and their ability to form water/water, oil/oil or even air/air vesicles [13]. However, important properties such as water permeability are still unknown. The water permeability of a membrane is an important parameter for the homeostasis of a cell with its environment [15]. Vesicles with a double layer of HFBI could potentially be used as drug carriers and for this it is also important to know the water permeability [16]. For bilayers in the field of water desalination, it is also an important aspect [3].

In this thesis, the water permeability of HFBI bilayers was determined using a droplet interface bilayer technique [17]. The effect of the insertion of an HFBI-cellulose fusion protein into these bilayers on the water permeability has been investigated. Molecular dynamic (MD) simulations, in collaboration with L. Starke of the working group of Prof. J. Hub, were used to attempt to explain the water permeabilities measured in the experiment. The production of HFBI vesicles was further developed in order to expand the use of HFBI vesicles, e.g. as drug carriers. To achieve a higher controllability and quantity, a microfluidic setup was initiated and the microfluidic jetting method was further developed. Furthermore, the influence of HFBI on lipid membrane pore formation as well as on lipid membrane stability was investigated.

However, macromolecules are not limited to the formation of bilayers and vesicles as an alternative to lipids. They have many different functions in cells. As a major

component of cell membranes and cell walls, they are also responsible for tethering and binding to surfaces, both biotic and abiotic. Cell adhesion is not only important for cell attachment to a surface, but also for tissue/biofilm organization, cell-cell interaction, and cell movement [18, 19]. In the field of medical implants, host-cell adhesion should be enhanced and bacterial adhesion prevented as much as possible [20]. Bacterial adhesion to implant material and biofilm formation is a major cause of implant-related infections and eventual implant removal [21, 22]. *Staphylococcus aureus* (*S. aureus*) is one of the main causes of these implant-related infections [22]. To reduce the biofilm formation of bacteria on abiotic surfaces such as implants, the first step of biofilm formation, adhesion, needs to be better understood. The adhesion process of *S. aureus*, but also other bacteria, is quite complex due to the many different macromolecules on the cell wall [23–26]. The exact role of macromolecules in the adhesion process of *S. aureus* is still not fully understood. Influences of surface roughness, hydrophobicity and electrical charge are mostly studied by adsorption experiments, counting the number of adhered cells or the coverage of the surface [27–37]. Thereby, adhesion parameters such as adhesion force, adhesion energy or rupture length are usually not considered.

The aim of this thesis is to gain a better understanding of the adhesion of *S. aureus* to abiotic surfaces. Adhesion parameters are measured by single-cell force spectroscopy (SCFS). SCFS is an atomic force microscope-based method for studying the adhesion of a single cell. Changing surface parameters such as surface roughness, hydrophobicity and charge, the influence on the adhesion of *S. aureus* was studied. To better understand the role of different cell wall macromolecules, the adhesion of *S. aureus* knock-out mutants was compared to each other and to wild type *S. aureus*. In addition, the cell wall composition of *S. aureus* and the $\Delta dltA$ mutant was investigated in close collaboration with B. Wieland from the group of Prof. M. Bischoff. For a deeper insight, measurements of the roughness dependence were coupled with Minkowski functionals and measurements of the hydrophobicity dependence were coupled with Monte-Carlo (MC) simulations in collaboration with E. Maikranz of the group of Prof. L. Santen. Furthermore, within a collaboration with C. Baltes of the group of Prof. F. Lautenschläger, the adhesion of human retinal pigment epithelial cells to fibronectin was measured. The role of focal adhesion size and actin length on adhesion parameters (adhesion force, adhesion energy, and rupture length) was further investigated.

2 Overview and Connectivity

This thesis contains five articles. Four of them have already been accepted for publication in peer-reviewed journals. This thesis also includes three additional chapters with results that are not yet available in manuscript form, but are relevant to the work presented in this dissertation. Main goal of all these studies is to gain understanding of the behavior of macromolecules at interfaces, be it in pure protein bilayers or in cell adhesion. The results obtained in one system, e.g. regarding the underlying forces in hydrophobin mono- and bilayers, could be used to better understand bacterial adhesion. In addition, the detailed characterization of hydrophobins led to the idea of investigating whether they could be used to tailor bacterial adhesion. Furthermore, the presentation of the results within the CRC 1027 has generated new project ideas within the scope of other groups, e.g. the study of the adhesion of human retinal pigment epithelial cells to fibronectin (group of Prof. Lautenschläger). The series of experiments are similar to the characterization of bacterial adhesion as well as the experimental method, single-cell force spectroscopy. New experimental approaches were also opened up by benefiting from the great knowledge in the field of microfluidics in Prof. Seemann's research group. The accompanying theoretical studies on the systems of this thesis, on bacterial adhesion (group of Prof. Santen) or on the water permeability of protein membranes (group of Prof. Hub) are further examples of cooperation within the CRC 1027. All experiments on bacteria were performed in close collaboration with the group of Prof. Bischoff.
To study the behavior of macromolecules at interfaces, this thesis focuses on two main topics: **(I)** the behavior of the hydrophobin HFBI at interfaces and **(II)** the behavior of cell wall macromolecules and focal adhesions in terms of cell adhesion.

(I) Hydrophobin HFBI bilayers are prepared using the droplet interface bilayer (DIB) technique. Microfluidic devices are used for vesicle preparation or incorporation studies of HFBI in lipid bilayers.

The publication by **Nolle *et al.* in *Langmuir* 2023** (Addendum I) describes the water permeability of pure protein bilayers. The investigated bilayers are composed of the amphiphilic protein HFBI produced by the fungus *Trichoderma reesei*. The main result of the study was that the HFBI bilayers are essentially impermeable to water. By inserting an HFBI-cellulose fusion protein into the HFBI bilayer, it is shown that water permeability can be induced by steric hindrance of the protein order. Additional molecular dynamics simulations could not reproduce this low water permeability, most likely because the simulations underestimated the protein-protein interactions. Due to their low water permeability and high stability against osmotic pressure HFBI bilayers are an interesting alternative for lipid bilayers, but also for liposomes.

Therefore, the vesicle production of HFBI bilayers has been further enhanced by improving the microfluidic jetting method and by establishing another method for protein vesicle production, the microfluidic setup (see section 5.1.2). A higher production rate could enable applications in the field of drug delivery, for example.

However, the use of HFBI is not limited to pure protein bilayers and vesicles. The question has been raised, whether HFBI proteins can transfer their properties of high stability against external influences to lipid bilayers. By incorporating HFBI proteins into a lipid bilayer, it has been shown that HFBI stabilizes pores formed in the lipid bilayer, thereby stabilizing the entire bilayer (see section 5.1.3).

Due to the stable formation of interfacial layers, HFBI was also tested as an anti-adhesive coating for the adhesion of *Staphylococcus aureus* (*S. aureus*) in **Nolle *et al.* in Addendum V** . Compared to the uncoated OTS surfaces, HFBI coatings induced a strong reduction of *S. aureus* adhesion forces. To understand this reduction, the interaction of the surface with the cell, in particular with the macromolecules of the bacterial cell wall, has to be studied.

(II) The role of macromolecules in cell adhesion is investigated using the method of single-cell force spectroscopy, which allows the measurement of adhesion parameters for a single cell. Bacterial adhesion of *S. aureus*, a common cause of hospital related infections, is studied by varying surface parameters (Addendum II–V). Additionally, the adhesion of different cell wall macromolecule mutants of *S. aureus* has been measured to get a deeper insight into the role of different macromolecules (Addendum IV and V).

It has been shown in **Spengler *et al.* in *Nanoscale* 2019** (Addendum II) that only the available contact area of macromolecules on nano-rough surfaces can explain the adhesion values of *S. aureus* on these rough surfaces. The adhesion force of *S. aureus* is reduced with increasing roughness in the size of cell wall macromolecules. Since the adhesion of *S. aureus* cells depends on the number of macromolecules that can tether to a surface, the question arises whether the ability of macromolecules to tether to a surface also varies with different surface hydrophobicity on smooth surfaces.

The difference in the adhesion process of *S. aureus* on hydrophobic and hydrophilic surfaces is investigated in **Maikranz *et al.* in *Nanoscale* 2020** (Addendum III). It is shown that on hydrophobic surfaces many cell wall macromolecules can attach to the surface, but only weakly. In contrast, on hydrophilic surfaces only a few cell wall macromolecules can adhere, but strongly. The next question was whether it is possible to identify the macromolecules that are important for adhesion to hydrophobic or hydrophilic surfaces.

In **Spengler *et al.* in *Nanoscale* 2021** (Addendum IV), the role of different cell wall macromolecules such as cell wall proteins and teichoic acids are investigated using *S. aureus* knock-out mutants. While teichoic acids support adhesion to hydrophobic and hydrophilic surfaces, cell wall macromolecules are crucial for adhesion to hydrophobic surfaces, whereas they play only a minor role in adhesion to hydrophilic surfaces. A strong reduction of the adhesion force of the more negatively charged SA113 $\Delta dltA$ knock-out mutant on hydrophilic surfaces suggested an influence of electrostatic interactions.

This has been investigated in **Nolle *et al.* in Addendum V** by introducing surfaces with HFBI coatings of different electrical charge. It is confirmed that the adhesion of *S. aureus* can be influenced by the electrical charge of hydrophilic surfaces.

The possibility to study the adhesion of single cells is however not only of interest in the field of bacterial adhesion, but also in the field of human epithelial cell adhesion. Additional measurements of the influence of macromolecules on the adhesion of human epithelial cells have shown a reduction in adhesion with a decrease in the size of the focal adhesions on fibronectin (see section 5.3).

The main part of this dissertation consists of four chapters that are outlined in the following.

- **Background and State of the Art**: The proteins and cells used are introduced and the basics of the forces acting on macromolecules at interfaces are explained. In addition, the current state of knowledge for the scientific topics covered in this thesis is discussed.
- **Materials and Methods**: The methods used in this thesis are described in this chapter. The focus of this chapter is on the methods newly introduced in the research group of Prof. Karin Jacobs within the scope of this thesis. A list of the materials and instruments used in this study is provided.
- **Results and Discussion**: The results of the publications and other results obtained during this dissertation are described and discussed in this chapter.
- **Summary and Outlook**: The results of this thesis are summarized and possible future projects based on this work are outlined.

3 Background and State of the Art

3.1 Macromolecules at Interfaces

Macromolecules are molecules composed of many smaller molecular units (monomers). Molecules with a molar mass greater than 1000 g/mol are generally referred to as macromolecules. Macromolecules can be classified by size, origin, molecular structure, use, or composition. When classifying macromolecules by origin, a distinction is made between inorganic and organic macromolecules, with biopolymers being a subset of organic macromolecules [1, 38]. In this work, we focus on biomacromolecules, which are important components of almost all biological systems [2]. The main classes of biomacromolecules are proteins, polysaccharides, and nucleic acids. The function of each of them is determined by primary (type and sequence of individual monomer units: amino acids, monosaccharides and nucleotides), secondary (arrangement of individual chain sequences), tertiary (spatial structure) and, for proteins, quaternary structure (binding of several protein units) [38, 39].

The properties of biomacromolecules at interfaces are as diverse as there are biointerfaces [2, 40]: Protein adsorption on solid surfaces is widely discussed and studied due to its importance in medicine and biomimetic materials [41–43]. Biomacromolecules are also an important component of cell membranes and cell walls [1, 44]. Thus, they play a crucial role in the functionality of cell membranes and cell walls. Membrane channels composed of several proteins (e.g. aquaporins [45, 46]) allow the cell to exchange material with its environment [47, 48], but they are also used by some bacteria as pore-forming toxins to kill other cells [49, 50]. The adhesion of prokaryotic or eukaryotic cells to surfaces is controlled by biomacromolecules (adhesins, focal adhesions, cell adhesion molecules) [51–55]. Biomacromolecules also have a decisive influence on cell stiffness [56–58].

The above mentioned functions of biomacromolecules are only a fraction of the properties that have been explored. The function of individual biomacromolecules relevant to this work will be discussed later in this thesis (see chapters 3.2 and 3.3). The behavior of biomacromolecules at interfaces is determined by the prevailing interfacial forces or, if present, by specific adhesion mechanisms [59, 60].

3.1.1 Interfacial Forces

For the adsorption of biomacromolecules on abiotic surfaces and thus for the adhesion of cells to abiotic surfaces, intermolecular forces are crucial, since here, specific adhesion mechanisms are absent. The interfaces considered in this work are liquid-liquid, liquid-gas, or liquid-solid. For the systems in this work, the biomacromolecules are always in aqueous solution, which is crucial for the intermolecular forces acting. Therefore, the intermolecular

forces in aqueous solution are briefly discussed below. For detailed descriptions of all acting forces, the reader is referred to the literature used for this section [61–64] and other dissertations of the working group of Prof. Karin Jacobs [65–67]. The relevance and the range of the interactions involved may vary for different adhesion and adsorption processes (biomacromolecule/surface).

Steric Repulsion

The steric interactions belong to the repulsive interactions. The forces originate from the fact that two fermions of the same quantum number cannot come infinitely close to each other as a consequence of the Pauli prohibition [68].

Similarly, the repulsive force generated by macromolecule-covered surfaces (e.g., cells or protein-coated surfaces) due to the increasing entrapment of these macromolecules is referred to as (entropic) steric repulsion. This repulsive force can, for example, increase the stability of suspensions [69]. Also colloidal solutions can be stabilized by adding synthetic polymers or biopolymers, as it is used in paints, cosmetics and also in pharmaceutical products [63]. The theories of this steric repulsion are complex and again depend on the type and density of the polymer coating [70–72].

Electrostatic Interactions - Electrical Double Layer

Electrostatic interactions occur between all charged particles, equal charges repel each other and opposite charges attract each other. Proteins are always charged due to their composition of different amino acids in aqueous solution. This charge varies with the pH of the surrounding medium; the pH at which the net charge of the protein is zero is called the isoelectric point (IEP).

Surfaces are also usually charged in the surrounding medium and attract opposite charges (ions or charged molecules) [61]. A layer of weakly bound counterions forms on the surface, called the Stern or Helmholtz layer. This is followed by another diffuse layer of counterions, the electric double-layer [63]. The potential of this diffusive layer can be measured and is called the zeta potential. The electrostatic force depends on the geometry of the interacting objects and decreases exponentially with the distance between them. The distance at which the electric potential decreases by 1/e is called the Debye length and serves as a measure of the electrostatic force. Under physiological conditions, the Debye length is about 10 nm [73].

Van der Waals Forces

The interaction between dipoles is described in terms of van der Waals forces. Three types of interactions are distinguished, depending on the type of dipoles interacting with each other. The interactions of two permanent dipoles are called Keesom interactions, the interactions of a permanent and an induced dipole are called Debye interactions, and the interactions of a fluctuating and an induced dipole are called London dispersion interactions [74].

The distance dependence is r^{-6} for two atoms, but this dependence can vary considerably for extended bodies. Hamaker introduced the approach of additive van der Waals forces for macroscopic extended bodies [75]. This excludes two dipoles interacting with a third molecule, which is really only true for dilute gases [61]. In describing the van der Waals forces, Lifshitz included the dielectric function as well as the refractive index [76]. The distance dependence therefore increases to r^{-1} for a sphere interacting with a flat surface [63]. In general, van der Waals forces are always attractive in nature. However, in a medium, van der Waals forces can cause non-identical molecules to repel each other. This occurs when the van der Waals force from one molecule to the medium is stronger than the van der Waals force between two non-identical molecules.[63].

DLVO Theory

By combining the description of the electrostatic double layer and the van der Waals forces, the coagulation of colloidal solutions can be described. This description is named after Derjaguin, Landau, Verwey and Overbeek, DLVO theory [77, 78].

Electrostatic repulsion increases slowly at very small distances, meaning that at small distances van der Waals attraction always exceeds electrostatic repulsion. This leads to a minimum of energy in the vicinity of the surface. The electric double layer creates an energy barrier that varies with surface charge and must be overcome for the system to reach its minimum. A second minimum can occur in a solution containing ions [63].

To describe more complex systems, an extension of the classical DLVO theory by acid-base (electron donor - electron acceptor) interactions has been made to include short-range interactions [62, 63]. The extended DLVO theory is called xDLVO. However, for the heterogeneity of nature, it is still difficult to break down the interfacial interactions to simple expressions.

Hydrogen Bonds

When two electronegative atoms "share" a hydrogen atom, it is called a hydrogen bond. However, it is not a true "sharing" because the hydrogen atom remains closer to the electron of the atom to which it is covalently bonded. The hydrogen bond is too strong to be a bond formed by van der Waals forces, and too weak to be a covalent bond. It can rather be described as a kind of electrostatic interaction [79]. Due to their electronegativity, mostly oxygen, nitrogen and fluorine form hydrogen bonds. Hydrogen bonding, though, is not easy to describe [63]. The role of hydrogen bonds in the structure of macromolecules is crucial [63, 80], for example the structure of deoxyribonucleic acid (DNA) [81] and proteins is determined by them [82, 83].

Hydrophobic and Hydrophilic Interactions

The property of water to preferentially form hydrogen bonds and thus avoid contact with molecules and surfaces with which it cannot form hydrogen bonds is known as the hydrophobic effect. This hydrophobic effect can be helpful in understanding hydrophobic

and hydrophilic interactions. Hydrophobic surfaces, surfaces that can form no or very few hydrogen bonds with the surrounding aqueous solution, experience a stronger attraction in water than they would, for example, in air. This is because the water molecules do not want to come into contact with the surface, so surface contact is preferred. Hydrophilic surfaces, on the other hand, prefer to form hydrogen bonds with the surrounding aqueous solution, thereby creating an additional steric barrier. Hydrophobic surfaces are those with a water contact angle greater than 90°, and all surfaces with a lower water contact angle are called hydrophilic surfaces. There are several approaches to the theoretical description of these interactions and the resulting force. The main approaches to describe the hydrophobic force are *via* a Laplace pressure approach, a hydration approach, or an electrostatic explanation approach [61, 63].

3.2 Hydrophobins

Hydrophobins are a family of surface-active proteins of filamentous fungi [84–87]. They are compact, globular proteins, some of them with strong amphiphilic behavior. Hydrophobins owe their surface activity to the spatial aggregation of hydrophobic amino acids in a hydrophobic patch [88, 89]. In the group of Prof. Jacobs they were initially chosen to facilitate the comparison between experiment and simulation, since hydrophobins are conformationally stable (four disulfide bridges [90, 91]) and the orientation at interfaces is well defined (amphiphilicity).

Hydrophobins can be divided into two classes, class I and class II hydrophobins. The main difference between these two classes is the solubility of the hydrophobin aggregates formed. While class I aggregates are very difficult to redissolve, class II aggregates can be dissolved in simple solvents such as ethanol [92].

The natural roles of hydrophobins in fungi are manifold. By attaching to the fungal boundary layer, hydrophobins can function to repel water, modify surface tension, and adhere to hydrophobic surfaces [87, 88, 93, 94].

Due to the strong amphiphilicity, certain hydrophobins became technically interesting for stabilizing emulsions and foams [95–97]. Hydrophobins have also attracted interest for applications in biomedicine, for example to influence the adhesion of proteins and cells [98, 99].

3.2.1 Hydrophobin HFBI

In this study, the class II hydrophobin HFBI (pronounced HFB-"one") as well as the HFBI charge mutant (HFBI D40Q/D43N) and the HFBI-cellulose fusion protein (HFBI-dCBM) were investigated for their interfacial behavior. HFBI is derived from the fungus *Trichoderma reesei* and has a molecular weight of 7.5 kDa [100].

The molecular structure of HFBI, see Figure 3.1a, consists of one alpha-helix, four beta-sheets, and the four disulfide bridges found in all hydrophobins. The hydrophobic patch is composed of 13 hydrophobic amino acids (Leu12, Val23, Leu24, Leu26, Ile27, Leu29, Val59, Ala60, Val62, Ala63, Ala66, Leu67, and Leu68, colored in red Fig. 3.1a)

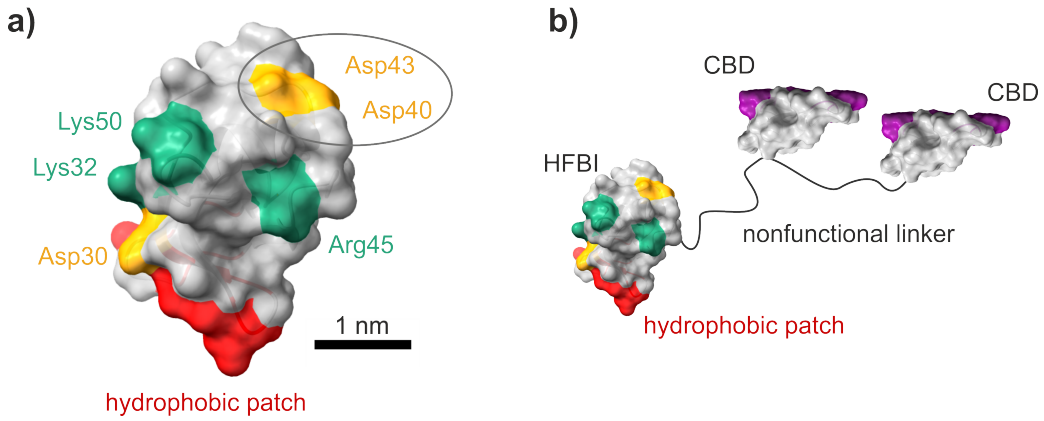

Figure 3.1: a) Molecular structure of hydrophobin HFBI (Protein Data Bank (PDB) entry 2FZ6 [101, 102]) with the hydrophobic patch marked in red. The charged side groups are colored green for basic and yellow for acidic (after [14]). The two acidic aspartic acids (Asp40, Asp43) are highlighted because they are replaced by neutral glutamine and asparagine in the HFBI charge mutant HFBI D40Q/D43N [103]. b) Sketch of the HFBI cellulose fusion protein HFBI-dCBM with its two cellulose binding domains (CBD), Cellobiohydrolase I from *Trichoderma reesei* (PDB entry 1CBH [104, 105], after [106]). To give an idea of the size ratio of the HFBI molecule to the two CBDs, the proteins are shown on the same scale.[a]

[a] Molecular structures of HFBI and Cellobiohydrolase I were drawn with UCSF ChimeraX, developed by the Resource for Biocomputing, Visualization, and Informatics at the University of California, San Francisco, with support from National Institutes of Health R01-GM129325 and the Office of Cyber Infrastructure and Computational Biology, National Institute of Allergy and Infectious Diseases [107].

[101]. In addition, HFBI has six charged side groups exposed to the surface, three basic and three acidic (colored in green (basic) and in yellow (acidic) Fig. 3.1a).

HFBI D40Q/D43N

The HFBI charge mutant HFBI D40Q/D43N lacks two negatively charged side groups (Asp40 and Asp43, see Fig. 3.1a). The two aspartic acids are replaced by the neutral amino acids glutamine and asparagine. The change in amino acids at the protein surface results in a shift to a higher pH for the isoelectric point (IEP). While HFBI has an IEP of 6.1, HFBI D40Q/D43N has an IEP of 7.0 [103].

HFBI-dCBM

HFBI-dCBM (HFBI-double cellulose binding molecule, also called HFBI-DCBD) consists of an HFBI protein connected by linkers (amino acid chains) to two cellulose binding domains (see Fig. 3.1b) [108]. The cellulose binding domains (cellobiohydrolase I, CBH I) are extracted from *Trichoderma reesei* as the protein HFBI [104]. The molecular mass of

the linkers and the two cellulose binding domains is about 11 kDa. Thus, the molecular mass of HFBI-dCBM is 18.5 kDa, more than twice the original mass of HFBI [108].

These proteins are used for their binding affinity to cellulose. Therefore, they are of interest in the field of composite materials [106, 109] and pharmaceutical nanotechnology [110, 111].

3.2.2 HFBI Interfaces

At the interface, HFBI forms a crystalline monolayer with a honeycomb structure [112, 113]. Most descriptions of the crystalline structure refer to HFBI monolayers formed at the water-air interface [114–117]. However, monolayers formed at the water-solid interface (highly oriented pyrolytic graphite, HOPG) have also been reported to have this crystalline structure [118]. Molecular dynamics simulations have determined that the unit cell consists of six HFBI proteins, as also seen in electron cryo-microscopy [119, 120]. Changes in the charged amino acids on the HFBI outer surface do not significantly alter the highly ordered structures of the proteins at interfaces [103, 118]. Instead, bulky fusion proteins introduce a steric hindrance to film formation at the water-air interface. Interfacial layers are still formed, but the structure of these films seems to be less highly ordered [110, 121].

During the adsorption process at the water-air interface, HFBI retains its conformation [122]. The amphiphilicity of HFBI proteins and their surface activity suggest an adsorption behavior similar to that of lipids. However, HFBI shows an almost constant adsorption rate, which is atypical for Langmuir-type kinetics [121]. The reasons for this adsorption behavior are not yet clear. One possible reason could be the high energy gain resulting from the binding of HFBI at the interface. HFBI has a significantly higher adsorption strength compared to other biomolecules, resulting in almost irreversible binding to interfaces (studied at the oil-water interface) [123].

Due to this high adsorption strength a water droplet containing HFBI does not shrink like a typical water droplet, but flattens at the top-surface (see section 4.5 Fig. 4.3a). Since the proteins do not detach from the water-air interface, the protein layer behaves elastically and forms wrinkles [116, 124]. These flattened HFBI droplets have been widely used to coat surfaces with an HFBI monolayer and to study the crystalline order of HFBI monolayers [103, 114–117]. The HFBI coatings alter the surface hydrophobicity of the coated surface [125, 126]. While a hydrophobic surface becomes hydrophilic, a hydrophilic surface becomes hydrophobic [127]. The binding strength of HFBI to surfaces could be measured *via* single molecule force spectroscopy and did show an enhanced binding strength of HFBI in the HFBI monolayer compared to single HFBI attached to the surface [127].

The applications of HFBI interfaces are versatile. HFBI interfacial layers can be used to stabilize emulsions [128, 129]. In beer production, this stabilizing effect is also negatively experienced in the area of unwanted beer gushing [129, 130]. HFBI fusion proteins have also shown great potential in the field of biotechnological and biomedical applications [110, 118, 131]. Furthermore, secondary protein adsorption on HFBI monolayers has been shown to be influenced by the HFBI coating and tunable by changing the charge of the HFBI surface [103]. First studies on bacterial adhesion on hydrophobin coatings (not

HFBI) have been performed and showed anti-adhesion effects [132, 133]. In this thesis, the adhesion of the bacterium *Staphylococcus aureus* to hydrophobin (HFBI) coated surfaces was tested, see Addendum V.

3.2.3 HFBI Bilayers and Vesicles

Besides the formation of HFBI monolayers, it has already been possible to produce HFBI bilayers and vesicles [13, 14]. HFBI bilayers and vesicles can be produced with a hydrophobic core (like lipids) but also with a hydrophilic core. Van der Waals forces seem to play an important role in the attraction of two monolayers to form a bilayer. The stability against lateral tension is extremely high for HFBI bilayers, while the adhesion energy is in the same order of magnitude as for lipids [14].

Vesicles could be produced by two different methods: microfluidic jetting and gel extrusion. By varying the bilayer core, water/water, oil/oil, and air/air vesicles could be produced. In addition, a functional gramicidin A channel could be incorporated into an HFBI vesicle [13]. This proved that a real bilayer is formed and the channel forming process is not essentially hindered.

It is precisely these properties of the HFBI bilayers and vesicles that have made them so interesting for the research group led by Prof. Karin Jacobs. Possible future applications include cargo transport and emulsion stabilization. Hydrophobin vesicles could transport not only water-soluble substances in water, but also oil-soluble substances in oil. Similarly, the more technical and application-oriented task of exploring the functions of channels and pores in the extremely stable HFBI bilayers could also be of future interest.

However, a number of questions remain to be answered. The fluidity of HFBI bilayers is still unclear. Channels can be incorporated, suggesting at least some fluidity in the bilayer [13]. Also, little is known about the characteristics of HFBI bilayers for use in physiological environments. Therefore, in this work, the water permeability of HFBI bilayers with a hydrophobic core and their stability to osmotic pressure were investigated (Addendum I). In addition, the preparation of HFBI vesicles was further developed to achieve a higher production rate and thus increase the potential applications of these vesicles (section 5.1.2). Due to the high stability of HFBI at interfaces, the incorporation of HFBI into lipid membranes and the influence on pore formation were also investigated (section 5.1.3).

The behavior of more complex biomacromolecular systems at interfaces can vary greatly due to the interplay of the different biomacromolecules. The adhesion behavior of cells is built precisely on this interplay of macromolecules at the cell surface.

3.3 *Staphylococcus Aureus*

Staphylococcus aureus (*S. aureus*) is a round (Greek: *kókkos*), 1 µm large (diameter), facultative anaerobic bacterium (prokaryote). In addition to its round shape, *S. aureus* owes its name to its cluster formation in grape-like form (Greek: *staphylé*) and its golden pigmentation (Latin: *aureus*). *S. aureus* is a colonizing opportunistic pathogen (COP)

[134], and as such a natural colonizer of humans [135], preferentially in the nose [136, 137]. Under certain negative circumstances (weakened immune system, open wounds, etc.) it can lead to infections [138]. The high adaptability of *S. aureus* leads to the development of resistance to possible treatments with antibiotics [139–141]. Methicillin-resistant *Staphylococcus aureus* (MRSA) is one of the main causes of infections in hospitals [142–144]. When a bacterium adheres to a surface, the first step of biofilm formation is complete and the next steps of biofilm formation are initiated: multiplication, exodus, maturation, and dispersal [145]. The formation of biofilms protects the bacteria from immune defenses [146] and antibiotics [21]. Once a biofilm is formed, it is very difficult to remove. In the case of implants, this often means removal of the entire implant [21, 22].

3.3.1 *Staphylococcus Aureus* Cell Wall

S. aureus is a gram-positive bacterium. In Figure 3.2 its cell membrane and its outer layer, the cell wall, are shown. The main component of the cell wall is peptidoglycan, a two-component polysaccharide layer. Various adhesion factors are anchored to it and to the underlying cell membrane (see Fig. 3.2). Adhesion factors include teichoic acids, which can be divided into lipoteichoic acids (LTAs) and wall teichoic acids (WTAs), as well as proteins, which can be divided into cell wall anchored proteins (CWA proteins) and non-cell wall anchored proteins (non-CWA proteins) [23]. The functions of the cell wall include cell shape [147], stability against osmotic stress [148, 149], and, importantly for this work, contact formation with the surface initiated by cell wall macromolecules [26, 150, 151] .

Peptidoglycan

The peptidoglycan of the bacterial cell wall is a unique polymer: It consists of two types of polysaccharide chains (N-acetylglucosamine and N-acetylmuramic acid) that are highly cross-linked by peptide bridges [153]. Peptidoglycan is subject to constant formation and degradation, which is essential during cell division [154, 155]. This process is supported by autolysin enzymes, which can cut the peptidoglycan network, leading to a rearrangement of the peptidoglycan [156, 157]. Autolysin activity is important not only for peptidoglycan rearrangement but also for the composition of CWA proteins [158].

This peptidoglycan layer has been selected as a target for antibiotics in several studies because of its critical role in the bacterial cell cycle [159–161]. More details about the structure and the function of peptidoglycan can be found in recent articles [162, 163]. The following description of *S. aureus* adhesion factors is based on several review articles on previously known adhesion factors of *staphylococci*, especially *S. aureus* [23, 24].

Teichoic Acids

Accounting for up to 60 % of the total cell wall mass, teichoic acids are a major component of the cell wall of gram-positive bacteria, including *S. aureus* [164]. The distinction between wall teichoic acids (WTAs) and lipoteichoic acids (LTAs) is based on their composition and

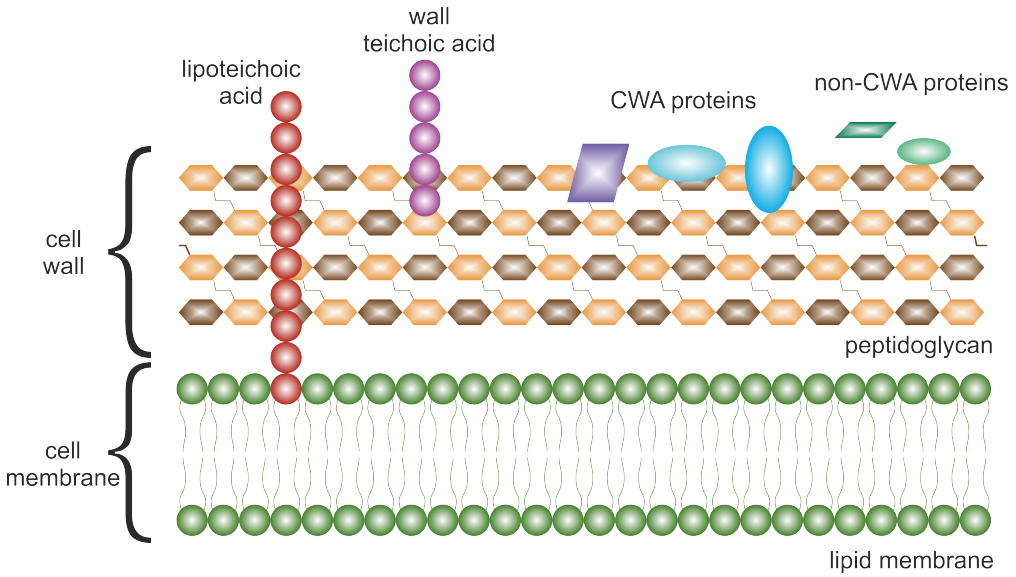

Figure 3.2: Schematic illustration of the bacterial cell wall of *S. aureus* and its adhesion factors (inspired from [65, 152]). The adhesion factors are lipoteichoic acids (LTAs), wall teichoic acids (WTAs), cell wall anchored proteins (CWA proteins) and non-cell wall anchored proteins (non-CWA proteins).

anchorage in the cell wall/cell membrane. Whereas WTAs consist of phosphate and ribitol groups and are covalently bound to the peptidoglycan layer, LTAs consist of phosphate and glycerol groups and are anchored to the cell membrane *via* glycolipids [24]. Glycosyl and D-alanyl esters are attached to the teichoic acids. Inhibition of D-alanylation by the absence of the gene *dltA*, which is important for the synthesis of D-alanylated lipoteichoic acids, results in a higher negative surface charge of the cell wall [165]. The *S. aureus* $\Delta dltA$ mutant, which has this deficiency in D-alanylation, has a reduced ability to adhere to polystyrene and glass [166]. The absence of *dltA* also results in a decrease in autolysin activity [167, 168], which in turn leads to a change in CWA protein composition [158]. Single changes in cell wall composition can always lead to multiple subsequent changes.

WTAs in particular appear to play an important role in the adhesion of *S. aureus* cells [164, 169]. The influence of WTAs can be tested using the *S. aureus* $\Delta tagO$ mutant. TagO is a gene that is responsible for the synthesis of WTAs. If this gene is missing, these cells lack WTAs, while the synthesis of LTAs is not affected [151]. The colonization of skin and nasal epithelial cells with *S. aureus* is largely influenced by the absence of WTAs [151, 170, 171].

Proteins

Proteins associated with *S. aureus* adhesion are abundant. A distinction is made between cell wall anchored (CWA) proteins and non-CWA proteins [23]. In the following, the two groups of cell wall proteins will be discussed and individual proteins will be presented.

The CWA proteins are generally bound to peptidoglycan by sortase A (SrtA) [172, 173]. Inhibition of SrtA therefore leads to a very strong loss of *S. aureus* CWA proteins and a simultaneous reduction of the binding affinity to fibronectin [174–176] and a reduced colonization of the nose [170]. There are more than 20 different CWA proteins on the *S. aureus* cell wall. Currently, five families of *S. aureus* CWA proteins are distinguished, although some discovered proteins have not yet been assigned to a family [23, 25].

Most CWA proteins are classified as belonging to the **MSCRAMM** (**microbial surface components recognizing adhesive matrix molecules**) family, which includes clumping factor A (ClfA) and B (ClfB). ClfA and ClfB are important for the adhesion of *S. aureus* [25, 177]. While ClfA binds to immobilized fibrinogen and is a part of the *S. aureus* system for immune escape [25, 178]. ClfB is more important for the colonization of the skin and of the nose [179–181]. Fibronectin binding protein A (FnBPA) and B (FnBPB) are other adhesins belonging to the MSCRAMM family. As their name suggests, they bind to fibronectin, but also to other extracellular matrix (ECM) components [182–184] and are an *S. aureus* invasion factor [185, 186]. The second family to be mentioned is the **near iron transporter (NEAT) motif protein** family. A protein of this family which is associated with adhesion is the iron-regulated surface protein A (IsdA). In addition to its role in iron acquisition, it can bind to desquamated nasal epithelial cells and is therefore also active in colonization of the nose [187, 188]. The **tandemly repeated three-helical bundle protein** family consists of only one protein, Protein A (SpA). It induces *S. aureus* cell aggregation [189] and can cause inflammation of lung epithelial cells [190]. There are also the **G5-E repeat protein** family with the surface protein G (SasG), which promotes nasal colonization [191], and the **L-lectin/cadherin-like protein** family with the serine-rich adhesin of platelets (SraP) protein, which promotes human platelet adhesion [192]. Further information on all *S. aureus* CWA proteins can be found in the literature [23–26].

There is also a variety of different non-CWA proteins at the *S. aureus* cell wall. A protein family that is often associated with cell adhesion is the **SERAM** (**secretable expanded repertoire adhesive molecule**) family. Adhering to fibrinogen, fibronectin and other ECM components the extracellular adherence protein (Eap) and the extracellular matrix protein (Emp) are two important *S. aureus* adhesins [23, 24, 193]. In addition to its multiple adhesive binding capabilities, Eap has also been attributed invasive and immunomodulatory properties as well as negative effects on the wound healing process [194]. Recently, it has also been shown that Eap can modify plaque formation [195] due to its ability to influence immune cell immigration [196, 197]. Besides the SERAM family, there are **autolysins**. These are non-CWA proteins that may have adhesive properties in addition to their enzymatic properties [23, 24]. The autolysin Atl, in addition to having an indirect effect on cell adhesion by affecting the distribution of CWA proteins [158], also has a direct effect on adhesion by binding to ECM components of human endothelial cells [198].

The role of different adhesion factors of the *S. aureus* cell wall on the adhesion were studied in this thesis, see Addendum IV and V.

3.4 Bacterial Adhesion

Bacterial adhesion is mediated by cell wall macromolecules. Depending on the type of surface to which the bacterium adheres, adhesion may be mediated by specific and/or non-specific adhesion mechanisms.

On the one hand, specific adhesion mechanisms, are mechanisms that take place *via* specific receptor-ligand interactions. The binding to the ligand is mostly established by specific cell wall macromolecules (receptors). For example, MSCRAMMs mostly bind to the corresponding ligand *via* the dock lock latch mechanism or the collagen hug mechanism [26]. For receptor-ligand binding, hydrophobic interactions and hydrogen bonding are of major importance [178, 199, 200].

On the other hand nonspecific adhesion mechanisms are caused solely by interfacial forces between the cell surface and the substrate being adhered to. A reduced adhesion of *Staphylococcus carnosus* due to van der Waals forces could be measured by changing the subsurface (thicker oxygen layer on a silicon surface) without changing other surface parameters (roughness, hydrophobicity, surface energy) [201]. However, also interfacial interactions such as electrostatic and hydrophobic interactions have been shown to play a role in bacterial adhesion [202–206]. It is important to note that the forces between the macromolecules and the surfaces must be considered for cell-surface adhesion. Using single-cell force spectroscopy (SCFS) it was shown that *S. aureus* can build up a force towards the surface before the cell wall even touches the surface [207]. This can only be explained by the cell wall macromolecules tethering to the surface. Therefore, the macromolecules must be included in the force description of a bacterium adhering to a surface.

3.4.1 Influence of Surface Properties to *Staphylococcus aureus* Adhesion

In this work we focus on the role of the macromolecules in non-specific adhesion mechanisms. Therefore, we used abiotic surfaces with different parameters in roughness, hydrophobicity, surface charge. In order to better classify the results of this dissertation, the state of the art of *S. aureus* adhesion research with respect to these surface parameters is considered separately below.

Surface Roughness

The roughness and structure of a surface can affect the adhesion of bacteria, including *S. aureus*. There are several studies that have investigated the influence of surface roughness on the adhesion of *S. aureus*.

Most of the studies used methods that allowed the bacteria to freely adsorb to the surface and then measured the adhesion by the number of adherent cells. Therefore, there are no concrete adhesion force values measured. Lu *et al.* [27] measured the adhesion of *Staphylococcus aureus*, *Escherichia coli* (*E. coli*) and *Pseudomonas aeruginosa* (*P. aeruginosa*) on PDMS (polydimethylsiloxane) surfaces with $0.5-4\,\mu m$ grooves. It was observed that the size of the bacteria compared to the size of the structure was

an important factor for bacterial adhesion. When the structure was smaller than the size of the bacteria, adhesion was most effectively reduced. Considering the roughness in the range below the size of *S. aureus*, on randomly structured titanium oxide films of different thickness and roughness (root mean square (RMS): 16–32 nm), an increase in *S. aureus* adhesion was observed with decreasing roughness [28]. However, there was no significant difference in adhesion between surfaces with roughness around 26 nm and 32 nm. Measurements on nanostructured PDMS showed the same trend of reduced adhesion on rougher surfaces in the nanometer scale [29]. The adhesion of *S. aureus* on rough PDMS was strongly reduced (RMS = 14 nm) compared to smooth PDMS (RMS = 1 nm). Measurements with *E. coli* showed the same trend but to a lower extent. Decreasing the roughness even more to the lower nanometer range on hydrophilic glass surfaces (RMS: 1.6 nm, 2.8 nm) [30] or on hydrophobic titanium films (RMS: 0.18 nm, 0.52 nm) [31] showed also an increase of adhered *S. aureus* cells with lower roughness. However, on the glass surfaces, this difference was not as pronounced as for *E.coli* and *P. aeruginosa*. While on the hydrophobic titanium *P. aeruginos* showed no difference in adhered cells between both roughnesses.

In addition, atomic force microscope (AFM) studies were performed to measure the effect of surface roughness on the adhesion of *S. aureus* cells. A lateral force was applied to already adhered *S. aureus* cells *via* an AFM cantilever, and the cells that did not detach due to the applied lateral force could be counted [208]. Adhesion was compared on polished, unpolished, and abraded stainless steel. The polished and abraded stainless steel showed a linear unidirectional surface structure. Peak to valley distance varied between these two surfaces from 0.04 µm (polished) to 0.3 µm (abraded). In contrast to the other studies presented, the adhesion was stronger on the rougher surfaces, the abraded steel. Two other AFM studies used SCFS to study the adhesion force of *S. aureus* on silicon nanopillars, with a pillar-to-pillar in the range of 200 – 800 nm [209, 210]. Compared to smooth silicon surfaces they could record a decrease of adhesion force for *S. aureus*, however, the adhesion did not differ strongly between the different pillar-to-pillar distances.

In some studies, the contact area is discussed as the reason for the changes in adhesion with altered surface roughness. So far, the bacterial-surface contact is often described as a simple sphere touching a surface. The macromolecules of the cell surface are neglected. In this context, a study has shown that the cell wall macromolecules of *S. aureus* are crucial for determining the contact area [211]. The contact area of *S. aureus* can vary greatly from cell to cell due to the macromolecules and averages to a circular contact area with radii of 150–350 nm on smooth silicon surfaces.

However, it should be noted that the exact relationship between the contact area of macromolecules and rough surfaces is still not well understood. The description of the surface roughness by simple RMS values and the description of the cell as a simple sphere are not sufficient. Concrete values for adhesion, such as adhesion force or adhesion energy, are also needed to describe a possible correlation. Therefore, a new study was initiated and its results are described in Addendum II.

Surface Hydrophobicity

The tethering of cell wall macromolecules to a surface and thus the adhesion of *S. aureus* to abiotic surfaces is also strongly influenced by hydrophobic interactions [203, 207, 211–214]. By creating a surface with a sharp transition from hydrophobic surface properties (advancing water contact angle (WCA): 112°) to hydrophilic (advancing WCA: 8°), it was shown that the adhesion force differs by more than an order of magnitude with strong adhesion on the hydrophobic surface [211]. By exploiting the altered adhesion on hydrophilic and hydrophobic surfaces, it was then possible to determine the contact area of *S. aureus* on smooth surfaces as mentioned above. The same influence of hydrophobic interactions on the tethering of cell wall macromolecules could also be shown for other bacteria (gram-positive and gram-negative).

Some studies also report a negative effect on *S. aureus* adhesion by creating superhydrophobic surfaces [32, 33]. However, the superhydrophobicity of these surfaces is highly dependent on the roughness of the surface. The surfaces are superhydrophobic at the macroscopic scale, but at the microscopic scale, where the macromolecules bind to the surface, this hydrophobicity can be different. Therefore, this effect cannot be considered separately from the introduced surface roughness. In Addendum III, bacterial adhesion to smooth surfaces of different hydrophobicity was studied.

Surface Charge

It has long been known and studied that electrostatic interactions affect bacterial adhesion [215, 216]. Many bacteria have an overall negative surface charge, including *S. aureus* [217, 218]. Electrostatic interaction with charged surfaces is therefore expected, and given the overall cell surface charge of *S. aureus*, attraction to positively charged surfaces and repulsion from negatively charged surfaces would not be surprising. Several studies confirm better adhesion to positively charged surfaces for the negatively charged *S. aureus* cells [34–37]. For example, Zhu *et al.* used different polymers to build (layer-by-layer) surfaces with different IEPs [34]. Surface coverage tests for *S. aureus* were performed at pH 7.4 in phosphate buffered saline (PBS). Surfaces with an IEP of 9.7, 7.3, and 6.4 were tested and showed surface coverage of 45 %, 5 %, and nearly 0 %, respectively. Since the surface layer always consisted of the same polymer (polyethyleneimine), the chemical properties were kept constant. However, the effects of van der Waals forces due to the different layer thicknesses were not taken into account.

There are also other studies showing the opposite effect of surface charge on adhesion [219, 220]. Polarizing hydroxyapatite (HAp) electrically and allowing bacteria to adhere, showed a faster adhesion of *S. aureus* on negatively charged HAp [219]. Also the colony size was altered by the charge of the HAp, there were more bacteria in a colony on the negatively charged HAp compared to the number of bacteria in a colony on positively charged HAp. However, it was already discussed in the paper that this surface charge effect could be due to a direct effect of the electrostatic force on the bacteria or due to positive charges from the medium covering the negatively charged surface and allowing the cell to bind.

All of these measurements were again performed by allowing the bacteria to adsorb freely to the surface. Therefore, there is a lack of concrete adhesion values like adhesion force for the influence of charge on *S. aureus* adhesion. To fill this gap, SCFS measurements on surfaces of different charge were accomblished in this thesis, see Addendum V.

3.5 Human Retinal Pigment Epithelial Cells

Eukaryotes include animal, plant, and fungal cells. Human eukaryotic cells are not surrounded by a cell wall, but "only" by a cytoplasmic membrane, which distinguishes them from prokaryotes. In addition, an eukaryotic cell has a nucleus. This nucleus is clearly separated from the other cell components by a membrane. In this chapter, human retinal pigment epithelial (RPE-1) cells will be briefly described.

The retinal pigment epithelium (RPE) is a single layer of polygonal cells that attach to the photoreceptors on one side and to Bruch's membrane on the other. By having tight junctions between the RPE cells, they form a selective barrier between the retina and the choroid [221, 222]. The RPE-1 cell line is commonly used for migration studies because RPE cells can migrate in a mesenchymal but also amoeboid manner [223–225].

Amoeboid migration relies on a constant retrograde flow of actin, which can only be observed under confinement. Unlike mesenchymal migration, amoeboid migration is frictional. The cells do not establish a connection to the environment, but the movement depends on the contractile forces of the actin network. [226–228]. It could be shown by leukocytes that for adhesion under confinement, the adhesive transmembrane proteins, integrin, do not take part in the movement of the cell [229]. In contrast, mesenchymal migration is based on cell adhesion to the underlying surface [227, 230]. The connection of the cytoskeleton to the adhesive surface is formed by focal adhesions. Focal adhesions are clusters of proteins (mostly integrins) on the cell surface that can bind to the ECM and are connected to the actin network [231].

Changing the size of the actin filaments by adding the actin stabilizer miuraenamide A (MiuA) showed an influence on the number and size of focal adhesions [232]. The focal adhesions showed a higher number but a smaller size for stabilized actin in RPE-1 cells. This change also resulted in reduced mesenchymal migration. The underlying adhesion forces of this reduced mesenchymal adhesion were investigated in this work, see section 5.3.

4 Materials and Methods

This chapter describes proteins, cells and other material as well as methods used for this thesis and refers to additional literature where relevant. A focus is set on methods newly introduced to the working group of Prof. Karin Jacobs within this thesis.

Furthermore, a list of instruments and materials used in this work at Saarland University is attached for a better overview.

4.1 HFBI Purification and Solutions

Lyophilized hydrophobin HFBI was purified at VTT, Technial Research Centre of Finland, Espoo [112, 233, 234] and prepared from the mycelium of the HFBI overexpressing *Trichoderma reesei* strain VTT-D-98692. The process consists of four steps: protein extraction from the mycelium, berol extrusion *via* aqueous two-phase systems (ATPS), high-performance liquid chromatography (HPLC) and, as the last step, freeze-drying of the purified HFBI [234]. Usually, the Finnish group around Dr. A. Paananen has sent us the needed lyophilized HFBI proteins. However, to get a feeling for the production process, I stayed with the group and was performing the purification process myself under supervision of D. Bozzhigitova and Dr. M. Lienemann.

For the first step, the frozen mycelium (Fig. 4.1a) is divided into small pieces and 30–50 mg are placed in a plastic bag in a water bath at room temperature until ice is melted. This thawed mycelium is then mixed in a glass beaker at a concentration of 5 mg/ml with a solution containing 4 M guanidinium hydrochloride (GDM-HCl) – 0.2 M tris-(hydroxymethyl)-aminomethane hydrochloride (Tris-HCl) solution with a pH adjusted to 7, first with a Polytron homogenizer (8000 rpm, 2-3 times for 30 seconds, Kinematica, Swiss) for coarse mixing and then with an electronic stirrer (120 rpm for two to three hours) to obtain a homogeneous solution. After centrifugation (5000 rpm, 25 min, 20 °C) of this mixture, the supernatant is decanted for further use.

In the second step, the supernatant is mixed with ultra pure water (MilliQ) at a 1:1 ratio, filtered (Miracloth 475855-1R, Millipore), and pH adjusted to a pH of 5.5 to 6 with 1 M acetic acid. The nonionic surfactant Berol 532 (Akzo Nobel, Sweden) is then added at a concentration of 2 % (w/v) and stirred until a homogeneous solution is formed. This mixture is then allowed to settle for at least two hours up to overnight for the first aqueous two-phase separation (Fig. 4.1b). Berol is binding the proteins and thereby concentrating these in the upper detergent phase over the buffer phase. To remove unbound material, the detergent phase is mixed with 50 mM sodium acetate (NaAc) – 40 mM ethylenediaminetetraacetic acid (EDTA, pH 5.15) at a ratio (v/v) of approximately 2:1 and the phase separation is performed again (about 1 hour) in an

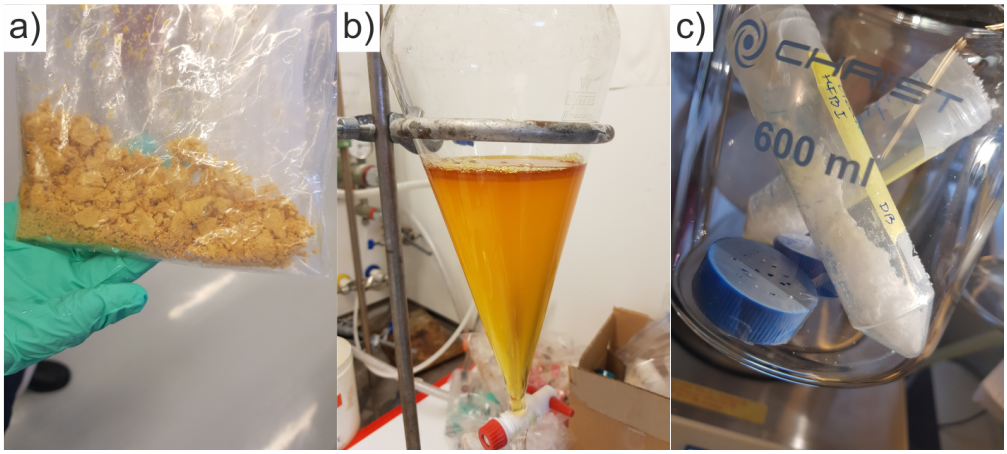

Figure 4.1: Different stages of the HFBI purification process: a) HFBI mycelium in frozen state, b) first aqueous two-phase system (ATPS) separation, c) freeze-dried, purified HFBI.

aqueous two-phase system. HFBI is transferred from the detergent phase to the buffer phase by back-extraction with isobutanol. For this purpose, additional buffer (50 mM NaAc – 40 mM EDTA, pH 5.15) is added in a ratio of 1:6 to the detergent phase as well as isobutanol in a tenfold higher amount than the detergent volume. After careful mixing again, a two-phase separation is initiated for at least 30 min, but can also be done overnight. Isobutanol is binding to Berol and thereby releases the HFBI protein into the buffer phase. This back-extraction step can be repeated several times with the detergent phase to ensure maximum protein yield.

The resulting buffer protein solution is sonicated, centrifuged, and then purified by high-performance liquid chromatography (HPLC, Äkta Explorer, Pharmacia, Sweden) using a Vydac C4 column (1 x 20 cm, Vydac, USA) and a solvent gradient of acetonitrile (0–100 %) containing trifluoroacetic acid as a pairing agent at a concentration of 0.1%. The purity and protein content of HPLC elution fractions are determined by ultra performance liquid chromatography (UPLC) and absorption spectroscopy at λ=230 nm, respectively. Samples containing concentrated and sufficiently pure HFBI are pooled, frozen and lyophilized (Fig. 4.1c).

The resulting lyophilized HFBI is storable and was dissolved in 10 mM NaAc buffer (∼pH 5) with adjusted protein and ion concentration as required by the experiment performed.

The HFBI charge mutant HFBI D40Q/D43N [103] and the HFBI cellulose fusion protein HFBI-dCBM [108] were produced from our collaborators at the VTT.

4.2 Droplet Interface Bilayer

A droplet interface bilayer (DIB) is a bilayer formed when two droplets covered with surface active molecules (micelles) are brought into contact [17, 235]. The DIB method is often used to determine the water permeability of a bilayer [5, 6, 236].

Two 10 mM NaAc droplets (radius: 052-0.62 mm) are placed in an oil bath (hexadecane) with an HFBI concentration of 4 µM. An osmotic concentration difference is created by adding KCl to one of the droplets. Since the droplets have a higher density than the oil used, they sink to the bottom. Therefore, the glass Petri dish used was previously coated with polydimethylsiloxane (PDMS) to prevent the droplets from spreading and sticking.

Following the adsorption rate described by Hähl *et al.* [121], the droplets are allowed 30 min to form a dense protein monolayer. These micelle-like droplets are contacted and a bilayer is formed at the contact site. The contact sites formed in this way are HFBI bilayers as shown by previous bilayer thickness measurements [13]. After the bilayer is formed, the perimeter of the droplet is determined and, assuming a spherical shape, the volume is calculated.

The osmotic gradient between the two droplets leads to a change in volume if the bilayer is permeable to water. The droplet with a high salt concentration becomes larger and the droplet with a low salt concentration becomes smaller. The permeability value can be calculated from the change in volume of the droplets. More detailed information on the determination of the permeability of HFBI bilayers and the setup used can be found in Addendum I.

4.3 Microfluidic Devices

For the results described in 5.1.2 and 5.1.3, microfluidic devices were used, which could be fabricated thanks to the close collaboration and the possibility to use the laboratory of the group of Prof. Seemann, Saarland University, Germany. Microfluidic devices were fabricated using soft-litography [237, 238]. The basic steps are described below.

- First, a detailed two-dimensional drawing of the desired channel structure is constructed in a dedicated graphics program such as AutoCAD. This structure is then printed inversely onto a photomask with an approximate resolution of 5 µm.
- In the clean room, a negative photoresist (SU-8 100) is applied to a cleaned silicon wafer and spin-coated to obtain a uniform film thickness. The thickness of the film determines the subsequent channel height. The coated silicon surfaces are then pre-baked on a hot plate.
- In the next step, the photomask is aligned on the photoresist and then exposed to UV light. This cross-links the photoresist area unprotected by the photomask, the channel structure, and is then stabilized by a post-bake on the hot plate.
- A developer (MR-dev 600) is then used to remove the non-crosslinked photoresist.

With these steps the silicon master production is completed. The silicon master can now be cast with PDMS (Sylgard 184) in a base to agent ratio of 10:1 and cured in an oven. After complete curing, the PDMS can be removed from the silicon master and the master can be reused. To close the channel structure, the PDMS structure is placed in air plasma together with a glass slide. This oxidizes the interfaces that come into contact with the plasma, and by pressing these two interfaces (PDMS and glass slide) together, they are covalently bonded to each other (Si-O-Si). The finished device is then re-hydrophobized overnight in an oven at 125 °C.

4.3.1 Electroporation Measurements

The electroporation measurements themselves were performed in a microfluidic setup similar to the one described in Khangholi *et al.* [239]. It is a microfluidic structure with two parallel channels (width: 300µm, height: 100µm) connected in the middle of the length by a small intersection (see Fig. 4.2).

The flow in this microfluidic structure is generated by hydrostatic pressure. The flow velocities in the two channels are determined by the height of two separate fluid reservoirs. The reservoirs are connected to the channels by Teflon tubing. To generate 1,2-Di-(9Z-octadecenoyl)-*sn*-glycero-3-phosphocholin (DOPC) bilayers, the entire microfluidic structure is first filled with 5 mg/ml DOPC dissolved in squalene. Then the two reservoirs containing 10 mM acetate buffer with a HFBI concentration of 0.1µM are connected to the inlets. This causes a flow in the two channels and water fingers are formed (see Fig. 4.2a). DOPC monolayers are formed at these water-oil interfaces. The large concentration difference between DOPC and HFBI ensures that the monolayers are almost exclusively pure DOPC monolayers. When the two water fingers are brought together at the intersection, a DOPC bilayer is formed (see Fig. 4.2b). The oil is pushed out of the bilayer at the sides or is absorbed by the PDMS. The HFBI proteins are then located in the water phase surrounding the bilayer.

An Ag/AgCl electrode in each of the two inlets allows a voltage to be applied across the bilayer using a patch clamp amplifier, EPC 10 USB, and the resulting currents to be measured. The voltage is continuously increased from the negative extreme ($|U_{max}| = 150 - 200$ mV) to the positive extreme in 5 mV steps. This applied voltage creates pores in the bilayer and the ion current changes accordingly. If the bilayer is stable, several voltage cycles can be performed.

4.4 *Staphylococcus Aureus* Strain and Growth Condition

Bacterial adhesion was studied in close collaboration with the working group of Prof. Bischoff, Saarland University, Germany, using the biofilm-positive SA113 laboratory strain of *Staphylococcus aureus*. In addition, SA113 $\Delta dltA$ [165], lacking D-alanine, SA113 $\Delta tagO$ [151], lacking most of the wall teichoic acids, and SA113 $\Delta srtA$ [170, 173], lacking cell wall anchored proteins, were utilized as SA113 knock-out mutants. All strains were provided by the working group of Prof. Peschel, University of Tübingen, Germany.

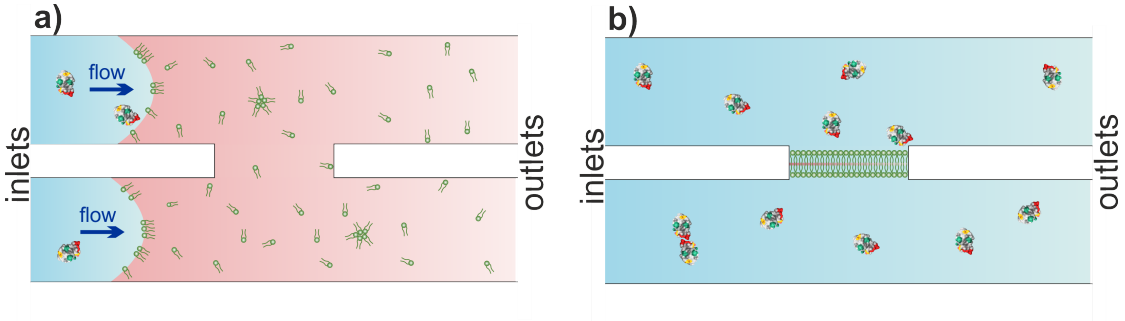

Figure 4.2: Schematic drawing of the microfluidic setup for electroporation measurements. a) Two water fingers with a low concentration of HFBI are slowly brought into contact. The lipids dissolved in the oil form a monolayer at the interface. b) After contacting the two water fingers, a lipid bilayer is formed. The surrounding water phase contains the HFBI molecules. HFBI molecules were taken from Figure 3.1a [104, 105, 107].

The *S. aureus* stock solutions are stored frozen at -80 °C. Due to laboratory conditions, a glycerol stock culture is prepared from it. This glycerol stock is stored at -20 °C and renewed approximately once a year. Every two weeks, new blood agar plates are prepared from the glycerol stock and incubated at 37 °C for three days. A single bacterial colony is then transferred from the colonized agar plates to 5 ml of tryptic soy broth (TSB) culture medium. This liquid culture is then incubated overnight at 37 °C and 150 rpm. To obtain bacterial cells in the exponential phase, a fresh culture is then prepared directly from the overnight culture on the day of the experiment. A small volume of the overnight culture is added to fresh TSB in a 1:100 ratio and allowed to grow for 2.5 hours under otherwise identical conditions.

The *S. aureus* cells are washed with phosphate buffered saline (PBS, pH 7.3–7.4) by centrifugation (3 min, 17,000 x g) and exchange of the supernatant with fresh PBS. This washing step is performed a total of three times. For further use of single bacteria, the solution was diluted tenfold with PBS.

4.5 Silicon Surfaces

Bacterial adhesion measurements were performed on differently treated silicon surfaces. Monocrystalline silicon wafers (SiO_2) with a natural oxide density of 1.7(2) nm and an advancing water contact angle (WCA) of 5(2)° were used as hydrophilic surfaces in this work. The SiO_2 surfaces are cleaned with peroxymonosulfuric acid, a 1:1 mixture of sulfuric acid and hydrogen peroxide, prior to any use or further processing. See Bellion *et al.* for a detailed description of the SiO_2 surface used [240].

In order to create surfaces with different levels of hydrophobicity, roughness and charge, the SiO_2 surfaces are further processed as described in brief:

- **Silanization** is performed with octadecyltrichlorosilane (OTS) according to Lessel *et al.* [241]. The OTS surfaces have an advancing WCA of 111(2)° with a roughness comparable to SiO_2 (RMS in the range of 0.1 to 0.2 nm). OTS surfaces are cleaned with ethanol, acetone and ultra pure water in the ultrasonic bath prior to every usage.

- **Black Silicon** surfaces of different roughness are prepared by a wet chemical etching process using hydrofluoric acid, hydrogen peroxide and water in a ratio of 2:7:16. A publication by Koynov *et al.* is used as the basic recipe [242], which is slightly modified as described in Addendum II and the dissertation of C. Spengler [65]. Surfaces with RMS values of 7 nm, 24 nm and 3 nm could be produced. These nanorough surfaces are then silanized with OTS as described above.

- **Hydrophobin HFBI** and **HFBI D40Q/D43N** are used to coat OTS surfaces and thereby render surface properties such as hydrophobicity (WCA around 30–40°) and the isoelectric point (IEP 6.1 and 7). Since this surface coating has been prepared for the first time within this thesis in the working group of Prof. Jacobs, it will be described in more detail in the following.

HFBI Coatings

The hydrophobin coatings with HFBI and the charge mutant HFBI D40Q/D43N are prepared in the same way. A 6 mM sodium acetate solution with a hydrophobin concentration of 4 µM is used for the coating. Any hydrophobin agglomerates in the protein solution are dissolved in an ultrasonic bath. A 60 µl hydrophobin droplet is then added to a freshly cleaned OTS surface. Two different methods were tried for the further procedure.

(I) After placing the droplet on the OTS surface, a waiting period of about 30 minutes is allowed until a dense layer of protein forms at the water-air interface and the droplet flattens as described in the literature (see Fig. 4.3a) [103, 114–117]. This hydrophobin layer formed at the water-air interface can then be removed with a second freshly cleaned OTS surface. The disadvantage of this method is that many artifacts result from the removal of the protein layer during the production of coatings in the centimeter range. For this reason, a second method of coating with hydrophobins has been developed.

(II) In the second method, after placing the hydrophobin droplet on the OTS surface, a second OTS surface is immediately placed on top. Thus, the HFBI monolayer is formed directly at the water-OTS interface. After a waiting period of 30 minutes, the whole assembly is placed in ultrapure water to wash off any residual proteins in solution. The coated OTS surface is then dipped several times in fresh ultrapure water to remove lightly adsorbed hydrophobins. The dried surfaces (both top and bottom OTS surfaces) have a WCA of 34(6)° and an RMS of 0.33(4) nm for HFBI. For HFBI D40Q/D43N the corresponding values are 39(4)° and 0.38(7) nm.

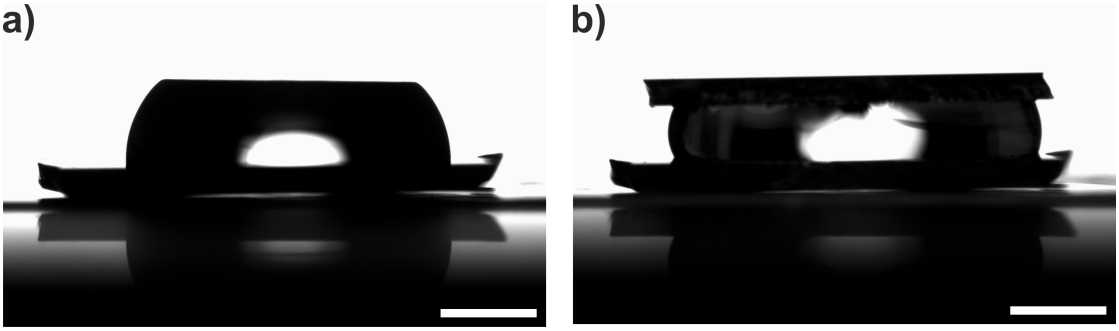

Figure 4.3: a) A flattened HFBI droplet on an OTS surface with a protein layer formed at the water-air interface. b) Selected method for producing hydrophobin-coated OTS surfaces by placing an OTS surface on top of the hydrophobin droplet. Shown is an HFBI droplet between two OTS surfaces.

4.6 Atomic Force Microscopy

Atomic force microscopy (AFM) was developed to determine the surface topography of non-conductive surfaces from the scanning tunneling microscope [243].

A sharp tip attached to a cantilever is moved over a surface. The position of the cantilever, and thus the possible bending or change in oscillation amplitude, is determined by the reflection of a laser beam focussed on the cantilever onto a 4-quadrant photodiode. More detailed descriptions of the setup and operating principle of an AFM can be found in numerous literature [244–247].

In this work, in addition to the determination of surface topography (Addendum II and V), the AFM was primarily used for force spectroscopy, more specifically single-cell force spectroscopy (SCFS, Addendum II – V), to study the adhesion of cells. The method of SCFS for bacteria, especially cocci, is well established in the group of Prof. Jacobs [65, 66]. A detailed guideline for bacterial immobilization, cantilever calibration and SCFS measurement methodology has been published by Thewes *et al.* [207]. Therefore, the basic principle of bacterial SCFS is briefly described and the similarities and differences to human cell SCFS measurements are shown.

Single-Cell Force Spectroscopy – *Staphylococcus aureus*

To determine *S. aureus* adhesion by SCFS, a single *S. aureus* cell is first immobilized on a tipless calibrated cantilever (MLCT-O). Polydopamine, a polymer derived from a bioadhesive mussel protein, is used for this purpose [248, 249]. This immobilization method does not affect the viability of the bacterium, checked *via* live/dead staining. To record the force-distance curves, the cantilever with the immobilized bacterium is slowly approached to the surface to be adhered (see Fig. 4.4, green curve). Depending on the interactions of the bacterium with the surface, a snap-in may occur at a certain distance, called the snap-in distance. The strength of this attraction is called the snap-in force. When the cell comes into contact with the surface, it is gently pushed onto the surface

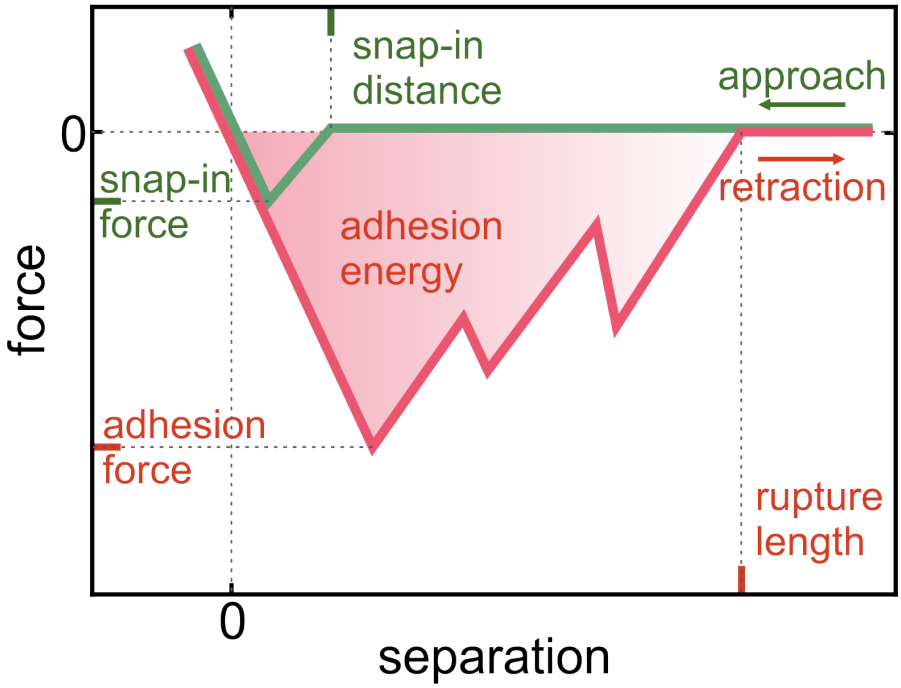

Figure 4.4: Sketch of a cell adhesion force-distance curve (approach and retraction) with typical adhesion parameters that can be determined.

by a preset force trigger (300 pN). It is possible to set an additional contact time during which the bacterium remains on the surface. In this work, an additional contact time of 5 s is used for *S. aureus* adhesion on hydrophilic surfaces, while no additional contact time is required on hydrophobic surfaces. The adhesion force can then be determined from the retraction curve as the maximum deviation from zero (see Fig. 4.4, red curve). The distance at which the force value becomes zero (in the noise of the baseline) and the bacterium has completely lost contact with the surface is called the rupture length. The adhesion energy is defined as the integral of the force over the distance.

Multiple force-distance curves can be recorded on a single bacterial cell. This allows adhesion measurements with the same cell on different surfaces.

Single-cell force Spectroscopy – Human Retinal Pigment Epithelial Cell

To measure the adhesion of human RPE-1 cells to fibronectin, the experimental protocol of bacterial SCFS was adapted. Since the specific adhesion to fibronectin is to be tested here, the cells are not immobilized on the cantilever before the measurement, but are detached directly from the fibronectin. For this purpose, another immobilization method is used, the FluidFM [250]. In this method, cells are immobilized on the cantilever by suction, using special cantilevers with a microfluidic channel connected to a pumping system.

RPE-1 cells were prepared in collaboration with the group of Prof. Lautenschläger. Tissue culture dishes (TPP, Trasadingen, Switzerland) were treated with plasma for 3 minutes, covered with 500 µl of fibronectin (25 µg/ml), incubated for 1 hour at room temperature, and then seeded with RPE-1 cells (1 x 106 cells/dish) and the compound used (dimethyl sulfoxide (DMSO) or MiuA). To ensure complete adhesion of the cells to the fibronectin, the cells were allowed to adhere for 4 hours in the incubator (37°C, 5% CO2). To maintain consistent conditions during single-cell force measurements, HEPES (4-(2-hydroxyethyl)piperazine-1-ethanesulfonic acid) is added to the cell medium (25 µl per 1 ml) and the cells are maintained at 37°C throughout (JPK PetriDishHeater™).

Single-cell force measurements are performed using a Nanowizard IV XP AFM with a CellHesion 200 head (Bruker Nano GmbH, Berlin, Germany) and a FluidFM microfluidic control system V2 Platinum (Cytosurge, Glattburg, Switzerland). The cell to be measured is approached (z-length 50 µm, z-velocity 0.8 µm/s) with a Cytosurge FluidFM micropipette (aperture 4 µm, stiffness 2 N/m), immobilized by negative pressure (-500 mbar) while the micropipette itself is held at a constant height or force, and then detached from the fibronectin by retracting the micropipette (z-length 50 µm, z-velocity 0.8 µm/s). This detachment process is monitored with an inverted light microscope (Zeiss AG, Oberkochen, Germany). The retraction curves obtained can be described similarly to the bacteria retraction curves using the same parameters (adhesion force, adhesion energy, and rupture length). JPK Data Processing version 7.0.128 is used for analysis.

4.7 Materials and Instrumentation

Chemicals and other consumables:

- 1,2-Di-(9Z-octadecenoyl)-*sn*-glycero-3-phosphocholin (DOPC), Avanti Polar Lipids, Alabaster, AL, USA
- 1-Oleoyl-*rac*-glycerol (Monoolein) $\geq$ 99 %, Merck KGaA, Darmstadt, Germany
- Acetic acid 100 %, VWR International GmbH, Darmstadt, Germany
- Acetone 99.98 %, Fisher Scientific GmbH, Schwerte, Germany
- AFM tips: HAR1-200-10, MLCT-O and ScanAsyst-Air, Bruker AFM Probes, Camarillo, CA, USA
- AFM tips: OMCL-AC160TS, Olympus Europa SE & Co. KG, Hamburg, Germany
- Blood agar (Tryptic soy broth with sheep blood), Fisher Scientific GmbH, Schwerte, Germany
- Developer MR-dev 600, micro resist technology, Gesellschaft für chemische Materialien spezieller Photoresistsysteme mbH, Berlin, Germany
- Disposable needles: Sterican® blunt, length: 25 mm, diameter: 0.40 mm, B. Braun SE, Melsungen, Germany

- Dopamine Hydrochloride 98 %, Merck KGaA, Darmstadt, Germany (former Sigma-Aldrich)
- Ethanol 99.8 %, VWR International GmbH, Darmstadt, Germany
- FluidFM tips: micropipette, aperture: 4 µm, stiffness 2 N/m, Cytosurge, Glattburg, Switzerland
- Hexadecane $\geq$ 99 %, Merck KGaA, Darmstadt, Germany
- Hydrogen peroxide (30 %, nonstabilized), Merck KGaA, Darmstadt, Germany
- Octadecyltrichlorosilane (OTS), Merck KGaA, Darmstadt, Germany
- Phosphate Buffered Saline (PBS), Merck KGaA, Darmstadt, Germany
- Photoresist SU-8-100, micro resist technology, Gesellschaft für chemische Materialien spezieller Photoresistsysteme mbH, Berlin, Germany
- Potassium Chloride 99, 5 %, Grüssing GmbH, Filsum, Germany
- Silicon Wafer, Siltronic AG, Burghausen, Germany
- Silver Wire 99, 99 %, diameter: 0.25 mm, Goodfellow Cambridge Limited - UK, Huntingdon, Great Britain
- Sodium acetate trihydrate, Merck KGaA, Darmstadt, Germany
- Sodium chloride $\geq$ 99 %, VWR International GmbH, Darmstadt, Germany
- Squalene $\geq$ 98 %, Merck KGaA, Darmstadt, Germany
- Sulphuric acid $\geq$ 96 %, VLSI Selectipur®, BASF, Ludwigshafen am Rhein, Germany
- Sylgard 184, Dow Corning, Midland, MI, USA
- Tissue culture dishes, TPP, Trasadingen, Switzerland
- Trishydroxymethylaminomethane hydrochloride (TRIS), Merck KGaA, Darmstadt, Germany
- Tryptic soy broth (TSB), VWR International GmbH, Darmstadt, Germany

Instruments and measurement devices:

- AFM: FastScan Bio with controller NanoScope V, Bruker Nano Surfaces, Santa Barbara, CA, USA
- AFM: BioScope Catalyst with controller NanoScope V, Bruker Nano Surfaces, Santa Barbara, CA, USA

- AFM: NanoWizard® 4 XP, with JPK NanoWizard® 4 XP AFM head, JPK CellHesion® 200 Head, Bruker Nano GmbH, Berlin, Germany
- Camera: ORCA-Fusion Digital CMOS camera, C14440-20UP, HAMAMATSU PHOTONICS DEUTSCHLAND GMBH, Herrsching am Ammersee, Germany
- Contact Angle Instrument: OCA 25, DataPhysics Instruments GmbH, Filderstadt, Germany
- FluidFM: FluidFM® microfluidic control system V2, Cytosurge AG, Glattburg, Switzerland
- High Speed Camera: Fastcam SA3, Photron Deutschland GmbH, Reutlingen, Germany
- Macroscope: Leica Z16 APO, Leica Microsystems GmbH, Wetzlar, Germany
- Micromanipulator: MOM-202D, NARISHIGE INTERNATIONAL LTD., London, Great Britain
- Microscope: Leica DM 2700M with a Leica MC170 HD camera, Leica Microsystems GmbH, Wetzlar, Germany
- Microscope: Axio Observer 7, inverted optical microscope, Carl Zeiss Microscopy Deutschland GmbH, Oberkochen, Germany
- Petri Dish Heater: JPK PetriDishHeater™ for BioMAT™, Bruker Nano GmbH, Berlin, Germany
- pH meter: SevenExcellence with perfectION electrode for fluoride concentration measurement, Mettler Toledo, Gießen, Germany
- Physical Vapor Deposition Device: Univex 300, Leybold Heraeus, Köln, Germany
- Plasma Cleaner: PDC-32 G, Harrick Plasma Ithaca, NY, USA
- Plasma Cleaner: Femto, Diener electronic GmbH & Co. KG, Ebhausen, Germany
- Pumping system: multiboard 2 with a highdriver 4, mp6-liq and mp6-gas pumps, Bartels Mikrotechnik GmbH, Dortmund, Germany
- Voltage Amplifier: HEKA EPC 10 USB, Multi Channel Systems MCS GmbH, Reutlingen, Germany
- Water purifier: GenPure, Thermo Fisher Scientific Inc., Waltham, MA, USA

5 Results and Discussion

For many different phenomena in biological systems, knowledge of the behavior of macromolecules at interfaces is of paramount importance. Protein adsorption at interfaces, bilayer formation, incorporation of molecules into a bilayer, and cell adhesion are just a few examples of phenomena where macromolecules play a crucial role. In this chapter, the main results of this thesis are presented. Additional information on results already published or available in manuscript form can be found in the Addendum.

5.1 Hydrophobin HFBI at Interfaces

After Hähl *et al.* showed that hydrophobins can be used to produce stable vesicles that can even contain a functional ion channel (gramicidin A), it was clear that further studies of this system were needed to be able to use it technically [13]. Such surface-active molecules are very useful for technical applications, for example for stabilizing emulsions or for drug delivery or other packaging issues. Due to its strong amphiphilicity, HFBI is a very good candidate for these requirements and the characterization of its properties in monolayers and bilayers is therefore of high technological relevance. In particular, water permeability is an important physiological property of a membrane and is therefore carefully determined in this thesis (chapter 5.1.1). In chapter 5.1.2 the preparation of vesicles from pure HFBI protein bilayers was further developed, and in chapter 5.1.3 the behavior of hydrophobins on a lipid bilayer was investigated. In addition, HFBI was used to study the influence of surface charge on bacterial adhesion of *Staphylococcus aureus*, which is described in chapter 5.2.4.

5.1.1 Water Permeability of HFBI Bilayers

For the use of membrane and vesicle systems in medical applications such as biomimetics and vesicle-based drug delivery, water permeability is an important property. Water permeability describes the passage of water molecules through the membrane and thus influences the interaction between the two sides of the membrane. The water permeability of pure HFBI bilayers has been studied in detail and is described by **Nolle *et al.* in Langmuir (accepted)** (Addendum I). Water permeability was measured by bringing two HFBI monolayer coated droplets (micelles) into contact. A so-called droplet interface bilayer (DIB) is formed at the contact surface between the two droplets (see section 4.2). If an ion concentration difference is applied between the two contacting droplets, an osmotic pressure is applied to the system, which can be balanced by a flow of water into the droplet with the higher salt concentration. By recording the change in droplet size over time, the water permeability can be calculated (see Addendum I)

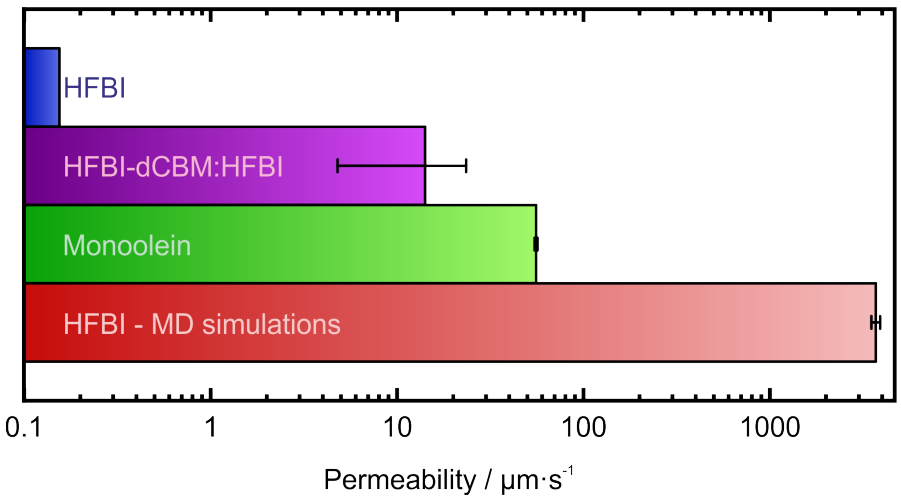

Figure 5.1: Bar chart of water permeability values of different bilayer systems. The blue bar represents the maximum water permeability value including the standard error of pure HFBI wild type bilayers. The water permeability of HFBI-dCBM:HFBI bilayers with a ratio of 0.4:1 is shown in purple, and experimental water permeability data from monoolein bilayers are shown in green. Water permeability values obtained from MD simulations of dense HFBI-β bilayers are displayed in red.

At a salt concentration difference of approximately 1 M, the water permeability values measured for HFBI bilayers are below the experimental resolution of 1 µm/s (Fig. 5.1 blue bar). This permeability is surprisingly low compared to that of simple lipid bilayers, which are in the range of 10 – 160 µm/s [5, 15, 251, 252]. Such low values have only been achieved in densely packed bilayers, such as sphingomyelin:cholesterol bilayers, which can obtain a water permeability of about 2 – 4 µm/s [15, 252]. We collaborated with Professor Jochen Hub and his theoretical physics group to see if molecular dynamics (MD) simulations could confirm our results. However, their MD simulations predict a very large water permeability for HFBI bilayers, ranging from mm/s to cm/s (Fig. 5.1 red bar). Measurements on monoolein (1-Oleoyl-*rac*-glycerol) lipid bilayers were performed to test the measurement system and for comparison with HFBI bilayers. In agreement with literature values [5], monoolein bilayers show a low but well detectable water permeability (Fig. 5.1 green bar). To further ensure the accuracy of the measured water permeability values of the HFBI bilayers, the HFBI bilayer was examined for possible oil residues by adding a flourescent dye to the oil and measuring the fluorescence signal. No oil residues are detected, which is consistent with the results of the MD simulations of unstable oil layers between two HFBI monolayers. In mixed bilayers containing the HFBI fusion protein with two cellulose binding domains (HFBI-dCBM) in addition to the wild type HFBI protein, a detectable water permeability is observed (Fig. 5.1 purple bar). This not only confirms the formation of a proper bilayer but also demonstrates the potential variability of HFBI bilayers. Combined with the results of the MD simulations on the water permeability of the HFBI bilayer, we suggest that a restructuring of the order of the

proteins in a monolayer to a bilayer must take place. Unfortunately, MD simulations are currently limited by the lack of knowledge about the exact protein-protein interactions in the HFBI bilayer. To resolve uncertainties in the chosen force field, additional simulations with different force fields and water models were performed, but still the same effect of enormous water leakage through the HFBI bilayer was observed.

By studying the water permeability of HFBI bilayers, impressive contrasts to conventional lipid bilayers were revealed [5, 15, 252]. Very low permeability coupled with high stability against osmotic pressure makes these HFBI bilayers particularly interesting for use in biophysical and biotechnological applications, such as drug delivery [16]. What is still missing is the ability to produce hydrophobin vesicles in a single size on a larger scale. The first steps are described in the following chapter.

5.1.2 Hydrophobin Vesicle Production

In this work, the further development of HFBI bilayers into pure protein vesicles was pursued. The aim was to increase the potential of hydrophobins for applications such as drug delivery. In Hähl *et al.* [13], two methods for hydrophobin vesicle production are described: microfluidic jetting and gel extrusion. Within this work, however, the desired quantity of vesicles and the required control of vesicle production could not be achieved with either of the methods described. There are several other methods for the controlled preparation of lipid vesicles [253], some of which can be tried with modifications for the preparation of hydrophobin vesicles. The two most promising methods for the controlled production of HFBI vesicles were constructed in this work and are presented here. Method A is based on the microfluidic jetting method [13, 254], which was extended and improved. Method B uses a microfluidic system described by Karamdad *et al.* [255], that was slightly modified.

For method A, a controlled droplet interface bilayer (DIB) formation setup was used, see Figure 5.2a. A pumping system (multiboard2 with a highdriver4, Bartels, Dortmund, Germany) with four pumps connected in series (2 x mp6-liq and 2 x mp6-gas+, Bartels, Dortmund, Germany) allowed to control settings like bilayer size and flow rate. The best results were obtained when a voltage of 250 V and a frequency of 170 Hz were applied to the pump system. This corresponds to a flow rate of approximately 15000 µl/min [256]. A blunt cannula with a diameter of 0.4 mm is used as the outlet of the pressure device. With this system, vesicles can be produced in the range of milliseconds. The vesicle shown in Figure 5.2a has a diameter of about 1 mm. Since this setup is still in the adjustment phase, no information about the monodispersity can be given. Adjustments to the pumping circuit and the tubing used (diameter, length, stiffness) are planned to further optimize the pulse for microfluidic jetting of HFBI bilayers and to achieve higher throughput of HFBI vesicles.

Method B uses a microfluidic setup sketched in Figure 5.2 b. In the first step, monodisperse water-in-oil (10 mM NaAc-in-hexadecane) HFBI droplets are produced in a microfluidic channel system (diameter of 50 – 150 µm). For this purpose, fixed flow rates of a connected pump system are adjusted so that the HFBI droplets are pinched off as a function of the selected flow rates. The flow rate of the oil phase is selected to be at least

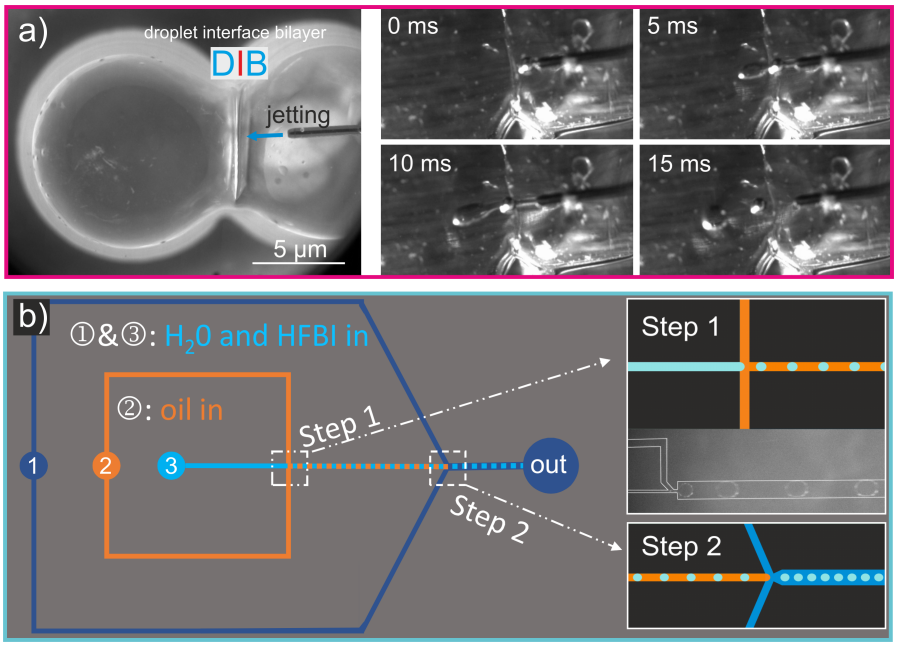

Figure 5.2: a) Microfluidic jetting system for hydrophobin vesicle formation by controlled pulsed water flow through a droplet interface bilayer (DIB) with a pumping system. The steps from bilayer deformation to vesicle formation by microfluidic jetting are shown in a time series of HFBI vesicle formation. b) Design of a microfluidic chip for the generation of hydrophobin vesicles. In the first step, droplets of a protein solution are generated in an oil-filled channel. Between step 1 and step 2, micelle-like droplets are formed after a certain time, depending on the size and protein concentration of the droplets. In the second step, the droplets are captured again in aqueous solutions and vesicles are formed.

ten times higher than the flow rate of the water phase in order to produce individual droplets (flow rates in the range of 0.1–20 µL/min). During this process, the HFBI droplet size can be adjusted. To ensure that a dense monolayer of HFBI molecules is formed at the interface between the droplet and the oil, HFBI droplets must be given enough time. Unfortunately, this step is not trivial because, unlike lipids, hydrophobins are not dissolved in the oil but in the water phase, so the HFBI concentration is crucial for the formation of a dense monolayer. If the concentration is too low, the density of HFBI at the interface is too low to cover the entire interface with an HFBI monolayer; if the concentration is too high, the HFBI droplets become gel-like and stick to the PDMS. The protein concentration is therefore adjusted to the droplet size so that the amount of protein in the droplet is just above the required amount to form a dense monolayer at the interface. The final step is to form a vesicle from the micelle by placing a second monolayer of HFBI "around" the first. This requires a stable boundary layer through which the water droplets with the HFBI monolayer can pass. However, this is still part of the current research, as adjustments to increase the stability of this transition still need to be investigated.

Both of the methods described are still in the optimization phase, and while vesicles have already been formed by microfluidic jetting, the production of vesicles using a microfluidic chip is still in the early stages. Recent findings that the formation of HFBI bilayers is likely to lead to protein rearrangement make methods such as the microfluidic technique described above very difficult. Making double emulsions instead of vesicles is one possibility. This would also depend on adjustments such as the choice of oil phase. For the production of HFBI vesicles, methods based on a bilayer, such as microfluidic jetting, are preferred. However, the constant need to create a new bilayer limits the production rate of vesicles. Therefore, a next step would be to develop an automated device to produce hydrophobin bilayers. In addition to the production of pure HFBI bilayers, there is of course also the possibility of incorporating HFBI proteins into lipid bilayers and thereby changing the properties of the lipid bilayers.

5.1.3 Hydrophobins in Lipid Bilayers

The class II hydrophobin HFBII has a stabilizing effect on biomimetic membranes according to the patent of Gil, Kristensen and Mainzer "Stabilization of biomimetic membranes" [257]. This is of great interest in the field of desalination and biosensors, since there, membrane stability is crucial and often requires stabilizers [258, 259]. In this thesis, the effect of HFBI incorporation into a DOPC bilayer on pore formation was investigated in a microfluidic setup combined with a HEKA EPC-10 patch clamp amplifier.

HFBI is easily incorporated into a microfluidically prepared planar DOPC bilayer. This increases the stability of the bilayer with respect to the applied voltages during electroporation measurements by a factor of 1.33 (DOPC/HFBI: 200 mV, DOPC: 150 mV, Fig. 5.3a upper graph). Compared to the pure DOPC bilayer at the same voltage, the ion flux through the DOPC/HFBI bilayer also increases (e.g. current increase by a factor of 5 at -100 pA and by a factor of 2 at 100 pA). In addition, a DOPC bilayer with a reservoir of HFBI proteins provided by the surrounding medium was subjected to several

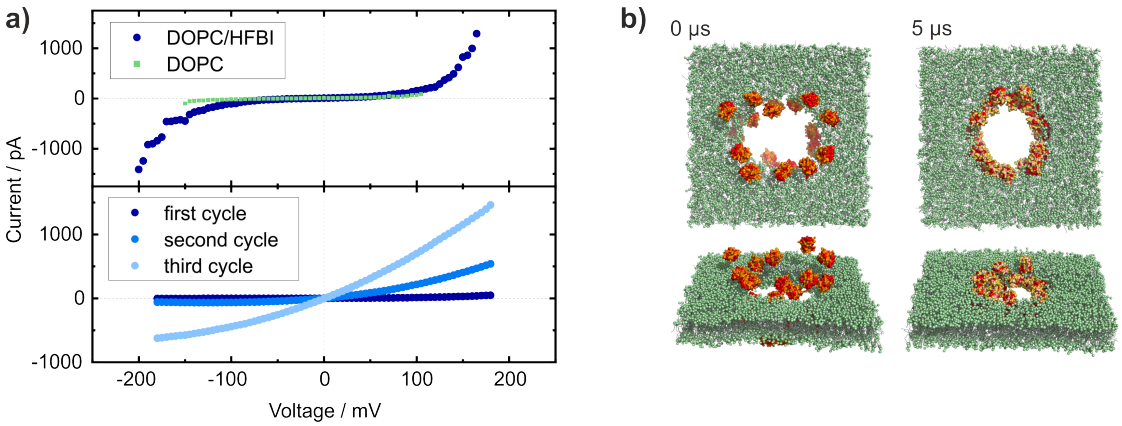

Figure 5.3: a) Electrophysiological measurements on DOPC bilayer with and without HFBI in the surrounding solution and multiple cycle measurements performed on a microfluidic chip. b) Coarse-grained simulation of HFBI interacting with a DOPC bilayer with a pore.

voltage cycles (Fig. 5.3a lower graph). For each cycle, the voltage was slowly increased from -180 mV to 180 mV after a pause of a few seconds. Electroporation measurements show a steady increase in ion flux during these measurements. It is interesting to note that a new cycle always starts at approximately the end value of the previous cycle.

These results clearly show that HFBI molecules are incorporated into the DOPC bilayer (increased stability and ion flux). However, this incorporation seems to be strongly favored by pores in the DOPC bilayer (increase in ion flux with voltage cycles). Additional measurements also showed that waiting before applying voltage did not increase the starting point of ion flux through the bilayer. The results therefore suggest that the hydrophobins are incorporated into the pore rims and that these edges, and thus the entire bilayer, are stabilized. Initial coarse-grained simulations by our collaborators in Professor Hub's group at the University of Saarland seem to confirm these results. Again, the hydrophobins are clearly incorporated at the pore rims (Fig. 5.3b).

HFBI is a potential molecule to support membrane stability in desalination due to the demonstrated stabilization of the lipid bilayer and its pores. Other properties such as how HFBI behaves with aquaporins, commonly used water channels in desalination [259], and how HFBI behaves in more complex membranes is part of future research. In addition, the behavior of HFBI in a lipid bilayer without the application of stress has yet to be elucidated.

5.2 Bacterial Adhesion

Macromolecules at the bacterial cell surface, for example cell wall anchored (CWA) proteins, wall teichoic acids (WTAs) or lipoteichoic acids (LTAs), play an important part in the nonspecific adhesion of bacteria to biotic and abiotic surfaces. In this work

several studies have been conducted to define the contribution of macromolecules in the adhesion of *Staphylococcus aureus* (*S. aureus*) to abiotic surfaces. The influence of surface roughness, hydrophobicity and also the charge has been linked to the interactions of cell wall macromolecules with the surface. In addition, various knock-out mutants exhibiting alterations in the properties of cell wall macromolecules were used to further investigate the specific role of different macromolecules.

5.2.1 Influence of Surface Roughness

Surface topography is an important surface property that has a major impact on the first step of biofilm formation, bacterial adhesion. Therefore, the adhesion of *S. aureus* to octadecyltrichlorosilane (OTS)-coated silicon surfaces of different roughness have been examined in detail by **Spengler *et al.* in *Nanoscale* 2019** (Addendum II). In addition, a correlation between the surface area accessible to cell wall macromolecules and the adhesion forces determined for the whole cell was established by combining the forces measured by single-cell force spectroscopy (SCFS) with Minkowsky functionals of the surface.

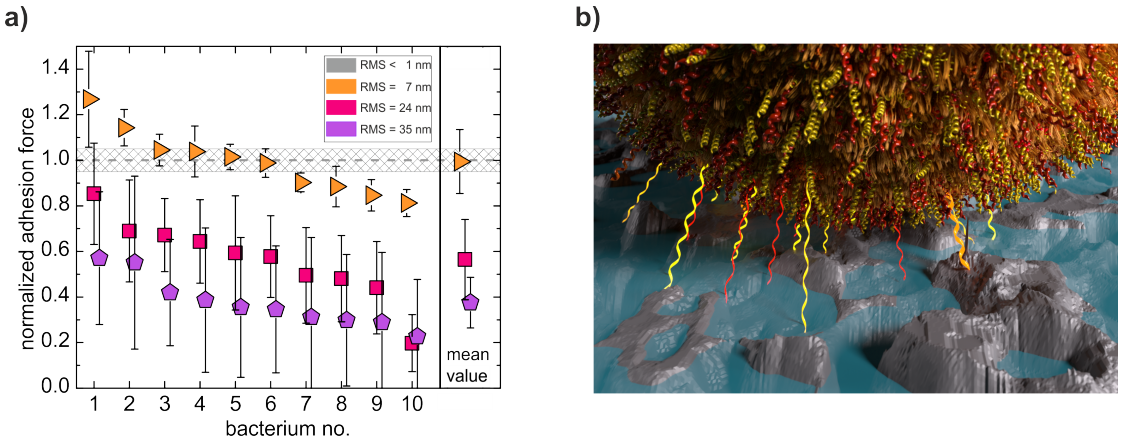

Figure 5.4: a) Normalized adhesion forces of individual *S. aureus* cells on hydrophobic silicon surfaces (OTS) with different degrees of roughness compared to their adhesion forces on smooth surfaces. (Adapted by Addendum II) b) Graphical visualization of the adhesion process of an *S. aureus* cell on an RMS = 35 nm rough OTS-coated silicon surface (real AFM data). The watershed used for the Minkowski measures is illustrated in blue.

Silicon surfaces of different roughness (RMS = 7 nm, 24 nm and 35 nm) have been used. Increased roughness has been produced by wet chemical etching in hydrofluoric acid. All surfaces used for this study have been coated with OTS for equal hydrophobicity. Adhesion forces of *S. aureus* cells have been measured in comparison to a smooth OTS covered silicon surface (RMS = 0.1 nm) and normalized to the adhesion force of the same specific cell. While the adhesion force of *S. aureus* on the 7 nm rough surface is in the range of the adhesion force on a smooth OTS surface, a further increase in roughness

is accompanied by a decrease in adhesion force (Fig. 5.4a). For the roughest sample (RMS = 35 nm), the adhesion force is reduced by approximately 60 %. In addition to the effect on *S. aureus* adhesion, surface roughness also has an effect on cell viability. As surface roughness increases, cell viability decreases.

Combining the results of SCFS with morphometric analysis using Minkowski functionals, it was shown that the reduced surface area accessible to cell wall macromolecules determines the adhesion force (Fig. 5.4b). Therefore, the amount of adherent cell wall macromolecules is a determining factor for the bacterial adhesion.

5.2.2 Influence of Surface Hydrophobicity

To define the more specific role of cell wall macromolecules in the adhesion process to abiotic surfaces, the adhesion forces of *S. aureus* on hydrophilic (SiO_2, advancing water contact angle 5(2)°[240]) and hydrophobic (OTS-coated SiO_2, advancing water contact angle 111(2)°[240, 241]) surfaces have been measured and analyzed in **Maikranz *et al.* in *Nanoscale* 2020** (Addendum III). SCFS has been performed to understand the adhesion process on these surfaces of different hydrophobicity and complemented by Monte-Carlo (MC) simulations.

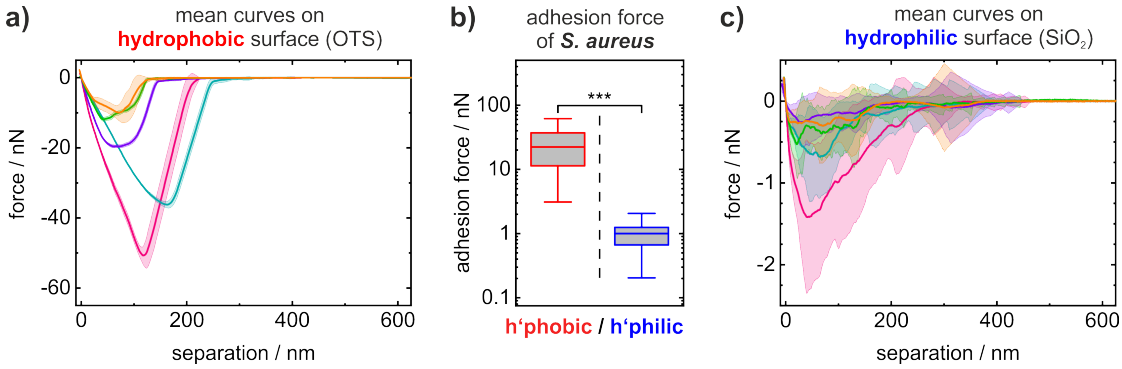

Figure 5.5: Adhesion of *S. aureus* cells on hydrophilic (SiO_2) and hydrophobic (OTS) surfaces. a,c) Mean retraction force distance curves with their standard error (shaded area) of five different *S. aureus* cells on SiO_2 and OTS surfaces. b) Box (Perc. 25, 75; Median) an whisker plot (min-to-max) of the mean adhesion force of more then 50 cells on each surface. For comparison an unpaired t-test has been performed (***, $p < 0.001$).

SCFS measurements show a great dependency of the mean adhesion forces of different *S. aureus* cells to the hydrophobicity of the surface. The median adhesion force of all measured cells to OTS is around 22-fold higher than to bare SiO_2 surfaces (Fig. 5.5b). Comparing the shape of force-distance curves of individual bacteria, differences between hydrophobic and hydrophilic surfaces become apparent. On hydrophobic surfaces (Fig. 5.5a), the retraction part of the force-distance curves of one and the same bacterium exhibit a comparatively smooth shape with little variation. The variation in adhesive forces of different *S. aureus* cells can be explained by the natural heterogeneity of the cells

as well as by a recently described patchiness of adhesive cell wall macromolecules on the cell wall [260]. In contrast, the shape of the retraction part of the force-distance curves on hydrophilic surfaces is 'spiky' and varies greatly for a single bacterium. Whereas the difference between individual bacterial cells is small (Fig. 5.5c).

These results are consistent with the idea that other bacterial macromolecules are involved in adhesion due to surface hydrophobicity. When in contact with a hydrophobic surface, a variety of macromolecules weakly adhere to the surface (smooth curves, little variation in the curves of a bacterium). On hydrophilic surfaces, only a few, strongly binding macromolecules are involved in the adhesion process ('spiky' curves, strong variation in the curves of a bacterium). Monte-Carlo simulations were able to reproduce the experimental curves with the help of the experimental force-distance curves. This supports our conclusion concerning the leading role of the bacterial cell wall macromolecules in the adhesion process.

5.2.3 Influence of Different Macromolecules

Based on the knowledge that different macromolecules are responsible for adhesion on hydrophobic and hydrophilic surfaces, the following question has been raised by **Spengler *et al.* in *Int. J. Mol. Sci* 2021** (Addendum IV): Is it possible to identify the macromolecules that are responsible for the adhesion?

To answer this question, SFCS measurements on SiO_2 and OTS surfaces have been performed using various *S. aureus* SA113 knock-out mutants with the following properties:

- SA113 $\Delta srtA$: deficiency of covalently bound cell wall proteins.
- SA113 $\Delta tagO$: lack of wall teichoic acids.
- SA113 $\Delta dltA$: deficiency of positively charged D-alanine groups on lipoteichoic acids.

The results have been compared with the adhesion forces of *S. aureus* wild type cells (SA113) published in Maikranz *et al.* [261]. The retraction curves of the three different SA113 mutants were examined for similarities and differences on OTS and SiO_2 (Figs. 5.6a,c), in addition, the retraction curves were compared with the retraction curves of SA113 wild type cells (Figs. 5.5a,c). On OTS surfaces, all retraction curves of the different mutants have a smooth shape with a high replication capacity for a single cell, similar to the retraction curves of SA113 cells. The retraction curves of SA113 $\Delta srtA$ and SA113 $\Delta dltA$ on the hydrophilic SiO_2 surfaces show a 'spiky' shape with a rather broad distribution for one single cell, comparable to SA113 retraction curves on hydrophilic surfaces. Only the SA113 $\Delta tagO$ cells show, similar to the curves on hydrophobic OTS, smooth shaped curves on the hydrophilic SiO_2 surfaces. Comparing the mean adhesion forces of the measured cells in a box and whisker plot (Fig. 5.6b), further differences become apparent: On hydrophobic surfaces, the adhesion forces of the SA113 mutants are all strongly reduced compared to the SA113 wild type. Among them, the $\Delta srtA$ mutant shows the largest reduction in adhesion force (reduction of the median to 13,%) and the

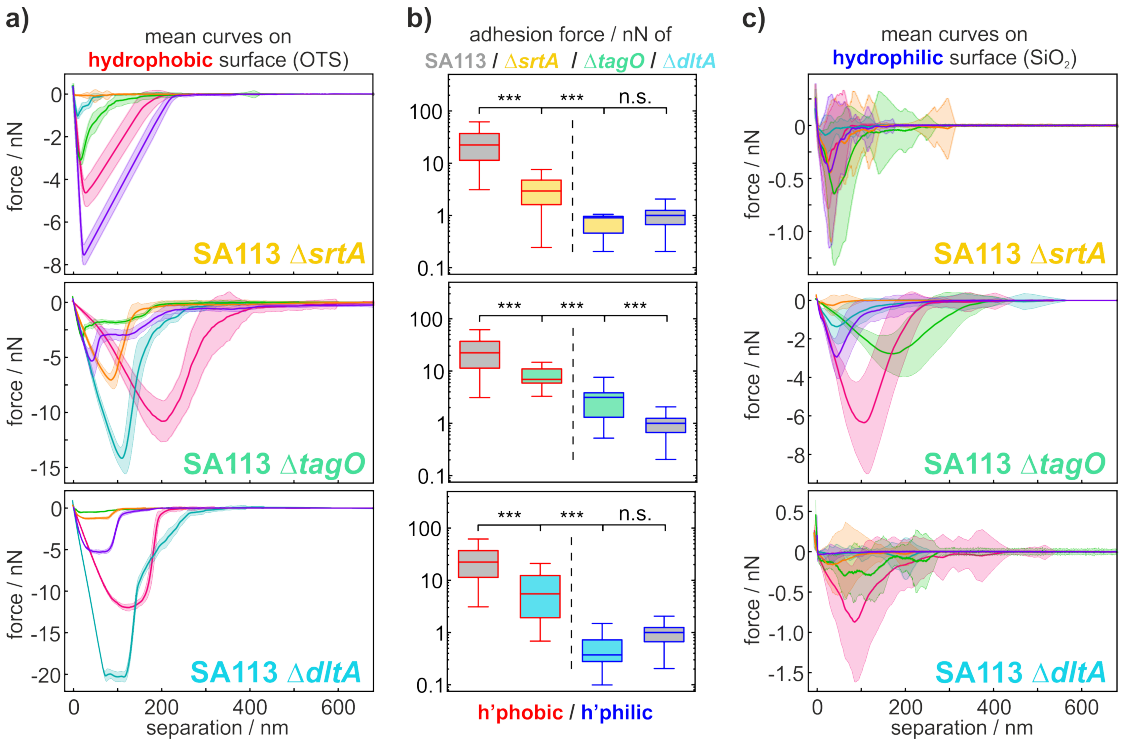

Figure 5.6: Adhesion of SA113 and mutant cells on hydrophobic (OTS) and hydrophilic (SiO_2) surfaces. a,c) Mean retraction force distance curves with their standard error (shaded area) of respectively five different SA113 $\Delta srtA$, SA113 $\Delta tagO$ and SA113 $\Delta dltA$ cells on OTS and SiO_2 surfaces. b) Mean adhesion force of at least 11 cells of each SA113 mutant on each surface compared to SA113 wild type cells [261] in box (Perc. 25, 75; median) and whisker plots (min-to-max). Ordinary one-way ANOVA and Dunnett's test (multiple comparison) and an unpaired t-test (pairwise comparison) have been performed (n.s., $p > 0.05$; ***, $p < 0.001$). Graph adapted by Addendum IV.

$\Delta dltA$ mutant shows the largest variance in measured adhesion forces (1 nN to 22 nN). A reduction in adhesion force on the hydrophilic SiO_2 surface compared to the hydrophobic OTS surface is evident for all mutants. However, the reduction itself differs in magnitude, with the $\Delta tagO$ mutant in particular showing a small reduction of only half the adhesion force. Thus, the $\Delta tagO$ mutant (3.1±1.0 nN) exhibits a higher median adhesion force than the wild type (1.0±0.3 nN) on SiO_2. The $\Delta srtA$ (0.9±0.1 nN) and $\Delta dltA$ (0.4±0.1 nN) mutants again exhibit reduced adhesion force compared to the SA113 wild type.

The measurements clearly show that any changes to the macromolecules of the bacterial cell wall lead to changes in bacterial adhesion to abiotic surfaces. The influence of distinct macromolecules on adhesion varies on surfaces with different wettability. While on hydrophobic surfaces any change in cell wall macromolecule composition significantly reduces (on average) adhesion, the change in adhesion on hydrophilic surfaces was not as pronounced. Thus, covalently bound cell wall proteins seem to play a crucial role in

adhesion on hydrophobic surfaces (median adhesion reduced by 87% compared to the wild type), whereas they play a rather minor role in adhesion on hydrophilic surfaces (reduced by 10%). Teichoic acids are crucial for adhesion on hydrophilic as well as on hydrophobic surfaces, although the effect is not as prominent on hydrophilic surfaces. In contrast, the change in the charge of the cell wall seems to play a role mainly on hydrophilic surfaces, as shown with the *ΔdltA* mutant, having a higher cytochrome *c* binding affinity than the wild type and a decreased adhesion on SiO_2 (reduced by 63%). It is this influence of electrostatic interactions on bacterial adhesion that is an interesting point for further material adaptations in the biomedical field and was therefore investigated in more detail as described in the next chapter. Also, in order to exclude side effects of macromolecule assembly on the bacterial cell wall, the protein composition of the SA113 mutants needs to be studied in more detail to identify more specific interactions.

5.2.4 Influence of Surface Charge

For a better understanding of the influence of electrostatic interactions between the bacterial macromolecules and the underlying surface, experiments with different cell and surface charge have been performed and discussed in **Nolle *et al.* to be submitted** (Addendum V). To obtain different surface charges of the bacteria, SA113 and SA113 *ΔdltA* cells were used. SA113 *ΔdltA* cells have a higher negative surface charge compared to the wild type. In addition, the surface charge of the adherent surface was altered by using a protein coating of amphiphilic hydrophobins. OTS surfaces were coated with the wild-type class II hydrophobin HFBI or the charge mutant HFBI D40Q/D43N, in which two aspartic acids were replaced by neutral amino acids, resulting in differences in zeta potential of about 25 mV at pH 7 [103]. Further characterization of the two HFBI coatings revealed only minor differences in surface properties like roughness (HFBI: 0.33(4) nm; HFBI D40Q/D43N: 0.38(7) nm) and wettability (static water contact angle (WCA), HFBI: 34(6)°; HFBI D40Q/D43N: 39(4)°). These differences are, however, not significant and should not lead to any measurable changes in the adhesion of *S. aureus*.

The results were compared to the adhesion forces on well studied surfaces (SiO_2, OTS) to better understand the adhesion forces on HFBI coated surfaces. Adhesion forces of SA113 are strongly reduced on the HFBI-coated surfaces (80±40 pN) compared to the adhesion forces on OTS surfaces (22±13 nN) before protein coating (Fig. 5.7a). This difference in adhesion force can mainly be described by the change of surface wettability. Due to the hydrophobin coating, the hydrophobic OTS surface becomes hydrophilic. However, even compared to the hydrophilic SiO_2 surfaces (1.0±0.3 nN) the adhesion forces are strongly reduced. As the SiO_2 surfaces (WCA: 5(2)°) have clearly a lower water contact angle, the surface wettability alone cannot cause the reduced adhesion forces. On hydrophilic surfaces, hydrogen bonding is important for *S. aureus* adhesion [261], and this bonding must be hindered on HFBI surfaces to explain the lower adhesion forces. A reduced ability to form hydrogen bonds due to a heterogeneous surface could be a possible explanation. This also fits with the statement, that for protein adsorption on hydrophobin surfaces mainly electrostatic interactions are crucial compared to other forces [262].

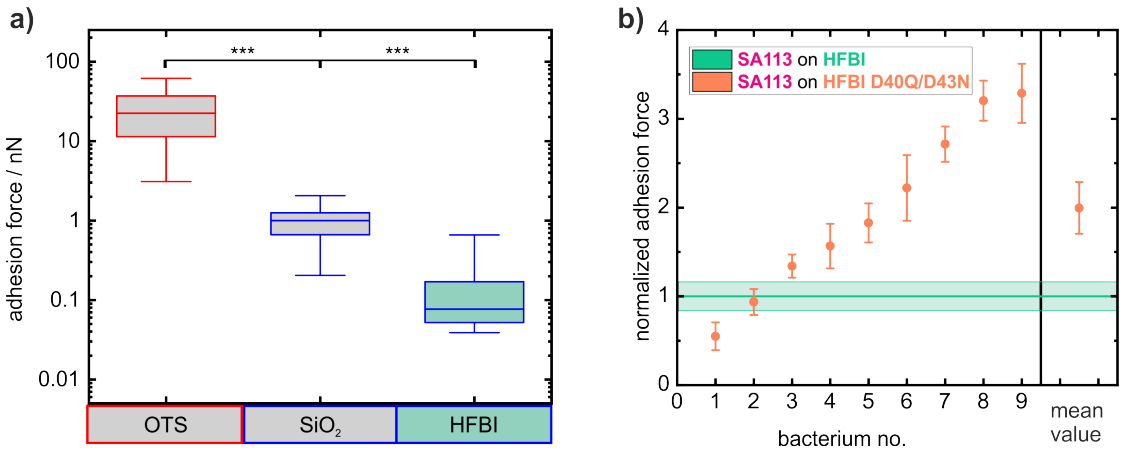

Figure 5.7: Adhesion forces of 9 *S. aureus* cells on HFBI-coated OTS surfaces. (a) Box plot (min-to-max) of the adhesion force of *S. aureus* cells on HFBI wild type surfaces, compared to adhesion forces on OTS and SiO_2 published in Maikranz *et al.* [261] (b) Comparison of the mean adhesion force of single *S. aureus* cell measured on HFBI and HFBI D40Q/D43N surfaces. Adhesion forces were normalized to the mean adhesion force on the HFBI surfaces, error bars depict the standard of the mean. For a better overview, the measured cells were sorted according to the normalized adhesion force on the HFBI D40Q/D43N surfaces. Graph adapted by Addendum V.

In a next step, the adhesion of single *S. aureus* cells was measured on HFBI and HFBI D40Q/D43N surfaces in direct comparison. A correlation between the zeta potential of the surface and the adhesion force of SA113 is evident when the adhesion forces of all measured cells are normalized to the mean value of the adhesion forces on HFBI surfaces (Fig. 5.7b). As the zeta potential increases, so does the adhesion force, with the mean adhesion force on the HFBI D40Q/D43N surfaces being twice as high. In addition, the measurements were repeated with the SA113 mutant *ΔdltA*. This mutant shows a reduced adhesion compared to SA113 cells as already described on hydrophilic SiO_2 surfaces (chapter 5.2.3). No effect of the surface charge can be detected (Addendum V).

Measurements on surfaces of different surface charge have shown that electrostatic interactions play a crucial role in the adhesion of *S. aureus* cells to hydrophilic surfaces. A negative charge of the surface to be adhered to can thus reduce the ability of the bacteria to adhere. The lack of a detectable effect of the surface charge on the adhesion of the SA113 mutant *ΔdltA* may have several reasons. For example, the adhesion of the *ΔdltA* mutant on the HFBI surfaces may already be prevented to such an extent that a charge difference of the present magnitude (≈25 mV) has no further effect. Furthermore, in collaboration with the group of Prof. Bischoff, Saarland University, Germany, we were able to detect a change in the composition of cell wall macromolecules in the *ΔdltA* mutant by sodium dodecylsulfate polyacrylamide gel electrophoresis (SDS-PAGE). This in turn could have an effect on the patchiness of the cell wall, which in turn could then lead to a change in the magnitude of the forces acting. These results may provide the

basis for a better understanding of the interaction of macromolecules at interfaces and also advance the use of HFBI-coated surfaces in biomedical research.

5.3 Influence of MiuA on RPE-1 Cell Adhesion

In order to understand the adhesion not only of prokaryotes, especially bacteria, but also of eukaryotes, measurements were performed on retinal pigment epithelial (RPE-1) cells. For the results of this work, the focus was on the influence of the size of focal adhesions of RPE-1 cells on cell adhesion. Our collaborators in the group of Prof. Lautenschläger, University of Saarland, Germany, have recently shown that adding the natural compound miuraenamide A (MiuA) stabilizes actin filaments, increases their length, and alters the number and size of focal adhesions [232]. MiuA-treated cells have more but smaller focal adhesions and an increased spreading area of the cell. Since focal adhesions are crucial for cell adhesion, the adhesion parameters (adhesion energy, adhesion force and rupture length) of MiuA-treated and untreated RPE-1 cells on fibronectin were measured by SCFS and compared.

Retraction curves of untreated (control, Fig. 5.8 a) and MiuA-treated (MiuA, Fig. 5.8 b) RPE-1 cells have a similar curve shape, but the order of the adhesion forces is different. While the adhesion energy (d) and force (e) are significantly reduced in the MiuA measurements compared to the control, there is no significant difference in the rupture length (f). Increasing the total area of focal adhesions of MiuA-treated RPE-1 cells does not result in increased adhesion. On the contrary, the adhesion energy is reduced to about 25 %. Thus, the individual focal adhesions that were reduced in area by MiuA treatment do not appear to have their full adhesion capacity. The unchanged rupture length despite the increased cell-substrate contact area cannot be fully explained. One possible explanation is that MiuA causes a shift of the nucleus to the center of the cell [232]. The nucleus serves as an attachment point for the peeling process, thus could minimize the rupture length. In addition, a general reduction in the adhesion force of individual focal adhesions could lead to this unchanged rupture length. This altered cell adhesion also has implications for cell migration of RPE-1 cells (Fig. 5.8 c). Our collaborators in the lab of Prof. Lautenschläger have shown that mesenchymal migration on fibronectin lines, in which cell adhesion plays a major role, is strongly minimized in MiuA-treated RPE-1 cells [232]. In contrast, recent unpublished measurements have shown that amoeboid migration under confinement in a PDMS channel, which is based on friction and not on adhesion, is not significantly different.

MiuA-treated RPE-1 cells show strongly reduced adhesion. This can be explained by changes in the size of the focal adhesions. The reduced adhesion strength of MiuA-treated RPE-1 cells has a strong effect on adhesion-based migration, while friction-based migration is unchanged. Changes in focal adhesions other than size remain to be investigated.

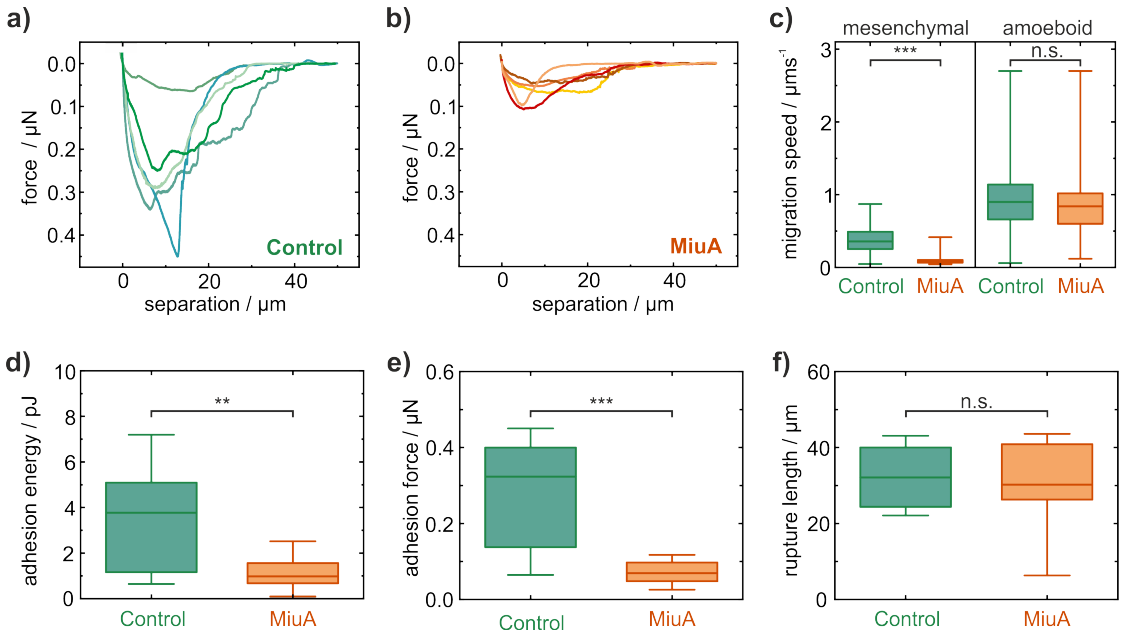

Figure 5.8: Adhesion measurements of RPE-1 cells without addition of any compound (control, green) and of RPE-1 cells after MiuA treatment (MiuA, orange). Five representative retraction curves of untreated (a) and MiuA-treated (b) RPE-1 cells are shown for a firs overview. Box plots (min-to-max) of adhesion parameters: adhesion energy (d), adhesion force (e), and rupture length (f), show the influence of cell treatment on the overall adhesion process. (c) Mesenchymal (left) and amoeboid (right) migration measurements (box plots, min-to-max). MiuA-treated RPE-1 cells on fibronectin lines (mesenchymal) show a strong reduction in migration speed, whereas the migration speed of MiuA-treated RPE-1 cells under confinement (amoeboid) is unchanged. Mesenchymal migration data are taken from Baltes *et al.* [232]. Unpaired t-test was performed to compare control and MiuA measurements: n.s., $p > 0.05$; **, $p < 0.01$; *** $p < 0.001$.

6 Summary and Outlook

6.1 Summary

The purpose of this thesis is to advance the understanding of the behavior of macromolecules at interfaces. Emphasis has been placed on two main topics: (I) The properties of the protein HFBI at interfaces, especially as a pure protein bilayer. (II) The role of macromolecules in the adhesion of cells, in particular the adhesion of *S. aureus* either by modifying the surface (roughness, hydrophobicity, charge) or the macromolecules on the *S. aureus* cell wall (SA113 knock-out mutants). A variety of measurement techniques has been used to study macromolecules at interfaces. While questions about the behavior of HFBI at interfaces have mainly been addressed microfluidically and by generating a droplet interface bilayer (DIB), the method of choice for cell adhesion has been single-cell force spectroscopy (SCFS).

In the first part (I), by improving the method of HFBI bilayer formation, properties such as water permeability were investigated. It was shown that the water permeability of these pure protein bilayers is vanishingly small, below the accuracy of the measurement. At the same time, the HFBI bilayers were found to be very stable with respect to osmotic pressure. Water permeability could be generated by introducing a steric hindrance through the HFBI-cellulose fusion protein HFBI-dCBM. An increase in permeability was observed with increasing HFBI-dCBM concentration in the pure protein bilayer. Combined with MD simulations, it was shown that the low water permeability of HFBI bilayers indicates that the proteins are reorganized when the bilayer is formed from two HFBI monolayers.

This low water permeability property raised the next question: How could this protein bilayer be used to generate vesicles? To answer this question, several vesicle preparation techniques were tested and the two most promising were described. The technique of microfluidic jetting could be used to produce vesicles, but optimizations for higher throughput are still needed. The production of vesicles by a microfluidic device by creating first micelles and "wrapping" a second hydrophobin layer around them is still in its infancy.

In addition to the study of pure HFBI protein bilayers, the incorporation of HFBI into DOPC bilayers was also considered. It was found that HFBI incorporation was enhanced by voltage-induced pore formation. Hydrophobins stabilize the edges of these pores and thus increase the overall stability of these DOPC bilayers.

In the second main part of this thesis (II), new insights into the interplay of many different macromolecules on the bacterial cell wall of *S. aureus* during adhesion were gained. Nanorough surfaces with a roughness dimension corresponding to the length of cell wall macromolecules were shown to affect the adhesion of *S. aureus*. A decrease in adhesion of approximately 60% was observed when the roughness was increased from

RMS = 7 nm to RMS = 35 nm. This change in adhesion may be directly related to the contact area accessible to the fluctuating cell wall macromolecules.

However, it became clear that the chemical nature of the surface is also important for macromolecules to tether to it. The adhesion strength of the bacterium was significantly affected by changes in the hydrophobicity of the surface. While a large number of macromolecules are able to bind to hydrophobic surfaces, only a small number of macromolecules are able to bind to hydrophilic surfaces. Furthermore, adhesion is not only influenced by the number of tethering macromolecules, but also by the interaction of many different macromolecules on the cell wall, as shown by measurements with different *S. aureus* knock-out mutants. Thus, adhesion involves many different macromolecules whose role in the adhesion process may vary, depending on the adherent surface.

The role of electrostatic interactions in bacterial adhesion to hydrophilic HFBI surfaces was investigated by combining the two main topics. Coatings with only a crucial difference in charge for bacterial adhesion were obtained by using HFBI and the charge-modified HFBI mutant HFBI D40Q/D43N. It was this difference in charge that resulted in a change in the strength of the adhesion of *S. aureus*. A higher affinity was found for less negatively charged surfaces of the same charge sign. Electrostatic interactions can therefore degrade adhesion of *S. aureus* to negatively charged hydrophilic surfaces.

However, macromolecules play a crucial role not only in bacterial adhesion but also in eukaryotic adhesion. RPE-1 cells with stabilized actin filaments and altered focal adhesions (smaller in size but more numerous) showed reduced adhesion compared to untreated RPE-1 cells.

6.2 Outlook

The interactions of macromolecules at interfaces, whether in artificial bilayers or in cell adhesion, is a very large field that needs to be further explored in the future. This thesis provides answers to some of the open questions, but also raises new follow-up questions.

For example, the exact structure of the HFBI molecules in the bilayer must be explored to understand and control the properties of these protein bilayers. Fabricating free-standing HFBI bilayers and scanning them with atomic force microscopy, electron microscopy, or tunneling microscopy could image the protein arrangement and thus elucidate the protein-protein interactions.

The incorporation of membrane channels and their function would be the next step to expand the potential applications of HFBI bilayers. For example, the incorporation of aquaporins into the HFBI bilayer could further promote water permeability and thus the potential of hydrophobins as a selective bilayer. Likewise, the incorporation of hydrophobins in a lipid bilayer needs to be further explored along these lines. Do the hydrophobins remain in the lipid membrane even in the absence of pores? How do the HFBI proteins behave in more complex membranes? All these questions can be addressed by the presented method of electroporation measurements in a microfluidic setup. Time-resolved voltage measurements as well as the use of other lipids could lead to further insights.

Not only bilayers, but also hydrophobin vesicles have to be investigated, for which the method of vesicle production has to be further optimized. To be able to produce a large number of vesicles, a high-throughput method such as the microfluidic system is needed. A large number of vesicles would allow to test the stability to acid or stress factors found in physiological conditions. The packaging of various compounds for use as potential drug carriers could also be tested. With the two methods presented in this work, it should be possible to introduce a compound during vesicle formation. Of course, possible destabilizing effects caused by the compound during the formation of the bilayer have to be taken into account. Alternatively, loading the vesicles after bilayer formation using the FluidFM with a nanosyringe could be considered. Furthermore, the production of oil-in-oil vesicles and a filling with different nutrients could be of great advantage for e.g. the food industry.

According to the results of this work, HFBI could also be used as a protein coating to reduce bacterial adhesion in biomedical applications such as implants. In this context, the production of antibacterial HFBI fusion proteins could lead to further progress. To be used as a biomedical coating, HFBI coatings need to be compared with other protein coatings currently in use (e.g. bovine serum albumin) and the bacterial adhesion of other bacteria has to be tested.

Developing antibacterial surface coatings also requires further research to understand how bacteria adhere. The forces involved on bacterial adhesion could be tested in greater detail varying the charge of the surfaces. These different surface properties could be achieved for example by surface functionalization with silanes with different endgroups or proteins like HFBI with charge mutants. The change of the surrounding medium (pH, ion concentrations) could not only lead to changes of the surface to adhere but also on the cell surface.

The role of individual macromolecules of the bacterial cell wall needs to be further investigated in the future. *S. aureus* mutants lacking individual adhesins (e.g. FnBPA/B) could lead to further elucidation of the role of individual macromolecules. Since the hypothesis of single changes in cell wall macromolecules may entail a number of other unanticipated changes, this should be supported by accurate protein analysis of the cell wall. Therefore, further experiments using the SDS-PAGE with additional mass spectrometry or western blotting should be performed. Another way to clarify the role of individual macromolecules is a bottom-up strategy by coating spheres with individual macromolecules to study their specific behavior in an adhesion process. It is important to note that interactions between different cell wall macromolecules can alter their behavior. This must be taken into account when interpreting the results. Already known surface properties can be used to avoid altering the cell itself and still study the role of cell wall macromolecules. A combination of surfaces with different roughness and hydrophobicity could lead to the elucidation of the role of individual macromolecules through different tether lengths and binding affinities to surfaces with different surface potential. In addition, experiments with other (e.g. gram-negative) bacteria are needed to test the general validity of the concepts of bacterial adhesion established for *S. aureus* adhesion.

These experiments represent only a small fraction of possible biophysical experiments that could be performed with macromolecules at interfaces. However, it would be a further step in understanding the behavior of HFBI proteins and bacterial cell wall macromolecules at interfaces.

Bibliography

[1] H. R. Horton, L. A. Moran, K. G. Scrimgeour, M. D. Perry, and J. D. Rawn, *Biochemie, 4., aktualisierte auflage* (Pearson Deutschland GmbH, 2008) (cited on pages 1, 7).

[2] A. R. Hall and M Geoghegan, "Polymers and biopolymers at interfaces", Reports on Progress in Physics **81**, 036601 (2018) 10.1088/1361-6633/aa9e9c (cited on pages 1, 7).

[3] J. R. Werber and M. Elimelech, "Permselectivity limits of biomimetic desalination membranes", Science Advances **4**, 10.1126/sciadv.aar8266 (2018) 10.1126/sciadv.aar8266 (cited on page 1).

[4] W. T. Al-Jamal and K. Kostarelos, "Liposomes: from a clinically established drug delivery system to a nanoparticle platform for theranostic nanomedicine", Accounts of Chemical Research **44**, 1094–1104 (2011) 10.1021/ar200105p (cited on page 1).

[5] Z. Michalak, M. Muzzio, P. J. Milianta, R. Giacomini, and S. Lee, "Effect of monoglyceride structure and cholesterol content on water permeability of the droplet bilayer", Langmuir **29**, 15919–15925 (2013) 10.1021/la4040535 (cited on pages 1, 23, 34–35).

[6] P. J. Milianta, M. Muzzio, J. Denver, G. Cawley, and S. Lee, "Water permeability across symmetric and asymmetric droplet interface bilayers: interaction of cholesterol sulfate with DPhPC", Langmuir **31**, 12187–12196 (2015) 10.1021/acs.langmuir.5b02748 (cited on pages 1, 23).

[7] K. R. Levental, J. H. Lorent, X. Lin, A. D. Skinkle, M. A. Surma, E. A. Stockenbojer, A. A. Gorfe, and I. Levental, "Polyunsaturated lipids regulate membrane domain stability by tuning membrane order", Biophysical Journal **110**, 1800–1810 (2016) 10.1016/j.bpj.2016.03.012 (cited on page 1).

[8] G. Sun, T.-S. Chung, K. Jeyaseelan, and A. Armugam, "Stabilization and immobilization of aquaporin reconstituted lipid vesicles for water purification", Colloids and Surfaces B: Biointerfaces **102**, 466–471 (2013) 10.1016/j.colsurfb.2012.08.009 (cited on page 1).

[9] W. SzymaŃski, D. Yilmaz, A. Koçer, and B. L. Feringa, "Bright ion channels and lipid bilayers", Accounts of Chemical Research **46**, 2910–2923 (2013) 10.1021/ar4000357 (cited on page 1).

[10] B. M. Discher, H. Bermudez, D. A. Hammer, D. E. Discher, Y.-Y. Won, and F. S. Bates, "Cross-linked polymersome membranes: vesicles with broadly adjustable properties", The Journal of Physical Chemistry B **106**, 2848–2854 (2002) 10.1021/jp011958z (cited on page 1).

[11] K. B. Vargo, R. Parthasarathy, and D. A. Hammer, "Self-assembly of tunable protein suprastructures from recombinant oleosin", Proceedings of the National Academy of Sciences **109**, 11657–11662 (2012) 10.1073/pnas.1205426109 (cited on page 1).

[12] S. Gudlur, P. Sukthankar, J. Gao, L. A. Avila, Y. Hiromasa, J. Chen, T. Iwamoto, and J. M. Tomich, "Peptide nanovesicles formed by the self-assembly of branched amphiphilic peptides", PLoS ONE **7**, edited by M. Gasset, e45374 (2012) 10.1371/journal.pone.0045374 (cited on page 1).

[13] H. Hähl, J. N. Vargas, A. Griffo, P. Laaksonen, G. Szilvay, M. Lienemann, K. Jacobs, R. Seemann, and J.-B. Fleury, "Pure protein bilayers and vesicles from native fungal hydrophobins", Advanced Materials **29**, 1602888 (2017) 10.1002/adma.201602888 (cited on pages 1, 13, 23, 33, 35).

[14] H. Hähl, J. N. Vargas, M. Jung, A. Griffo, P. Laaksonen, M. Lienemann, K. Jacobs, R. Seemann, and J.-B. Fleury, "Adhesion properties of freestanding hydrophobin bilayers", Langmuir **34**, 8542–8549 (2018) 10.1021/acs.langmuir.8b00575 (cited on pages 1, 11, 13).

[15] R Fettiplace and D. A. Haydon, "Water permeability of lipid membranes.", Physiological Reviews **60**, 510–550 (1980) 10.1152/physrev.1980.60.2.510 (cited on pages 1, 34–35).

[16] J. A. Opsteen, J. J. L. M. Cornelissen, and J. C. M. van Hest, "Block copolymer vesicles", Pure and Applied Chemistry **76**, 1309–1319 (2004) 10.1351/pac200476071309 (cited on pages 1, 35).

[17] H. Bayley, B. Cronin, A. Heron, M. A. Holden, W. L. Hwang, R. Syeda, J. Thompson, and M. Wallace, "Droplet interface bilayers", Molecular BioSystems **4**, 1191 (2008) 10.1039/b808893d (cited on pages 1, 23).

[18] K. Hori and S. Matsumoto, "Bacterial adhesion: from mechanism to control", Biochemical Engineering Journal **48**, 424–434 (2010) 10.1016/j.bej.2009.11.014 (cited on page 2).

[19] B. M. Gumbiner, "Cell adhesion: the molecular basis of tissue architecture and morphogenesis", Cell **84**, 345–357 (1996) 10.1016/s0092-8674(00)81279-9 (cited on page 2).

[20] D Pavithra and M. Doble, "Biofilm formation, bacterial adhesion and host response on polymeric implants - issues and prevention", Biomedical Materials **3**, 034003 (2008) 10.1088/1748-6041/3/3/034003 (cited on page 2).

[21] M. Wilkins, L. Hall-Stoodley, R. N. Allan, and S. N. Faust, "New approaches to the treatment of biofilm-related infections", Journal of Infection **69**, S47–S52 (2014) 10.1016/j.jinf.2014.07.014 (cited on pages 2, 14).

[22] W. Oliveira, P. Silva, R. Silva, G. Silva, G. Machado, L. Coelho, and M. Correia, "Staphylococcus aureus and staphylococcus epidermidis infections on implants", Journal of Hospital Infection **98**, 111–117 (2018) 10.1016/j.jhin.2017.11.008 (cited on pages 2, 14).

[23] K. A. Berry, M. T. A. Verhoef, A. C. Leonard, and G. Cox, "*Staphylococcus aureus* adhesion to the host", Annals of the New York Academy of Sciences **1515**, 75–96 (2022) 10.1111/nyas.14807 (cited on pages 2, 14–16).

[24] C. Heilmann, "Adhesion mechanisms of staphylococci", in *Advances in experimental medicine and biology* (Springer Netherlands, 2011), pages 105–123, 10.1007/978-94-007-0940-9_7 (cited on pages 2, 14–16).

[25] T. J. Foster, "Surface proteins of *Staphylococcus aureus*", Microbiology Spectrum **7**, edited by V. A. Fischetti, R. P. Novick, J. J. Ferretti, D. A. Portnoy, M. Braunstein, and J. I. Rood, 10.1128/microbiolspec.gpp3-0046-2018 (2019) 10.1128/microbiolspec.gpp3-0046-2018 (cited on pages 2, 16).

[26] T. J. Foster, J. A. Geoghegan, V. K. Ganesh, and M. Höök, "Adhesion, invasion and evasion: the many functions of the surface proteins of *Staphylococcus aureus*", Nature Reviews Microbiology **12**, 49–62 (2014) 10.1038/nrmicro3161 (cited on pages 2, 14, 16–17).

[27] N. Lu, W. Zhang, Y. Weng, X. Chen, Y. Cheng, and P. Zhou, "Fabrication of PDMS surfaces with micro patterns and the effect of pattern sizes on bacteria adhesion", Food Control **68**, 344–351 (2016) 10.1016/j.foodcont.2016.04.014 (cited on pages 2, 17).

[28] A. V. Singh, V. Vyas, R. Patil, V. Sharma, P. E. Scopelliti, G. Bongiorno, A. Podestà, C. Lenardi, W. N. Gade, and P. Milani, "Quantitative characterization of the influence of the nanoscale morphology of nanostructured surfaces on bacterial adhesion and biofilm formation", PLoS ONE **6**, edited by V. Bansal, e25029 (2011) 10.1371/journal.pone.0025029 (cited on pages 2, 18).

[29] L. Liu, B. Ercan, L. Sun, K. S. Ziemer, and T. J. Webster, "Understanding the role of polymer surface nanoscale topography on inhibiting bacteria adhesion and growth", ACS Biomaterials Science & Engineering **2**, 122–130 (2015) 10.1021/acsbiomaterials.5b00431 (cited on pages 2, 18).

[30] N. Mitik-Dineva, J. Wang, V. K. Truong, P. Stoddart, F. Malherbe, R. J. Crawford, and E. P. Ivanova, "*Escherichia coli*, *Pseudomonas aeruginosa*, and *Staphylococcus aureus* attachment patterns on glass surfaces with nanoscale roughness", Current Microbiology **58**, 268–273 (2008) 10.1007/s00284-008-9320-8 (cited on pages 2, 18).

[31] E. P. Ivanova, V. K. Truong, H. K. Webb, V. A. Baulin, J. Y. Wang, N. Mohammodi, F. Wang, C. Fluke, and R. J. Crawford, "Differential attraction and repulsion of *Staphylococcus aureus* and *Pseudomonas aeruginosa* on molecularly smooth titanium films", Scientific Reports **1**, 10.1038/srep00165 (2011) 10.1038/srep00165 (cited on pages 2, 18).

[32] P. Tang, W. Zhang, Y. Wang, B. Zhang, H. Wang, C. Lin, and L. Zhang, "Effect of superhydrophobic surface of titanium on *Staphylococcus aureus* adhesion", Journal of Nanomaterials **2011**, 1–8 (2011) 10.1155/2011/178921 (cited on pages 2, 19).

[33] B. J. Privett, J. Youn, S. A. Hong, J. Lee, J. Han, J. H. Shin, and M. H. Schoenfisch, "Antibacterial fluorinated silica colloid superhydrophobic surfaces", Langmuir **27**, 9597–9601 (2011) 10.1021/la201801e (cited on pages 2, 19).

[34] X. Zhu, D. Jańczewski, S. Guo, S. S. C. Lee, F. J. P. Velandia, S. L.-M. Teo, T. He, S. R. Puniredd, and G. J. Vancso, "Polyion multilayers with precise surface charge control for antifouling", ACS Applied Materials & Interfaces **7**, 852–861 (2014) 10.1021/am507371a (cited on pages 2, 19).

[35] S. Guo, D. Jańczewski, X. Zhu, R. Quintana, T. He, and K. G. Neoh, "Surface charge control for zwitterionic polymer brushes: tailoring surface properties to antifouling applications", Journal of Colloid and Interface Science **452**, 43–53 (2015) 10.1016/j.jcis.2015.04.013 (cited on pages 2, 19).

[36] S. Guo, M. Y. Kwek, Z. Q. Toh, D. Pranantyo, E.-T. Kang, X. J. Loh, X. Zhu, D. Jańczewski, and K. G. Neoh, "Tailoring polyelectrolyte architecture to promote cell growth and inhibit bacterial adhesion", ACS Applied Materials & Interfaces **10**, 7882–7891 (2018) 10.1021/acsami.8b00666 (cited on pages 2, 19).

[37] J. K. Oh, Y. Yegin, F. Yang, M. Zhang, J. Li, S. Huang, S. V. Verkhoturov, E. A. Schweikert, K. Perez-Lewis, E. A. Scholar, T. M. Taylor, A. Castillo, L. Cisneros-Zevallos, Y. Min, and M. Akbulut, "The influence of surface chemistry on the kinetics and thermodynamics of bacterial adhesion", Scientific Reports **8**, 10.1038/s41598-018-35343-1 (2018) 10.1038/s41598-018-35343-1 (cited on pages 2, 19).

[38] M. D. Lechner, K. Gehrke, and E. H. Nordmeier, *Makromolekulare Chemie* (Springer Berlin Heidelberg, 2014), 10.1007/978-3-642-41769-6 (cited on page 7).

[39] C. S. Tsai, *Biomacromolecules: introduction to structure, function and informatics* (John Wiley & Sons, Inc., Apr. 2007), 10.1002/0470080124 (cited on page 7).

[40] J. L. Brash and T. A. Horbett, "Proteins at interfaces", in *ACS symposium series* (American Chemical Society, May 1995), pages 1–23, 10.1021/bk-1995-0602.ch001 (cited on page 7).

[41] M. Wahlgren and T. Arnebrant, "Protein adsorption to solid surfaces", Trends in biotechnology **9**, 201–208 (1991) (cited on page 7).

[42] J. Barberi and S. Spriano, "Titanium and protein adsorption: an overview of mechanisms and effects of surface features", Materials **14**, 1590 (2021) 10.3390/ma14071590 (cited on page 7).

[43] W. van der Vegt, H. van der Mei, H. Wösten, J. Wessels, and H. Busscher, "A comparison of the surface activity of the fungal hydrophobin SC3p with those of other proteins", Biophysical Chemistry **57**, 253–260 (1996) 10.1016/0301-4622(95)00059-7 (cited on page 7).

[44] E. D. Korn, "Cell membranes: structure and synthesis", Annual Review of Biochemistry **38**, 263–288 (1969) 10.1146/annurev.bi.38.070169.001403 (cited on page 7).

[45] P. Agre, "Aquaporin water channels (nobel lecture)", Angewandte Chemie International Edition **43**, 4278–4290 (2004) 10.1002/anie.200460804 (cited on page 7).

[46] A. S. Verkman and A. K. Mitra, "Structure and function of aquaporin water channels", American Journal of Physiology-Renal Physiology **278**, F13–F28 (2000) 10.1152/ajprenal.2000.278.1.f13 (cited on page 7).

[47] C. Miller, "Integral membrane channels: studies in model membranes", Physiological Reviews **63**, 1209–1242 (1983) 10.1152/physrev.1983.63.4.1209 (cited on page 7).

[48] N. J. Yang and M. J. Hinner, "Getting across the cell membrane: an overview for small molecules, peptides, and proteins", in *Site-specific protein labeling* (Springer New York, Dec. 2014), pages 29–53, 10.1007/978-1-4939-2272-7_3 (cited on page 7).

[49] M. R. Gonzalez, M. Bischofberger, L. Pernot, F. G. van der Goot, and B. Frêche, "Bacterial pore-forming toxins: the (w)hole story?", Cellular and Molecular Life Sciences **65**, 493–507 (2007) 10.1007/s00018-007-7434-y (cited on page 7).

[50] M. D. Peraro and F. G. van der Goot, "Pore-forming toxins: ancient, but never really out of fashion", Nature Reviews Microbiology **14**, 77–92 (2015) 10.1038/nrmicro.2015.3 (cited on page 7).

[51] L. Harris, S. Foster, and R. Richards, "An introduction to staphylococcus aureus, and techniques for identifying and quantifying s. aureus adhesins in relation to adhesion to biomaterials: review", European Cells and Materials **4**, 39–60 (2002) 10.22203/ecm.v004a04 (cited on page 7).

[52] D. R. Critchley, "Focal adhesions – the cytoskeletal connection", Current Opinion in Cell Biology **12**, 133–139 (2000) 10.1016/s0955-0674(99)00067-8 (cited on page 7).

[53] P. Lipke, "What we do not know about fungal cell adhesion molecules", Journal of Fungi **4**, 59 (2018) 10.3390/jof4020059 (cited on page 7).

[54] L. Petruzzelli, M. Takami, and H. Humes, "Structure and function of cell adhesion molecules", The American Journal of Medicine **106**, 467–476 (1999) 10.1016/s0002-9343(99)00058-3 (cited on page 7).

[55] J.-M. Entenza, P. Moreillon, M. M. Senn, J. Kormanec, P. M. Dunman, B. Berger-Bächi, S. Projan, and M. Bischoff, "Role of sigmaB in the expression of *Staphylococcus aureus* cell wall adhesins ClfA and FnbA and contribution to infectivity in a rat model of experimental endocarditis", Infection and Immunity **73**, 990–998 (2005) 10.1128/iai.73.2.990-998.2005 (cited on page 7).

[56] R. Wheeler, R. D. Turner, R. G. Bailey, B. Salamaga, S. Mesnage, S. A. S. Mohamad, E. J. Hayhurst, M. Horsburgh, J. K. Hobbs, and S. J. Foster, "Bacterial cell enlargement requires control of cell wall stiffness mediated by peptidoglycan hydrolases", mBio **6**, edited by A. Casadevall, 10.1128/mbio.00660-15 (2015) 10.1128/mbio.00660-15 (cited on page 7).

[57] P. Loskill, P. M. Pereira, P. Jung, M. Bischoff, M. Herrmann, M. G. Pinho, and K. Jacobs, "Reduction of the peptidoglycan crosslinking causes a decrease in stiffness of the staphylococcus aureus cell envelope", Biophysical Journal **107**, 1082–1089 (2014) 10.1016/j.bpj.2014.07.029 (cited on page 7).

[58] P. W. Fowler, J. Hélie, A. Duncan, M. Chavent, H. Koldsø, and M. S. P. Sansom, "Membrane stiffness is modified by integral membrane proteins", Soft Matter **12**, 7792–7803 (2016) 10.1039/c6sm01186a (cited on page 7).

[59] H. J. Busscher and A. H. Weerkamp, "Specific and non-specific interactions in bacterial adhesion to solid substrata", FEMS Microbiology Letters **46**, 165–173 (1987) 10.1111/j.1574-6968.1987.tb02457.x (cited on page 7).

[60] J. Joseph-Silverstein and R. L. Silverstein, "Cell adhesion molecules: an overview", Cancer Investigation **16**, 176–182 (1998) 10.3109/07357909809050034 (cited on page 7).

[61] H.-J. Butt and M. Kappl, *Surface and interfacial forces* (Wiley-VCH Verlag GmbH & Co. KGaA, Jan. 2010), 10.1002/9783527629411 (cited on pages 8–10).

[62] C. J. Van Oss, *Interfacial forces in aqueous media*, eng, 2nd ed. (Boca Raton, Fla, 2006), http://www.loc.gov/catdir/enhancements/fy0648/2005035590-d.html (cited on pages 8–9).

[63] J. N. Israelachvili, *Intermolecular and surface forces*, eng, 3rd ed. (Burlington, MA, 2011) (cited on pages 8–10).

[64] M. Malmsten (Hrsg.), *Biopolymers at interfaces*, Vol. 110, surfaurfactant science series (CRC Press, 2003) (cited on page 8).

[65] C. Spengler, *Exploring microbial adhesion through targeted design of bacterial probes and substrates in afm-based force spectroscopy*, 2018, 10.22028/D291-27653 (cited on pages 8, 15, 26–27).

[66] N. Thewes, *Bacterial adhesion to abiotic surfaces: atomic force spectroscopy and monte carlo simulations*, 2016, 10.22028/D291-23183 (cited on pages 8, 27).

[67] H. Hähl, *Proteinadsorption an grenzflächen: bestimmung von adsorptionskinetik und adsorbatstruktur mittels reflexionsmethoden*, 2011 (cited on page 8).

[68] W. Pauli, "Über den zusammenhang des abschlusses der elektronengruppen im atom mit der komplexstruktur der spektren", Zeitschrift für Physik **31**, 765–783 (1925) 10.1007/bf02980631 (cited on page 8).

[69] E. W. Fischer, "Elektronenmikroskopische Untersuchungen zur Stabilität von Suspensionen in makromolekularen Lösungen", Kolloid-Zeitschrift **160**, 120–141 (1958) 10.1007/bf01503288 (cited on page 8).

[70] F. T. Hesselink, "Theory of the stabilization of dispersions by adsorbed macromolecules. i. statistics of the change of some configurational properties of adsorbed macromolecules on the approach of an impenetrable interface", The Journal of Physical Chemistry **75**, 65–71 (1971) 10.1021/j100671a011 (cited on page 8).

[71] F. T. Hesselink, A. Vrij, and J. T. G. Overbeek, "Theory of the stabilization of dispersions by adsorbed macromolecules. II. interaction between two flat particles", The Journal of Physical Chemistry **75**, 2094–2103 (1971) 10.1021/j100683a005 (cited on page 8).

[72] A. Vrij, "Polymers at interfaces and the interactions in colloidal dispersions", Pure and Applied Chemistry **48**, 471–483 (1976) 10.1351/pac197648040471 (cited on page 8).

[73] D. Leckband and J. Israelachvili, "Intermolecular forces in biology", Quarterly Reviews of Biophysics **34**, 105–267 (2001) 10.1017/s0033583501003687 (cited on page 8).

[74] F. London, "The general theory of molecular forces", Transactions of the Faraday Society **33**, 8b (1937) 10.1039/tf937330008b (cited on page 8).

[75] H. Hamaker, "The london—van der waals attraction between spherical particles", Physica **4**, 1058–1072 (1937) 10.1016/s0031-8914(37)80203-7 (cited on page 9).

[76] E. Lifshitz and M. Hamermesh, "The theory of molecular attractive forces between solids", in *Perspectives in theoretical physics*, Reprinted from Soviet Physics JETP 2, Part 1, 73, 1956 (Elsevier, 1992), pages 329–349, 10.1016/b978-0-08-036364-6.50031-4 (cited on page 9).

[77] B Derjaguin and L Landau, "Theory of the stability of strongly charged lyophobic sols and of the adhesion of strongly charged particles in solutions of electrolytes", Progress in Surface Science **43**, Received 1941, 30–59 (1993) 10.1016/0079-6816(93)90013-l (cited on page 9).

[78] E. J. W. Verwey, "Theory of the stability of lyophobic colloids.", The Journal of Physical and Colloid Chemistry **51**, 631–636 (1947) 10.1021/j150453a001 (cited on page 9).

[79] H. Umeyama and K. Morokuma, "The origin of hydrogen bonding. an energy decomposition study", Journal of the American Chemical Society **99**, 1316–1332 (1977) 10.1021/ja00447a007 (cited on page 9).

[80] M. L. Huggins, "50 years of hydrogen bond theory", Angewandte Chemie International Edition in English **10**, 147–152 (1971) 10.1002/anie.197101471 (cited on page 9).

[81] J. D. WATSON and F. H. C. CRICK, "Molecular structure of nucleic acids: a structure for deoxyribose nucleic acid", Nature **171**, 737–738 (1953) 10.1038/171737a0 (cited on page 9).

[82] L. Pauling, R. B. Corey, and H. R. Branson, "The structure of proteins: two hydrogen-bonded helical configurations of the polypeptide chain", Proceedings of the National Academy of Sciences **37**, 205–211 (1951) 10.1073/pnas.37.4.205 (cited on page 9).

[83] L. Pauling and R. B. Corey, "The pleated sheet, a new layer configuration of polypeptide chains", Proceedings of the National Academy of Sciences **37**, 251–256 (1951) 10.1073/pnas.37.5.251 (cited on page 9).

[84] H. A. Wösten and M. L. de Vocht, "Hydrophobins, the fungal coat unravelled", Biochimica et Biophysica Acta (BBA) - Reviews on Biomembranes **1469**, 79–86 (2000) 10.1016/s0304-4157(00)00002-2 (cited on page 10).

[85] J. R. Whiteford and P. D. Spanu, "Hydrophobins and the interactions between fungi and plants", Molecular Plant Pathology **3**, 391–400 (2002) 10.1046/j.1364-3703.2002.00129.x (cited on page 10).

[86] A. Hille-Rehfeld, "Die hydrophobine der pilze – vielzweckproteine mit anwendungspotential", Chemie in unserer Zeit **53**, 187–193 (2019) 10.1002/ciuz.201800881 (cited on page 10).

[87] M. B. Linder, "Hydrophobins: proteins that self assemble at interfaces", Current Opinion in Colloid & Interface Science **14**, 356–363 (2009) 10.1016/j.cocis.2009.04.001 (cited on page 10).

[88] J. G. Wessels, "Fungal hydrophobins: proteins that function at an interface", Trends in Plant Science **1**, 9–15 (1996) 10.1016/s1360-1385(96)80017-3 (cited on page 10).

[89] J. Hakanpää, A. Paananen, S. Askolin, T. Nakari-Setälä, T. Parkkinen, M. Penttilä, M. B. Linder, and J. Rouvinen, "Atomic resolution structure of the HFBII hydrophobin, a self-assembling amphiphile", Journal of Biological Chemistry **279**, 534–539 (2004) 10.1074/jbc.m309650200 (cited on page 10).

[90] O. M. H. de Vries, M. P. Fekkes, H. A. B. Wösten, and J. G. H. Wessels, "Insoluble hydrophobin complexes in the walls of schizophyllum commune and other filamentous fungi", Archives of Microbiology **159**, 330–335 (1993) 10.1007/bf00290915 (cited on page 10).

[91] M. B. Linder, G. R. Szilvay, T. Nakari-Setälä, and M. E. Penttilä, "Hydrophobins: the protein-amphiphiles of filamentous fungi", FEMS Microbiology Reviews **29**, 877–896 (2005) 10.1016/j.femsre.2005.01.004 (cited on page 10).

[92] J. Wessels, "Developmental regulation of fungal cell wall formation", Annual review of phytopathology **32**, 413–437 (1994) (cited on page 10).

[93] H. Wösten, F. Schuren, and J. Wessels, "Interfacial self-assembly of a hydrophobin into an amphipathic protein membrane mediates fungal attachment to hydrophobic surfaces.", The EMBO Journal **13**, 5848–5854 (1994) 10.1002/j.1460-2075.1994.tb06929.x (cited on page 10).

[94] H. A. B. Wösten, "Hydrophobins: multipurpose proteins", Annual Review of Microbiology **55**, 625–646 (2001) 10.1146/annurev.micro.55.1.625 (cited on page 10).

[95] A. J. Green, K. A. Littlejohn, P. Hooley, and P. W. Cox, "Formation and stability of food foams and aerated emulsions: hydrophobins as novel functional ingredients", Current Opinion in Colloid & Interface Science **18**, 292–301 (2013) 10.1016/j.cocis.2013.04.008 (cited on page 10).

[96] C. Alamprese, M. Rollini, A. Musatti, P. Ferranti, and A. Barbiroli, "Emulsifying and foaming properties of a hydrophobin-based food ingredient from *Trichoderma reesei*: a phenomenological comparative study", LWT **157**, 113060 (2022) 10.1016/j.lwt.2021.113060 (cited on page 10).

[97] E. S. Basheva, P. A. Kralchevsky, N. C. Christov, K. D. Danov, S. D. Stoyanov, T. B. J. Blijdenstein, H.-J. Kim, E. G. Pelan, and A. Lips, "Unique properties of bubbles and foam films stabilized by HFBII hydrophobin", Langmuir **27**, 2382–2392 (2011) 10.1021/la104726w (cited on page 10).

[98] H. A. B. Wösten and K. Scholtmeijer, "Applications of hydrophobins: current state and perspectives", Applied Microbiology and Biotechnology **99**, 1587–1597 (2015) 10.1007/s00253-014-6319-x (cited on page 10).

[99] K. Scholtmeijer, J. G. H. Wessels, and H. A. B. Wösten, "Fungal hydrophobins in medical and technical applications", Applied Microbiology and Biotechnology **56**, 1–8 (2001) 10.1007/s002530100632 (cited on page 10).

[100] T. Nakari-Setala, N. Aro, N. Kalkkinen, E. Alatalo, and M. Penttila, "Genetic and biochemical characterization of the trichoderma reesei hydrophobin HFBI", European Journal of Biochemistry **235**, 248–255 (1996) 10.1111/j.1432-1033.1996.00248.x (cited on page 10).

[101] J. Hakanpää, G. R. Szilvay, H. Kaljunen, M. Maksimainen, M. Linder, and J. Rouvinen, "Two crystal structures of trichoderma reesei hydrophobin hfbi—the structure of a protein amphiphile with and without detergent interaction", Protein Science **15**, 2129–2140 (2006) 10.1110/ps.062326706 (cited on page 11).

[102] J. Hakanpää and J. Rouvinen, *Crystal structure of hydrophobin HFBI*, Aug. 2006, 10.2210/pdb2fz6/pdb (cited on page 11).

[103] M. Lienemann, M. S. Grunér, A. Paananen, M. Siika-aho, and M. B. Linder, "Charge-Based Engineering of Hydrophobin HFBI: Effect on Interfacial Assembly and Interactions", Biomacromolecules **16**, 1283–1292 (2015) 10.1021/acs.biomac.5b00073 (cited on pages 11–12, 22, 26, 43).

[104] P. J. Kraulis, G. M. Clore, M. Nilges, T. A. Jones, G. Pettersson, J. Knowles, and A. M. Gronenborn, "Determination of the three-dimensional solution structure of the c-terminal domain of cellobiohydrolase i from trichoderma reesei. a study using nuclear magnetic resonance and hybrid distance geometry-dynamical simulated annealing", Biochemistry **28**, 7241–7257 (1989) 10.1021/bi00444a016 (cited on pages 11, 25).

[105] G. Clore and A. Gronenborn, *DETERMINATION OF THE THREE-DIMENSIONAL STRUCTURE OF THE c-TERMINAL DOMAIN OF CELLOBIOHYDROLASE i FROM TRICHODERMA REESEI. a STUDY USING NUCLEAR MAGNETIC RESONANCE AND HYBRID DISTANCE GEOMETRY-DYNAMICAL SIMULATED ANNEALING*, Jan. 1990, 10.2210/pdb1cbh/pdb (cited on pages 11, 25).

[106] P. Laaksonen, A. Walther, J.-M. Malho, M. Kainlauri, O. Ikkala, and M. B. Linder, "Genetic engineering of biomimetic nanocomposites: diblock proteins, graphene, and nanofibrillated cellulose", Angewandte Chemie International Edition **50**, 8688–8691 (2011) 10.1002/anie.201102973 (cited on pages 11–12).

[107] E. F. Pettersen, T. D. Goddard, C. C. Huang, E. C. Meng, G. S. Couch, T. I. Croll, J. H. Morris, and T. E. Ferrin, "UCSF ChimeraX: structure visualization for researchers, educators, and developers", Protein Science **30**, 70–82 (2020) 10.1002/pro.3943 (cited on pages 11, 25).

[108] M. B. Linder, M. Qiao, F. Laumen, K. Selber, T. Hyytiä, T. Nakari-Setälä, and M. E. Penttilä, "Efficient purification of recombinant proteins using hydrophobins as tags in surfactant-based two-phase systems", Biochemistry **43**, 11873–11882 (2004) 10.1021/bi0488202 (cited on pages 11–12, 22).

[109] J.-M. Malho, C. Ouellet-Plamondon, M. Rüggeberg, P. Laaksonen, O. Ikkala, I. Burgert, and M. B. Linder, "Enhanced plastic deformations of nanofibrillated cellulose film by adsorbed moisture and protein-mediated interactions", Biomacromolecules **16**, 311–318 (2014) 10.1021/bm501514w (cited on page 12).

[110] S. Varjonen, P. Laaksonen, A. Paananen, H. Valo, H. Hähl, T. Laaksonen, and M. B. Linder, "Self-assembly of cellulose nanofibrils by genetically engineered fusion proteins", Soft Matter **7**, 2402 (2011) 10.1039/c0sm01114b (cited on page 12).

[111] H. Valo, M. Kovalainen, P. Laaksonen, M. Häkkinen, S. Auriola, L. Peltonen, M. Linder, K. Järvinen, J. Hirvonen, and T. Laaksonen, "Immobilization of protein-coated drug nanoparticles in nanofibrillar cellulose matrices—enhanced stability and release", Journal of Controlled Release **156**, 390–397 (2011) 10.1016/j.jconrel.2011.07.016 (cited on page 12).

[112] A. Paananen, E. Vuorimaa, M. Torkkeli, M. Penttilä, M. Kauranen, O. Ikkala, H. Lemmetyinen, R. Serimaa, and M. B. Linder, "Structural hierarchy in molecular films of two class II hydrophobins", Biochemistry **42**, 5253–5258 (2003) 10.1021/bi034031t (cited on pages 12, 21).

[113] K. Kisko, G. R. Szilvay, E. Vuorimaa, H. Lemmetyinen, M. B. Linder, M. Torkkeli, and R. Serimaa, "Self-assembled films of hydrophobin proteins HFBI and HFBII studied in situ at the air/water interface", Langmuir **25**, 1612–1619 (2008) 10.1021/la803252g (cited on page 12).

[114] G. R. Szilvay, A. Paananen, K. Laurikainen, E. Vuorimaa, H. Lemmetyinen, J. Peltonen, and M. B. Linder, "Self-assembled hydrophobin protein films at the air-water interface: structural analysis and molecular engineering", Biochemistry **46**, 2345–2354 (2007) 10.1021/bi602358h (cited on pages 12, 26).

[115] A. S. O. Vrielink, P. H. Bomans, E. J. Vredenbregt, M. J. Wirix, N. A. Sommerdijk, O. Luiten, and I. K. Voets, "Suspended crystalline films of protein hydrophobin i (HFBI)", Journal of Colloid and Interface Science **447**, 107–112 (2015) 10.1016/j.jcis.2015.01.073 (cited on pages 12, 26).

[116] R. Yamasaki, Y. Takatsuji, H. Asakawa, T. Fukuma, and T. Haruyama, "Flattened-top domical water drops formed through self-organization of hydrophobin membranes: a structural and mechanistic study using atomic force microscopy", ACS Nano **10**, 81–87 (2016) 10.1021/acsnano.5b04049 (cited on pages 12, 26).

[117] H. Fan, B. Wang, Y. Zhang, Y. Zhu, B. Song, H. Xu, Y. Zhai, M. Qiao, and F. Sun, "A cryo-electron microscopy support film formed by 2d crystals of hydrophobin HFBI", Nature Communications **12**, 10.1038/s41467-021-27596-8 (2021) 10.1038/s41467-021-27596-8 (cited on pages 12, 26).

[118] R. Yamasaki, Y. Takatsuji, M. Lienemann, H. Asakawa, T. Fukuma, M. Linder, and T. Haruyama, "Electrochemical properties of honeycomb-like structured HFBI self-organized membranes on HOPG electrodes", Colloids and Surfaces B: Biointerfaces **123**, 803–808 (2014) 10.1016/j.colsurfb.2014.10.018 (cited on page 12).

[119] A. Magarkar, N. Mele, N. Abdel-Rahman, S. Butcher, M. Torkkeli, R. Serimaa, A. Paananen, M. Linder, and A. Bunker, "Hydrophobin film structure for HFBI and HFBII and mechanism for accelerated film formation", PLoS Computational Biology **10**, edited by M. Nilges, e1003745 (2014) 10.1371/journal.pcbi.1003745 (cited on page 12).

[120] K. Kisko, M. Torkkeli, E. Vuorimaa, H. Lemmetyinen, O. H. Seeck, M. Linder, and R. Serimaa, "Langmuir–blodgett films of hydrophobins HFBI and HFBII", Surface Science **584**, 35–40 (2005) 10.1016/j.susc.2004.12.036 (cited on page 12).

[121] H. Hähl, A. Griffo, N. Safaridehkohneh, J. Heppe, S. Backes, M. Lienemann, M. B. Linder, L. Santen, P. Laaksonen, and K. Jacobs, "Dynamic assembly of class II hydrophobins from t. reesei at the air–water interface", Langmuir **35**, 9202–9212 (2019) 10.1021/acs.langmuir.9b01078 (cited on pages 12, 23).

[122] K. Meister, A. Bäumer, G. R. Szilvay, A. Paananen, and H. J. Bakker, "Self-assembly and conformational changes of hydrophobin classes at the air–water interface", The Journal of Physical Chemistry Letters **7**, 4067–4071 (2016) 10.1021/acs.jpclett.6b01917 (cited on page 12).

[123] D. L. Cheung, "Molecular simulation of hydrophobin adsorption at an oil–water interface", Langmuir **28**, 8730–8736 (2012) 10.1021/la300777q (cited on page 12).

[124] D. Riccobelli, H. H. Al-Terke, P. Laaksonen, P. Metrangolo, A. Paananen, R. H. Ras, P. Ciarletta, and D. Vella, "Flattened and wrinkled encapsulated droplets: shape morphing induced by gravity and evaporation", Physical Review Letters **130**, 10.1103/physrevlett.130.218202 (2023) 10.1103/physrevlett.130.218202 (cited on page 12).

[125] L. Winandy, F. Hilpert, O. Schlebusch, and R. Fischer, "Comparative analysis of surface coating properties of five hydrophobins from aspergillus nidulans and trichoderma reseei", Scientific Reports **8**, 10.1038/s41598-018-29749-0 (2018) 10.1038/s41598-018-29749-0 (cited on page 12).

[126] I. Goldian, S. Jahn, P. Laaksonen, M. Linder, N. Kampf, and J. Klein, "Modification of interfacial forces by hydrophobin HFBI", Soft Matter **9**, 10627 (2013) 10.1039/c3sm51924d (cited on page 12).

[127] B. Li, X. Wang, Y. Li, A. Paananen, G. R. Szilvay, M. Qin, W. Wang, and Y. Cao, "Single-molecule force spectroscopy reveals self-assembly enhanced surface binding of hydrophobins", Chemistry - A European Journal **24**, 9224–9228 (2018) 10.1002/chem.201801730 (cited on page 12).

[128] A. R. Cox, F. Cagnol, A. B. Russell, and M. J. Izzard, "Surface properties of class II hydrophobins from *Trichoderma reesei* and influence on bubble stability", Langmuir **23**, 7995–8002 (2007) 10.1021/la700451g (cited on page 12).

[129] B. Niu, D. Wang, Y. Yang, H. Xu, and M. Qiao, "Heterologous expression and characterization of the hydrophobin HFBI in pichia pastoris and evaluation of its contribution to the food industry", Amino Acids **43**, 763–771 (2011) 10.1007/s00726-011-1126-5 (cited on page 12).

[130] T. Sarlin, T. Nakari-Setälä, M. Linder, M. Penttilä, and A. Haikara, "Fungal hydrophobins as predictors of the gushing activity of malt", Journal of the Institute of Brewing **111**, 105–111 (2005) 10.1002/j.2050-0416.2005.tb00655.x (cited on page 12).

[131] Y. Takatsuji, R. Yamasaki, A. Iwanaga, M. Lienemann, M. B. Linder, and T. Haruyama, "Solid-support immobilization of a "swing" fusion protein for enhanced glucose oxidase catalytic activity", Colloids and Surfaces B: Biointerfaces **112**, 186–191 (2013) 10.1016/j.colsurfb.2013.07.051 (cited on page 12).

[132] R. Devine, P. Singha, and H. Handa, "Versatile biomimetic medical device surface: hydrophobin coated, nitric oxide-releasing polymer for antimicrobial and hemocompatible applications", Biomaterials Science **7**, 3438–3449 (2019) 10.1039/c9bm00469f (cited on page 13).

[133] I. Sorrentino, M. Gargano, A. Ricciardelli, E. Parrilli, C. Buonocore, D. de Pascale, P. Giardina, and A. Piscitelli, "Development of anti-bacterial surfaces using a hydrophobin chimeric protein", International Journal of Biological Macromolecules **164**, 2293–2300 (2020) 10.1016/j.ijbiomac.2020.07.301 (cited on page 13).

[134] L. B. Price, B. A. Hungate, B. J. Koch, G. S. Davis, and C. M. Liu, "Colonizing opportunistic pathogens (COPs): the beasts in all of us", PLOS Pathogens **13**, edited by D. A. Hogan, e1006369 (2017) 10.1371/journal.ppat.1006369 (cited on page 14).

[135] M. F. Q. VandenBergh, E. P. F. Yzerman, A. van Belkum, H. A. M. Boelens, M. Sijmons, and H. A. Verbrugh, "Follow-up of *Staphylococcus aureus* nasal carriage after 8 years: redefining the persistent carrier state", Journal of Clinical Microbiology **37**, 3133–3140 (1999) 10.1128/jcm.37.10.3133-3140.1999 (cited on page 14).

[136] R. E. O. Williams, "HEALTHY CARRIAGE OF *STAPHYLOCOCCUS AUREUS* : ITS PREVALENCE AND IMPORTANCE", Bacteriological Reviews **27**, 56–71 (1963) 10.1128/br.27.1.56-71.1963 (cited on page 14).

[137] A. van Belkum, N. J. Verkaik, C. P. de Vogel, H. A. Boelens, J. Verveer, J. L. Nouwen, H. A. Verbrugh, and H. F. L. Wertheim, "Reclassification of *Staphylococcus aureus* nasal carriage types", The Journal of Infectious Diseases **199**, 1820–1826 (2009) 10.1086/599119 (cited on page 14).

[138] J Kluytmans, A van Belkum, and H Verbrugh, "Nasal carriage of staphylococcus aureus: epidemiology, underlying mechanisms, and associated risks", Clinical Microbiology Reviews **10**, 505–520 (1997) 10.1128/cmr.10.3.505 (cited on page 14).

[139] H. F. Chambers and F. R. DeLeo, "Waves of resistance: staphylococcus aureus in the antibiotic era", Nature Reviews Microbiology **7**, 629–641 (2009) 10.1038/nrmicro2200 (cited on page 14).

[140] R. Serra, R. Grande, L. Butrico, A. Rossi, U. F. Settimio, B. Caroleo, B. Amato, L. Gallelli, and S. de Franciscis, "Chronic wound infections: the role of *Pseudomonas aeruginosa* and *Staphylococcus aureus*", Expert Review of Anti-infective Therapy **13**, 605–613 (2015) 10.1586/14787210.2015.1023291 (cited on page 14).

[141] B. P. Howden, S. G. Giulieri, T. W. F. Lung, S. L. Baines, L. K. Sharkey, J. Y. H. Lee, A. Hachani, I. R. Monk, and T. P. Stinear, "Staphylococcus aureus host interactions and adaptation", Nature Reviews Microbiology **21**, 380–395 (2023) 10.1038/s41579-023-00852-y (cited on page 14).

[142] L. M. Weiner-Lastinger, S. Abner, J. R. Edwards, A. J. Kallen, M. Karlsson, S. S. Magill, D. Pollock, I. See, M. M. Soe, M. S. Walters, and M. A. Dudeck, "Antimicrobial-resistant pathogens associated with adult healthcare-associated infections: summary of data reported to the national healthcare safety network, 2015–2017", Infection Control & Hospital Epidemiology **41**, 1–18 (2019) 10.1017/ice.2019.296 (cited on page 14).

[143] N. A. Turner, B. K. Sharma-Kuinkel, S. A. Maskarinec, E. M. Eichenberger, P. P. Shah, M. Carugati, T. L. Holland, and V. G. Fowler, "Methicillin-resistant *Staphylococcus aureus*: an overview of basic and clinical research", Nature Reviews Microbiology **17**, 203–218 (2019) 10.1038/s41579-018-0147-4 (cited on page 14).

[144] I. M. Gould, M. Z. David, S. Esposito, J. Garau, G. Lina, T. Mazzei, and G. Peters, "New insights into meticillin-resistant *Staphylococcus aureus* (MRSA) pathogenesis, treatment and resistance", International Journal of Antimicrobial Agents **39**, 96–104 (2012) 10.1016/j.ijantimicag.2011.09.028 (cited on page 14).

[145] D. E. Moormeier and K. W. Bayles, "*Staphylococcus aureus* biofilm: a complex developmental organism", Molecular Microbiology **104**, 365–376 (2017) 10.1111/mmi.13634 (cited on page 14).

[146] T. D. Scherr, C. E. Heim, J. M. Morrison, and T. Kielian, "Hiding in plain sight: interplay between *Staphylococcal* biofilms and host immunity", Frontiers in Immunology **5**, 10.3389/fimmu.2014.00037 (2014) 10.3389/fimmu.2014.00037 (cited on page 14).

[147] R. G. Bailey, R. D. Turner, N. Mullin, N. Clarke, S. J. Foster, and J. K. Hobbs, "The interplay between cell wall mechanical properties and the cell cycle in *Staphylococcus aureus*", Biophysical Journal **107**, 2538–2545 (2014) 10.1016/j.bpj.2014.10.036 (cited on page 14).

[148] P. MITCHELL and J. MOYLE, "Permeability of the envelopes of *Staphylococcus aureus* to some salts, amino acids, and non-electrolytes", Journal of General Microbiology **20**, 434–441 (1959) 10.1099/00221287-20-2-434 (cited on page 14).

[149] M. Kuroda, Y. Tanaka, R. Aoki, D. Shu, K. Tsumoto, and T. Ohta, "*Staphylococcus aureus* giant protein ebh is involved in tolerance to transient hyperosmotic pressure", Biochemical and Biophysical Research Communications **374**, 237–241 (2008) 10.1016/j.bbrc.2008.07.037 (cited on page 14).

[150] L. M. F. de Oliveira, M. Steindorff, M. N. Darisipudi, D. M. Mrochen, P. Trübe, B. M. Bröker, M. Brönstrup, W. Tegge, and S. Holtfreter, "Discovery of staphylococcus aureus adhesion inhibitors by automated imaging and their characterization in a mouse model of persistent nasal colonization", Microorganisms **9**, 631 (2021) 10.3390/microorganisms9030631 (cited on page 14).

[151] C. Weidenmaier, A. Peschel, Y.-Q. Xiong, S. A. Kristian, K. Dietz, M. R. Yeaman, and A. S. Bayer, "Lack of wall teichoic acids in *Staphylococcus aureus* leads to reduced interactions with endothelial cells and to attenuated virulence in a rabbit model of endocarditis", The Journal of Infectious Diseases **191**, 1771–1777 (2005) 10.1086/429692 (cited on pages 14–15, 24).

[152] L. Brown, J. M. Wolf, R. Prados-Rosales, and A. Casadevall, "Through the wall: extracellular vesicles in gram-positive bacteria, mycobacteria and fungi", Nature Reviews Microbiology **13**, 620–630 (2015) 10.1038/nrmicro3480 (cited on page 15).

[153] W. Vollmer, D. Blanot, and M. A. D. Pedro, "Peptidoglycan structure and architecture", FEMS Microbiology Reviews **32**, 149–167 (2008) 10.1111/j.1574-6976.2007.00094.x (cited on page 14).

[154] J. T. Park and T. Uehara, "How bacteria consume their own exoskeletons (turnover and recycling of cell wall peptidoglycan)", Microbiology and Molecular Biology Reviews **72**, 211–227 (2008) 10.1128/mmbr.00027-07 (cited on page 14).

[155] J. Reith and C. Mayer, "Peptidoglycan turnover and recycling in gram-positive bacteria", Applied Microbiology and Biotechnology **92**, 1–11 (2011) 10.1007/s00253-011-3486-x (cited on page 14).

[156] S. J. Foster, "Molecular characterization and functional analysis of the major autolysin of staphylococcus aureus 8325/4", Journal of Bacteriology **177**, 5723–5725 (1995) 10.1128/jb.177.19.5723-5725.1995 (cited on page 14).

[157] S Yamada, M Sugai, H Komatsuzawa, S Nakashima, T Oshida, A Matsumoto, and H Suginaka, "An autolysin ring associated with cell separation of *Staphylococcus aureus*", Journal of Bacteriology **178**, 1565–1571 (1996) 10.1128/jb.178.6.1565-1571.1996 (cited on page 14).

[158] A. C. Leonard, M. I. Goncheva, S. E. Gilbert, H. Shareefdeen, L. E. Petrie, L. K. Thompson, C. M. Khursigara, D. E. Heinrichs, and G. Cox, "Autolysin-mediated peptidoglycan hydrolysis is required for the surface display of *Staphylococcus aureus* cell wall-anchored proteins", Proceedings of the National Academy of Sciences **120**, 10.1073/pnas.2301414120 (2023) 10.1073/pnas.2301414120 (cited on pages 14–16).

[159] M. Jukič, K. Rožman, M. Sova, H. Barreteau, and S. Gobec, "Anthranilic acid inhibitors of undecaprenyl pyrophosphate synthase (UppS), an essential enzyme for bacterial cell wall biosynthesis", Frontiers in Microbiology **9**, 10.3389/fmicb.2018.03322 (2019) 10.3389/fmicb.2018.03322 (cited on page 14).

[160] M. Rajagopal and S. Walker, "Envelope structures of gram-positive bacteria", in *Current topics in microbiology and immunology* (Springer International Publishing, 2015), pages 1–44, 10.1007/82_2015_5021 (cited on page 14).

[161] T. Do, J. E. Page, and S. Walker, "Uncovering the activities, biological roles, and regulation of bacterial cell wall hydrolases and tailoring enzymes", Journal of Biological Chemistry **295**, 3347–3361 (2020) 10.1074/jbc.rev119.010155 (cited on page 14).

[162] T. Dörr, P. J. Moynihan, and C. Mayer, "Editorial: bacterial cell wall structure and dynamics", Frontiers in Microbiology **10**, 10.3389/fmicb.2019.02051 (2019) 10.3389/fmicb.2019.02051 (cited on page 14).

[163] M. Wang, G. Buist, and J. M. van Dijl, "*Staphylococcus aureus* cell wall maintenance – the multifaceted roles of peptidoglycan hydrolases in bacterial growth, fitness, and virulence", FEMS Microbiology Reviews **46**, 10.1093/femsre/fuac025 (2022) 10.1093/femsre/fuac025 (cited on page 14).

[164] R. van Dalen, A. Peschel, and N. M. van Sorge, "Wall teichoic acid in staphylococcus aureus host interaction", Trends in Microbiology **28**, 985–998 (2020) 10.1016/j.tim.2020.05.017 (cited on pages 14–15).

[165] A. Peschel, M. Otto, R. W. Jack, H. Kalbacher, G. Jung, and F. Götz, "Inactivation of the *dlt* operon in *Staphylococcus aureus* confers sensitivity to defensins, protegrins, and other antimicrobial peptides", Journal of Biological Chemistry **274**, 8405–8410 (1999) 10.1074/jbc.274.13.8405 (cited on pages 15, 24).

[166] M. Gross, S. E. Cramton, F. Götz, and A. Peschel, "Key role of teichoic acid net charge in *Staphylococcus aureus* colonization of artificial surfaces", Infection and Immunity **69**, edited by E. I. Tuomanen, 3423–3426 (2001) 10.1128/iai.69.5.3423-3426.2001 (cited on page 15).

[167] A. Peschel, C. Vuong, M. Otto, and F. Götz, "The d-alanine residues of *Staphylococcus aureus* teichoic acids alter the susceptibility to vancomycin and the activity of autolytic enzymes", Antimicrobial Agents and Chemotherapy **44**, 2845–2847 (2000) 10.1128/aac.44.10.2845-2847.2000 (cited on page 15).

[168] V. Cafiso, T. Bertuccio, S. Purrello, F. Campanile, C. Mammina, A. Sartor, A. Raglio, and S. Stefani, "*dltA* overexpression: a strain-independent keystone of daptomycin resistance in methicillin-resistant *Staphylococcus aureus*", International Journal of Antimicrobial Agents **43**, 26–31 (2014) 10.1016/j.ijantimicag.2013.10.001 (cited on page 15).

[169] S. Brown, J. P. S. Maria, and S. Walker, "Wall teichoic acids of gram-positive bacteria", Annual Review of Microbiology **67**, 313–336 (2013) 10.1146/annurev-micro-092412-155620 (cited on page 15).

[170] C. Weidenmaier, J. F. Kokai-Kun, E. Kulauzovic, T. Kohler, G. Thumm, H. Stoll, F. Götz, and A. Peschel, "Differential roles of sortase-anchored surface proteins and wall teichoic acid in *Staphylococcus aureus* nasal colonization", International Journal of Medical Microbiology **298**, 505–513 (2008) 10.1016/j.ijmm.2007.11.006 (cited on pages 15–16, 24).

[171] C. Weidenmaier and A. Peschel, "Teichoic acids and related cell-wall glycopolymers in gram-positive physiology and host interactions", Nature Reviews Microbiology **6**, 276–287 (2008) 10.1038/nrmicro1861 (cited on page 15).

[172] S. K. Mazmanian, G. Liu, H. Ton-That, and O. Schneewind, "*Staphylococcus aureus* sortase, an enzyme that anchors surface proteins to the cell wall", Science **285**, 760–763 (1999) 10.1126/science.285.5428.760 (cited on page 16).

[173] S. Dramsi, S. Magnet, S. Davison, and M. Arthur, "Covalent attachment of proteins to peptidoglycan", FEMS Microbiology Reviews **32**, 307–320 (2008) 10.1111/j.1574-6976.2008.00102.x (cited on pages 16, 24).

[174] K.-B. Oh, M.-N. Oh, J.-G. Kim, D.-S. Shin, and J. Shin, "Inhibition of sortase-mediated staphylococcus aureus adhesion to fibronectin via fibronectin-binding protein by sortase inhibitors", Applied Microbiology and Biotechnology **70**, 102–106 (2006) 10.1007/s00253-005-0040-8 (cited on page 16).

[175] R. G. Kruger, B. Otvos, B. A. Frankel, M. Bentley, P. Dostal, and D. G. McCafferty, "Analysis of the substrate specificity of the *Staphylococcus aureus* sortase transpeptidase SrtA", Biochemistry **43**, 1541–1551 (2004) 10.1021/bi035920j (cited on page 16).

[176] B.-S. Park, J.-G. Kim, M.-R. Kim, S.-E. Lee, G. R. Takeoka, K.-B. Oh, and J.-H. Kim, "*Curcuma longa* l. constituents inhibit sortase A and *Staphylococcus aureus* cell adhesion to fibronectin", Journal of Agricultural and Food Chemistry **53**, 9005–9009 (2005) 10.1021/jf051765z (cited on page 16).

[177] P. Herman-Bausier, C. Labate, A. M. Towell, S. Derclaye, J. A. Geoghegan, and Y. F. Dufrêne, "*Staphylococcus aureus* clumping factor a is a force-sensitive molecular switch that activates bacterial adhesion", Proceedings of the National Academy of Sciences **115**, 5564–5569 (2018) 10.1073/pnas.1718104115 (cited on page 16).

[178] V. K. Ganesh, J. J. Rivera, E. Smeds, Y.-P. Ko, M. G. Bowden, E. R. Wann, S. Gurusiddappa, J. R. Fitzgerald, and M. Höök, "A structural model of the *Staphylococcus aureus* ClfA-fibrinogen interaction opens new avenues for the design of anti-staphylococcal therapeutics", PLoS Pathogens **4**, edited by T. Koehler, e1000226 (2008) 10.1371/journal.ppat.1000226 (cited on pages 16–17).

[179] A. M. Towell, C. Feuillie, P. Vitry, T. M. D. Costa, M. Mathelié-Guinlet, S. Kezic, O. M. Fleury, M. A. McAleer, Y. F. Dufrêne, A. D. Irvine, and J. A. Geoghegan, "*Staphylococcus aureus* binds to the n-terminal region of corneodesmosin to adhere to the stratum corneum in atopic dermatitis", Proceedings of the National Academy of Sciences **118**, 10.1073/pnas.2014444118 (2020) 10.1073/pnas.2014444118 (cited on page 16).

[180] M. E. Mulcahy, J. A. Geoghegan, I. R. Monk, K. M. O'Keeffe, E. J. Walsh, T. J. Foster, and R. M. McLoughlin, "Nasal colonisation by *Staphylococcus aureus* depends upon clumping factor b binding to the squamous epithelial cell envelope protein loricrin", PLoS Pathogens **8**, edited by A. Peschel, e1003092 (2012) 10.1371/journal.ppat.1003092 (cited on page 16).

[181] K. A. Lacey, M. E. Mulcahy, A. M. Towell, J. A. Geoghegan, and R. M. McLoughlin, "Clumping factor b is an important virulence factor during *Staphylococcus aureus* skin infection and a promising vaccine target", PLOS Pathogens **15**, edited by A. Prince, e1007713 (2019) 10.1371/journal.ppat.1007713 (cited on page 16).

[182] T. J. Foster, "The remarkably multifunctional fibronectin binding proteins of *Staphylococcus aureus*", European Journal of Clinical Microbiology & Infectious Diseases **35**, 1923–1931 (2016) 10.1007/s10096-016-2763-0 (cited on page 16).

[183] F. M. Burke, A. D. Poto, P. Speziale, and T. J. Foster, "The a domain of fibronectin-binding protein b of *Staphylococcus aureus* contains a novel fibronectin binding site", FEBS Journal **278**, 2359–2371 (2011) 10.1111/j.1742-4658.2011.08159.x (cited on page 16).

[184] F. M. Keane, A. Loughman, V. Valtulina, M. Brennan, P. Speziale, and T. J. Foster, "Fibrinogen and elastin bind to the same region within the a domain of fibronectin binding protein a, an MSCRAMM of *Staphylococcus aureus*", Molecular Microbiology **63**, 10.1111/j.1365-2958.2006.05552.x (2007) 10.1111/j.1365-2958.2006.05552.x (cited on page 16).

[185] B. Sinha, P. P. Francois, O. Nusse, M. Foti, O. M. Hartford, P. Vaudaux, T. J. Foster, D. P. Lew, M. Herrmann, and K.-H. Krause, "Fibronectin-binding protein acts as *Staphylococcus aureus* invasin via fibronectin bridging to integrin $\alpha_5\beta_1$", Cellular Microbiology **1**, 101–117 (1999) 10.1046/j.1462-5822.1999.00011.x (cited on page 16).

[186] R. C. Massey, M. N. Kantzanou, T. Fowler, N. P. J. Day, K. Schofield, E. R. Wann, A. R. Berendt, M. Hook, and S. J. Peacock, "Fibronectin-binding protein a of *Staphylococcus aureus* has multiple, substituting, binding regions that mediate adherence to fibronectin and invasion of endothelial cells", Cellular Microbiology **3**, 839–851 (2001) 10.1046/j.1462-5822.2001.00157.x (cited on page 16).

[187] S. R. Clarke, M. D. Wiltshire, and S. J. Foster, "IsdA of *Staphylococcus aureus* is a broad spectrum, iron-regulated adhesin", Molecular Microbiology **51**, 1509–1519 (2004) 10.1111/j.1365-2958.2003.03938.x (cited on page 16).

[188] S. R. Clarke, K. J. Brummell, M. J. Horsburgh, P. W. McDowell, S. A. S. Mohamad, M. R. Stapleton, J. Acevedo, R. C. Read, N. P. J. Day, S. J. Peacock, J. J. Mond, J. F. Kokai-Kun, and S. J. Foster, "Identification of in vivo - expressed antigens of *Staphylococcus aureus* and their use in vaccinations for protection against nasal carriage", The Journal of Infectious Diseases **193**, 1098–1108 (2006) 10.1086/501471 (cited on page 16).

[189] N. Merino, A. Toledo-Arana, M. Vergara-Irigaray, J. Valle, C. Solano, E. Calvo, J. A. Lopez, T. J. Foster, J. R. Penadés, and I. Lasa, "Protein a-mediated multicellular behavior in *Staphylococcus aureus*", Journal of Bacteriology **191**, 832–843 (2009) 10.1128/jb.01222-08 (cited on page 16).

[190] M. I. Gómez, M. O'Seaghdha, M. Magargee, T. J. Foster, and A. S. Prince, "*Staphylococcus aureus* protein a activates TNFR1 signaling through conserved IgG binding domains", Journal of Biological Chemistry **281**, 20190–20196 (2006) 10.1074/jbc.m601956200 (cited on page 16).

[191] F. M. Roche, M. Meehan, and T. J. Foster, "The *Staphylococcus aureus* surface protein SasG and its homologues promote bacterial adherence to human desquamated nasal epithelial cells", Microbiology **149**, 2759–2767 (2003) 10.1099/mic.0.26412-0 (cited on page 16).

[192] Y.-H. Yang, Y.-L. Jiang, J. Zhang, L. Wang, X.-H. Bai, S.-J. Zhang, Y.-M. Ren, N. Li, Y.-H. Zhang, Z. Zhang, Q. Gong, Y. Mei, T. Xue, J.-R. Zhang, Y. Chen, and C.-Z. Zhou, "Structural insights into SraP-mediated *Staphylococcus aureus* adhesion to host cells", PLoS Pathogens **10**, edited by P. M. Sullam, e1004169 (2014) 10.1371/journal.ppat.1004169 (cited on page 16).

[193] T. Chavakis, K. Wiechmann, K. T. Preissner, and M. Herrmann, "*Staphylococcus aureus* interactions with the endothelium", Thrombosis and Haemostasis **94**, 278–285 (2005) 10.1160/th05-05-0306 (cited on page 16).

[194] J. Eisenbeis, *Der einfluss des multifunktionalen extrazellulären adhäsionsproteins (eap) von Staphylococcus aureus auf die morphologie und funktion von eukaryotischen zellen*, de, 2019, 10.22028/D291-31415 (cited on page 16).

[195] M. Salzmann, H. Platzer, M. Mussbacher, M. Derler, M. Lenz, P. Haider, M. Brekalo, J. B. Kral-Pointner, S. Kastl, W. S. Speidl, K. T. Preissner, U. Schubert, M. Bischoff, P. Uhrin, J. Wojta, and P. J. Hohensinner, "*Staphylococcus aureus* extracellular adherence protein (eap) reduces immune cell phenotype in developing but not in established atherosclerotic lesions", Biochimica et Biophysica Acta (BBA) - Molecular Basis of Disease **1869**, 166616 (2023) 10.1016/j.bbadis.2022.166616 (cited on page 16).

[196] C. Xie, P. Alcaide, B. V. Geisbrecht, D. Schneider, M. Herrmann, K. T. Preissner, F. W. Luscinskas, and T. Chavakis, "Suppression of experimental autoimmune encephalomyelitis by extracellular adherence protein of *Staphylococcus aureus*", Journal of Experimental Medicine **203**, 985–994 (2006) 10.1084/jem.20051681 (cited on page 16).

[197] H. Wang, J. von Rohrscheidt, J. Roehrbein, T. Peters, A. Sindrilaru, D. Kess, K. T. Preissner, and K. Scharffetter-Kochanek, "Extracellular adherence protein of *Staphylococcus aureus* suppresses disease by inhibiting t-cell recruitment in a mouse model of psoriasis", Journal of Investigative Dermatology **130**, 743–754 (2010) 10.1038/jid.2009.310 (cited on page 16).

[198] N. Hirschhausen, T. Schlesier, M. A. Schmidt, F. Götz, G. Peters, and C. Heilmann, "A novel staphylococcal internalization mechanism involves the major autolysin atl and heat shock cognate protein hsc70 as host cell receptor", Cellular Microbiology **12**, 1746–1764 (2010) 10.1111/j.1462-5822.2010.01506.x (cited on page 16).

[199] Y. Zong, Y. Xu, X. Liang, D. R. Keene, A. Höök, S. Gurusiddappa, M. Höök, and S. V. L. Narayana, "A 'collagen hug' model for *Staphylococcus aureus* CNA binding to collagen", The EMBO Journal **24**, 4224–4236 (2005) 10.1038/sj.emboj.7600888 (cited on page 17).

[200] L. F. Milles, K. Schulten, H. E. Gaub, and R. C. Bernardi, "Molecular mechanism of extreme mechanostability in a pathogen adhesin", Science **359**, 1527–1533 (2018) 10.1126/science.aar2094 (cited on page 17).

[201] P. Loskill, H. Hähl, N. Thewes, C. T. Kreis, M. Bischoff, M. Herrmann, and K. Jacobs, "Influence of the subsurface composition of a material on the adhesion of staphylococci", Langmuir **28**, 7242–7248 (2012) 10.1021/la3004323 (cited on page 17).

[202] S. Kalasin, J. Dabkowski, K. Nüsslein, and M. M. Santore, "The role of nano-scale heterogeneous electrostatic interactions in initial bacterial adhesion from flow: a case study with *Staphylococcus aureus*", Colloids and Surfaces B: Biointerfaces **76**, 489–495 (2010) 10.1016/j.colsurfb.2009.12.009 (cited on page 17).

[203] N. Thewes, P. Loskill, P. Jung, H. Peisker, M. Bischoff, M. Herrmann, and K. Jacobs, "Hydrophobic interaction governs unspecific adhesion of staphylococci: a single cell force spectroscopy study", Beilstein Journal of Nanotechnology **5**, 1501–1512 (2014) 10.3762/bjnano.5.163 (cited on pages 17, 19).

[204] R. J. Doyle, "Contribution of the hydrophobic effect to microbial infection", Microbes and Infection **2**, 391–400 (2000) 10.1016/s1286-4579(00)00328-2 (cited on page 17).

[205] M. C. M. van Loosdrecht, J. Lyklema, W. Norde, and A. J. B. Zehnder, "Bacterial adhesion: a physicochemical approach", Microbial Ecology **17**, 1–15 (1989) 10.1007/bf02025589 (cited on page 17).

[206] M. C. M. van Loosdrecht, W. Norde, J. Lyklema, and A. J. B. Zehnder, "Hydrophobic and electrostatic parameters in bacterial adhesion", Aquatic Sciences **52**, 103–114 (1990) 10.1007/bf00878244 (cited on page 17).

[207] N. Thewes, A. Thewes, P. Loskill, H. Peisker, M. Bischoff, M. Herrmann, L. Santen, and K. Jacobs, "Stochastic binding of staphylococcus aureus to hydrophobic surfaces", Soft Matter **11**, 8913–8919 (2015) 10.1039/c5sm00963d (cited on pages 17, 19, 27).

[208] R. D. Boyd, J. Verran, M. V. Jones, and M. Bhakoo, "Use of the atomic force microscope to determine the effect of substratum surface topography on bacterial adhesion", Langmuir **18**, 2343–2346 (2002) 10.1021/la011142p (cited on page 18).

[209] F. Hizal, C.-H. Choi, H. J. Busscher, and H. C. van der Mei, "Staphylococcal adhesion, detachment and transmission on nanopillared si surfaces", ACS Applied Materials & Interfaces **8**, 30430–30439 (2016) 10.1021/acsami.6b09437 (cited on page 18).

[210] P. W. Doll, K. Doll, A. Winkel, R. Thelen, R. Ahrens, M. Stiesch, and A. E. Guber, "Influence of the available surface area and cell elasticity on bacterial adhesion forces on highly ordered silicon nanopillars", ACS Omega **7**, 17620–17631 (2022) 10.1021/acsomega.2c00356 (cited on page 18).

[211] C. Spengler, N. Thewes, P. Jung, M. Bischoff, and K. Jacobs, "Determination of the nano-scaled contact area of staphylococcal cells", Nanoscale **9**, 10084–10093 (2017) 10.1039/c7nr02297b (cited on pages 18–19).

[212] R. M. A. Sullan, J. K. Li, P. J. Crowley, L. J. Brady, and Y. F. Dufrêne, "Binding forces of *Streptococcus mutans* p1 adhesin", ACS Nano **9**, 1448–1460 (2015) 10.1021/nn5058886 (cited on page 19).

[213] A. Beaussart, S. El-Kirat-Chatel, P. Herman, D. Alsteens, J. Mahillon, P. Hols, and Y. F. Dufrêne, "Single-cell force spectroscopy of probiotic bacteria", Biophysical Journal **104**, 1886–1892 (2013) 10.1016/j.bpj.2013.03.046 (cited on page 19).

[214] A. Beaussart, A. E. Baker, S. L. Kuchma, S. El-Kirat-Chatel, G. A. O'Toole, and Y. F. Dufrêne, "Nanoscale adhesion forces of *Pseudomonas aeruginosa* type IV pili", ACS Nano **8**, 10723–10733 (2014) 10.1021/nn5044383 (cited on page 19).

[215] M. T. Criado, C. M. Ferreirós, and V. Sainz, "Adherence and hydrophobicity inNeisseria meningitidis and their relationship with surface charge", Medical Microbiology and Immunology **174**, 151–156 (1985) 10.1007/bf02298125 (cited on page 19).

[216] A. Weerkamp, H. Uyen, and H. Busscher, "Effect of zeta potential and surface energy on bacterial adhesion to uncoated and saliva-coated human enamel and dentin", Journal of Dental Research **67**, 1483–1487 (1988) 10.1177/00220345880670120801 (cited on page 19).

[217] J. S. Dickson and M Koohmaraie, "Cell surface charge characteristics and their relationship to bacterial attachment to meat surfaces", Applied and Environmental Microbiology **55**, 832–836 (1989) 10.1128/aem.55.4.832-836.1989 (cited on page 19).

[218] G Beck, E Puchelle, C Plotkowski, and R Peslin, "Effect of growth on surface charge and hydrophobicity of staphylococcus aureus", Annales de l'Institut Pasteur / Microbiologie **139**, 655–664 (1988) 10.1016/0769-2609(88)90070-1 (cited on page 19).

[219] M. Ueshima, S. Tanaka, S. Nakamura, and K. Yamashita, "Manipulation of bacterial adhesion and proliferation by surface charges of electrically polarized hydroxyapatite", Journal of Biomedical Materials Research **60**, 578–584 (2002) 10.1002/jbm.10113 (cited on page 19).

[220] J. Shen, P. Gao, S. Han, R. Y. Kao, S. Wu, X. Liu, S. Qian, P. K. Chu, K. M. Cheung, and K. W. Yeung, "A tailored positively-charged hydrophobic surface reduces the risk of implant associated infections", Acta Biomaterialia **114**, 421–430 (2020) 10.1016/j.actbio.2020.07.040 (cited on page 19).

[221] S. Yang, J. Zhou, and D. Li, "Functions and diseases of the retinal pigment epithelium", Frontiers in Pharmacology **12**, 10.3389/fphar.2021.727870 (2021) 10.3389/fphar.2021.727870 (cited on page 20).

[222] M. Boulton and P. Dayhaw-Barker, "The role of the retinal pigment epithelium: topographical variation and ageing changes", Eye **15**, 384–389 (2001) 10.1038/eye.2001.141 (cited on page 20).

[223] Y.-J. Liu, M. L. Berre, F. Lautenschlaeger, P. Maiuri, A. Callan-Jones, M. Heuzé, T. Takaki, R. Voituriez, and M. Piel, "Confinement and low adhesion induce fast amoeboid migration of slow mesenchymal cells", Cell **160**, 659–672 (2015) 10.1016/j.cell.2015.01.007 (cited on page 20).

[224] M. Kobayashi, K. Tokuda, Y. Kobayashi, C. Yamashiro, S.-H. Uchi, M. Hatano, and K. Kimura, "Suppression of epithelial-mesenchymal transition in retinal pigment epithelial cells by an MRTF-a inhibitor", Investigative Opthalmology & Visual Science **60**, 528 (2019) 10.1167/iovs.18-25678 (cited on page 20).

[225] M. Raab, M. Gentili, H. de Belly, H.-R. Thiam, P. Vargas, A. J. Jimenez, F. Lautenschlaeger, R. Voituriez, A.-M. Lennon-Duménil, N. Manel, and M. Piel, "ESCRT III repairs nuclear envelope ruptures during cell migration to limit DNA damage and cell death", Science **352**, 359–362 (2016) 10.1126/science.aad7611 (cited on page 20).

[226] R. J. Hawkins and R. Voituriez, "Mechanisms of cell motion in confined geometries", Mathematical Modelling of Natural Phenomena **5**, 84–105 (2010) 10.1051/mmnp/20105104 (cited on page 20).

[227] M. Bergert, A. Erzberger, R. A. Desai, I. M. Aspalter, A. C. Oates, G. Charras, G. Salbreux, and E. K. Paluch, "Force transmission during adhesion-independent migration", Nature Cell Biology **17**, 524–529 (2015) 10.1038/ncb3134 (cited on page 20).

[228] R. J. Hawkins, M. Piel, G. Faure-Andre, A. M. Lennon-Dumenil, J. F. Joanny, J. Prost, and R. Voituriez, "Pushing off the walls: a mechanism of cell motility in confinement", Physical Review Letters **102**, 10.1103/physrevlett.102.058103 (2009) 10.1103/physrevlett.102.058103 (cited on page 20).

[229] T. Lämmermann, B. L. Bader, S. J. Monkley, T. Worbs, R. Wedlich-Söldner, K. Hirsch, M. Keller, R. Förster, D. R. Critchley, R. Fässler, and M. Sixt, "Rapid leukocyte migration by integrin-independent flowing and squeezing", Nature **453**, 51–55 (2008) 10.1038/nature06887 (cited on page 20).

[230] S. SenGupta, C. A. Parent, and J. E. Bear, "The principles of directed cell migration", Nature Reviews Molecular Cell Biology **22**, 529–547 (2021) 10.1038/s41580-021-00366-6 (cited on page 20).

[231] K. Burridge, "Focal adhesions: a personal perspective on a half century of progress", The FEBS Journal **284**, 3355–3361 (2017) 10.1111/febs.14195 (cited on page 20).

[232] C. Baltes, D. G. Thalla, U. Kazmaier, and F. Lautenschläger, "Actin stabilization in cell migration", Frontiers in Cell and Developmental Biology **10**, 10.3389/fcell.2022.931880 (2022) 10.3389/fcell.2022.931880 (cited on pages 20, 45–46).

[233] S. Askolin, T. Nakari-Setälä, and M. Tenkanen, "Overproduction, purification, and characterization of the *Trichoderma reesei* hydrophobin HFBI", Applied Microbiology and Biotechnology **57**, 124–130 (2001) 10.1007/s002530100728 (cited on page 21).

[234] M. Linder, K. Selber, T. Nakari-Setälä, M. Qiao, M. Kula, and M. Penttilä, "The hydrophobins HFBI and HFBII from *Trichoderma reesei* showing efficient interactions with nonionic surfactants in aqueous two-phase systems", Biomacromolecules **2**, 511–517 (2001) 10.1021/bm0001493 (cited on page 21).

[235] W. L. Hwang, M. Chen, B. Cronin, M. A. Holden, and H. Bayley, "Asymmetric droplet interface bilayers", Journal of the American Chemical Society **130**, 5878–5879 (2008) 10.1021/ja802089s (cited on page 23).

[236] J.-B. Fleury, "Enhanced water permeability across a physiological droplet interface bilayer doped with fullerenes", RSC Advances **10**, 19686–19692 (2020) 10.1039/d0ra01413c (cited on page 23).

[237] D. B. Weibel, W. R. DiLuzio, and G. M. Whitesides, "Microfabrication meets microbiology", Nature Reviews Microbiology **5**, 209–218 (2007) 10.1038/nrmicro1616 (cited on page 23).

[238] Y. Xia and G. M. Whitesides, "SOFT LITHOGRAPHY", Annual Review of Materials Science **28**, 153–184 (1998) 10.1146/annurev.matsci.28.1.153 (cited on page 23).

[239] N. Khangholi, R. Seemann, and J.-B. Fleury, "Simultaneous measurement of surface and bilayer tension in a microfluidic chip", Biomicrofluidics **14**, 10.1063/1.5137810 (2020) 10.1063/1.5137810 (cited on page 24).

[240] M. Bellion, L. Santen, H. Mantz, H. Hähl, A. Quinn, A. Nagel, C. Gilow, C. Weitenberg, Y. Schmitt, and K. Jacobs, "Protein adsorption on tailored substrates: long-range forces and conformational changes", Journal of Physics: Condensed Matter **20**, 404226 (2008) 10.1088/0953-8984/20/40/404226 (cited on pages 25, 40).

[241] M. Lessel, O. Bäumchen, M. Klos, H. Hähl, R. Fetzer, M. Paulus, R. Seemann, and K. Jacobs, "Self-assembled silane monolayers: an efficient step-by-step recipe for high-quality, low energy surfaces", Surface and Interface Analysis **47**, 557–564 (2015) 10.1002/sia.5729 (cited on pages 26, 40).

[242] S. Koynov, M. S. Brandt, and M. Stutzmann, "Black nonreflecting silicon surfaces for solar cells", Applied Physics Letters **88**, 10.1063/1.2204573 (2006) 10.1063/1.2204573 (cited on page 26).

[243] G. Binnig, C. F. Quate, and C. Gerber, "Atomic force microscope", Physical Review Letters **56**, 930–933 (1986) 10.1103/physrevlett.56.930 (cited on page 27).

[244] P. Eaton and P. West, *Atomic force microscopy* (Oxford university press, 2010) (cited on page 27).

[245] B. Bhushan, *Springer handbook of nanotechnology* (Springer, 2017) (cited on page 27).

[246] B. Voigtländer, *Scanning probe microscopy: atomic force microscopy and scanning tunneling microscopy* (Springer, 2015) (cited on page 27).

[247] K. D. Sattler, *Handbook of nanophysics: principles and methods* (CRC press, 2010) (cited on page 27).

[248] S. Kang and M. Elimelech, "Bioinspired single bacterial cell force spectroscopy", Langmuir **25**, 9656–9659 (2009) 10.1021/la902247w (cited on page 27).

[249] H. Lee, J. Rho, and P. B. Messersmith, "Facile conjugation of biomolecules onto surfaces via mussel adhesive protein inspired coatings", Advanced Materials **21**, 431–434 (2009) 10.1002/adma.200801222 (cited on page 27).

[250] L. Hofherr, C. Müller-Renno, and C. Ziegler, "FluidFM as a tool to study adhesion forces of bacteria - optimization of parameters and comparison to conventional bacterial probe scanning force spectroscopy", PLOS ONE **15**, edited by K. G. Blank, e0227395 (2020) 10.1371/journal.pone.0227395 (cited on page 28).

[251] J. C. Mathai, S. Tristram-Nagle, J. F. Nagle, and M. L. Zeidel, "Structural determinants of water permeability through the lipid membrane", The Journal of General Physiology **131**, 69–76 (2007) 10.1085/jgp.200709848 (cited on page 34).

[252] M. B. Lande, J. M. Donovan, and M. L. Zeidel, "The relationship between membrane fluidity and permeabilities to water, solutes, ammonia, and protons.", Journal of General Physiology **106**, 67–84 (1995) 10.1085/jgp.106.1.67 (cited on pages 34–35).

[253] D. van Swaay and A. deMello, "Microfluidic methods for forming liposomes", Lab on a Chip **13**, 752 (2013) 10.1039/c2lc41121k (cited on page 35).

[254] J. C. Stachowiak, D. L. Richmond, T. H. Li, A. P. Liu, S. H. Parekh, and D. A. Fletcher, "Unilamellar vesicle formation and encapsulation by microfluidic jetting", Proceedings of the National Academy of Sciences **105**, 4697–4702 (2008) 10.1073/pnas.0710875105 (cited on page 35).

[255] K. Karamdad, R. V. Law, J. M. Seddon, N. J. Brooks, and O. Ces, "Preparation and mechanical characterisation of giant unilamellar vesicles by a microfluidic method", Lab on a Chip **15**, 557–562 (2015) 10.1039/c4lc01277a (cited on page 35).

[256] *Data sheet mp6 micropump*, Bartels Mikrotechnik, (May 2023) https://www.bartels-mikrotechnik.de/wp-content/uploads/simple-file-list/EN/Manuals-and-Data-Sheets/mp6_micropumps_Datasheet.pdf (visited on 07/10/2023) (cited on page 35).

[257] M. I. P. Gil, J. B. Kristensen, and S. E. Mainzer, "Stabilization of biomimetic membranes", patent (Mar. 2019), US Patent 10,226,744, https://patents.google.com/patent/US10226744B2/en (cited on page 37).

[258] C. H. Nielsen, "Biomimetic membranes for sensor and separation applications", Analytical and Bioanalytical Chemistry **395**, 697–718 (2009) 10.1007/s00216-009-2960-0 (cited on page 37).

[259] C. Tang, Y. Zhao, R. Wang, C. Hélix-Nielsen, and A. Fane, "Desalination by biomimetic aquaporin membranes: review of status and prospects", Desalination **308**, 34–40 (2013) 10.1016/j.desal.2012.07.007 (cited on pages 37–38).

[260] C. Spengler, E. Maikranz, B. Glatz, M. A. Klatt, H. Heintz, M. Bischoff, L. Santen, A. Fery, and K. Jacobs, "The adhesion capability of *Staphylococcus aureus* cells is heterogeneously distributed over the cell envelope", 10.1101/2021.01.05.425282 (2021) 10.1101/2021.01.05.425282 (cited on page 41).

[261] E. Maikranz, C. Spengler, N. Thewes, A. Thewes, F. Nolle, P. Jung, M. Bischoff, L. Santen, and K. Jacobs, "Different binding mechanisms of *Staphylococcus aureus* to hydrophobic and hydrophilic surfaces", Nanoscale **12**, 19267–19275 (2020) 10.1039/d0nr03134h (cited on pages 41–44).

[262] Z. Wang, M. Lienemann, M. Qiau, and M. B. Linder, "Mechanisms of Protein Adhesion on Surface Films of Hydrophobin", Langmuir **26**, 8491–8496 (2010) 10.1021/la101240e (cited on page 43).

Addenda

Publications

I Hydrophobin bilayer as water impermeable protein membrane

Authors: **F. Nolle**,[1,*] L. Starke,[2,*] A. Griffo,[1,4,5] M. Lienemann,[3] K. Jacobs,[1,4] R. Seemann,[1] J. Fleury,[1] J. Hub,[2] H. Hähl,[1]

[1] Experimental Physics and Center for Biophysics, Saarland University, 66123 Saarbrücken, Germany.
[2] Department of Theoretical Physics, Saarland University, D-66123 Saarbrücken, Germany.
[3] VTT Technical Research Centre of Finland Ltd., Espoo 02150, Finland
[4] Max Planck School Matter to Life, Jahnstraße 29, 69120 Heidelberg, Germany
[5] Max Planck Institute for Medical Research Heidelberg, 69120 Heidelberg, Germany
[*] These authors contributed equally to this work.

Reprinted with permission from *Langmuir*, 2023, **39**, 13790–13800.
hhttps://doi.org/10.1021/acs.langmuir.3c01006
ACS Articles on Request author-directed link: http://pubs.acs.org/articlesonrequest/AOR-NPWTW27ZNMPAZDDSBRFE

Author contributions:
***F.N.**: data curation, investigation, methodology, visualization, writing—original draft, and writing—review and editing. L.S.: investigation, methodology, visualization, writing—original draft, and writing—review and editing. A.G.: methodology, and writing—review and editing. M.L.: resources, and writing—review and editing. K.J.: supervision, and writing—review and editing. R.S.: supervision, and writing—review and editing. J.F.: conceptualization, methodology, supervision, and writing—review and editing. J.H.: conceptualization, methodology, supervision of MD simulations, writing—original draft, and writing—review and editing. H.H.: conceptualization, methodology, software, supervision of experiments, and writing—review and editing. All authors have read and agreed to the published version of the manuscript.*

Abstract – One of the most important properties of membranes is their permeability of water and other small molecules. A targeted change in permeability allows the passage of molecules to be controlled. Vesicles made of membranes with low water permeability are preferable for drug delivery, for example, because they are more stable and better maintain the drug concentration inside. This study reports on the very low water permeability of pure protein membranes composed of a bilayer of the amphiphilic protein hydrophobin

HFBI. Using a droplet-interface bilayer setup, we demonstrate that HFBI bilayers are essentially impermeable to water. HFBI bilayers withstand by far larger osmotic pressures than lipid membranes. Only by disturbing the packing of the proteins in the HFBI bilayer, a measurable water permeability is induced. To investigate possible molecular mechanisms causing the near-zero permeability, we used all-atom molecular dynamics simulations of various HFBI bilayer models. The simulations suggest that the experimental HFBI bilayer permeability is neither compatible with a lateral honeycomb structure, as found for HFBI monolayers, nor with a residual oil layer within the bilayer, or with a disordered lateral packing similar to the packing in lipid bilayers. These results suggest that the low permeabilities of HFBI and lipid bilayers rely on different mechanisms. With their extremely low but adaptable permeability and high stability, HFBI membranes could be used as an osmotic pressure-insensitive barrier in situations where lipid membranes fail, such as desalination membranes.

Hydrophobin bilayer as water impermeable protein membrane

Friederike Nolle,[†,‖] Leonhard J. Starke,[‡,‖] Alessandra Griffo,[†,¶,⊥] Michael Lienemann,[§] Karin Jacobs,[†,¶] Ralf Seemann,[†] Jean-Baptiste Fleury,[†] Jochen S. Hub,[*,‡] and Hendrik Hähl[*,†]

†*Department of Experimental Physics, Saarland University, D-66123 Saarbrücken, Germany*

‡*Department of Theoretical Physics, Saarland University, D-66123 Saarbrücken, Germany*

¶*Max Planck School, Matter to Life, Jahnstraße 29, 69120 Heidelberg, Germany*

§*VTT Technical Research Centre of Finland Ltd., Espoo 02150, Finland*

‖*These authors contributed equally to this work.*

⊥*Max Planck Institute for Medical Research Heidelberg, 69120 Heidelberg, Germany*

E-mail: jochen.hub@uni-saarland.de; h.haehl@physik.uni-saarland.de

Abstract

One of the most important properties of membranes is their permeability of water and other small molecules. A targeted change in permeability allows the passage of molecules to be controlled. Vesicles made of membranes with low water permeability are preferable for drug delivery, for example, because they are more stable and better maintain the drug concentration inside. This study reports on the very low water permeability of pure protein membranes composed of a bilayer of the amphiphilic protein hydrophobin HFBI. Using a droplet-interface bilayer setup, we demonstrate that HFBI bilayers are essentially impermeable to water. HFBI bilayers withstand by far larger

osmotic pressures than lipid membranes. Only by disturbing the packing of the proteins in the HFBI bilayer, a measurable water permeability is induced. To investigate possible molecular mechanisms causing the near-zero permeability, we used all-atom molecular dynamics simulations of various HFBI bilayer models. The simulations suggest that the experimental HFBI bilayer permeability is neither compatible with a lateral honeycomb structure, as found for HFBI monolayers, nor with a residual oil layer within the bilayer, or with a disordered lateral packing similar to the packing in lipid bilayers. These results suggest that the low permeabilities of HFBI and lipid bilayers rely on different mechanisms. With their extremely low but adaptable permeability and high stability, HFBI membranes could be used as an osmotic pressure-insensitive barrier in situations where lipid membranes fail, such as desalination membranes.

Keywords

Permeability, Droplet Interface Bilayers, Biological membrane, Hydrophobin, Nanobio interface, Molecular dynamics simulations

Introduction

All living cells are surrounded by lipid membranes fulfilling similar tasks despite their different structures and chemical compositions. Membranes are responsible for the compartmentalization of living cells and control the selective transport between these compartments. The regulation of water permeability is particularly important for maintaining cell homeostasis,[1] enabling the cell to respond to external influences, such as salt concentration or pH. Controlling water permeability is also relevant in the field of biomimetics for potential biotechnological and biomedical applications,[2–4] for instance as nanocarriers, and has therefore been addressed by various experimental and theoretical studies.[5–7] The lipid composition, as well as the content of proteins, channels, or nanoparticles, strongly influence the

permeability, as has been shown in numerous experimental studies using planar lipid bilayers[8–13] or liposomes.[14–17] Artificial membranes with controlled permeability have been formed using several other building blocks besides lipids,[18] such as fatty acids, synthetic lipids, (block co-)polymers,[19–21] engineered proteins, or peptides.[22,23] Another possible building block for artificial membranes are amphiphilic proteins like the protein HFBI, which has been used to form pure protein membranes.[24]

HFBI is a globular protein from the family of class II hydrophobins produced by the filamentous fungus *Trichoderma reesei*.[25] The molecular surface of HFBI contains a characteristic nonpolar region, also known as a hydrophobic patch, which enables the fungus to attach to hydrophobic solid surfaces, such as wood,[26] and to expose the hydrophilic protein regions to the solvent.[27–29] At the air–water interface, HFBI forms highly ordered honeycomb-like monolayers as shown experimentally by atomic force microscopy[30–33] and cryogenic electron microscopy.[34] These ordered monolayers have been described computationally by protein–protein docking and molecular dynamics simulations.[35] HFBI monolayers at the air–water interface resemble phospholipids in their layer-forming properties: both, HFBI and lipids orient their hydrophobic parts towards the air. Yet, it was shown that the formation of HFBI monolayers is mainly controlled by steric and electrostatic interactions and therefore differs from the adsorption kinetics of phospholipids and other surfactants.[36]

Hydrophobin boundary layers have been used for the coatings of surfaces,[37,38] for immobilization of molecules and cells,[39,40] or for therapeutic applications such as drug delivery.[41,42] Maiolo *et al.*[42] encapsulated gold nanoparticles in a hydrophobin monolayer shell, thereby preventing the premature release of drugs and allowing a concentrated drug release at the target site *in vivo*.

Joining two hydrophobin boundary layers leads to the formation of stable protein double layers.[24,43,44] By contacting two HFBI layers with their hydrophobic sides, a bilayer membrane can be formed between two aqueous compartments, similar to black lipid membranes. Such HFBI bilayers have previously been formed before in a microfluidic setup allowing both

optical access and electrophysiological measurements.[24,43] Thus, properties such as adhesion between the bilayer sheets, bilayer thickness and ion transport across the bilayer have already been studied. In addition, these HFBI bilayers exhibit high stability and exceptional resistance to lateral stress, which also facilitated the formation of vesicles from these bilayers.[24] Yet, the molecular structure and water permeability of these HBFI bilayers are still unknown. Knowledge of the latter would, however, facilitate their use in medical applications such as biosensing, biomimetics and vesicle-based drug delivery.

In this study, planar HFBI bilayers were generated at the contact site of two micelles. These HFBI droplet-interface bilayers (DIB) were used to determine the water permeability of the pure protein bilayers. The water permeability value was found to be extremely low. The aim of this work is to explore and explain this low water permeability in experiments and molecular dynamics (MD) simulations and to look for ways to disrupt the order of the protein membrane in order to be able to control the water permeability.

Results and Discussion

Volume change of droplet pairs due to osmotic gradient

By bringing two buffer droplets of different salinity in hexadecane surrounded by protein monolayers into close contact, a droplet interface bilayer (DIB) is formed (Figure 1a). An osmotic pressure, caused by the difference in salinity leads to a flux of water from the droplet with lower salinity to the one with higher salinity, if the bilayer is water-permeable. Figures 1b and 1c show an HFBI-coated droplet pair with an osmotic concentration difference of 1.717 osmol/L immediately after contact (left) and 6 minutes later (right). No volume changes were optical discernible. For comparison and closer examination, we recorded the volume change of droplet pairs covered with HFBI in hexadecane, cf. blue data in Figure 1d and droplet pairs with monoolein in squalene, cf. green data in Figure 1d with an osmotic concentration difference of 0.259 osmol/L. (Squalene was chosen for the oil phase

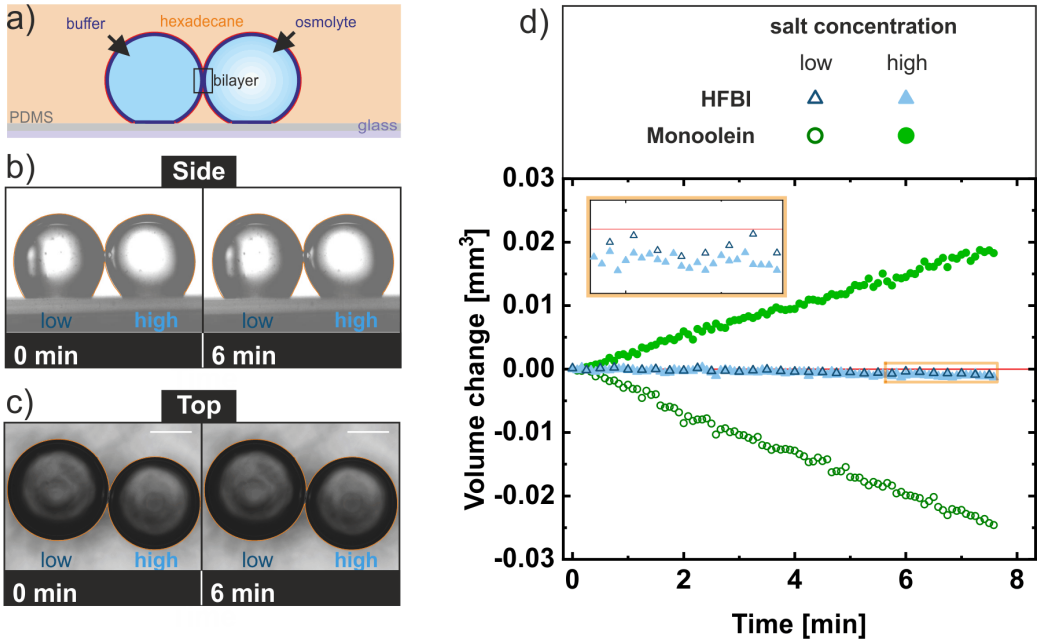

Figure 1: Droplet Interface Bilayer (DIB) experiments. a) Sketch from the side of the experimental setup of two HFBI-coated buffer droplet pairs of different salt concentrations on PDMS-covered glass substrate. b)-c) Side and top view of two HFBI-coated buffer droplets brought into contact and forming a DIB. Due to the different salt concentrations (1.717 osmol/L) of the two droplets, the water permeability was measured by observing the volume changes of the individual droplets over time. The contour of the droplet pairs (orange) at the beginning of the measurements was copied and pasted into the image taken at 6 min. Scalebar indicates a size of 500 µm. d) Volume change of droplets over time with pairs of monoolein (green circles) and HFBI (blue triangles) coated droplets. In both measurements, the osmotic concentration difference between the two droplets in contact was 0.259 osmol/L. The inset shows an enlargement of the volume change of the HFBI-coated droplet pair for the last two minutes. The red line indicates the zero volume change.

due to the improved stability of the bilayer with respect to bilayers formed in hexadecane.) Compared to bilayers formed by other lipids, monoolein forms bilayers with a relatively low permeability.[8,13,45] Still, no discernible volume change was observed for HFBI droplet pairs in comparison to Monoolein droplet pairs. To confirm that no remaining oil in the bilayer was the reason for this water impermeability, we used BODIPY as an oil tracer.[46] No oil was detected in the bilayer with this method (Figure S1). For these pure protein bilayers, it was also previously shown by capacitance measurements that essentially no hexadecane remains

between the layers.[24]

A small volume decrease (about 0.001 mm^3) was observed in both HFBI-covered droplets (see inset to Figure 1d). This water loss was characterized in single-droplet measurements as diffusion of water into hexadecane with a diffusion coefficient in the range of 4–6·10^3 $\mu m^2/s$ (Table S1). Since this diffusion coefficient is in the same range as for simple water droplets in hexaxdecane, this result implies that the water passes through the hydrophobin monolayer without any additional hindrance. Hence, it was necessary to account for the water diffusion into hexadecane by correcting the data before calculating the membrane permeability. For this purpose, the total volume loss of a pair of droplets was determined and this loss was added to the volume of the individual droplets - according to the ratio of their surface areas. Thus, in the corrected data, the influx of one droplet was equal to the outflux of the second droplet. After this correction, the data for HFBI membrane suggest that there is no water exchange between the droplets, so no values for water permeability were calculated. In contrast, there was a clear difference in volume change for the monoolein droplet pairs in squalene, however, the volume loss ($\sim 0.025\,mm^3$) of the droplet with the low salinity was larger than the volume gain ($\sim 0.020\,mm^3$) of the droplet with high salinity. This indicated that there was also an overall volume loss into squalene. The permeability obtained from the corrected data for the monoolein membranes was 56 µm/s ± 1 µm/s at 30 °C and thus in the range reported in other studies (58 µm/s ± 3 µm/s at 25 °C in squalene).[8]

These results show that under the tested experimental conditions for HFBI membranes, in contrast to monoolein membranes, (i) the flux through the HFBI membrane is smaller than the flux into the surrounding hexadecane and (ii) the chosen time interval and osmotic concentration difference is insufficient to determine a water permeability for pure protein membranes. Therefore, the osmotic concentration difference as well as the time interval were largely increased in the experiments described below.

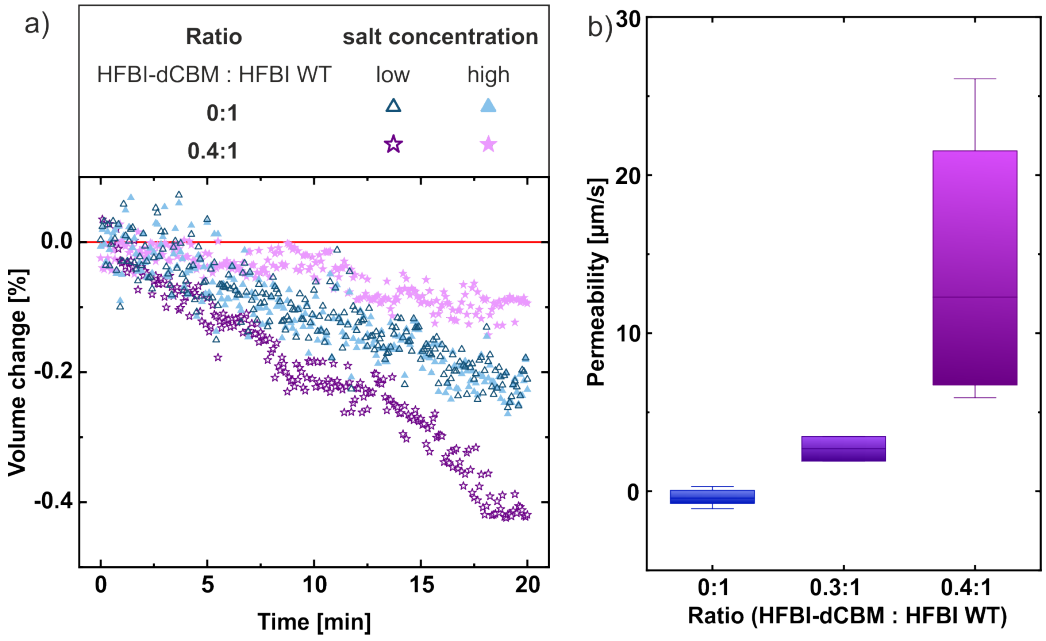

Figure 2: a) Volume change in percent of droplets, with initial size of $V_0 = 0.7$–$0.9\,\mathrm{mm}^3$, over time with droplet pairs having a HFBI-dCBM:HFBI WT ratio of 0:1 (blue triangles) and 0.4:1 (purple stars). b) Box and whisker plots (min-to-max) of the mean permeability values of several HFBI membranes in presence of the mutant HFBI-dCBM in different weight ratios. Osmotic concentration difference: 1.717 osmol/L for pure HFBI membranes and 0.086 osmol/L for HFBI-dCBM:HFBI mixtures, Temperature: 30 °C

Permeability of pure HFBI membranes

For more precise measurements of the water permeability of the HFBI membranes, the osmotic concentration difference between the droplets was increased to 1.717 osmol/L and the observation time was extended to 30 min after initial contact. HFBI membranes are capable to resist this high osmotic pressure and are stable over long periods of time, up to several days (in contrast to lipid membranes, which cannot form stable membranes under these osmotic conditions).

However, the results of the second series of experiments (Figure 2a, blue triangles) were similar to the results of the previous ones: both droplets shrink in the same range of order. It is noteworthy that for the given contact area and high osmotic pressure, a permeability of only

about 6 µm/s would be sufficient to compensate for the diffusion of water into hexadecane, *i.e.*, to keep the volume of the droplet with the high salt concentration constant. Thus, even without further analysis, the measurements show that the water permeability of the HFBI membrane is well below 6 µm/s.

After volume correction, no volume transfer from the low salinity droplet to the high salinity droplet is detectable. Taking into account the average size of the droplets and their common contact area, as well as the error in volume determination ($8{\cdot}10^{-4}\,\mathrm{mm}^3$), permeabilities with an accuracy of 1 µm/s are accessible. With this accuracy of the current setup, the observed water permeability of HFBI membranes is indistinguishable from zero (see methods: Error analysis in the determination of experimental membrane water permeability). These results are surprising given that water passes through HFBI monolayers into the oil just as unimpeded as through uncoated water droplets (Table S1). The permeability through the HFBI monolayers can be understood based on the known honeycomb structure at the air–water interface.[30,32] Thus, for the membrane, we hypothesize a rearrangement of proteins into a much more densely packed arrangement.

To test this hypothesis, the structure of the monolayer (composed exclusively of wild-type HFBI) was disrupted by inserting the bulky HFBI fusion protein HFBI-dCBM, which is composed of two cellulose–binding domains bound to the wild-type HFBI domain.[47] Weight ratios of 0.3:1 and 0.4:1 of HFBI-dCBM:HFBI WT were used in the bulk concentration of the droplets. The osmotic concentration difference 0.086 osmol/L was chosen at a temperature of 30 °C. The results of these experiments are displayed in Figure 2b and the experimental data corrected for the water loss into the oil are shown in the SI, Figure S2. In contrast to the experiments with pure HFBI membrane, clear differences in the volume change were observed for both mixing ratios tested. Volume decrease occurred still in all droplets, although the volume loss was significantly less in the droplets with high salt concentration than in the droplets with low salt concentration. (Figure 2a, purple stars). This results in clearly detectable positive permeability values of around 3 µm/s for the ratio of 0.3:1 (HFBI-

dCBM:HFBI) and up to 27 µm/s for the ratio 0.4:1 (Figure 2b). For the latter ratio a higher variation of permeability values was observed, yet always higher than for the ratio of 0.3:1. Apparently, the addition of HFBI-dCBM resulted in a detectable flux between two droplets with an osmotic gradient. This demonstrates that the impermeability of the pure HFBI WT membrane to water and ions is the reason why no significant volume change occurs across the bilayer between the droplet pair.

To conclude, within the tested regime of osmotic gradients of 0.259 to 1.717 osmol/L, which was generated by the addition of either KCl or NaCl (see SI), pure HFBI membranes are impermeable to water within our measurement accuracy of about 1 µm/s. The permeability is much lower compared to water permeability values estimated by fluorescence self-quenching in liposomes composed of palmitoyloleoylglycerophosphocholine (POPC) and cholesterol, which have water permeabilities between (72 ± 18) µm/s (pure POPC) and (13 ± 5) µm/s (POPC): Cholesterol ratio 60:40).[14] The permeability of HFBI is even lower than the permeability of densely packed sphingomyelin:cholesterol (60:40) membranes of (2.2 ± 0.4) µm/s, although their permeabilities may be of a similar order.[14] Water permeability of HFBI membranes can be achieved by adding a bulky HFBI fusion protein, but at the tested ratios, it is still low compared to monoolein and other lipid membranes.

To better understand the effect of HFBI ordering in the membrane on its water permeability, MD simulations were initiated. MD simulations were already successfully used previously to study water permeation across lipid membranes,[48] aquaporins,[49,50] and other nanopores.[51] Furthermore, MD simulations were used to study class-II hydrophobins within solution[52] and at interfaces.[35,53,54]

MD simulations of HFBI monolayers at the air – water interface are stable

To obtain molecular models of the HFBI monolayers and bilayers, and to study water permeation over HFBI bilayers in atomic detail, we used all-atom MD simulations. As starting

conformations, we used the monolayer arrangements obtained *via* protein–protein docking by Magarkar *et al.*,[35] which were designed to reproduce the honeycomb structure observed in HFBI monolayers.[30] The authors reported two different unit cell models termed HFBI-α and HFBI-β (Figure S4). The two models exhibit an overall similar monolayer packing yet with distinct protein-protein interfaces, as evident from the relative orientation of the α-helices within the unit cells (Figure S4). Two salt bridges were found in the HFBI-β unit cell with a dominating one between Asp^{30} and Lys^{32} suggesting a higher stability compared to the HFBI-α unit cell. To reveal the interactions of water with the HFBI monolayer, we performed simulations of the HFBI monolayer based on the HFBI-β unit cell at the air – water interface at constant pressure (Figure 3a). Over four independent 400 ns simulations, the monolayer was largely stable, exhibiting only a minor decrease of the lateral simulation box size of $\sim$ 1 to 2% reflecting a minor tightening of the protein–protein interfaces (Figure 3c). Analysis of density profiles along the membrane normal reveals large overlap between the protein and

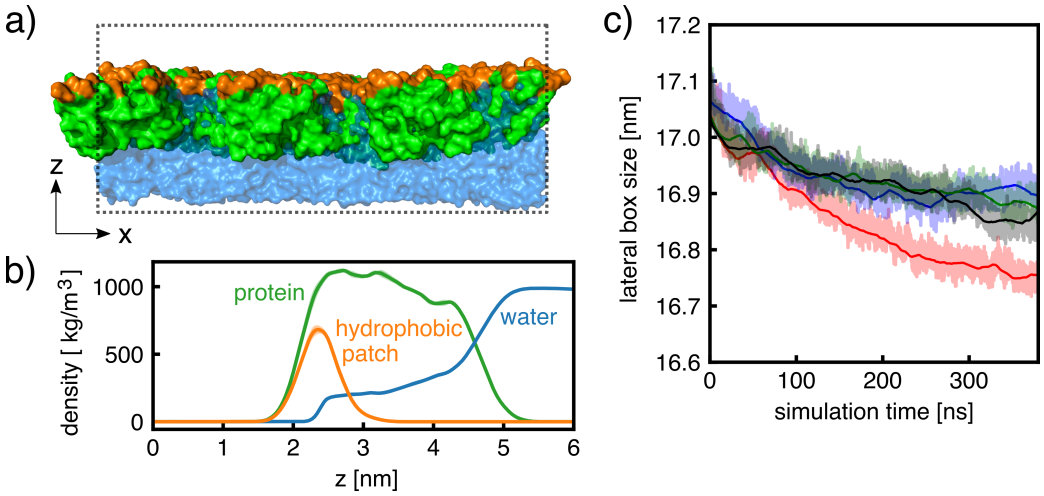

Figure 3: HFBI monolayer simulations. a) Side view of simulation system shown in surface representation composed of proteins (green) with hydrophobic patches (orange) and water (blue). The simulation box is shown as a dotted black line. b) Mass density along the membrane normal averaged over four independent simulations. c) First lateral box dimension versus time taken from four independent simulations (shaded areas). Lines show running averages to guide the eye.

water densities, demonstrating that the HFBI monolayer is largely hydrated (Figure 3b). Notably, the water density extends partly into the layer of hydrophobic patches, rationalized by the polar side chain of Gln^{65} and by polar backbone atoms in the hydrophobic patch. Overall, the monolayer simulations based on the unit cells proposed by Magarkar *et al.*[35] are compatible with the experimentally observed honeycomb structure of the monolayer. A similar simulation of the HFBI monolayer at an hexadecane/water interface was performed in addition, again showing that the honeycomb structure is stable (Supporting Information).

MD simulations of bilayers with honeycomb structure exhibit massive water leakage

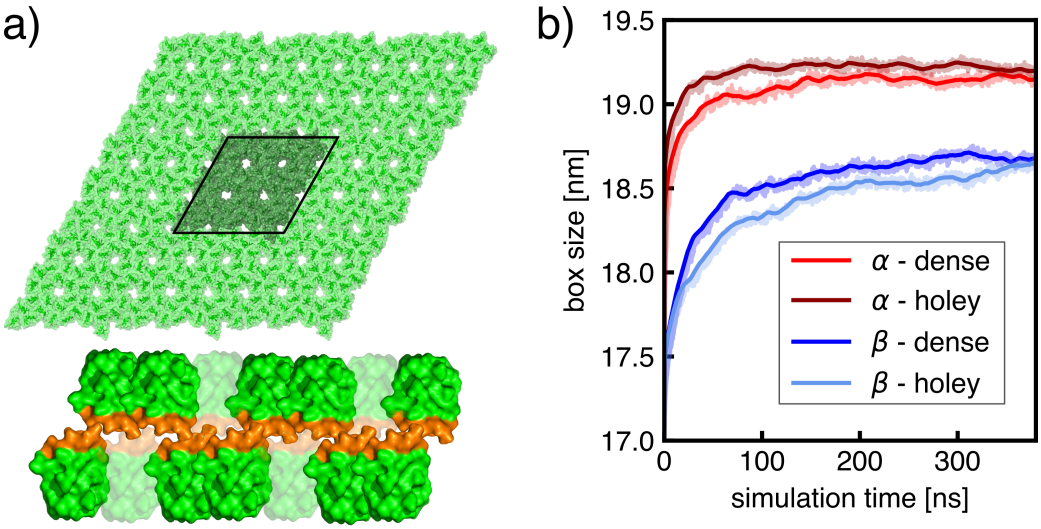

Figure 4: a) Top: Top view of simulation setup of HFBI with a honeycomb structure. One simulation cell is highlighted in dark green. Light green regions depict periodic images of the cell. Bottom: schematic view of the "dense" overlay of two laterally displaced monolayers with cavities spanning only one leaflet. b) Example of expansion of the first lateral box dimension during simulations based on the HFBI-α (red) and HFBI-β (blue) unit cells,[35] either composed of the "dense" or the "holey" membrane model (see legend).

Next, we used MD simulations to test whether the honeycomb structure observed in

monolayers is compatible with the low water permeability of HFBI membranes observed with our DIB experiments. To this end, we overlaid two monolayers with the hydrophobic patches facing each other based on two different lateral arrangements: the cavities of the honeycomb structure were either aligned (i) between the two leaflets, such that large continuous transmembrane pores were formed, denoted "holey membrane"; (ii) or the cavities were laterally displaced such that the cavities spanned only one leaflet, denoted "dense membrane" (Figure 4a, bottom). Each lateral arrangement was built either with the α or the β model by Magarkar *et al.*[35] Within 400 ns of simulation, we observed massive water permeation across the transmembrane pores of the holey structure. However, major water leakage was also observed in the dense structure with laterally displaced cavities. By counting water permeation events over the bilayer, we obtained permeabilities in the range of 400 to 24.000 µm/s in stark contrast to the experimental results (Table 1). In addition, the simulation box expanded laterally by 5 to 10% over the simulation time, resulting in a destabilization of the lattice structure due to translational movement of the individual proteins (Figure 4b), suggesting that the initial membrane configuration was not optimal. To exclude that the observed water leakage is a force field related artifact, we carried out additional simulations with the OPLSaa[55] and AMBER99SB[56] force fields as well as simulations using the CHARMM36m force field in combination with the OPC water model.[57] All simulations showed the same qualitative behaviour of rapid water intrusion indicating that the observed effect is not a force field-specific artifact (Fig S6). Analysis of density profiles of protein and water confirms that water increasingly penetrates the bilayer within the first 100 ns of simulation, such that the water molecules are located at the hydrophobic patch at a reduced density of $\sim$400 kg/m^3 (Figure 5). The penetration of water is not surprising considering that water was in contact with the hydrophobic patches even in the monolayer simulations (Figure 3). These findings suggest that the mere presence of the thin hydrophobic patch is insufficient to exclude water permeation across the HFBI bilayer. Additional simulations of honeycomb bilayers including a thin film of hexadecane between the monolayers were performed (see Supplementary

Information). These simulations confirmed the experimental observation that no residual oil film remains, which could prohibit water permeation.

Table 1: Water permeability of HFBI bilayers based on the HFBI-α and -β unit cells with dense or holey lateral arrangements.

System	H_2O Permeability [µm/s]		
HFBI-α, dense	10000	±	2000
HFBI-α, holey	23920	±	50
HFBI-β, dense	3700	±	200
HFBI-β, holey	9800	±	500
Disordered HFBI	13000	±	8200
Experiments	0	±	1

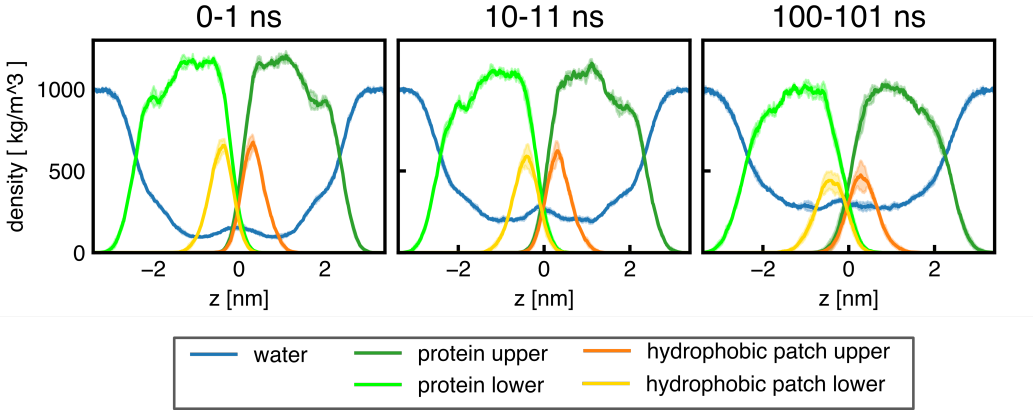

Figure 5: Mass densities of HFBI (green), hydrophobic patches (orange) and water (blue) for the "dense" HFBI bilayer based on the HFBI-β unit cell taken from different time intervals 0–1 ns (left), 10–11 ns (middle), 100–101 ns (right). Contributions from the upper and lower leaflet are plotted in different shades (see legend).

Exceptionally tight protein-protein interactions are required to explain low water permeability

Lipid bilayers represent a two-dimensional fluid, in which the lipid molecules are relatively loosely packed. Water permeation in those bilayers is suppressed owing to the nanometer-

sized hydrophobic core, which disfavors the partitioning of polar water molecules. We used MD simulations to test whether a laterally dense, irregular hydrophobin packing, similar to the lipid packing in lipid bilayers, would be sufficient to exclude water permeation. In free MD simulations, however, hydrophobins did not form laterally tight packing within accessible simulation times in consequence of long-living protein–protein contacts. Hence, we devised a multi-step protocol based on coarse-grained (CG) models, lateral compression simulations using large lateral pressures and high temperatures, followed by backmapping of the CG to atomistic models (see Supplementary Methods). Such an artificial protocol does not give insight into the physical self-assembly or reorganization process, but it provides a structural model of a densely packed hydrophobin bilayer, as evident from the continuous (transparent) molecular surface rendered in Figure 6b. This model was used as a starting point for further simulations.

However, as illustrated in Figure 6c, even the densely packed hydrophobin bilayer was penetrated by water within short simulation times, irrespective of the equilibrium protocol (Supplementary Information). Visual inspection of the simulations showed that the water penetrated primarily at contact sites with Asp^{30} and Lys^{32} residues, rationalized by the high water affinity of these ionic residues. Furthermore, other polar residues at the protein–protein interfaces became rapidly hydrated, such as Gln^{16}, Thr^{20}, Gln^{69}, Thr^{70}, and Asn^{72}. These water protrusions further caused the loss of some protein–protein contacts and led to a lateral expansion of the bilayer by approx. 7–10%. After 100 ns of simulation, the bilayer was largely hydrated. The permeability was approx. 1 cm/s, which was incompatible with our experimental data (Table 1). These findings demonstrate that overall tight but irregular lateral packing of HFBI monomers, similar to the lipid packing according to the two-dimensional fluid mosaic model of lipid membranes, is insufficient to rationalize the experimental water permeabilities. Instead, we propose that well-defined and enormously tight protein-protein interactions are required to form a stable densely packed bilayer. The required reorganization process needs to introduce not only a few specific bonds that link

the proteins together (as was the case for the unit cells at the air–water interface), but needs to form a near-perfect interlocked protein-protein interfaces to act as an effective barrier against water penetration. Such a reorganization process occurs most likely at time scales inaccessible to MD simulations and thus can not be resolved within this study.

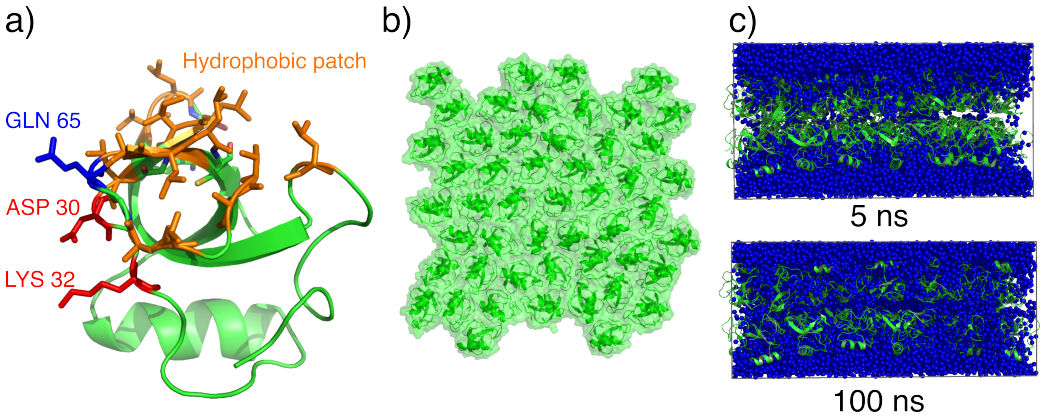

Figure 6: a) Scheme of HFBI structure. Secondary structure is shown in green, hydrophobic patch in orange including the side chains. In addition, the charged side residues Asp^{30} and Lys^{32} as well as the polar side chain of Gln^{65} are highlighted in red and blue, respectively. b) Graphical representation of a dense disordered HFBI monolayer (top view) after compression procedure. c) Snapshots (side view) from two different time points of a HFBI bilayer simulation build of two monolayers as represented in b). Water is shown in blue.

Conclusions

Using a DIB setup, we showed that pure HFBI membranes are impermeable to water within the experimental accuracy of $\sim$1 µm/s. Hence, HFBI membranes provide novel biocompatible membranes with exceptionally low water permeability and high stability.

We used MD simulation to test several structural hypotheses for rationalizing the low HFBI permeability. These hypotheses were based on low-resolution structural data of HFBI monolayers, which revealed a monolayer honeycomb structure,[30–33] and on the expectation that physiochemical mechanisms applying to lipid membranes might likewise apply to HFBI membranes. The simulations suggest that the large cavities in the honeycomb structure are

incompatible with the experimentally found low HFBI membrane permeability. The cavities of the honeycomb structured HFBI monolayer became rapidly hydrated, leading to major leakage over the membranes. In addition, our simulations together with analysis of the HFBI structures excluded the possibility that the low water permeability is caused by an extended hydrophobic core as present in lipid bilayers (thickness of 2–3 nm), since the hydrophobic patch of HFBI forming the central layer is only few Ångströms thick. The hydrophobicity of the HFBI bilayer core is further reduced by the presence of polar atoms of the protein backbone and by the Gln^{65} side chain. The presence of an only Ångström-thick hydrophobic layer is reflected by the extended hydration of hydrophobin monolayers at the water – air interface (Figure 3), where the water density reaches up to the layer of the hydrophobic patch. The simulations revealed water leakage even for a dense yet irregular lateral HFBI packing (Figure 6), similar to the irregular lateral packing in lipid bilayers according to the fluid mosaic model. Hence, the presence of the moderately apolar Ångström-thick layer is far from sufficient to explain the low permeability of the HFBI membrane.

To experimentally demonstrate that the low permeability is indeed an intrinsic property of the HFBI membrane, we used a HFBI variant with two cellulose–binding domains. The additional domains led to increased water permeability comparable to the permeability in monoolein, likely by precluding the formation of a tight lateral packing of HFBI monomers. Furthermore, we excluded experimentally, and by simulations, the possibility that the low water permeability is caused by a residual film of oil between the HFBI leaflets.

Based on these results, we propose that the formation of a HFBI membrane from two HFBI monolayers in a honeycomb structure trigger a lateral rearrangement of HFBI monolayers, leading to an exceptionally dense packing with well-defined, stable protein–protein interfaces. We anticipate that such interfaces are at least as tight as found in sphingomyelin:cholesterol membranes, which exhibit a comparable low water permeability. Owing to long-lasting protein–protein interactions, these lateral rearrangements likely occur on long time scales that are currently inaccessible to MD simulations. Hence, to rationalize the ex-

perimentally found low water permeability by atomic models and by MD simulations, it will be critical to obtain atomic-level structural information in future studies, for instance *via* cryo-electron microscopy or NMR spectroscopy, which may help in defining the protein–protein interfaces and, thereby, guide future simulations.

To conclude, we found that HFBI membranes exhibit exceptionally low water permeability and are capable of withstanding high osmotic pressures. These features are in contrast to lipid membranes, hence opening new options for using HFBI membranes as robust biomimetic membranes with pre-selected properties, for instance by incorporation of functional channels.[24] This study lays the foundation for developing hydrophobin membranes towards a biocompatible platform for biophysical or biotechnological applications.

Methods

HFBI HFBI is a class II hydrophobin naturally produced by the filamentous fungus *Trichoderma reesei*. It is highly amphiphilic with a hydrophobic patch and a kind of "hydrophilic pole".[43] Due to its compact size (ca. 7.5 kDa) and the presence of four disulfide bridges, HFBI is an exceptionally stable protein. In addition to the wild type, the HFBI variant HFBI-dCBM (ca. 18.5 kDa) was used.[58] In this non-natural protein, two cellulose binding domains are bound to HFBI *via* a 24 amino acid long, unstructured linker (11 kDa).[47] The lyophilized HFBI proteins used in this work were produced and purified at VTT (Espoo, Finland), as described in Paananen *et al.*[59]

Lyophilized HFBI was dissolved in 10 mM acetate buffer (∼pH 5) at a concentration of 100 µM. This stock solution was diluted to a concentration of 4 µM for further use. At this concentration, the droplets (radii: 0.52–0.62 mm) contain almost double the amount of proteins than needed for full surface coverage of 0.45 µmol/m^2.[36] The dilution was carried out either by addition of a 10 mM acetate buffer with an ionic strength of 6 mM for the droplets with the low salt concentrations or the same buffer supplemented with KCl to obtain an

ionic strength of 954 mM for the droplets with high salt concentraion. Therefore, a pair of droplets with an osmotic concentration difference of 1.717 osmol/L or 0.259 osmol/L and for the HFBI-dCBM droplets of 0.086 osmol/L (osmotic coefficient: $\phi = 0.9$, number of ions KCl dissociates: $n = 2$) were produced. All the protein solutions were stored at 4 °C and sonicated prior to usage.

Monoolein Solutions Monoolein (Sigma-Aldrich, M7765, $\geq 99\,\%$) was dissolved in squalene (Sigma-Aldrich, S3626, $\geq 98\,\%$) (10 mg/ml) at 45 °C for around 20 min. The water droplets in the measurements with monoolein were prepared with an osmotic concentration difference of 0.259 osmol/L.

Measurement Setup All experimental measurements with HFBI were carried out in n-hexadecane (Sigma-Aldrich, 8.20633, $\geq 99\,\%$) and all measurements with monoolein in squalene (Sigma-Aldrich, S3626, $\geq 98\,\%$). Hexadecane was chosen as the surrounding medium because it has already been shown that a HFBI bilayer can be produced in this oily phase.[43] Squalene was used instead of hexadecane as a surrounding medium for monoolein as no stable bilayers could be formed with monoolein in hexadecane. In order to avoid hexadecane crystallization, a temperature of 30 °C was chosen for all measurements, which is above the melting point of hexadecane (18.18 °C). To ensure a small contact area between the introduced droplets and the bottom, but also to prevent complete spreading of the droplets on the bottom, glass Petri dishes were coated with PDMS (Sylgard 184-Dow Corning) in order to increase their hydrophobicity (see Figure 1a).

Bilayer Formation - Droplet Interface Bilayers The bilayer formation for the water permeability measurements were oriented on the so-called "DIB"-method (Droplet Interface Bilayer[60,61]), that was previously used to calculate the permeability of lipid bilayers.[8,9,13] Therefore, small droplets (radii: 0.52–0.62 mm) of aqueous solution were formed in oil. After a relaxation time of at least 30 minutes, during which the molecules were allowed to adsorb

at the interface of the droplets and form a dense monolayer,[36] two droplets with different osmotic concentrations were brought into contact with a metal needle to form a bilayer. The contact area formed in this way has already been shown to be a protein bilayer and is impermeable to ions, as shown by measurements of the layer thickness and voltage-clamped membrane current.[24]

The droplets were imaged by a top view light microscopy (Leica DMI 2700M equipped with camera Leica MC170 HD) and their volume change recorded for up to 30 minutes. The droplet volumes and bilayer area were estimated from the recorded images. For determination of the droplets' cross-sectional area from the images, a MATLAB program developed in-house was used. The grayscale images were first segmented in foreground and background by thresholding. These foreground and background markers were then used to support edge-detection and a final watershed segmentation to mark the droplets and the dividing line. The cross-sectional droplet area and the length of the dividing line were then used to calculate the volume of the droplets and the area of the bilayer, respectively, assuming a spherical shape of the droplets and a circular contact area.

Furthermore, a lateral control measurement by an optical contact angle instrument (OCA 25, Data Pyhsics Instruments GmbH) was carried out during which no flattening of the droplets could be observed (see Fig. 1b), in contrast to hydrophobin droplets in air.[32]

Measurement noise in the determination of the cross-sectional area results in an error in the determination of the equivalent radius of 0.1 pixels, which corresponds to a measurement accuracy in the volume of $8{\cdot}10^{-4}\,\mathrm{mm}^3$ for the considered droplet volume. Using typical values (initial volume, osmotic concentration, contact area), the permeability accuracy is 9 µm/s for the low salt concentration and 1 µm/s for the increased salt concentration. The permeability accuracy improves with higher osmotic concentration difference due to an increased volume change over time.

Setup of atomistic molecular dynamics (MD) simulations of HFBI monolayers at the air–water interface MD simulations were set up and carried out with the GROMACS software.[62] The HFBI structure files were retrieved from the protein data bank (entry 2fz6).[63] Crystal water and zinc ions were removed from the structure. The HFBI monolayers were constructed from one of the hexameric unit cells proposed by Magarkar *et al.*,[35] denoted HFBI-β (Figure S4b). For the HFBI simulations at the air–water interface, nine of such unit cells were assembled in a 3×3 shape into a hexagonal lattice structure and centered in a triclinic box with dimensions 17.1 nm $\times$ 17.1 nm $\times$ 8.5 nm. Water was added in a slab between 2.1 nm $<$ z $<$ 6.0 nm to generate the air–water interface. The water layer was stabilized using flat-bottom position restraints with a force constant of 200 kJ/(mol nm^2). The system contained 54 protein monomers and $\approx$ 20,000 water molecules, which summed up to $\approx$ 120,000 atoms. The CHARMM36m[64] force field together with the TIP3P water model[65] was used for the all-atomistic simulations. Virtual hydrogen site construction was enabled throughout, allowing a time step of 4 fs.[66] The temperature was kept constant using the velocity-rescale thermostat[67] at 300 K. Pressure coupling at 1 bar was applied using the Berendsen barostat in the lateral (xy) membrane direction .[68] Electrostatic interactions were calculated using the particle-mesh Ewald method.[69] Lennard-Jones interactions were cut off at 1.0 nm. Water molecules were constrained with SETTLE.[70] All other bonds were constrained with LINCS.[71] An initial constant volume (NVT) equilibration simulation over 50 ns was performed followed by four independent 400 ns simulations. Mass density profiles along the membrane normal were calculated using the gromacs tool 'gmx density'.

Setup of honeycomb bilayer simulations HFBI monolayers were constructed as described above using both proposed monolayer structures HFBI-α and HFBI-β (Figure S4). For each monolayer, nine of such unit cells were assembled in a 3×3 shape into a hexagonal lattice structure and centered in a triclinic box with dimensions 16.41 nm $\times$ 16.41 nm $\times$ 10 nm for HFBI-α and 17.16 nm $\times$ 17.16 nm $\times$ 10 nm for HFBI-β. Two copies of a monolayer

were placed on top of each other such that the hydrophobic patches pointed inwards. The upper and the lower monolayer were placed in two lateral arrangements: For the holey bilayer, the holes of the honeycomb structure were placed on top of each other, such that large transmembrane cavities were formed. In addition, for a dense bilayer the holes in the upper layer were laterally displaced relative to the lower bilayer, such that the holes in one leaflet were covered by proteins of the other leaflet. The simulation box was filled with explicit water molecules and with Na^+ and Cl^- ions to reach a concentration of 0.1 mol/L. The system contained 108 protein monomers, $\sim$30,000 water molecules and ions, which summed up to $\sim$200,000 atoms. All simulation parameters were identical to the honeycomb monolayer simulations at the interface, except that the pressure coupling was also applied separately along the membrane normal (z) direction and no position restraints were used. For each setup, three independent simulations of 400 ns each were carried out. Mass density profiles were calculated as stated above.

Setup of disordered and laterally compressed bilayers A densely packed disordered bilayer was generated using a multi-step protocol, which is described in detail in the Supporting Material. In short, the following steps were carried out: (i) HFBI monomers in coarse-grained (CG) representation were placed at random positions in the x-y plane, modelled with the MARTINI22 force field.[72,73] The layer was compressed laterally in a simulation with a lateral pressure of 1200 bar and a temperature of 3600 K, while stabilizing the internal HFBI structures with elastic networks. (ii) The system was cooled down to 300 K using a simulated annealing. (iii) The two resulting densely packed monolayers were combined to form a bilayer, and the CG system was equilibrated at constant volume. (iv) The CG models were backmapped to atomistic models with the Backward software.[74] Since the secondary structure and certain side chain arrangements disagreed with the crystal structures after the CG-to-atomistic backmapping, we ran simulations with additional restraints to anneal the structure towards the correct crystallographic secondary structure. (v) After the addition of

water and NaCl at 0.1 mol/L, the system was simulated for 100 ns at 300 K and 1 bar using the same parameters as described above.

Permeability Calculations The permeation of water molecules across a membrane can be described by the permeation events per time ($\Phi(t)$) through a given surface area (A):

$$P_f = \frac{\Phi(t)}{A\Delta c(t)} \tag{1}$$

where $\Delta c(t)$ is the concentration difference between the two sides of the membrane. Experimentally, water permeability is usually determined by the change in volume of a pair of droplets (DIB) of different salt concentrations. Therefore Φ can be described by the volume change of the drops $\mathrm{d}V/\mathrm{d}t \cdot 1/\nu_W$ (ν_W= molar volume of water) and equation (1) results into:[10,45,75]

$$\frac{\mathrm{d}V(t)}{\mathrm{d}t} = -P_f A \nu_W \Delta c(t) \tag{2}$$

By assuming a negligible salt concentration of the drop of low salt concentration, the equation (2) can be integrated over the time to be able to use the values obtained from the experiments.

$$\left(\frac{V(t)}{V_0}\right)^2 = 1 + \left(\frac{2P_f A \nu_w C_0}{V_0}\right) t \tag{3}$$

V_0 is the volume and C_0 the concentration difference of the two drops at the beginning of the measurement. Using this linear relationship, the permeability can be determined *via* the change in volume of the droplets. The volume change is corrected for the volume loss of the droplets in the oil by assuming that the inflow into one droplet is equal to the outflow through the membrane of the second droplet. The volume change was investigated after the formation of a double layer until the double layer broke apart or a maximum time of 30 minutes was reached. Mean permeability values were then calculated by a linear fit.

In contrast to the experiments, the MD simulations contain an equal number of ions on both sides of the membrane due to the periodic boundary conditions. Therefore, there is approximately equal water flux in both directions, *i.e.* nearly zero net flux. However, the simulation system may be considered as an overlay of a water concentration gradient c in one direction with a gradient $-c$ in the other direction, where $c = 55\,\mathrm{mol/L}$ is the concentration of water. Hence, the number of permeation events N (in any direction) per simulation time t was translated into the membrane permeability with

$$P_f = \frac{N}{2Atc} \tag{4}$$

Here, the factor 1/2 corrects for the fact that we summed permeation events in both directions. The water permeability P_f of the HFBI-bilayers were computed as in Zocher *et al.*[76] Accordingly, the position along the membrane normal (*i.e.* the z coordinate) was recorded for all oxygen atoms of water. Three layers were defined along the z axis: A core layer spanning the membrane center and two outer layers that cover the water on top of and below the membrane. A permeation event was registered if the particle passed from one outer layer through the core layer to the other outer layer. This protocol excludes the possibility that water molecules diffusing across the periodic boundaries are misinterpreted as permeation events. It is known that the TIP3P model produces diffusion coefficient values that are larger than the experimental observed ones.[77] We therefore determined the diffusion coefficient of pure TIP3P water from a 5 ns simulation of pure water and found that the diffusion coefficient was increased by a factor of 2.49 relative to experiments at 298.15 K.[77] Hence, we corrected the computed P_f by the same factor.

Error analysis in the determination of experimental membrane water permeability In Figure 7, the permeabilities for the pure HFBI membranes also assume negative values, which is physically implausible. After correction of the water loss into the hexadecane, the droplet with the higher salt content of the droplet pair does not always increase in

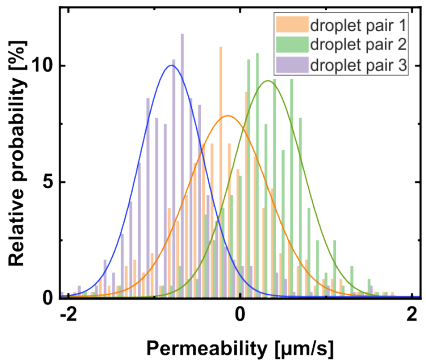

Figure 7: Distribution of permeability values calculated for every single time step for three pure HFBI wild type membranes.

volume, it can also shrink and thus lead to a negative sign of the permeability. Systematic errors, as *e.g.*, in the calculation of the droplet volume from the cross-section images, might cause this observation, however, compared to the resolution of the experimental system, this systematic error is small: The permeability values scattered with $\pm 0.5\,\mu m/s$ around -0.4 µm/s (Figure 2b, data for pure HFBI). The resolution estimated from the inherent scatter in the droplet area determination is approx. $1\,\mu m/s$ (standard deviation of the Gaussian distribution), as can be seen in the distribution of the evaluated permeability values for every time step (Figure 7). The two sources of error are therefore of the same order of magnitude, whereas the scattering determines the lowest possible resolution. Thus, in the current setup, the water permeability of HFBI bilayers is indistinguishable from zero.

Author Contributions

F.N.: data curation, investigation, methodology, visualization, writing—original draft, and writing—review and editing. L.S.: investigation, methodology, visualization, writing—original draft, and writing—review and editing. A.G.: methodology, and writing—review and editing. M.L.: resources, and writing—review and editing. K.J.: supervision, and writing—review and editing. R.S.: supervision, and writing—review and editing. J.F.: conceptualization, methodology, supervision, and writing—review and editing. J.H.: concep-

tualization, methodology, supervision of MD simulations, writing—original draft, and writing—review and editing. H.H.: conceptualization, methodology, software, supervision of experiments, and writing—review and editing. All authors have read and agreed to the published version of the manuscript.

Acknowledgement

This study was supported by the Deutsche Forschungsgemeinschaft (DFG, German Research Foundation) *via* SFB 1027, subprojects B1, B4 and B7 and the German Federal Ministry of Education and Research (BMBF) by the Max Planck School Matter to Life. Computing resources supported by the DFG *via* INST 256/539-1 is acknowledged. Furthermore, this work was supported by an Academy Research Fellowship grant awarded to ML by the Academy of Finland (Decision No. 321723). The authors thank T. Faidt for technical help.

Supporting Information Available

The following files are available free of charge.

- Additional details to experiments, and simulations.

References

(1) Fettiplace, R.; Haydon, D. A. Water Permeability of Lipid Membranes. *Physiological Reviews* **1980**, *60*, 510–550.

(2) Werber, J. R.; Elimelech, M. Permselectivity Limits of Biomimetic Desalination Membranes. *Science advances* **2018**, *4*, eaar8266.

(3) Leggio, L.; Arrabito, G.; Ferrara, V.; Vivarelli, S.; Paternò, G.; Marchetti, B.;

Pignataro, B.; Iraci, N. Mastering the Tools: Natural Versus Artificial Vesicles in Nanomedicine. *Advanced healthcare materials* **2020**, *9*, 2000731.

(4) Mao, H.; Wei, C.; Gong, Y.; Wang, S.; Ding, W. Mechanical and Water-Resistant Properties of Eco-Friendly Chitosan Membrane Reinforced with Cellulose Nanocrystals. *Polymers* **2019**, *11*, 166.

(5) Kali, R.; Andini, E.; Milner, S. T. Molecular Dynamics Simulation Based Design of Biomimetic Membrane with Artificial Water Channels. *Journal of Membrane Science* **2021**, *630*, 119279.

(6) Song, W.; Joshi, H.; Chowdhury, R.; Najem, J. S.; Shen, Y.-x.; Lang, C.; Henderson, C. B.; Tu, Y.-M.; Farell, M.; Pitz, M. E., et al. Artificial Water Channels Enable Fast and Selective Water Permeation through Water-Wire Networks. *Nature nanotechnology* **2020**, *15*, 73–79.

(7) Rall, D.; Menne, D.; Schweidtmann, A. M.; Kamp, J.; von Kolzenberg, L.; Mitsos, A.; Wessling, M. Rational Design of Ion Separation Membranes. *Journal of Membrane Science* **2019**, *569*, 209–219.

(8) Michalak, Z.; Muzzio, M.; Milianta, P. J.; Giacomini, R.; Lee, S. Effect of Monoglyceride Structure and Cholesterol Content on Water Permeability of the Droplet Bilayer. *Langmuir* **2013**, *29*, 15919–15925.

(9) Milianta, P. J.; Muzzio, M.; Denver, J.; Cawley, G.; Lee, S. Water Permeability across Symmetric and Asymmetric Droplet Interface Bilayers: Interaction of Cholesterol Sulfate with DPhPC. *Langmuir* **2015**, *31*, 12187–12196.

(10) Lopez, M.; Evangelista, S. E.; Morales, M.; Lee, S. Enthalpic Effects of Chain Length and Unsaturation on Water Permeability across Droplet Bilayers of Homologous Monoglycerides. *Langmuir* **2017**, *33*, 900–912.

(11) Lopez, M.; Denver, J.; Evangelista, S. E.; Armetta, A.; Domizio, G. D.; Lee, S. Effects of Acyl Chain Unsaturation on Activation Energy of Water Permeability across Droplet Bilayers of Homologous Monoglycerides: Role of Cholesterol. *Langmuir* **2018**, *34*, 2147–2157.

(12) Rosenberg, P. A.; Finkelstein, A. Water Permeability of Gramicidin A-Treated Lipid Bilayer Membranes. *Journal of General Physiology* **1978**, *72*, 341–350.

(13) Fleury, J.-B. Enhanced Water Permeability across a Physiological Droplet Interface Bilayer Doped with Fullerenes. *RSC Advances* **2020**, *10*, 19686–19692.

(14) Lande, M. B.; Donovan, J. M.; Zeidel, M. L. The Relationship between Membrane Fluidity and Permeabilities to Water, Solutes, Ammonia, and Protons. *J Gen Physiol* **1995**, *106*, 67–84.

(15) Terreno, E.; Sanino, A.; Carrera, C.; Castelli, D. D.; Giovenzana, G. B.; Lombardi, A.; Mazzon, R.; Milone, L.; Visigalli, M.; Aime, S. Determination of water permeability of paramagnetic liposomes of interest in MRI field. *Journal of Inorganic Biochemistry* **2008**, *102*, 1112–1119.

(16) Gier, J. D.; Mandersloot, J.; Deenen, L. V. Lipid composition and permeability of liposomes. *Biochimica et Biophysica Acta (BBA) - Biomembranes* **1968**, *150*, 666–675.

(17) Yang, B.; van Hoek, A. N.; Verkman, A. S. Very High Single Channel Water Permeability of Aquaporin-4 in Baculovirus-Infected Insect Cells and Liposomes Reconstituted with Purified Aquaporin-4. *Biochemistry* **1997**, *36*, 7625–7632.

(18) Brea, R. J.; Hardy, M. D.; Devaraj, N. K. Towards Self-Assembled Hybrid Artificial Cells: Novel Bottom-Up Approaches to Functional Synthetic Membranes. *Chemistry - A European Journal* **2015**, *21*, 12564–12570.

(19) Eswari, J. S.; Naik, S. A Critical Analysis on Various Technologies and Functionalized Materials for Manufacturing Dialysis Membranes. *Materials Science for Energy Technologies* **2020**, *3*, 116–126.

(20) Lin, H. Plasticization-Enhanced Hydrogen Purification Using Polymeric Membranes. *Science* **2006**, *311*, 639–642.

(21) Kumar, M.; Grzelakowski, M.; Zilles, J.; Clark, M.; Meier, W. Highly Permeable Polymeric Membranes Based on the Incorporation of the Functional Water Channel Protein Aquaporin Z. *Proceedings of the National Academy of Sciences* **2007**, *104*, 20719–20724.

(22) Vargo, K. B.; Parthasarathy, R.; Hammer, D. A. Self-Assembly of Tunable Protein Suprastructures from Recombinant Oleosin. *Proceedings of the National Academy of Sciences* **2012**, *109*, 11657–11662.

(23) Wagner, A. M.; Quandt, J.; Söder, D.; Garay-Sarmiento, M.; Joseph, A.; Petrovskii, V. S.; Witzdam, L.; Hammoor, T.; Steitz, P.; Haraszti, T.; Potemkin, I. I.; Kostina, N. Y.; Herrmann, A.; Rodriguez-Emmenegger, C. Ionic Combisomes: A New Class of Biomimetic Vesicles to Fuse with Life. *Advanced Science* **2022**, *9*, 2200617.

(24) Hähl, H.; Vargas, J. N.; Griffo, A.; Laaksonen, P.; Szilvay, G.; Lienemann, M.; Jacobs, K.; Seemann, R.; Fleury, J.-B. Pure Protein Bilayers and Vesicles from Native Fungal Hydrophobins. *Advanced Materials* **2017**, *29*, 1602888.

(25) Linder, M. B.; Szilvay, G. R.; Nakari-Setälä, T.; Penttilä, M. E. Hydrophobins: the Protein-Amphiphiles of Filamentous Fungi. *FEMS Microbiology Reviews* **2005**, *29*, 877–896.

(26) Wösten, H. A.; Wessels, J. G. Hydrophobins, from Molecular Structure to Multiple Functions in Fungal Development. *Mycoscience* **1997**, *38*, 363–374.

(27) Peng, C.; Liu, J.; Zhao, D.; Zhou, J. Adsorption of Hydrophobin on Different Self-Assembled Monolayers: The Role of the Hydrophobic Dipole and the Electric Dipole. *Langmuir* **2014**, *30*, 11401–11411.

(28) Hakala, T. J.; Laaksonen, P.; Saikko, V.; Ahlroos, T.; Helle, A.; Mahlberg, R.; Hähl, H.; Jacobs, K.; Kuosmanen, P.; Linder, M. B.; Holmberg, K. Adhesion and Tribological Properties of Hydrophobin Proteins in Aqueous Lubrication on Stainless Steel Surfaces. *RSC Advances* **2012**, *2*, 9867.

(29) Goldian, I.; Jahn, S.; Laaksonen, P.; Linder, M.; Kampf, N.; Klein, J. Modification of Interfacial Forces by Hydrophobin HFBI. *Soft Matter* **2013**, *9*, 10627.

(30) Szilvay, G. R.; Paananen, A.; Laurikainen, K.; Vuorimaa, E.; Lemmetyinen, H.; Peltonen, J.; Linder, M. B. Self-Assembled Hydrophobin Protein Films at the Air-Water Interface: Structural Analysis and Molecular Engineering. *Biochemistry* **2007**, *46*, 2345–2354.

(31) Linder, M. B. Hydrophobins: Proteins that Self Assemble at Interfaces. *Current Opinion in Colloid & Interface Science* **2009**, *14*, 356–363.

(32) Yamasaki, R.; Takatsuji, Y.; Asakawa, H.; Fukuma, T.; Haruyama, T. Flattened-Top Domical Water Drops Formed through Self-Organization of Hydrophobin Membranes: A Structural and Mechanistic Study Using Atomic Force Microscopy. *ACS Nano* **2015**, *10*, 81–87.

(33) Li, B.; Wang, X.; Li, Y.; Paananen, A.; Szilvay, G. R.; Qin, M.; Wang, W.; Cao, Y. Single-Molecule Force Spectroscopy Reveals Self-Assembly Enhanced Surface Binding of Hydrophobins. *Chemistry - A European Journal* **2018**, *24*, 9224–9228.

(34) Fan, H.; Wang, B.; Zhang, Y.; Zhu, Y.; Song, B.; Xu, H.; Zhai, Y.; Qiao, M.; Sun, F. A Cryo-Electron Microscopy Support Film Formed by 2D Crystals of Hydrophobin HFBI. *Nature Communications* **2021**, *12*, 7257.

(35) Magarkar, A.; Mele, N.; Abdel-Rahman, N.; Butcher, S.; Torkkeli, M.; Serimaa, R.; Paananen, A.; Linder, M.; Bunker, A. Hydrophobin Film Structure for HFBI and HFBII and Mechanism for Accelerated Film Formation. *PLoS Computational Biology* **2014**, *10*, e1003745.

(36) Hähl, H.; Griffo, A.; Safaridehkohneh, N.; Heppe, J.; Backes, S.; Lienemann, M.; Linder, M. B.; Santen, L.; Laaksonen, P.; Jacobs, K. Dynamic Assembly of Class II Hydrophobins from T. reesei at the Air–Water Interface. *Langmuir* **2019**, *35*, 9202–9212.

(37) Wösten, H. A. B.; Scholtmeijer, K. Applications of Hydrophobins: Current State and Perspectives. *Applied Microbiology and Biotechnology* **2015**, *99*, 1587–1597.

(38) Hektor, H. J.; Scholtmeijer, K. Hydrophobins: Proteins with Potential. *Current Opinion in Biotechnology* **2005**, *16*, 434–439.

(39) Kostiainen, M. A.; Szilvay, G. R.; Lehtinen, J.; Smith, D. K.; Linder, M. B.; Urtti, A.; Ikkala, O. Precisely Defined Protein–Polymer Conjugates: Construction of Synthetic DNA Binding Domains on Proteins by Using Multivalent Dendrons. *ACS Nano* **2007**, *1*, 103–113.

(40) Rothbauer, M.; Küpcü, S.; Sticker, D.; Sleytr, U. B.; Ertl, P. Exploitation of S-Layer Anisotropy: pH-Dependent Nanolayer Orientation for Cellular Micropatterning. *ACS Nano* **2013**, *7*, 8020–8030.

(41) Valo, H. K.; Laaksonen, P. H.; Peltonen, L. J.; Linder, M. B.; Hirvonen, J. T.; Laaksonen, T. J. Multifunctional Hydrophobin: Toward Functional Coatings for Drug Nanoparticles. *ACS Nano* **2010**, *4*, 1750–1758.

(42) Maiolo, D.; Pigliacelli, C.; Moreno, P. S.; Violatto, M. B.; Talamini, L.; Tirotta, I.; Piccirillo, R.; Zucchetti, M.; Morosi, L.; Frapolli, R.; Candiani, G.; Bigini, P.; Metrangolo, P.; Bombelli, F. B. Bioreducible Hydrophobin-Stabilized Supraparticles for Selective Intracellular Release. *ACS Nano* **2017**, *11*, 9413–9423.

(43) Hähl, H.; Vargas, J. N.; Jung, M.; Griffo, A.; Laaksonen, P.; Lienemann, M.; Jacobs, K.; Seemann, R.; Fleury, J.-B. Adhesion Properties of Freestanding Hydrophobin Bilayers. *Langmuir* **2018**, *34*, 8542–8549.

(44) Basheva, E. S.; Kralchevsky, P. A.; Danov, K. D.; Stoyanov, S. D.; Blijdenstein, T. B. J.; Pelan, E. G.; Lips, A. Self-Assembled Bilayers from the Protein HFBII Hydrophobin: Nature of the Adhesion Energy. *Langmuir* **2011**, *27*, 4481–4488.

(45) Thiam, A. R.; Bremond, N.; Bibette, J. From Stability to Permeability of Adhesive Emulsion Bilayers. *Langmuir* **2012**, *28*, 6291–6298.

(46) Tawfik, H.; Puza, S.; Seemann, R.; Fleury, J.-B. Transport Properties of Gramicidin A Ion Channel in a Free-Standing Lipid Bilayer Filled With Oil Inclusions. *Frontiers in Cell and Developmental Biology* **2020**, *8*, 531229.

(47) Laaksonen, P.; Walther, A.; Malho, J.-M.; Kainlauri, M.; Ikkala, O.; Linder, M. B. Genetic Engineering of Biomimetic Nanocomposites: Diblock Proteins, Graphene, and Nanofibrillated Cellulose. *Angewandte Chemie* **2011**, *123*, 8847–8850.

(48) Awoonor-Williams, E.; Rowley, C. N. Molecular Simulation of Nonfacilitated Membrane Permeation. *Biochim. Biophys. Acta – Biomembranes* **2016**, *1858*, 1672–1687.

(49) Hub, J. S.; Grubmüller, H.; de Groot, B. L. Dynamics and Energetics of Permeation through Aquaporins. What Do We Learn from Molecular Dynamics Simulations? *Handb Exp Pharmacol* **2009**, *190*, 57–76.

(50) Hub, J. S.; Aponte-Santamaría, C.; Grubmüller, H.; de Groot, B. L. Voltage-Regulated Water Flux through Aquaporin Channels in Silico. *Biophys. J.* **2010**, *99*, L97–L99.

(51) Lynch, C. I.; Rao, S.; Sansom, M. S. P. Water in Nanopores and Biological Channels: A Molecular Simulation Perspective. *Chem. Rev.* **2020**, *120*, 10298–10335.

(52) Riccardi, L.; Mereghetti, P. Induced fit in protein multimerization: The HFBI case. *PLoS Computational Biology* **2016**, *12*, e1005202.

(53) Yu, H.; Yang, S.; Chen, Z.; Xu, Z.; Quan, X.; Zhou, J. Orientation and Conformation of Hydrophobin at the Oil–Water Interface: Insights from Molecular Dynamics Simulations. *Langmuir* **2022**, *38*, 6191–6200.

(54) Vodopivec, A. A.; Chen, Y.; Russo, P. S.; Hung, F. R. Molecular dynamics simulations of nanostructures formed by hydrophobins and oil in seawater. *The Journal of Physical Chemistry B* **2021**, *125*, 7886–7899.

(55) Robertson, M. J.; Tirado-Rives, J.; Jorgensen, W. L. Improved peptide and protein torsional energetics with the OPLS-AA force field. *Journal of chemical theory and computation* **2015**, *11*, 3499–3509.

(56) Lindorff-Larsen, K.; Piana, S.; Palmo, K.; Maragakis, P.; Klepeis, J. L.; Dror, R. O.; Shaw, D. E. Improved side-chain torsion potentials for the Amber ff99SB protein force field. *Proteins: Structure, Function, and Bioinformatics* **2010**, *78*, 1950–1958.

(57) Izadi, S.; Anandakrishnan, R.; Onufriev, A. V. Building water models: a different approach. *The journal of physical chemistry letters* **2014**, *5*, 3863–3871.

(58) Linder, M. B.; Qiao, M.; Laumen, F.; Selber, K.; Hyytiä, T.; Nakari-Setälä, T.; Penttilä, M. E. Efficient Purification of Recombinant Proteins using Hydrophobins As Tags in Surfactant-Based Two-Phase Systems. *Biochemistry* **2004**, *43*, 11873 – 11882.

(59) Paananen, A.; Vuorimaa, E.; Torkkeli, M.; Penttilä, M.; Kauranen, M.; Ikkala, O.; Lemmetyinen, H.; Serimaa, R.; Linder, M. B. Structural Hierarchy in Molecular Films of Two Class II Hydrophobins†. *Biochemistry* **2003**, *42*, 5253–5258.

(60) Bayley, H.; Cronin, B.; Heron, A.; Holden, M. A.; Hwang, W. L.; Syeda, R.; Thompson, J.; Wallace, M. Droplet Interface Bilayers. *Molecular BioSystems* **2008**, *4*, 1191.

(61) Hwang, W. L.; Chen, M.; Cronin, B.; Holden, M. A.; Bayley, H. Asymmetric Droplet Interface Bilayers. *Journal of the American Chemical Society* **2008**, *130*, 5878–5879.

(62) Abraham, M. J.; Murtolad, T.; Schulz, R.; Páll, S.; Smith, J. C.; Hessa, B.; Lindahl, E. GROMACS:High Performance Molecular Simulations Through Multi-Level Parallelism from Laptops to Supercomputers. *SoftwareX* **2015**, *1-2*, 19–25.

(63) Hakanpää, J.; Szilvay, G. R.; Kaljunen, H.; Maksimainen, M.; Linder, M.; Rouvinen, J. Two Crystal Structures of Trichoderma Reesei Hydrophobin HFBI—The Structure of a Protein Amphiphile with and without Detergent Interaction. *Protein Science* **2006**, *15*, 2129–2140.

(64) Huang, J.; Rauscher, S.; Nawrocki, G.; Ran, T.; Feig, M.; de Groot, B. L.; Grubmüller, H.; MacKerell, A. D. CHARMM36m: an Improved Force Field for Folded and Intrinsically Disordered Proteins. *Nature Methods* **2016**, *14*, 71–73.

(65) Jorgensen, W. L.; Chandrasekhar, J.; Madura, J. D.; Impey, R. W.; Klein, M. L. Comparison of Simple Potential Functions for Simulating Liquid Water. *The Journal of Chemical Physics* **1983**, *79*, 926–935.

(66) Bjelkmar, P.; Larsson, P.; Cuendet, M. A.; Hess, B.; Lindahl, E. Implementation of the CHARMM Force Field in GROMACS: Analysis of Protein Stability Effects from Correction Maps, Virtual Interaction Sites, and Water Models. *Journal of chemical theory and computation* **2010**, *6*, 459–466.

(67) Bussi, G.; Donadio, D.; Parrinello, M. Canonical Sampling through Velocity Rescaling. *The Journal of Chemical Physics* **2007**, *126*, 014101.

(68) Berendsen, H. J. C.; Postma, J. P. M.; van Gunsteren, W. F.; DiNola, A.; Haak, J. R. Molecular Dynamics with Coupling to an External Bath. *The Journal of Chemical Physics* **1984**, *81*, 3684–3690.

(69) Essmann, U.; Perera, L.; Berkowitz, M. L.; Darden, T.; Lee, H.; Pedersen, L. G. A Smooth Particle Mesh Ewald Method. *The Journal of Chemical Physics* **1995**, *103*, 8577–8593.

(70) Miyamoto, S.; Kollman, P. A. Settle: An Analytical Version of the SHAKE and RATTLE Algorithm for Rigid Water Models. *Journal of computational chemistry* **1992**, *13*, 952–962.

(71) Hess, B. P-LINCS: A Parallel Linear Constraint Solver for Molecular Simulation. *Journal of Chemical Theory and Computation* **2007**, *4*, 116–122.

(72) Marrink, S. J.; Risselada, H. J.; Yefimov, S.; Tieleman, D. P.; de Vries, A. H. The MARTINI Force Field: Coarse Grained Model for Biomolecular Simulations. *The Journal of Physical Chemistry B* **2007**, *111*, 7812–7824.

(73) Monticelli, L.; Kandasamy, S. K.; Periole, X.; Larson, R. G.; Tieleman, D. P.; Marrink, S.-J. The MARTINI Coarse-Grained Force Field: Extension to Proteins. *Journal of chemical theory and computation* **2008**, *4*, 819–834.

(74) Wassenaar, T. A.; Pluhackova, K.; Böckmann, R. A.; Marrink, S. J.; Tieleman, D. P. Going Backward: A Flexible Geometric Approach to Reverse Transformation from Coarse Grained to Atomistic Models. *Journal of Chemical Theory and Computation* **2014**, *10*, 676–690.

(75) Olbrich, K.; Rawicz, W.; Needham, D.; Evans, E. Water Permeability and Mechanical Strength of Polyunsaturated Lipid Bilayers. *Biophysical Journal* **2000**, *79*, 321–327.

(76) Zocher, F.; Wennberg, C. L.; Pohl, P.; Hub, J. Local Micro-Partition Coefficients Govern Solute Permeability of Cholesterol-Containing Membranes. *Biophysical Journal* **2013**, *104*, 82a.

(77) Mills, R. Self-diffusion in Normal and Heavy Water in the Range 1-45.deg. *The Journal of Physical Chemistry* **1973**, *77*, 685–688.

TOC Graphic

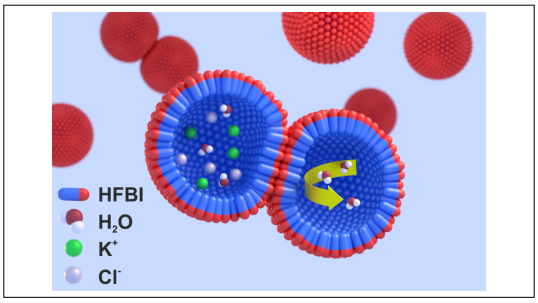

Supporting Information: Hydrophobin bilayer as water impermeable protein membrane

Friederike Nolle,[†,‖] Leonhard J. Starke,[‡,‖] Alessandra Griffo,[†,¶,⊥] Michael Lienemann,[§] Karin Jacobs,[†,¶] Ralf Seemann,[†] Jean-Baptiste Fleury,[†] Jochen S. Hub,[*,‡] and Hendrik Hähl[*,†]

†*Department of Experimental Physics, Saarland University, D-66123 Saarbrücken, Germany*

‡*Department of Theoretical Physics, Saarland University, D-66123 Saarbrücken, Germany*

¶*Max Planck School, Matter to Life, Jahnstraße 29, 69120 Heidelberg, Germany*

§*VTT Technical Research Centre of Finland Ltd., Espoo 02150, Finland*

‖*These authors contributed equally to this work.*

⊥*Max Planck Institute for Medical Research Heidelberg, 69120 Heidelberg, Germany*

E-mail: jochen.hub@uni-saarland.de; h.haehl@physik.uni-saarland.de

Supporting Information

Water transport across a HFBI monolayer in Hexadecane

The solubility of water in n-hexadecane is very low (ca. 3 mmol/L at 30 °C[1]), yet not zero. Therefore, water droplets in hexadecane will shrink over time as water molecules cross the water-oil interface and diffuse into the oil. To measure the water diffusion into hexadecane, single buffer droplets (with and without HFBI and KCl) were injected into a hexadecane bath at 30 °C with a hollow needle. Ensuring a total protein coverage of the droplet interface

for the droplets with HFBI, all droplets were added into hexadecane half an hour prior to measurement. Volume changes of these single droplets were observed with a top-view light microscope as described in the manuscript. To account for the loss of water into the surrounding oil, we quantify the volume of individual droplets consisting of pure water as well as of acetate buffer, with and without proteins in hexadecane over a period of 30 minutes. For all droplets, a clear decrease in volume was observed. The flux per area was thereby similar for all recorded droplets, *i.e.* independent of the presence of additional salt or proteins (Table S1).

Table S1: Water flux and diffusion values of different solutions with and without surrounding hydrophobin monolayer.

Solution	Water flux per area [10^{-4} µm/s]	Diffusion [10^3 µm^2/s]
Pure water	5.3 ± 1.1	5.5 ± 1.0
Buffer (I = 6 mM)	4.7 ± 0.9	4.8 ± 1.0
Buffer (I = 954 mM)	5.0 ± 1.0	5.1 ± 0.9
HFBI + buffer (I = 6 mM)	5.9 ± 0.8	6.0 ± 0.7
HFBI + buffer (I = 954 mM)	4.8 ± 0.7	5.1 ± 0.7

Using the diffusion equation and Fick's first law, we calculated the diffusion coefficient (D) of water from the drop into the oil by considering the solubility of water in hexadecane ($c_s = 0.003$ mol/L), assuming that there is an approximately linear relationship with temperature[1] *via*

$$D = \frac{V_0 - V(t)}{4\pi c_s \upsilon_w \int_0^t r(t)dt'} \tag{1}$$

where $\upsilon_w = 18$ g/mol is the molar mass of water, V is the current droplet volume and V_0 is the droplet volume at time $t = 0$ and r is radius of the droplet. Complete saturation of the hexadecane with water was not achieved because the additional oil-air interface at the top of the oil bath allowed the water to evaporate. Effective diffusion values were determined to be in the range of 4–6·10^3 µm^2/s using eq. (1), which take a possible additional hindrance by an interfacial layer into account.

Thus, the volume change of droplets in the DIB setup is not solely caused by the water transport across the membrane that is formed between two droplets of different salt concentration, but also by the diffusion of the buffer through the monolayer of the drops in contact with the oil. In most studies[2–4] using the DIB method, this effect can be disregarded as the flux through a lipid membrane between two droplets is, typically, much larger than the self-dilution of the individual droplets. However, for the measurement of permeabilities in the µm/s range as relevant in our case, buffer diffusion into the oil must be taken into account.

Oil-free membrane

To visualize the oil around the droplets and investigate a suspected oil layer between the droplets (Figure S1), fluorescence microscopy measurements were performed with hexadecane stained with BODIPY (Thermo Fisher - 493/503 dye (Cat. No. D3922)). Preparation steps were identical to the permeability measurements described in the main text. Only the salinity difference was chosen to be zero. A stack of microscopy images was recorded with height steps of 5 µm between the slices at an Axiovert 7 Zeiss with a colibri 7 (LED) illumination and rendered as a 3D image by software Zen Zeiss. In the images, no signal in the fluorescence channel could be detected in the contact area between the droplets. Thus, no evidence of oil between the individual HFBI layers was found, which could form an additional permeation barrier.

Data processing

To extract the permeability from the droplets' volume change data, the volume loss into the surrounding oil was added to the data, as described in the main text. In Figure S2 data from the main text are presented after this correction step. Figure S2a depicts the situation for a pure HFBI bilayer showing almost no volume exchange through the bilayer and S2b the situation for a 0.4:1 HFBI-dCBM:HFBI WT ratio, showing a water flow through the mem-

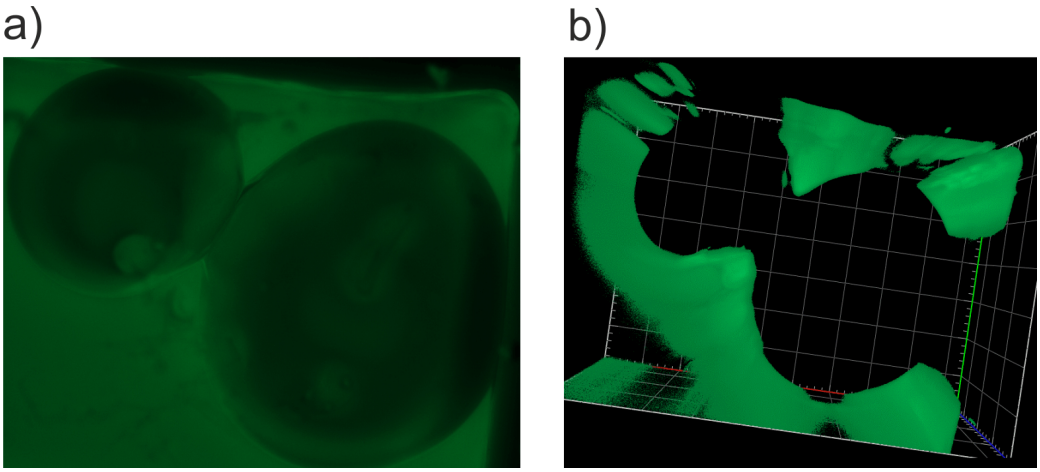

Figure S1: a) Top view of two identical HFBI-coated buffer droplets. Green shows the fluorescence signal of the BODIPY in the entire setup. b) 3D image stack in 5 µm steps over the z-height of the formed HFBI membrane. Green represents the fluorescence signal of the dyed oil in the plane of the membrane and excludes the dye above or below the membrane. A square of the drawn grid has a length of 600 µm each in x-, y- and z-direction.

brane from the droplet of low salt concentration into the droplet of high salt concentration.

Water permeability using NaCl as osmolyte

Volume changes of two different droplet pairs with NaCl (1.717 osmol/L) instead of KCl as the osmotic pressure causing salt were recorded, resulting in permeabilities below the resolution limit ($P_f = 0.7$ and 0.4 µm/s) similar to droplets with KCl. Experimental setup was else identical to the measurements with KCl. Fig. S3 compares measurements with NaCl and KCl.

MD simulation of HFBI monolayer at the oil–water interface

We ran an additional simulation of the HFBI monolayer at an hexadecane–water interface to investigate the stability of the honeycomb structure under the experimental conditions present in the DIB setup. As starting configuration, we used the HFBI monolayer based

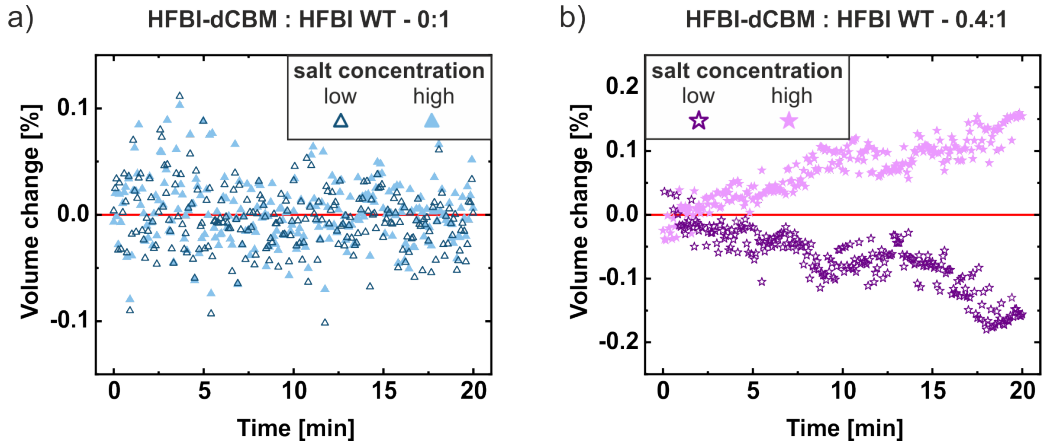

Figure S2: Relative volume changes, corrected for volume loss into oil, of two droplet pairs with different HFBI-dCBM:HFBI-WT ratios (a) 0:1 and b) 0.4:1). In each case, the filled symbols represent the droplet with high salt concentration and the open symbols represent the droplet with low salt concentration. The osmotic concentration difference was a) 1.717 osmol/L and b) 0.086 osmol/L. Temperature was kept constant at 30 °C.

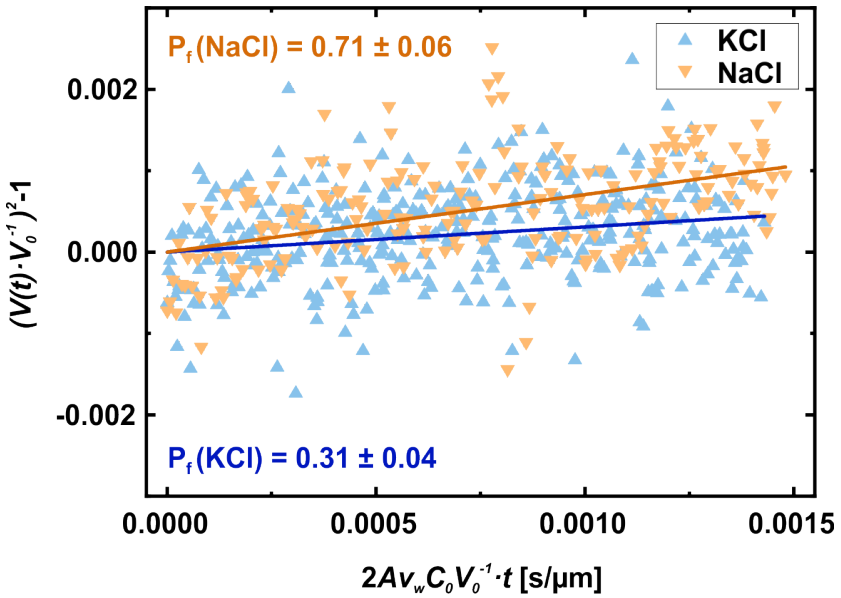

Figure S3: Comparing measurements using NaCl instead of KCl as the osmotic active molecule in the droplet of high salt concentration. The axes are chosen according to formula 3 so that the slope of the linear fit of the data corresponds to the mean permeability value of the membrane shown.However, both permeability values are below the resolution limit of our experiment.

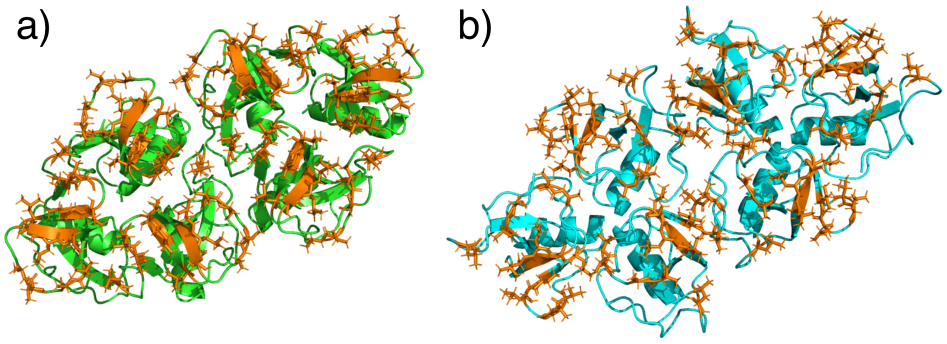

Figure S4: Proposed unit cells of HFBI hexamers from docking simulations[5] termed a) HFBI-α and b) HFBI-β. Monomers are shown in cartoon representation with the hydrophobic patch represented as orange sticks. Note the differences between the HFBI monomer interfaces as evident from the distinct orientation of the α-helices.

on the β unit cell at the air–water interface as described in the main text. An additional layer of hexadecane oil with a thickness of $\sim$ 3.2 nm was generated in a separate simulation box with identical x-y dimensions, composed of 1560 molecules corresponding to a density of 0.77 g/cm at room temperature.[6] This layer was inserted above the hydrophobic patch of the HFBI monolayer. Parameters for hexadecane were taken from alkane parameters by CHARMM36m, augmented with alkane–water interactions suggested by Krämer *et al.*.[7] Lennard-Jones interactions were treated with the cut-off scheme as described in the CHARMM specifications. The temperature was controlled at 310 K by velocity rescaling[8] and the pressure at 1 bar using the Berendsen barostat.[9] Flat bottom position restraints with a force constant of 200 kJ/mol nm^2 for both the oil and the water layer were defined such that jumps over the periodic boundary were prevented while allowing the transport through the protein layer. We ran 10 ns for equilibration at constant volume, followed by 25 ns equilibration at constant pressure with pressure coupling only applied in x-y direction. Next, we carried out a 400 ns production simulation at 1 bar and 310 K. Water diffusion through the HFBI monolayer was detected using the method used to calculate water permeation through the bilayer (see main text). Here, the central layer was defined by the maximum and minimum z coordinate of the hydrophobic patch taken from the last simulation frame.

Consequently, the upper layer corresponded to the water phase and the lower layer to the oil phase.

During the simulation, water slowly penetrated the oil phase and vice versa, resulting in minor local deformations of the HFBI monolayer (Figure S5). Nevertheless, the honeycomb structure remained stable over the whole simulation. In the simulation time, we observed approx. 100 events of water molecule diffusion into the oil phase, showing that the simulations follow qualitatively the experiential observations. Quantitatively, however, we observed fewer events compared to simulations, which is expected because the TIP3P water models does not reproduce the experimental water/oil partition coefficient. This is explained by the fact that TIP3P has been parameterized to reproduce bulk properties and not properties of individual water molecules in oil, as has been reported previously.[10]

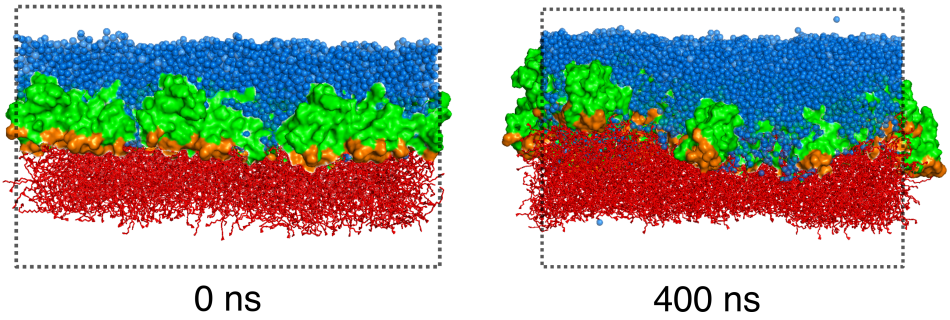

Figure S5: Snapshots of simulations of HFBI monolayer at the oil–water interface at 0 and 400 ns. The protein is shown in surface representation in green with the hydrophobic patch colored in orange. Hexadecane is shown as red sticks and water oxygens as blue spheres respectively. Dotted lines indicate the simulation box.

Variation of force fields and water model

To exclude that the choice of the protein force field or water influences the key findings of this study, we carried out additional simulations of the 'dense' HFBI bilayer based on the β unit cell with using the following combinations of protein force field and water model: AMBER99SB/TIP3P, OPLSaa/TIP3P, or CHARMM36m/OPC. For AMBER99SB/TIP3P,

Lennard-Jones interactions were truncated at 1.0 nm; for the other two combinations, Lennard-Jones interactions were truncated at 1.4 nm. All other simulations parameters were chosen as described above. Each setup was simulated at least for 15 ns and the water density profile was computed for different time intervals as shown in Fig. S6. In all cases water penetrated the membrane core within few nanoseconds, demonstrating that the key findings are not influenced by the force field.

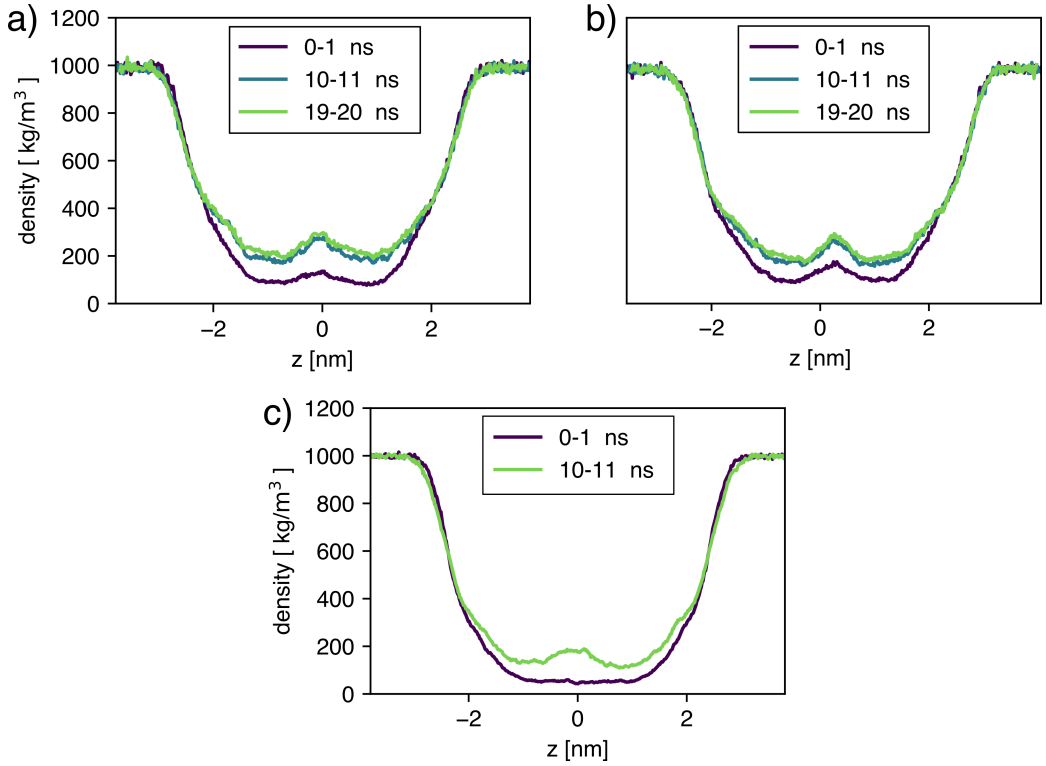

Figure S6: Water mass densities from simulations of the 'dense' HFBI bilayer based on the HFBI-β unit cell using different force fields and water models. Densities are averaged over intervals of 1 ns each. a) Simulation using the AMBER99SB force field and the TIP3P water model, b) OPLSaa force field and TIP3P water model, and c) CHARMM36m force field and the OPC water model. After 10 ns, water has penetrated the hydrophobic membrane core ($z \approx 0$ nm), independent of the choice of the force field or water model.

MD simulations are compatible with oil-free hydrophobin bilayers

To rationalize the low water permeability found experimentally, we hypothesized that a thin hexadecane layer of only a few atom layers remains between the monolayers and, thereby, prevents water transfer between neighboring hydrophobin monolayers. To test such an hypothesis, we carried out two MD simulations with a thin hexadecane film between the two hydrophobin layers with thicknesses of 1.3 nm and 0.5 nm, corresponding to approximately 6 or 3 hexadecane molecules per hydrophobin monomer respectively (Figure S7). The bilayer simulation system with the central hexadecane film was built from the dense bilayer configuration based on the HFBI-β unit cell. Again, each monolayer was composed of 3×3 unit cells. The protein bilayer was setup as described before, however with an additional gap in between the monolayers. The thin layer of hexadecane with a thickness of ~ 1.3 nm was generated in a separate simulation box with identical x-y dimensions, composed of 676 molecules corresponding to a density of 0.77 g/cm at room temperature.[6] The hexadecane layer was inserted into the gap between the HFBI monolayers, and the system was compressed in z-direction, while constraining the x-y-coordinates of the hexadecane atoms. To generate another system with an even thinner hexadecane layer, every second oil molecule was removed from the initial setup, followed again by compression along the z direction, thereby reducing the distance between the monolayers while maintaining the hexadecane film structure. The temperature was again controlled at 310 K with the velocity-rescale thermostat[8] and the pressure to 1 bar using the Parrinello-Rahman barostat.[11] For each system, one simulation of 400 ns was performed.

However, the hexadecane film ruptures within the simulation time and allows water leakage over the membrane. Simultaneously, the hexadecane aggregates to form oil droplets at the monolayer cavities. This effect was even more pronounced in the simulation with the reduced amount of hexadecane (Figure S7). In the experimental context, these oil droplets would eventually be absorbed by the oil reservoirs. These findings agree well with the notion

of an oil-free hydrophobin bilayer[12] and with the absence of BODIPY inside the membrane in the experiments described above (Figure S1). In addition, this data suggest that the low water permeability cannot be explained by residual oil but must instead be a consequence of tight packing between hydrophobin monomers.

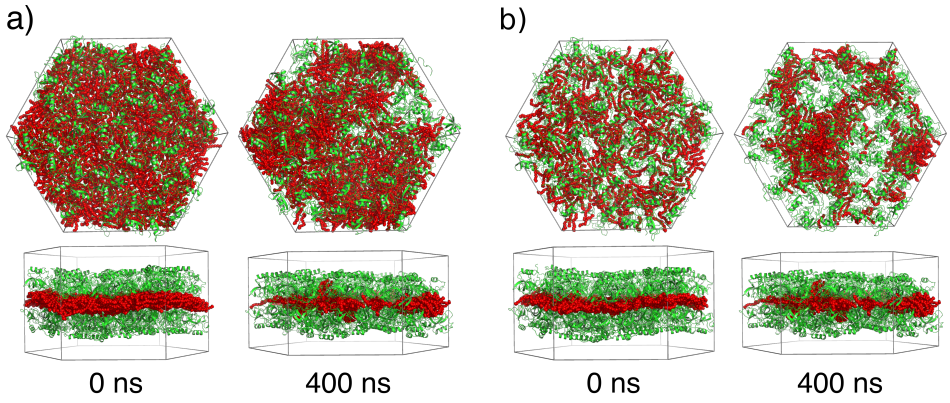

Figure S7: Simulation snapshots of simulations of HFBI bilayer with a hexadecane oil film (red) in between the protein layers with a) 6 or b) 3 hexadecane molecules per hydrophobin. The oil film ruptures and the hexadecane molecules start to fill the cavities between the proteins as seen in the lower panel (400 ns snapshots).

Detailed protocol of laterally compressed disordered bilayer setup

To generate a structural model of a densely packed HFBI bilayer the following simulation protocol was run consisting of five steps, as outlined in the main text and described in detail in the following:

Coarse grained layer setup and compression (i): A single HFBI protein was extracted from the crystal structure (PDB database entry 2fz6[13]), crystal water and zinc ions were removed. The atomic structure was converted into coarse-grained (CG) representation with the martinize.py script.[14,15] The protein was stabilized with an elastic bond network between the backbone beads and a set of manually defined distance constraints to prevent large side chain rotations, which would otherwise disrupt the secondary structure after backmapping

to atomistic resolution (Table S2). The force constants for these restraints were set to 500 kJ/(mol·nm^2). 50 monomers were placed in a plane at randomly selected x-y positions with the hydrophobic patches all facing towards the same direction, consistent with the orientation at an air–water interface. To rapidly compress the system, short simulations at $T = 3600$ K and $p = 1200$ bar were carried out for 20 ns. During those simulations position restraints in z-direction with a force constant of 1000 kJ/(mol·nm^2) were applied to ensure that the monolayer does not fold or bend. The time step was set to 1.25 fs to avoid instabilities during the simulation. Here, the cut-off values for Lennard-Jones and Coulomb interactions was set to 0.8 nm.

Annealing (ii): An annealing simulation was performed to relax the system and to allow the formation of tight and stable contacts between the monomers. To this end, the temperature was linearly decreased down to 300 K over a range of 100 ns.

Bilayer setup and constant volume equilibration (iii): The final frame of two independent compression simulations (steps i, ii) were equilibrated at constant volume for another 10 ns at 300 K. Afterwards both monolayers were overlayed, such that the hydrophobic cores are oriented inwards. The energy of the system was minimized, and the system was simulated for another 10 ns.

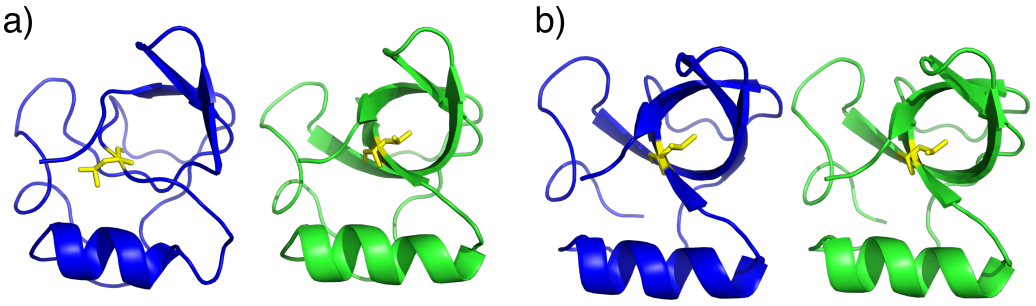

Figure S8: Comparison between a backmapped HFBI structure (blue) with the original crystal structure (green) before (a) and after the refinement of the secondary structure (b). An example for a side chain flip (LYS 56) is highlighted in yellow in each structure.

Backmapping to atomistic resolution (iv): Backmapping of the coarse grained systems followed the method by Wassenaar *et al.*[16] which consists of the actual backmapping process followed by a set of short MD simulations to relax the system. One potential issue of the backmapping procedure to an atomistic model is a potential loss of secondary structure. While certain deviations may be restored by running a long equilibration of the protein,[16] a full recovery of the secondary structure was only achieved by taking additional measures. Accordingly, we added (i) an additional elastic bond network between the C_α atoms and (ii) distance restraints between atoms to enforce the formation of the original hydrogen bond network of the crystal structure, which defined the secondary structure. For this purpose, the initial distances for the hydrogen bonds in the crystal structure were used. By gradually turning on these hydrogen bond restraints, the original secondary structure can be restored. First, a short pulling simulation was performed over 100 ps, with increasing the force constants from 40 to 4000 kJ/(mol nm^2), followed by a pulling simulation at constant force over 10 ns. Throughout the simulations, the elastic network force constants were kept at 500 kJ/(mol nm^2) as before. Visual inspection revealed excellent agreement of the refined HFBI structures with the crystal structure conformations (Figure S8). In the initial backmapped structure most of the characteristic beta barrel is lost, due to lost hydrogen bonds after large side chain rearrangements (Figure S8a). After the pulling simulations, the flipped side chain is in the correct orientation and the secondary structure of the backmapped protein is fully restored (Figure S8b).

Solvation (v): The refined dense bilayer was solvated with TIP3P water. Na^+ and Cl^- ions were added to a concentration of 0.1 mol/L followed by an energy minimization. The solvent structure was equilibrated at constant pressure conditions over 2 ns with position restraints on the backbone atoms. Subsequently, all position restraints were removed and the system was simulated for 100 ns at 300 K and 1 bar.

Table S2: Additional distance restraints in the coarse-grained martini HFBI setup between beads i and j indicated by bead type, residue name, and residue number. Abbreviations of bead types: BB - backbone beads, SCk - k^{th} side chain bead

Bead i	Bead j	Distance [nm]
SC1 CYS 18	SC1 LEU 55	0.4
SC1 GLN 21	BB CYS 68	0.55
SC3 PHE 43	BB LEU 55	0.4
SC3 PHE 12	SC1 LEU 25	0.44
SC1 GLN 16	BB ALA 62	0.5
BB CYS 56	SC1 GLN 69	0.58
SC1 PRO 15	SC2 PHE 43	0.57

Extended equilibration does not prevent water leakage

Given the large forces present during compression and backmapping, we furthermore tested an extended equilibration protocol of the 'dry' compressed bilayer prior to solvation. To this end, we first carried out a constant volume equilibration over 5 ns of the backmapped and refined structure followed by a constant pressure equilibration with pressure coupling applied only in x-y direction over 400 ns. Next, we solvated the system as described above and carried out short equilibration at constant pressure over 5 ns with position restraints applied on the protein backbone atoms using a force constant of 1000 kJ/mol nm^2. Finally, a 200 ns production simulation at 1 bar and 300 K without position restraints was carried out. In this setup, we again observed water penetration on the nanosecond time scale as evident from water densities calculated at different time intervals (Figure S9).

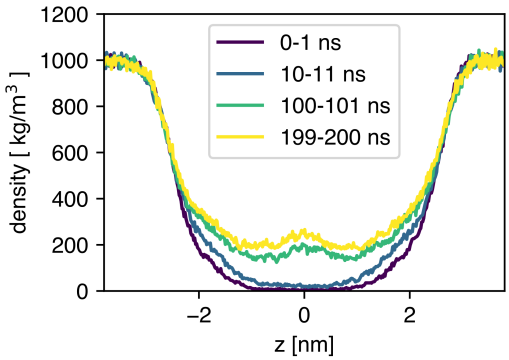

Figure S9: Water mass densities from simulations of the 'disordered' bilayer after a more extensive equilibration protocol which includes a prolonged 'dry' equilibration without water. Compared to the previous simulations (e.g. Fig. 5) water penetration is slower but nevertheless reaches densities in the order of ~ 200 kg/m^3.

References

(1) Schatzberg, P. SOLUBILITIES OF WATER IN SEVERAL NORMAL ALKANES FROM C7TO C161. *The Journal of Physical Chemistry* **1963**, *67*, 776–779.

(2) Milianta, P. J.; Muzzio, M.; Denver, J.; Cawley, G.; Lee, S. Water Permeability across Symmetric and Asymmetric Droplet Interface Bilayers: Interaction of Cholesterol Sulfate with DPhPC. *Langmuir* **2015**, *31*, 12187–12196.

(3) Michalak, Z.; Muzzio, M.; Milianta, P. J.; Giacomini, R.; Lee, S. Effect of Monoglyceride Structure and Cholesterol Content on Water Permeability of the Droplet Bilayer. *Langmuir* **2013**, *29*, 15919–15925.

(4) Fleury, J.-B. Enhanced Water Permeability across a Physiological Droplet Interface Bilayer Doped with Fullerenes. *RSC Advances* **2020**, *10*, 19686–19692.

(5) Magarkar, A.; Mele, N.; Abdel-Rahman, N.; Butcher, S.; Torkkeli, M.; Serimaa, R.; Paananen, A.; Linder, M.; Bunker, A. Hydrophobin Film Structure for HFBI and

HFBII and Mechanism for Accelerated Film Formation. *PLoS Computational Biology* **2014**, *10*, e1003745.

(6) DDB Saturated Lipid Density. `http://ddbonline.ddbst.de/DIPPR105DensityCalculation/DIPPR105CalculationCGI.exe?component=Hexadecane`, Accessed on May 25, 2023.

(7) Krämer, A.; Pickard, F. C.; Huang, J.; Venable, R. M.; Simmonett, A. C.; Reith, D.; Kirschner, K. N.; Pastor, R. W.; Brooks, B. R. Interactions of Water and Alkanes: Modifying Additive Force Fields to Account for Polarization Effects. *Journal of Chemical Theory and Computation* **2019**, *15*, 3854–3867.

(8) Bussi, G.; Donadio, D.; Parrinello, M. Canonical Sampling through Velocity Rescaling. *The Journal of Chemical Physics* **2007**, *126*, 014101.

(9) Berendsen, H. J. C.; Postma, J. P. M.; van Gunsteren, W. F.; DiNola, A.; Haak, J. R. Molecular Dynamics with Coupling to an External Bath. *The Journal of Chemical Physics* **1984**, *81*, 3684–3690.

(10) Venable, R. M.; Kramer, A.; Pastor, R. W. Molecular dynamics simulations of membrane permeability. *Chemical reviews* **2019**, *119*, 5954–5997.

(11) Parrinello, M.; Rahman, A. Polymorphic Transitions in Single Crystals: A New Molecular Dynamics Method. *Journal of Applied Physics* **1981**, *52*, 7182–7190.

(12) Hähl, H.; Vargas, J. N.; Griffo, A.; Laaksonen, P.; Szilvay, G.; Lienemann, M.; Jacobs, K.; Seemann, R.; Fleury, J.-B. Pure Protein Bilayers and Vesicles from Native Fungal Hydrophobins. *Advanced Materials* **2017**, *29*, 1602888.

(13) Hakanpää, J.; Szilvay, G. R.; Kaljunen, H.; Maksimainen, M.; Linder, M.; Rouvinen, J. Two Crystal Structures of Trichoderma Reesei Hydrophobin HFBI—The Structure of

a Protein Amphiphile with and without Detergent Interaction. *Protein Science* **2006**, *15*, 2129–2140.

(14) Marrink, S. J.; Risselada, H. J.; Yefimov, S.; Tieleman, D. P.; de Vries, A. H. The MARTINI Force Field: Coarse Grained Model for Biomolecular Simulations. *The Journal of Physical Chemistry B* **2007**, *111*, 7812–7824.

(15) Monticelli, L.; Kandasamy, S. K.; Periole, X.; Larson, R. G.; Tieleman, D. P.; Marrink, S.-J. The MARTINI Coarse-Grained Force Field: Extension to Proteins. *Journal of chemical theory and computation* **2008**, *4*, 819–834.

(16) Wassenaar, T. A.; Pluhackova, K.; Böckmann, R. A.; Marrink, S. J.; Tieleman, D. P. Going Backward: A Flexible Geometric Approach to Reverse Transformation from Coarse Grained to Atomistic Models. *Journal of Chemical Theory and Computation* **2014**, *10*, 676–690.

II Strength of bacterial adhesion on nanostructured surfaces quantified by substrate morphometry

Authors: C. Spengler,[1] **F. Nolle**,[1] J. Mischo,[1] T. Faidt,[1] S.Grandthyl,[1] N. Thewes,[1] M. Koch,[2] F. Müller,[1] M. Bischoff,[3] M.A. Klatt,[4] and K. Jacobs[1]

[1] Department of Experimental Physics, Saarland University, Campus E2 9, 66123 Saarbrücken, Germany.
[2] INM - Leibnitz Institute for New Materials, Campus D2 2, 66123 Saarbrücken, Germany.
[3] Institute of Medical Microbiology and Hygiene, Saarland University, 66421 Homburg/Saar, Germany.
[4] Institute of Stochastics, Karlsruhe Institute of Technology, 76131 Karlsruhe, Germany.

Reprinted with permission from *Nanoscale*, 2019, **11**, 19713.
https://doi.org/10.1039/c9nr04375f

Author contributions:
*C.S., N.T., M.B., K.J. designed research. C.S., **F.N.**, J.M. performed AFM and viability measurements. S.G., F.M. performed XPS measurements. M.K. performed REM measurements. M.A.K. performed Minkowski analyses. C.S., **F.N.**, J.M., T.F., S.G., F.M., M.A.K. analyzed data. C.S., M.B., M.A.K., K.J. wrote the manuscript with the help of all other authors.*

Abstract – Microbial adhesion and the subsequent formation of resilient biofilms at surfaces are decisively influenced by substrate properties, such as the topography. To date, studies that quantitatively link surface topography and bacterial adhesion are scarce, as both are not straightforward to quantify. To fill this gap, surface morphometry combined with single-cell force spectroscopy was performed on surfaces with irregular topographies on the nano-scale. As surfaces, hydrophobized silicon wafers were used that were etched to exhibit surface structures in the same size range as the bacterial cell wall molecules. The surface structures were characterized by a detailed morphometric analysis based on Minkowski functionals revealing both qualitatively similar features and quantitatively different extensions. We find that as the size of the nanostructures increases, the adhesion forces decrease in a way that can be quantified by the area of the surface that is available for the tethering of cell wall molecules. In addition, we observe a bactericidal effect, which is more pronounced on substrates with taller structures but does not influence adhesion. Our results can be used for a targeted development of 3D-structured materials for/against

bio-adhesion. Moreover, the morphometric analysis can serve as a future gold standard for characterizing a broad spectrum of material structures.

Nanoscale

COMMUNICATION

View Article Online
View Journal | View Issue

Cite this: *Nanoscale*, 2019, **11**, 19713

Received 22nd May 2019,
Accepted 2nd September 2019
DOI: 10.1039/c9nr04375f

rsc.li/nanoscale

Strength of bacterial adhesion on nanostructured surfaces quantified by substrate morphometry†

Christian Spengler,[a] Friederike Nolle,[a] Johannes Mischo,[a] Thomas Faidt,[a] Samuel Grandthyll,[a] Nicolas Thewes,[a] Marcus Koch,[b] Frank Müller,[a] Markus Bischoff,[c] Michael Andreas Klatt‡[d] and Karin Jacobs*[a]

Microbial adhesion and the subsequent formation of resilient biofilms at surfaces are decisively influenced by substrate properties, such as the topography. To date, studies that quantitatively link surface topography and bacterial adhesion are scarce, as both are not straightforward to quantify. To fill this gap, surface morphometry combined with single-cell force spectroscopy was performed on surfaces with irregular topographies on the nano-scale. As surfaces, hydrophobized silicon wafers were used that were etched to exhibit surface structures in the same size range as the bacterial cell wall molecules. The surface structures were characterized by a detailed morphometric analysis based on Minkowski functionals revealing both qualitatively similar features and quantitatively different extensions. We find that as the size of the nanostructures increases, the adhesion forces decrease in a way that can be quantified by the area of the surface that is available for the tethering of cell wall molecules. In addition, we observe a bactericidal effect, which is more pronounced on substrates with taller structures but does not influence adhesion. Our results can be used for a targeted development of 3D-structured materials for/against bio-adhesion. Moreover, the morphometric analysis can serve as a future gold standard for characterizing a broad spectrum of material structures.

Introduction

Bacterial biofilms can cause serious problems in many medical, biological and industrial applications.[1–3] Once formed, they are chemically and mechanically robust and therefore very difficult to remove.[4,5] A promising approach in biofilm prevention is to inhibit the first step of its formation, which is the adhesion of bacterial cells to surfaces. An important substrate property for the adhesion of bacterial cells is the surface topography, which has therefore been addressed in numerous studies,[6–9] especially in the prevention of biofouling, a subject of ongoing discussion.[8–10] However, in the literature no universal approach to quantify bacterial adhesion on nanostructured surfaces can be found since previous studies mostly feature two main drawbacks: lack of (i) quantitative adhesion force determination and (ii) detailed surface characterization.

(i) Bacterial adhesion on structured surfaces has often been examined in adsorption experiments by immersing the structured surfaces in bacterial suspensions.[11–15] Although this approach is intuitive and mimics the natural situation of bacterial colonization quite accurately, the results from different labs are hard to compare since too many parameters are involved that cannot be controlled accurately. For example, the processes of obtaining the number of adhering cells may differ: in some cases, the sample is first dried and then coated with gold in order to count the bacteria later in electron microscopy images[11,12] or by conductance microbiology.[13] It is also difficult to describe the rinsing of loosely bound cells and the removal of adsorbed cells for plating or counting in all parameters. These problems can be overcome by quantitative measurements of actual bacterial adhesion forces (the force required to detach the cell from the surface) under controlled conditions. Hence, we used single-cell force spectroscopy (SCFS), a well-established method for quantitative adhesion force measurements of living bacterial cells.[16–26]

(ii) Many studies have used different types of topographically (regularly[27–32] or randomly[11–15,33–36]) structured surfaces

[a]*Department of Experimental Physics, Saarland University, Campus E2 9, 66123 Saarbrücken, Germany. E-mail: k.jacobs@physik.uni-saarland.de; Fax: +49 (0)681 302 71700; Tel: +49 (0)681 302 71777*
[b]*INM – Leibniz Institute for New Materials, Campus D2 2, 66123 Saarbrücken, Germany*
[c]*Institute of Medical Microbiology and Hygiene, Saarland University, 66421 Homburg/Saar, Germany*
[d]*Institute of Stochastics, Karlsruhe Institute of Technology, 76131 Karlsruhe, Germany*
†Electronic supplementary information (ESI) available. See DOI: 10.1039/C9NR04375F
‡Present address: Department of Physics, Princeton University, Jadwin Hall, Princeton, NJ 08544-0001, USA.

View Article Online
Communication Nanoscale

without a detailed morphological characterization. There are a number of parameters to describe surface morphologies:[37,38] for example, the average roughness or the root mean square (RMS) roughness are very descriptive parameters that are, therefore, often used in bacterial adhesion studies. Other measures, such as the skewness or the kurtosis of the surface, are less intuitive, but give additional information about the surface geometry.[35,36] However, all these parameters are local shape descriptors that are insensitive to global features because they do not distinguish between arbitrary permutations of the positions of different heights. Therefore, these parameters do not fully characterize the surface morphologies, which makes it difficult to compare the results of different studies. One way to overcome these problems in describing the topography are the so-called Minkowski functionals that we therefore used in our study.[39]

Minkowski functionals are comprehensive and efficient shape descriptors from integral geometry[40] that contain, put simply, the complete additive – and hence robust – shape information (according to Hadwiger's theorem).[41] Since they are versatile geometric measures, they have already been widely used in statistical physics and pattern analysis (see ref. 42–48 and references therein). There, an integral geometry-based analysis using the Minkowski functionals has been termed morphometry.[48] With this method, height data of nanostructured surfaces can be analysed using three-dimensional Minkowski functionals or the level sets at different heights using two-dimensional Minkowski functionals (for explanatory figures, see the ESI†).

In 2D, the Minkowski functionals of a domain can be intuitively interpreted as its area, perimeter, and Euler characteristic. The latter is a topological constant, which is given for a compact body by its number of components minus its number of holes.

In this study, we used *Staphylococcus aureus* (*S. aureus*), a Gram-positive, biofilm-forming bacterium that is a frequent cause of severe infections,[49] and measured the adhesion forces of single cells to nanostructured surfaces (see Fig. 1 for an about-to-scale sketch) that are characterized by their Minkowski functionals and show how the strength of bacterial adhesion can be quantified with the help of these functionals. We focus on nanostructures since the radius of the contact area of bacteria like *S. aureus* to flat surfaces is only in the range of some hundred nanometers.[50]

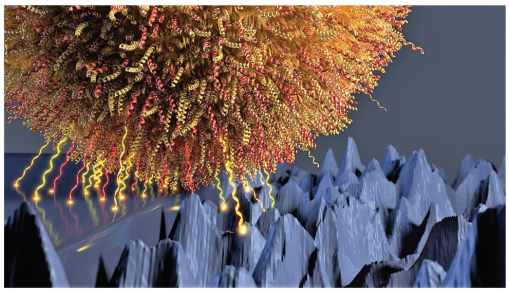

Fig. 1 Bacterial cell adhering to a partially smooth and nanostructured surface (represented by real AFM data).

Results and discussion

Surface morphometry

In order to create suitable substrates for the quantification of the influence of surface nanostructures on bacterial adhesion, we etched clean silicon wafers in a mixture of fluoric acid, hydrogen peroxide and water for different periods of time (90 s, 180 s, 360 s).[51] Beforehand, the surfaces were covered with small gold clusters as catalysts for the etching process. These clusters were applied by physical vapor deposition[52] and afterwards removed by immersing the wafers in aqua regia. Then, the wafers were rendered hydrophobic because strong bacterial adhesion is governed by hydrophobic interaction.[53,54] This was achieved by covering them with a self-assembling monolayer of silanes according to a standard recipe[55] (the quality of the silane monolayer was checked by contact angle measurements and AFM experiments in quantitative nanomechanical mapping; for details, see the ESI†). As shown in Fig. 2a, on the formerly smooth surfaces, etching created characteristic nanostructures, whose lateral and vertical dimensions increased with increasing etching time. The structures feature sharp edges on all surfaces and their shape seems similar in general.

To characterize the surface structures in a quantitative way, the hydrophobized substrates were imaged by atomic force microscopy (AFM) at different positions with high aspect ratio tips. Before further analysis, the surface was reconstructed by unfolding the recorded image and the tip geometry. As a simple parameter – and for comparison to other studies – the RMS roughness of each surface was determined (and was used as label for the different surfaces). Its value increases with increasing etching time: 7 ± 1 nm for the 90 s etched surface, 24 ± 1 nm for the 180 s etched surface, and 35 ± 1 nm for the 360 s etched surface.

For a more detailed characterization, the Minkowski functionals of all AFM images were calculated and averaged over different positions on each surface[47] (for a visual explanation of the Minkowski functionals of level sets, see Fig. S2 in the ESI†).[45,46] Since the maximum height range of the samples varies, the functionals were normalized to their respective maximum height value. In Fig. 2b and c, the specific perimeter and the Euler characteristic density are plotted in dependence of this normalized threshold height (absolute values and data of surface area are given in Fig. S3 in the ESI†). For all surfaces, both functionals have similar shapes, with only their extents varying: the specific perimeter features a very smooth shape with a single maximum for all substrates. The position of the maximum differs slightly between the different substrates (for an explanation, see Fig. S6 in the ESI†). The Euler characteristic density has, in every case, for low threshold heights, a minimum with negative values and at larger heights, a

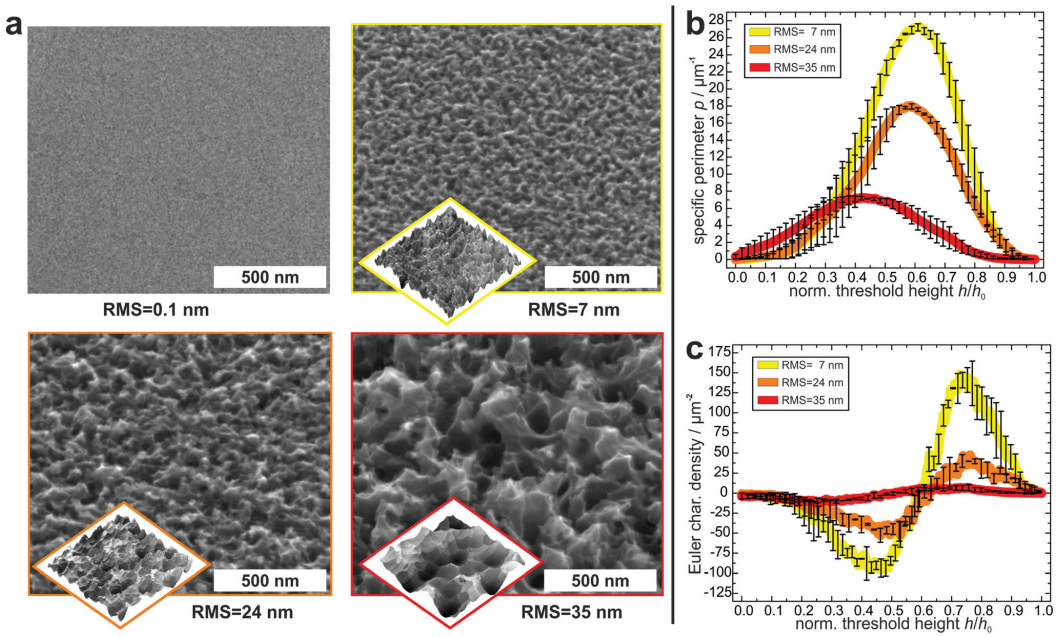

Fig. 2 (a) Scanning electron microscopy (SEM, big) and atomic force microscopy (AFM, small) images of the surfaces before etching and after etching for 90 s, 180 s and 360 s (from top left to bottom right). SEM images are tilted by 53°. The AFM images show a scan area of 1 × 1 µm^2 and total *z*-scales of 55 nm, 130 nm and 180 nm, respectively. The RMS values have been determined by AFM. (b and c) Averaged specific perimeter (b) and Euler characteristic density (c) of the nanostructured substrates as a function of the normalized threshold height (for clarity, only for every 20th data point is an error bar shown).

maximum with positive values. Due to the different RMS values, the peaks and dips, especially for the surface with an RMS value of 35 nm occur at different values of normalized threshold height. The Minkowski functionals thus characterize quantitative differences between the surfaces. These differences pertain mainly to the absolute values of the specific perimeter and Euler characteristic density: both quantities have the highest values for the surface with 7 nm RMS roughness, lower values for the surface with 24 nm RMS roughness and the lowest values for the surface with 35 nm RMS roughness. This means that the lateral dimensions of the etched structures are smaller for the surfaces that were etched for shorter times.

Overall, the Minkowski analysis confirms the morphological similarity between the surfaces, allowing for a systematic investigation of the influence of differently sized nanostructures on bacterial adhesion. Whether the differences are due to statistical fluctuations, pixelization errors, or physically relevant qualitative differences between the surfaces, is beyond the scope of this study and not relevant for our further analysis.

Moreover, these analyses show that all etched surfaces feature a sub-micron topography with dimensions in the same range as the radius of the bacterial contact area, which is about 150–300 nm.[50]

Bacterial adhesion is known to be affected not only by surface chemistry, but also by the subsurface of a material through long-ranging van der Waals forces.[57] Hence, to exclude potential influences originating from differences in surface and subsurface composition, XPS measurements of all substrates were performed before silanization, showing that the roughened surfaces oxidize immediately after etching. Since this surface oxide layer has the same thickness as the oxide layers of the unetched substrates (XPS spectra are given in Fig. S1 in the ESI†), all surfaces used can be considered chemically identical.

Effect of the nanostructure on bacterial adhesion

To quantify the impact of the nano-topography on the adhesive strength of bacteria, we performed single-cell force spectroscopy measurements on each etched surface and on a smooth surface as a reference. Thereto, a single viable *S. aureus* cell was immobilized on a tipless cantilever and force–distance curves were recorded in buffer at room temperature.[53,54,58] From these curves the so-called adhesion force, *i.e.* the maximum force needed to detach the cell from the surface, was calculated.

Fig. 3 shows the mean adhesion forces of all tested cells on each type of surface. Of note, adhesion forces of *S. aureus* on

View Article Online
Communication Nanoscale

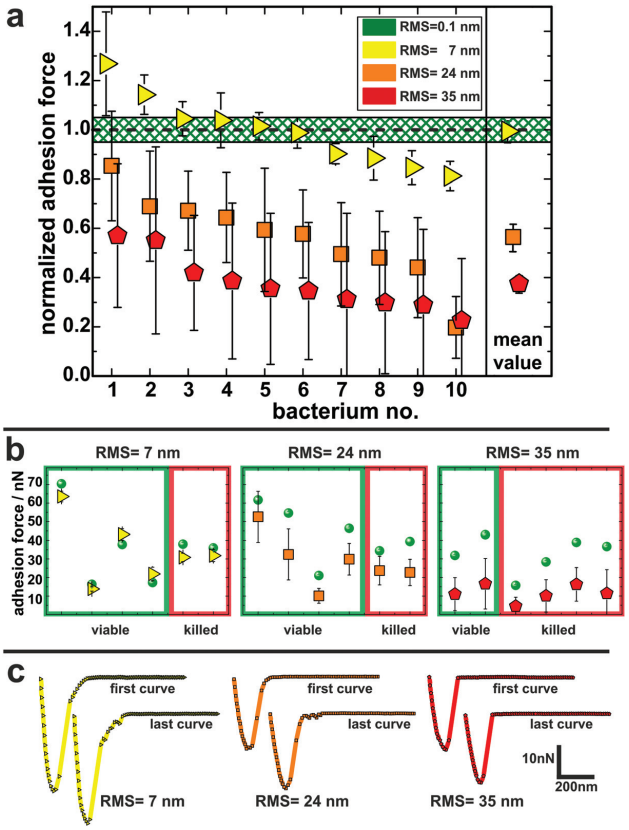

Fig. 3 (a) Adhesion forces of in total 30 *S. aureus* cells determined on the three types of nanostructured surfaces. Data are normalized to their individual adhesion force on the smooth silicon surface (marked in green). Error bars depict the standard deviation of the adhesion force distribution for every individual cell and – in the case of the mean value – the error of the mean adhesion force determined from every cell (for reasons of clarity, cells are sorted in order of decreasing reduction in adhesion force). (b) Measured adhesion forces of cells that were found to be viable/killed after single-cell force spectroscopy: green spheres show the adhesion force on the smooth surface, colored symbols the adhesion force of the corresponding cell on the nanostructured surfaces. Notably, killing of the cells only occurred after contact to the nanostructured surfaces (if no error bar is shown, it is in fact smaller than the symbol size). (c) First and last force–distance curve recorded on each nanostructured surfaces with an exemplary cell that was found to be killed afterwards.

hydrophobic surfaces are very cell-individual, *i.e.* they can differ markedly between different cells.[50] Therefore, for each cell, its mean adhesion force determined on the smooth surface was normalized to 1.0 and its adhesion force on the etched surface was adjusted accordingly (non-normalized values are given in Fig. 3b and Fig. S5 in the ESI†). On the surface with 7 nm RMS roughness (yellow triangles in Fig. 3a), adhesion forces range from 80–130% of the forces recorded on the smooth surface with a mean value matching the adhesion force on the smooth surface. On the surface with 24 nm RMS roughness (orange squares in Fig. 3a), cells feature adhesion forces between 30% and 90% of the ones observed on the smooth surface with a mean value of 56(6)%.§ Adhesion forces on the roughest surface (red pentagons in Fig. 3a) vary between 25% and 60% of the forces recorded on the smooth surface. The mean value on the roughest surface is 38(4)% of the value determined on the smooth surface.

The results of the adhesion force measurements can be interpreted in such a way that the contact between a cell and a surface is mediated primarily by cell wall macromolecules tethering to the substrate[53,54] and thus the adhesive strength of a single cell is determined by the total number of such tethering macromolecules. A recent study indicated that these macromolecules in the *S. aureus* cell wall can extend by approximately 50 nm due to thermal fluctuations, a length hereinafter referred to as 'tether length'.[54] The value of 50 nm for the tether length is confirmed by the snap-in separations obtained from the force–displacement curves of our adhesion

experiments (for data, see Fig. S7 in the ESI†). Based on this, Fig. 4 a sketches our proposed molecular picture of bacterial adhesion to nanostructured surfaces: on the smooth silicon surface, a high number or even all surface macromolecules within a certain area, called the contact area,[50] tether to the surface, and thus adhesion is strongest. Then, with increasing roughness, more and more cell wall macromolecules can no longer reach the surface *via* thermal fluctuations resulting in a smaller number of tethered molecules. This means that the rougher the surface, the lower the bacterial adhesion force.

In other words, on the nanostructured surfaces, in a certain depth d of the sample (measured from the highest point downwards), only a certain fraction of the total area of the smooth surface is accessible by tethering molecules as visualized in Fig. 4b: for some depth values, *e.g.* d_1, the accessible surface area (blue line in Fig. 4b) is smaller than the area of a smooth wafer (green scan line in Fig. 4b). Then, at a certain depth (d_2) the accessible surface area is approximately equal to the area of a smooth wafer, while for larger depth values, *e.g.* d_3, the nanostructured substrate offers more surface area than a smooth wafer. These data are quantitatively shown in Fig. 4c: the accessible surface area of each nanostructured substrate is plotted as a function of the depth from the top of the surface, whereby the data are normalized to the surface area of a smooth wafer as explained in Fig. 4b.

These curves can be used to explain the adhesion forces on nanostructured substrates in a quantitative way: assuming that the primary reason for reduced adhesion is the reduced accessible surface area, for each curve, this ratio of surface areas equals the ratio of reduced adhesion forces from Fig. 3 (vertical rectangles in Fig. 4c). Thus, the latter can be associated with a corresponding depth that is accessible from the typical top of the surface, whose measurement is described in Fig. S8 in the ESI† (horizontal rectangles in Fig. 4c).

The plot shows that on the surface with 7 nm RMS roughness, after about 30 nm from top, the accessible surface area is already at 100% and all cell wall macromolecules (with an average tether length of 50 nm) responsible for adhesion can

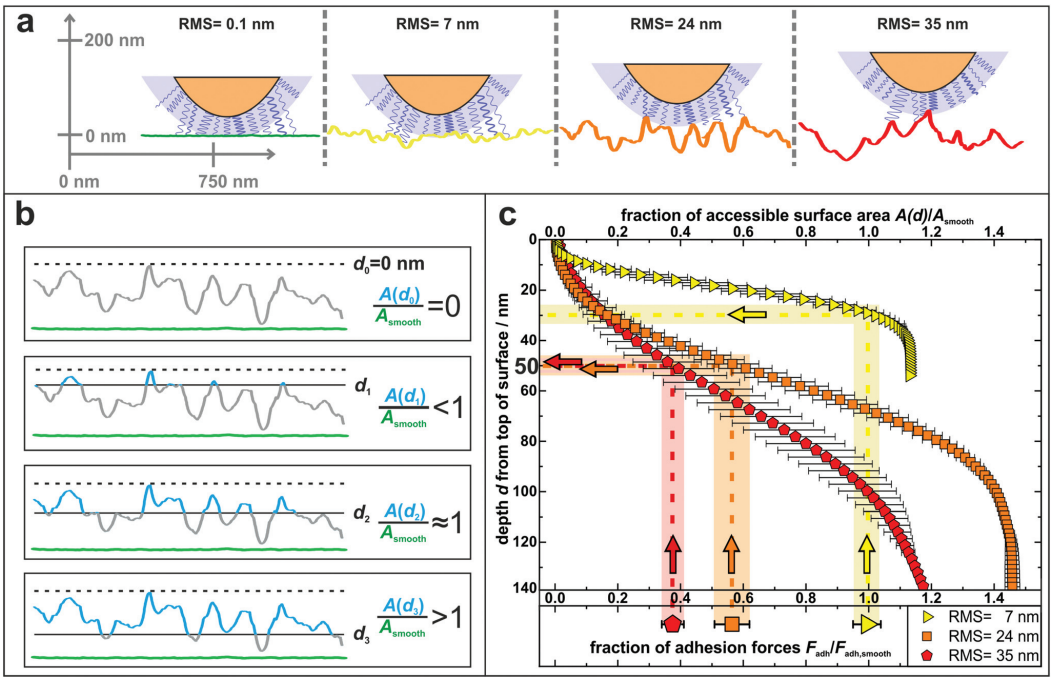

Fig. 4 (a) Sketch to illustrate the adhesion of *S. aureus* mediated by macromolecular tethering on different nanostructured surfaces: the bigger the surface structures, the lower is the number of macromolecules that are able to reach the substrate. Notably, only few molecules are drawn on the cell wall, whereas their density is in reality much higher, as symbolized by the blue shaded layer. All surfaces are represented by real AFM scan lines. (b) Visual explanation of the data shown in part c: accessible surface area (blue lines) of a nanostructured substrate compared to the surface area of a smooth substrate (green lines) for four exemplary depth values d_0–d_3. (c) Depth d from top of the surface and corresponding fraction of accessible surface area of all nanostructured substrates compared to the total surface area of a smooth substrate. The light-colored vertical rectangles show the relative decrease of adhesion forces on the nanostructured surfaces (the center line of each rectangle indicates the mean value of adhesion forces and the width corresponds to the error of the mean from Fig. 3). The horizontal rectangles indicate the corresponding depth in which this fraction of surface area is accessible.

View Article Online
Communication Nanoscale

reach the surface and, therefore, the adhesive strength is the same as on the smooth wafer. Some cells even show a stronger adhesion than on the smooth surface, which can be explained, besides by statistical fluctuations, by the fact that the total surface area on the nanostructured substrate is – for distances from the top greater than 30 nm – larger than on the smooth wafer. Hence, cell wall macromolecules with tether lengths of 50 nm can 'find' even more binding sites resulting in stronger adhesion.[59,60] For the surfaces with 24 nm and 35 nm RMS roughness, the ratios of surface areas that correspond to the reduced adhesion forces of 56(6)% and 38(4)% are both accessible in a depth of 45–55 nm. This depth perfectly matches the *S. aureus* tether length of 50 nm, a fact that strongly supports our hypothesis that the reason for reduced adhesion forces is primarily caused by the reduced accessible surface area.

The quantitative influence of surface roughness on the adhesion of *S. aureus* cells can probably be transferred to other (Gram-positive) bacteria (see Fig. S9 in the ESI† for experiments with *Staphylococcus carnosus*). However, it should be mentioned that the exact range of surface roughness that best prevents adhesion depends on the average tether length of the cell wall macromolecules and in part on the contact area. Both quantities may vary for different species. In addition, care should be taken when transferring our results to surfaces where other effects, such as surface deformations due to rather flexible structures (see Fig. S10 in the ESI†), may dominate the adhesive behaviour of bacteria. The same might be true for the bactericidal properties of our substrates which are described below.

Since other studies have reported bactericidal effects of surfaces with structures similar to those of our substrates,[61–64] it was of particular interest for us to determine the impact of the nano-topography on the viability of the cells used in our study. Therefore, we performed live/dead staining for some of the cells after adhesion measurements. In doing so, we also checked if there is a correlation between the measured adhesion of particular cells and their viability after the experiment. It shows that the fraction of dead cells increases with increasing size of surface structures: on the smooth silicon, none of the tested cells were killed. On the surfaces with 7 nm and 24 nm RMS roughness, one third of the tested cells were killed and on the roughest surface, two thirds of the tested cells were found dead after measurements. Interestingly, no correlation between the adhesion force (or the change in adhesion force) and the viability of the corresponding cell can be observed in adhesion force measurements (Fig. 3b). Accordingly, the characteristic shape of the force–distance curves did not change in the course of several measurements with cells that were found to be dead at the end of the experiment (Fig. 3c). Hence, it seems that, surprisingly, the viability of a cell does not influence its adhesive strength – at least not for the time scales (approximately one hour) and the conditions of our experiments and for the used surfaces.

In the literature, the bactericidal properties of structured surfaces are usually attributed to the penetration or intrusion and subsequent stretching of the bacterial cell wall by 'spiky' features on the substrate.[61–64] On the one hand, our experiments suggest that the size of these features on the roughest surface is generally most effective for killing because the fraction of dead cells is the largest on this substrates. On the other hand, cell death on a certain surface seems to depend on the particular cell respectively its locally varying cell wall properties at the contact area.[65] For some cells, the layer of cell wall molecules may be (locally) very dense and/or thick and therefore so 'strong' that it prevents the spiky structures from deeply intruding the cell wall. Other cells, in contrast, may have a less dense and/or thinner rather 'weak' macromolecular layer and can, therefore, be penetrated by the spiky structures. Interestingly, the adhesion force of an individual cell is not correlated to its viability after adhesion force measurement (see Fig. 3b). Therefore, we can conclude that a more 'robust' macromolecular layer is not necessarily a more 'adhesive' layer. Notably, we determined the viability only for a limited number of cells. Hence, to give a general statement about the bactericidal effect of our nanostructured surfaces, the number of these measurements should be increased and additional experiments (for example, in a flow chamber setup) should be performed.

Conclusions

In summary, we have shown that surface morphometry is quantitatively related to the strength of bacterial adhesion on surfaces with a nano-scaled topography. Our single-cell force spectroscopy measurements on etched silicon surfaces revealed that the adhesion force of *S. aureus* cells to nanostructured substrates decreases with increasing size of surface structures. The most important outcome is that a detailed characterization by Minkowski functionals allows a direct correlation between surface nanostructures and bacterial adhesion forces: since the adhesive strength is determined by the number of cell wall macromolecules tethering to the surface, the reduced accessible surface area on the nanostructured substrates for cell wall molecules with average tether lengths of 50 nm matches the reduced mean adhesion forces on the nano-topographies remarkably well. Quantifying the variances of tether lengths, surface areas and adhesion forces and determining whether they are also related to each other is an interesting question for future research.

In addition, we have shown that the nanostructure of our substrates influences the viability of bacteria after contact: similar to the adhesive strength, the percentage of viable cells on the nanostructured surfaces decreases with increasing surface roughness while the adhesive strength of individual cells is not influenced by their viability.

Our results can be of importance in industry and medicine since nanostructured surfaces are increasingly used in various applications (for example, as materials for bioreactors or prosthetics).[2,3] For scenarios, in which bacterial adhesion is unwanted, our results can provide suggestions regarding surface topography: while molecularly smooth surfaces or

those with structures larger than the cells display a favorable adhesion ground for bacteria, this property is markedly reduced on surfaces that feature structures in the same size range as the macromolecules of the bacterial cell wall. At the same time, this size range also seems to be effective for killing cells by contact with these structures. Furthermore, our study shows the strong potential of surface characterization using Minkowksi functionals since this method provides universal morphological information allowing, for example, a precise comparison of different surfaces.

Materials and methods

Silicon wafers

Silicon wafers in (100) orientation with a resistivity of 10–20 Ω cm were purchased from Siltronic (Burghausen, Germany). They feature a native silicon oxide layer with a thickness of 1.7(2) nm as determined by ellipsometry.[66] The wafers are by default polished to an RMS roughness of 0.09(2) nm as determined by AFM.[66]

Preparation of the nanostructured surfaces

In a first step, silicon surfaces were covered with a gold layer of a nominal film thickness of 2 nm which was determined with a quartz crystal microbalance by physical vapor deposition. As is known, this procedure does not result in a continuous gold film, but in gold clusters of sub-micron size.[52] Subsequently, following a recipe by Koynov *et al.*,[51] the gold-covered silicon was etched by immersing the wafers in a mixture of fluoric acid (HF, 40%), hydrogen peroxide (H_2O_2, 35%) and water for 90 s, 180 s and 360 s, respectively. Residues from the etching solution were removed by extensively rinsing the etched wafers in ultra-pure water. After etching, the gold clusters were removed by immersing the wafers in aqua regia (1 : 3 mixture of HNO_3 (65%) and HCl (37%)) for 25 min. Afterwards, the wafers were rinsed again with ultra-pure water to remove possible leftovers of the acid. X-ray photoelectron spectroscopy (XPS) confirmed that no gold was present on the surface after this treatment (an XPS overview spectrum is given in Fig. S1a†). To render the wafers hydrophobic, they were covered with a self-assembling monolayer of silanes according to a standard recipe.[55] Right before every set of experiments with bacteria, all surfaces were cleaned in ultrasonic baths of ethanol and acetone for 3 min each. After cleaning, the surfaces were dried under a stream of pure nitrogen.

Bacteria

For this study, cells of the *S. aureus* strain SA113 were used. Bacteria from a deep-frozen stock solution were grown on a blood agar plate for 2.5 days at 37 °C. Such a plate was used for two weeks at the maximum. For the experiments, one colony from the plate was transferred into 5 ml of sterile tryptic soy broth (TSB) and cultured for 16 h at 37 °C under agitation (150 rpm). From this culture, 40 μl were transferred into 4 ml of fresh TSB and cultured once more for 2.5 h at 37 °C and 150 rpm. Finally, 1 ml was taken from this culture and washed three times by centrifuging for 3 min at 17 000*g*, replacing the supernatant by 1 ml of fresh phosphate buffered saline (PBS, pH 7.3) and thoroughly vortexing. This procedure results in a bacterial suspension with an optical density at 600 nm (OD_{600}) of 0.2–0.3.

Viability measurements

To check the viability of the cells, the BacLight assay purchased from Molecular Probes, Eugene, USA was used. It consists of Syto 9 and propidium iodide. After excitation, the Syto 9 stain emits green light when bound to nucleic acids in bacteria. In contrast, propidium iodide, which can only enter the porous cell wall of dead bacterial cells, emits red light and causes a reduction of the binding between the Syto 9 stain and the bacterial nucleic acids. Hence, after staining a bacterial solution with the BacLight mixture and illuminating it with white light, viable cells glow green and dead cells red. After adhesion measurements, we placed the used cantilever including the immobilized cell in a drop (1 ml) of the staining assay. To achieve best results, the stain was left to act on the cell for 10 min in the dark. Thereafter, its residues were removed by carefully replacing the drop by fresh PBS for three times. Care was taken that the cantilever with the cell never was completely dry. Then, the cell on the cantilever was observed by fluorescence microscopy.

Force–distance measurements

We recorded force–distance curves on a Bioscope Catalyst (Bruker-Nano, Santa Barbara, USA) with single viable bacterial cells immobilized on a tipless cantilever (MLCT-0, Bruker-Nano) with nominal spring constants of 0.01 N m^{-1} and 0.3 N m^{-1}. A detailed description of how the cells were attached to the cantilevers can be found in the paper by Thewes *et al.*,[67] in short: tipless cantilevers were cleaned in an air-plasma and afterwards covered with a thin layer of dopamine by immersing them in a solution of 4 mg ml^{-1} dopamine hydrochloride in TRIS/HCL-buffer for one hour. The cantilevers were then cleaned in ultrapure water and dried in a clean room environment. The cantilevers' spring constant and deflection sensitivity were calibrated before each set of measurements. To pick up a single cell, a very dilute bacterial suspension was placed on a Petri dish that was observed with an inverse optical microscope equipped with a micromanipulator. The calibrated cantilever is then connected to the micromanipulator and approached from above to the sedimented bacterial cells in the Petri dish. In a final step, the cantilever is carefully lowered onto a single cell and gently pressed onto it so that the cell adheres to the cantilever. This bacterial probe is afterwards carefully inserted in the microscope without drying out the cell.

For every force–distance curve, the approach and retraction distance was 800 nm with a retraction velocity of 800 nm s^{-1}. The force trigger, *i.e.* the force with which the cell is pressed onto the surface, was set to 300 pN which does hardly deform the cell or change its contact area[50,68] (for a more detailed dis-

cussion of the chosen force trigger, see the ESI†). Curves were recorded with 0 s surface delay time which corresponds to a 'real' contact time below 0.5 s.[53,58] For each individual cell, 100 force–distance curves were recorded on the smooth as well as on a nanostructured surface in a rectangular pattern with a distance of 1 μm between each curve. To exclude that probing the smooth/nanostructured surfaces might alter the adhesive behaviour of the bacterial cell, the first 50 curves were recorded on the smooth surface and the next 50 were recorded on the nanostructured surface. Then, again, the smooth surface and afterwards the nanostructured surface was probed by 50 curves each. By comparing the adhesion of each set of curves on the smooth/nanostructured surface, it was ensured that the adhesion behavior was not changed during the recording of several force–distance curves on the different surfaces (as it was also seen before on smooth silicon[53,68]).

AFM surface topography measurements

The surface topography was measured in tapping mode with an Icon FastscanBio (Bruker-Nano, Santa Barbara, USA) in air using high aspect ratio tips (HAR1-200-10, Bruker-Nano) with a nominal spring constant of 42 N m^{-1} in soft tapping mode with an image resolution of 1024 × 1024 pixels. The scan area was 1 μm × 1 μm for the 90 s and 180 s etched substrates. The 360 s etched surface fluctuates strongly and so do its geometrical properties. To reduce the statistical error, we scanned a larger observation window of 3 μm × 3 μm. Systematic effects of the lower physical resolution on the total surface area should be less than 3%, as estimated from the other surface when we artificially reduced the resolution. The resolution in *z*-direction was below 0.5 nm. From these images, the AFM tip shape was determined and the real surface was reconstructed by deconvoluting the recorded image and the tip geometry using the software Gwyddion. For every type of surface, several AFM images were recorded and analyzed, providing average values and standard deviations for RMS roughnesses and Minkowski functionals.

Minkowski analysis

The level sets of the AFM images and their three-dimensional triangulations were analyzed using Minkowski functionals. In the latter case, the triangulation was constructed using the 'Advancing Front Surface Reconstruction' from CGAL.[56] Using the 3D Minkowski software Karambola,[47] the surface area was computed as a function of the height. More precisely, as a function of the difference in height to the maximal peak within the observation window, the surface area was computed for all those triangles whose lowest vertex was above this threshold. In the first case, the AFM images were converted into pixelated gray scale maps and then into black-and-white images *via* thresholding. A pixel whose height is above a threshold h turns white, all others become black. The three two-dimensional Minkowski functionals of the white domains were then computed as a function of the threshold height h using the software Papaya.[46] To reduce the pixelization errors, a standard marching square algorithm was applied.[45] Edge effects from the observation window were avoided by using minus-sampling boundary conditions (the outermost pixels were used for the boundary conditions). To avoid dependencies on lateral dimensions of the AFM scans so-called densities of Minkowski functionals are used, *i.e.* the functionals are rescaled by the size of the observation window.

Electronmicroscopy measurements

For the scanning electron microscopy (SEM) measurements, a FEI (Hilsboro, USA) Quanta 400 FEG SEM in high vacuum mode was used. Secondary electron images were collected at 10 kV and 15 kV accelerating voltage under different tilting angles.

Author contributions

C.S., N.T., M.B., K.J. designed research. C.S., F.N., J.M. performed AFM and viability measurements. S.G., F.M. performed XPS measurements. M.K. performed REM measurements. M.A.K. performed Minkowski analyses. C.S., F.N., J.M., T.F., S.G., F.M., M.A.K. analyzed data. C.S., M.B., M.A.K., K.J. wrote the manuscript with the help of all other authors.

Conflicts of interest

There are no conflicts to declare.

Acknowledgements

The authors thank Günter Marchand (Mitranz Mikrotechnologie-Transferzentrum, Saarland University) for etching the substrates. Work was funded by the German Research Foundation (DFG) within the framework of the Collaborative Research Center SFB 1027 (project B2). M. A. K. acknowledges support of the DFG through the research group 'Geometry and Physics of Spatial Random Systems' (GPSRS) under grants number HU1874/3-2, and LA965/6-2.

Notes and references

§ Values in brackets indicate the standard error of the mean.

1 J. W. Costerton and L. Montanaro, *Int. J. Artif. Organs*, 2007, **30**, 757–763.
2 D. Neut, H. C. van der Mei, S. K. Bulstra and H. J. Busscher, *Acta Orthop.*, 2007, **78**, 299–308.
3 J. A. Callow and M. E. Callow, *Nat. Commun.*, 2011, **2**, 244.
4 O. Lieleg, M. Caldara, R. Baumgärtel and K. Ribbeck, *Soft Matter*, 2011, **7**, 3307–3314.
5 C. S. Laspidou, L. A. Spyrou and N. Aravas, *Math. Biosci.*, 2014, **251**, 11–15.
6 K. Anselme, P. Davidson, A. M. Popa, M. Giazzon, M. Liley and L. Ploux, *Acta Biomater.*, 2010, **6**, 3824–3846.

7 L. Rizzello, B. Sorce, S. Sabella, G. Vecchio, A. Galeone, V. Brunetti, R. Cingolani and P. P. Pompa, *ACS Nano*, 2011, **5**, 1865–1876.
8 Y. Lu, S. Sathasivam, J. Song, C. R. Crick, C. J. Carmalt and I. P. Parkin, *Science*, 2015, **347**, 1132–1135.
9 D. P. Linklater, M. De Volder, V. A. Baulin, M. Werner, S. Jessl, M. Golozar, L. Maggini, S. Rubanov, E. Hanssen, S. Juodkazis and E. P. Ivanova, *ACS Nano*, 2018, **12**, 6657–6667.
10 J. Li, K. Zhang, L. Ruan, S. F. Chin, N. Wickramasinghe, H. Liu, V. Ravikumar, J. Ren, H. Duan, L. Yang, *et al.*, *Nano Lett.*, 2018, **18**, 4180–4187.
11 E. P. Ivanova, V. K. Truong, J. Y. Wang and C. C. Berndt, *Langmuir*, 2010, **26**, 1973–1982.
12 V. K. Truong, S. Rundell, R. Lapovok and Y. Estrin, *Appl. Microbiol. Biotechnol.*, 2009, **83**, 925–937.
13 S. H. Flint, J. D. Brooks and P. J. Bremer, *J. Food Eng.*, 2000, **43**, 235–242.
14 L. C. Hsu, J. Fang and D. A. Borca, *Appl. Environ. Microbiol.*, 2013, **79**, 2703.
15 S. D. Puckett, E. Taylor, T. Raimondo and T. J. Webster, *Biomaterials*, 2010, **31**, 706–713.
16 S. Kang and M. Elimelech, *Langmuir*, 2009, **25**, 9656–9659.
17 S. El-Kirat-Chatel, A. Beaussart, C. D. Boyd, G. A. O'Toole and Y. F. Dufrêne, *ACS Chem. Biol.*, 2013, **9**, 485–494.
18 A. Beaussart, S. El-Kirat-Chatel, P. Herman, D. Alsteens, J. Mahillon, P. Hols and Y. F. Dufrêne, *Biophys. J.*, 2013, **104**, 1886–1892.
19 A. Beaussart, S. El-Kirat-Chatel, R. M. A. Sullan, D. Alsteens, P. Herman, S. Derclaye and Y. F. Dufrêne, *Nat. Protoc.*, 2014, **9**, 1049.
20 A. Beaussart, M. Abellán-Flos, S. El-Kirat-Chatel, S. P. Vincent and Y. F. Dufrêne, *Nano Lett.*, 2016, **16**, 1299–1307.
21 C. Formosa-Dague, C. Feuillie, A. Beaussart, S. Derclaye, S. Kucharíková, I. Lasa, P. Van Dijck and Y. F. Dufrêne, *ACS Nano*, 2016, **10**, 3443–3452.
22 C. Formosa-Dague, Z.-H. Fu, C. Feuillie, S. Derclaye, T. J. Foster, J. A. Geoghegan and Y. F. Dufrêne, *Nanoscale Horiz.*, 2016, **1**, 298–303.
23 C. Spengler, N. Thewes, F. Nolle, T. Faidt, N. Umanskaya, M. Hannig, M. Bischoff and K. Jacobs, *J. Mol. Recognit.*, 2017, **30**, e2615.
24 Y. F. Dufrêne, *ACS Nano*, 2017, **11**, 19–22.
25 T. D. Becke, S. Ness, R. Gürster, A. F. Schilling, A.-M. di Guilmi, S. Sudhop, M. Hilleringmann and H. Clausen-Schaumann, *ACS Nano*, 2018, **12**, 549–558.
26 C. Feuillie, C. Valotteau, L. Makart, A. Gillis, J. Mahillon and Y. F. Dufrêne, *Nano Lett.*, 2018, **18**, 5821–5826.
27 T. R. Scheuerman, A. K. Camper and M. A. Hamilton, *J. Colloid Interface Sci.*, 1998, **208**, 23–33.
28 A. I. Hochbaum and J. Aizenberg, *Nano Lett.*, 2010, **10**, 3717–3721.
29 C. Díaz, P. L. Schilardi and R. C. Salvarezza, *Langmuir*, 2007, **23**, 11206–11210.
30 D. Perera-Costa, J. M. Bruque, M. L. González-Martín, A. C. Gómez-García and V. Vadillo-Rodríguez, *Langmuir*, 2014, **30**, 4633–4641.
31 N. Lu, W. Zhang, Y. Weng, X. Chen, Y. Cheng and P. Zhou, *Food Control*, 2016, **68**, 344–351.
32 K. K. Sakimoto, C. Liu, J. Lim and P. Yang, *Nano Lett.*, 2014, **14**, 5471–5476.
33 Y. Wu, J. P. Zitelli, K. S. TenHuisen, X. Yu and M. R. Libera, *Biomaterials*, 2011, **32**, 951–960.
34 V. K. Truong, V. Pham and A. Medvedev, *Appl. Microbiol. Biotechnol.*, 2015, **99**, 6831–6840.
35 E. P. Ivanova, V. K. Truong, H. K. Webb and V. A. Baulin, *Sci. Rep.*, 2011, **1**, 165.
36 A. V. Singh, V. Vyas, R. Patil, V. Sharma and P. E. Scopelliti, *PLoS One*, 2011, **6**, e25029.
37 E. Gadelmawla, M. Koura, T. Maksoud, I. Elewa and H. Soliman, *J. Mater. Process. Technol.*, 2002, **123**, 133–145.
38 R. J. Crawford, H. K. Webb, V. K. Truong, J. Hasan and E. P. Ivanova, *Adv. Colloid Interface Sci.*, 2012, **179**, 142–149.
39 G. E. Schröder-Turk, W. Mickel, S. C. Kapfer, M. A. Klatt, F. M. Schaller, M. J. F. Hoffmann, N. Kleppmann, P. Armstrong, A. Inayat, D. Hug, M. Reichelsdorfer, W. Peukert, W. Schwieger and K. Mecke, *Adv. Mater.*, 2011, **23**, 2535–2553.
40 R. Schneider and W. Weil, *Stochastic and Integral Geometry (Probability and Its Applications)*, Springer, Berlin, 2008.
41 H. Hadwiger, *Vorlesungen über Inhalt, Oberfläche und Isoperimetrie*, Springer, Berlin, 1957.
42 M. A. Klatt, G. E. Schröder-Turk and K. Mecke, *Med. Phys.*, 2017, **44**, 3663–3675.
43 K. Mecke, *Int. J. Mod. Phys. B*, 1998, **12**, 861–899.
44 K. Jacobs, R. Seemann and K. Mecke, *Statistical Physics and Spatial Statistics*, Springer, 2000, 72–91.
45 H. Mantz, K. Jacobs and K. Mecke, *J. Stat. Mech.: Theory Exp.*, 2008, **12**, P12015.
46 G. E. Schröder-Turk, S. Kapfer, B. Breidenbach, C. Beisbart and K. Mecke, *J. Microsc.*, 2010, **238**, 57–74.
47 G. E. Schröder-Turk, W. Mickel, S. C. Kapfer, F. M. Schaller, B. Breidenbach, D. Hug and K. Mecke, *New J. Phys.*, 2013, **15**, 083028.
48 D. Göring, M. A. Klatt, C. Stegmann and K. Mecke, *Astron. Astrophys.*, 2013, **555**, A38.
49 F. D. Lowy, *N. Engl. J. Med.*, 1998, **339**, 520–532.
50 C. Spengler, N. Thewes, P. Jung, M. Bischoff and K. Jacobs, *Nanoscale*, 2017, **9**, 10084–10093.
51 S. Koynov, M. S. Brandt and M. Stutzmann, *Appl. Phys. Lett.*, 2006, **88**, 203107.
52 I. Doron-Mor, Z. Barkay, N. Filip-Granit, A. Vaskevich and I. Rubinstein, *Chem. Mater.*, 2004, **16**, 3476–3483.
53 N. Thewes, P. Loskill, P. Jung, H. Peisker, M. Bischoff, M. Herrmann and K. Jacobs, *Beilstein J. Nanotechnol.*, 2014, **5**, 1501–1512.
54 N. Thewes, A. Thewes, P. Loskill, H. Peisker, M. Bischoff, M. Herrmann, L. Santen and K. Jacobs, *Soft Matter*, 2015, **11**, 8913–8919.

55 M. Lessel, O. Bäumchen, M. Klos, H. Hähl, R. Fetzer, M. Paulus, R. Seemann and K. Jacobs, *Surf. Interface Anal.*, 2015, **47**, 557–564.
56 T. K. F. Da and D. Cohen-Steiner, *CGAL User and Reference Manual*, CGAL Editorial Board, 4.12 edn, 2018.
57 P. Loskill, H. Hähl, N. Thewes, C. T. Kreis, M. Bischoff, M. Herrmann and K. Jacobs, *Langmuir*, 2012, **28**, 7242–7248.
58 A. Beaussart, P. Herman and S. El, *Nanoscale*, 2013, **5**, 10894–10900.
59 R. D. Boyd, J. Verran, M. V. Jones and M. Bhakoo, *Langmuir*, 2002, **18**, 2343–2346.
60 K. A. Whitehead, D. Rogers, J. Colligon, C. Wright and J. Verran, *Colloids Surf., B*, 2006, **51**, 44–53.
61 E. P. Ivanova, J. Hasan, H. K. Webb and V. K. Truong, *Small*, 2012, **8**, 2489–2494.
62 E. P. Ivanova, J. Hasan, H. K. Webb, G. Gervinskas, S. Juodkazis, V. K. Truong, A. H. Wu, R. N. Lamb, V. A. Baulin, G. S. Watson, J. A. Watson, D. E. Mainwaring and R. J. Crawford, *Nat. Commun.*, 2013, **4**, 2838.
63 S. Pogodin, J. Hasan, V. A. Baulin, H. K. Webb and V. K. Truong, *Biophys. J.*, 2013, **104**, 835–840.
64 C. M. Bhadra, V. K. Truong, V. Pham and M. Al Kobaisi, *Sci. Rep.*, 2015, **5**, 16817.
65 J. M. Monteiro, P. B. Fernandes, F. Vaz, A. R. Pereira, A. C. Tavares, M. T. Ferreira, P. M. Pereira, H. Veiga, E. Kuru, M. S. VanNieuwenhze, *et al.*, *Nat. Commun.*, 2015, **6**, 8055.
66 M. Bellion, L. Santen, H. Mantz, H. Hähl, A. Quinn, A. Nagel, C. Gilow, C. Weitenberg and Y. Schmitt, *J. Phys.: Condens. Matter*, 2008, **20**, 404226.
67 N. Thewes, P. Loskill, C. Spengler, S. Hümbert, M. Bischoff and K. Jacobs, *Eur. Phys. J. E: Soft Matter Biol. Phys.*, 2015, **38**, 140.
68 P. Loskill, P. M. Pereira, P. Jung, M. Bischoff, M. Herrmann, M. G. Pinho and K. Jacobs, *Biophys. J.*, 2014, **107**, 1082–1089.

Electronic Supplementary Material (ESI) for Nanoscale.

SUPPORTING INFORMATION FOR: 'Strength of bacterial adhesion on nanostructured surfaces quantified by substrate morphometry'

Christian Spengler,[a] Friederike Nolle,[a] Johannes Mischo,[a] Thomas Faidt,[a] Samuel Grandthyll,[a] Nicolas Thewes,[a] Marcus Koch,[b] Frank Müller,[a] Markus Bischoff,[c] Michael A. Klatt,[d‡] and Karin Jacobs[a]

[a] Department of Experimental Physics, Saarland University, Campus E2 9, 66123 Saarbrücken, Germany. Fax: +49 (0)681 302 71700; Tel: +49 (0)681 302 71777; E-mail: k.jacobs@physik.uni-saarland.de
[b] INM – Leibniz Institute for New Materials, Campus D2 2, 66123 Saarbrücken, Germany.
[c] Institute of Medical Microbiology and Hygiene, Saarland University, 66421 Homburg/Saar, Germany.
[d] Institute of Stochastics, Karlsruhe Institute of Technology, 76131 Karlsruhe, Germany.
‡ Present address: Department of Physics, Princeton University, Jadwin Hall, Princeton, NJ 08544-0001, USA

XPS Spectrum of a Nanostructured Silicon Surface

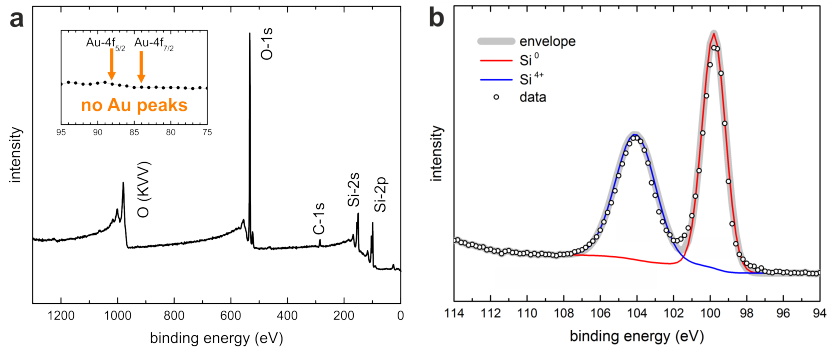

Fig. S1 a) Survey spectrum of a nanostructured surface after cleaning with aqua regia: since there are no Au peaks detectable at energies of about 84 eV and 88 eV (see inset), the gold layer was completely removed by the acid. b) XPS Si-2p data (open circles) of a nanostructured surface (270 s in fluoric acid). The Si^0 line is shown in red (please note that the Si-2p spin orbit splitting is not resolved) and the Si^{4+} line is shown in blue. The ratio of their intensities is used to calculate the oxide layer thickness [1].

Figure S1 shows the XPS data of the Si-2p core level of a (exemplary) nanostructured substrate with both peaks assigned to Si^0 contributions from the bulk and Si^{4+} contributions from the oxide layer. When comparing the intensities of both contributions it is straightforward to estimate the thickness of the oxide layer to be 3.2–4.0 nm. However, it has to be noted that these values have to be considered as an upper limit, since the Si^{4+} contribution is overestimated in the experiment on a nanostructured surface. Due to the high surface sensitivity in XPS, only a thickness of about 1–2 nm is probed and the surface sensitivity increases with increasing the polar angle (i. e. the angle between the surface normal and the direction of the emission of the photoelectrons). For a nanostructured surface, the surface normals of local surface areas

are distributed over a wide range (if compared to a smooth Si wafer) and, therefore, a large part of the overall surface is probed with enhanced surface sensitivity, causing an increased Si^{4+} contribution.

As a consequence, the thickness of the oxide layer of about 3.2–4.0 nm, as probed in experiments on a nanostructured surface, does not really differ from the thickness of about 1.7 nm[1], as probed in experiments on a smooth Si wafer and it is not expected that bacterial adhesion is much affected by the difference in the thickness of the oxide layer[2].

Quality of the Silanization

Table S1 shows water contact angles and hysteresis on the silanized nanostructured surfaces. Compared to the smooth samples (where we know from previous experiments that the silane monolayer is dense and homogeneous[3]), on all nanostructured surfaces, the advancing contact angle as well as the contact angle hysteresis increases. This is in accordance with the literature for structured hydrophobic surfaces[3,4].

Table S1 Advancing water contact angle and hysteresis for all surfaces. The numbers in brackets give the error from three measurements each.

RMS roughness	0.1 nm	7 nm	24 nm	35 nm
Advancing CA	111(1)°	154(2)°	153(3)°	158(2)°
Hysteresis	4(2)°	43(3)°	32(1)°	21(2)°

In addition, the nanostructured surfaces were scanned under water with a hydrophobized AFM tip ('Scanasyst-fluid+' by Bruker) in quantitative nanomechanical mapping (QNM) mode. Fig. S2 shows an overlay of the 3D structure of the topography and the adhesion force between tip and surface for a silanized silicon surface with 7 nm RMS roughness and a PDMS surface that was produced by mold casting the silicon substrate (see page 9 for more details). For both samples, the images are very similar in absolute values of adhesion as well as in the distribution of larger and weaker adhesion sites: significant adhesion (> 1 nN) is visible on every point of the surfaces. Adhesion on both samples is the strongest in the valleys of the surfaces for geometrical reasons, i. e. due to the enlarged interaction area between tip and valley[5]. Since the PDMS substrate has a homogeneous surface chemistry, one would expect a patchy adhesion response of the silanized sample (either around the valleys or around the tips or shoulders) if the silanization was not homogeneous. Hence, we deduce from both experiments (contact angle and adhesion measurements) that the silanization is homogeneous.

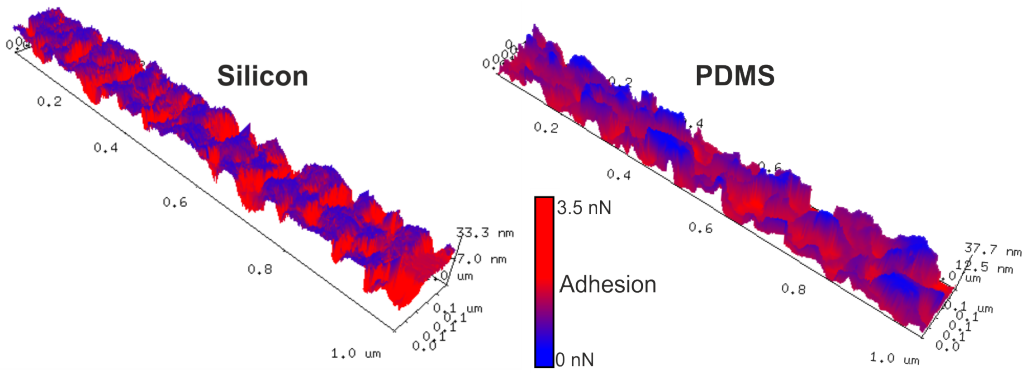

Fig. S2 Overlay of height data (geometry) and adhesion forces (color) between a hydrophobized tip and the surfaces of a silanized silicon and a PDMS surface with 7 nm RMS roughness. (Note, that the high aspect ratio tips needed to scan the rougher surfaces are not hydrophobic and, therefore, only the surface with the lowest RMS value was scanned as an example.)

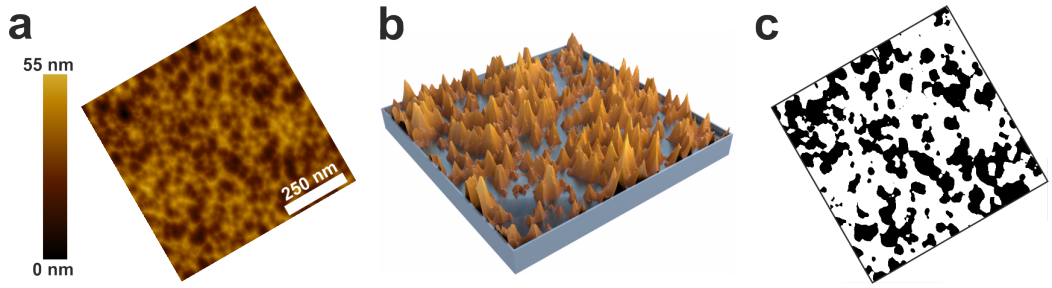

Fig. S3 a) Top view of a deconvoluted (and rotated) AFM image of the nanostructured surface. b) Three dimensional view of the surface from (a) 'filled' with water to a certain threshold height h_t. c) Corresponding black-and-white representation of the image from (a) and threshold height h_t.

Exemplary Visualization of the Minkowski Functionals

For the Minkowski analysis, the AFM images are converted to several different black-and-white images. This conversion is illustrated in Fig. S3 for one exemplary threshold height: the three dimensional structure of the surface is 'filled' from the bottom with water until a certain level (i. e. the threshold height) is reached. Then, each part of the surface above the water level is converted to white and each part below the water level to black, which results in the image shown in Fig. S3 c.

The way in which the Minkwoski measures are obtained from the black-and-white images is shown in Fig. S4 for three exemplary threshold heights: to obtain the Euler characteristic of a certain image, the number of white (black) unconnected regions of the image is counted positively (negatively), represented by the small numbers in Fig. S4 a. The second and third Minkowski measure are the perimeter of the black and the area of the white regions, as indicated by the red lines and green areas in Fig. S4 b and c. Performing this analysis for all threshold heights and plotting the three Minkowski measures in dependence of each threshold height, the graph shown in Fig. S4 d is obtained, which contains the complete additive shape information of the surface.

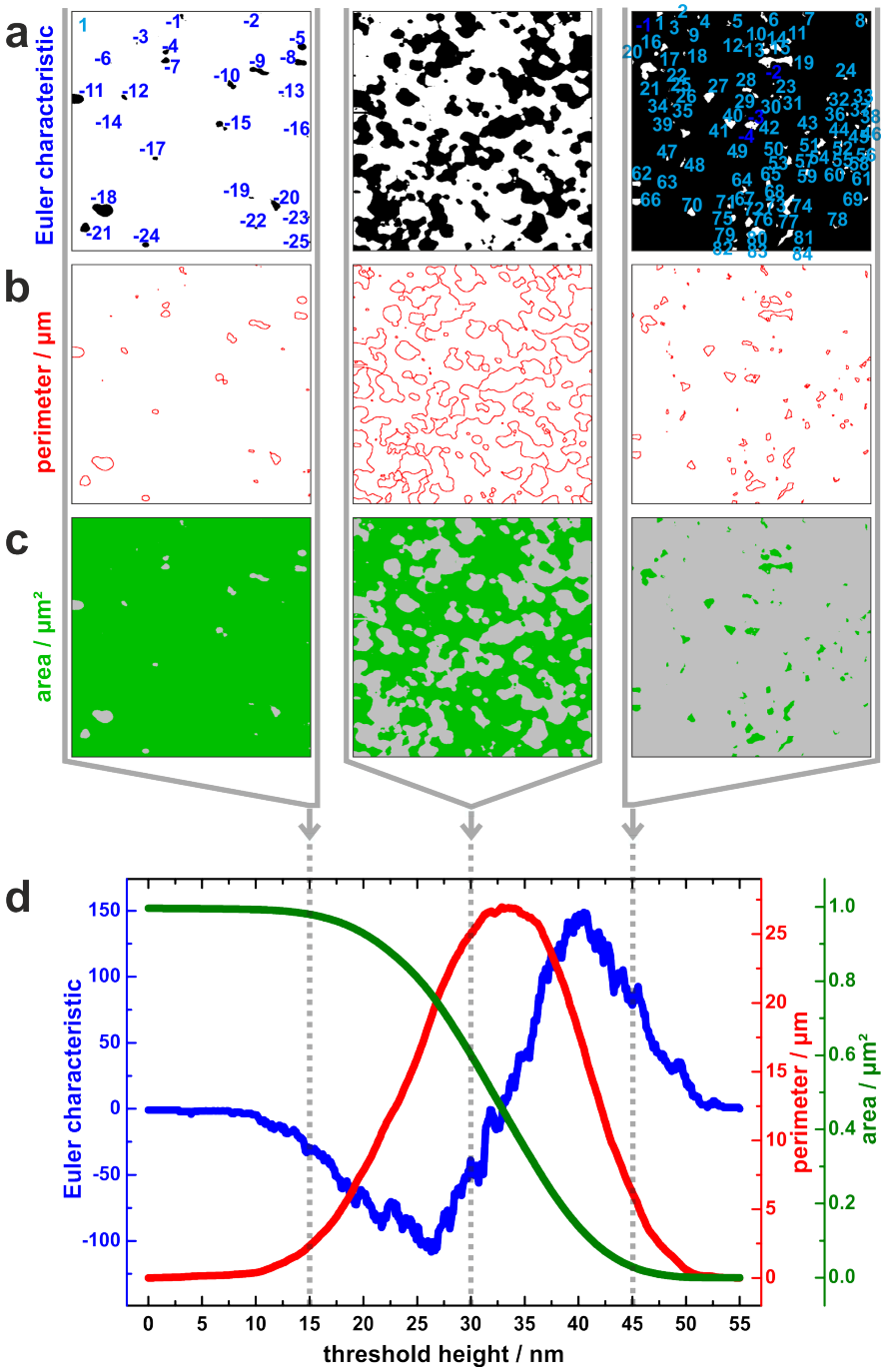

Fig. S4 Visualization of the Minkowski functionals for an AFM topography scan of an etched Si wafer (7 nm RMS roughness) for three different threshold heights (15 nm, 30 nm, 45 nm). (In the middle panel of the Euler characteristic, no numbers are given for reasons of clarity.)

Not Normalized Minkowski Functionals of the Nanostructured Surfaces

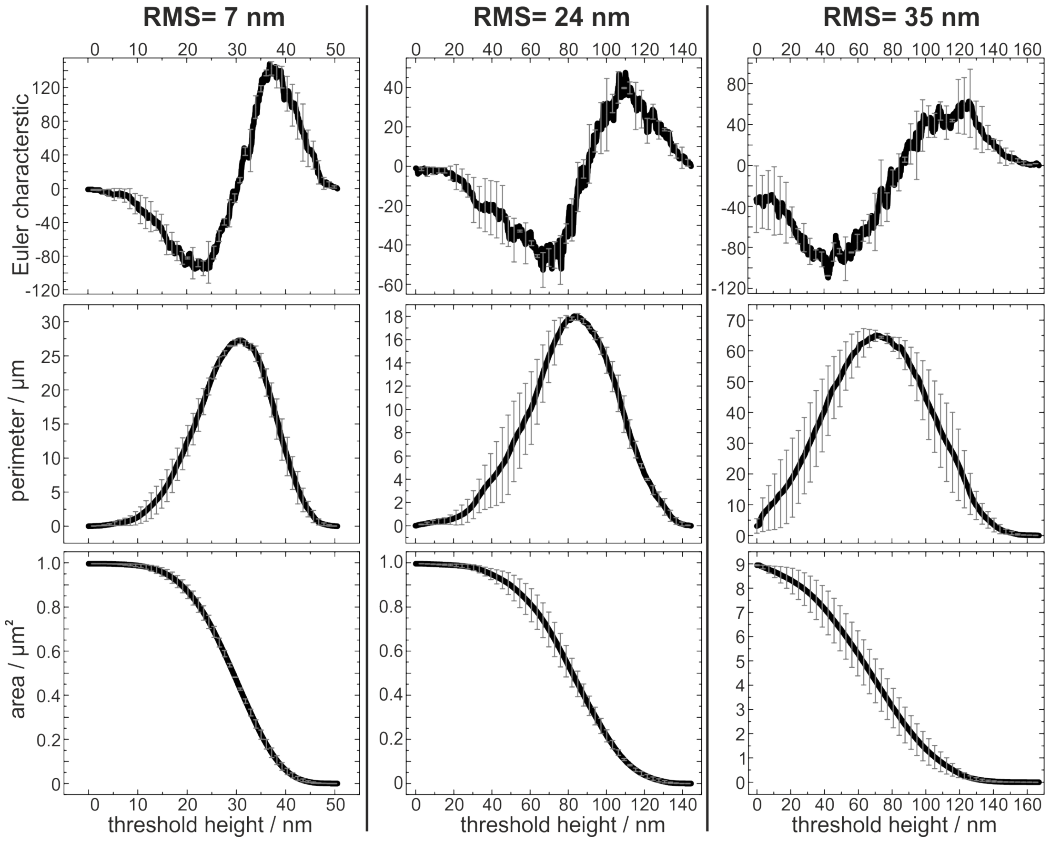

Fig. S5 Minkowski functionals in dependence of the threshold height for all surfaces (averaged over different surfaces of the same etching time). For the surfaces with RMS values of 7 nm and 24 nm the scan size was 1 μm^2 while it was 9 μm^2 for the surface with an RMS value of 35 nm.

Reason for the Force Trigger of 300 pN

The concept of this work is to study bacterial adhesion under conditions as close as possible to the natural situation where they adsorb and attach 'freely' from a planktonic state. Hence, the 'real energies' that drive bacteria to a surface are in the range of a few *kT*, i. e. it is our experimental setup to apply as low forces as possible by the AFM cantilever. 300 pN were used as the maximum force with which the cells were 'pressed' onto the surfaces since lower forces were not applicable in the used setup. The question arises at which applied force the bacterium deforms. In this case, the applied force must overcome the turgor pressure of the cell. In another study, we were exactly probing this and found that changes in turgor pressure of *S. aureus* (initiated by adding salt) were not detected using a maximum applied force of 1 000 pN, yet were observable at 5 000 pN[6,7]. To see changes of the contact area of the bacteria on smooth surfaces, one also must press relatively hard: as we were able to show on *S. aureus* in another study[6,8], using up to 3 000 pN, the contact area remains unchanged, and it needs at least 30 000 pN to see changes of the contact area radius of 10–20 %. In other words, to probe the influence of higher applied forces, these forces must be orders of magnitude higher and are far away from the situation 'as close as possible to nature', that we want to study. Moreover, probing the penetration depth using higher forces, is risky since the cell wall can rupture[7] and is therefore beyond the scope of the present study.

Not Normalized Adhesion Forces on Nanostructured Hydrophobic Silicon

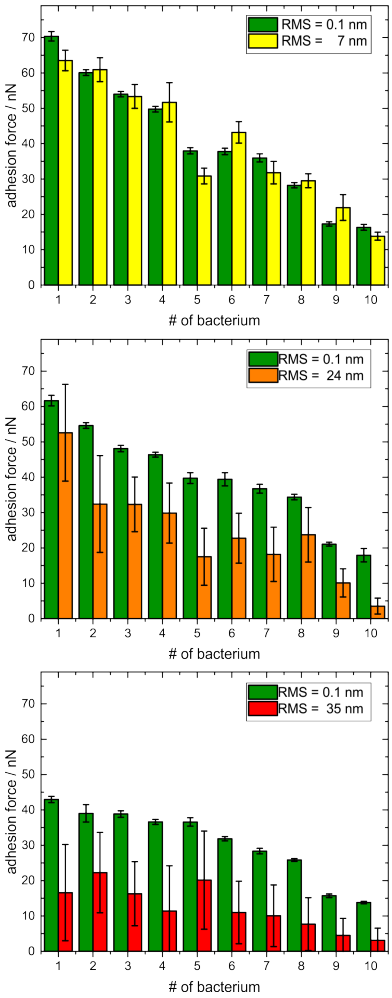

Fig. S6 Adhesion forces of 3×10 *S. aureus* cells to hydrophobic silicon of different roughness. With each cell, 200 force-distance curves were taken: first 50 force-distance curves on the smoothest surface, then 50 on one of the nanostructured surfaces, then again 50 curves on the smooth surface, and again 50 curve on the nanostructured surface. The forces on the smooth and nanostructured surfaces are shown as green and yellow/orange/red bars, respectively.

Tether Lengths of the Cells Used in Adhesion Experiments

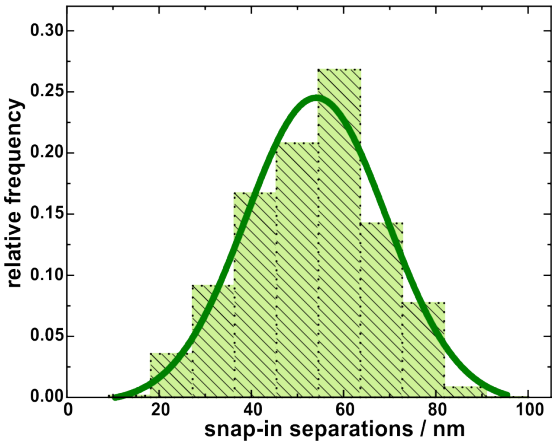

Fig. S7 Histogram (and Gaussian fit) of the snap-in separations determined from all force-distance curves of the adhesion measurements on the smooth hydrophobic silicon surface. The mean tether length of the 30 used cells is 53(3) nm. (The value in brackets gives the standard error of the mean.)

Correction of the 'Depth'-axis

For the x-axis in Fig. S8 (and the corresponding axis in Fig. 4 c in the main manuscript) the following must be considered: for all three substrates, the curves of the real surface area feature a 'flat' part at their beginning. For the surface with 7 nm RMS roughness, this part is very short (few nm) while it is rather long for the surface with 35 nm RMS roughness (several tens of nm). The reason for these flat parts of the curves is the fact that the top of all surfaces consist of very steep 'peaks'. The size and number of these peaks vary greatly for the different surfaces (e. g., the top 30 nm of the surface with 35 nm RMS roughness consist of 3 peaks/μm^2 while they consist of 57 peaks/μm^2 for the surface with 24 nm RMS roughness). Given the average radii of the contact area of *S. aureus* cells of about 150–300 nm[8], and since these peaks are distributed over the entire surface, an *S. aureus* cell approaching the substrate from above will not necessarily come in contact with these high structures, but only reaches the surface at lower height values. We call the average value of these heights 'mean surface top height' and have determined it numerically, as described in the next paragraph.

Thereto, we randomly positioned a large number of circles (here: 10,000) all with a radius of 250 nm (the average contact area radius for *S. aureus*[8]) on the images of the nanostructured surfaces and determined the height at which these circles first come into contact to the surface from above, i. e. the highest point inside each circle. The average of these values for all circles and each set of surfaces give the 'mean surface top height' for all sample sets. The distances of these heights from the absolute top heights are 34 nm, 6 nm and 2 nm for the surfaces with RMS roughnesses of 35 nm, 24 nm and 7 nm, respectively. Thus, the x-axis for each curve in Fig. S8 a can be corrected by shifting it in positive direction by the calculated distances. This way, we obtain the 'typical distance from top' for each surface (colored x-axes in Fig. S8). Instead of shifting the axes, also each data set can be shifted in negative x-direction by the corresponding mean surface top height (Fig. S8 b). Thereby, averaging the axis and shifting by the mean surface top height afterwards (as described above) gave the same curves as the inverse order, i. e. that for every circle mentioned above a curve with the corresponding x-axis was calculated and all these curves were averaged thereafter.

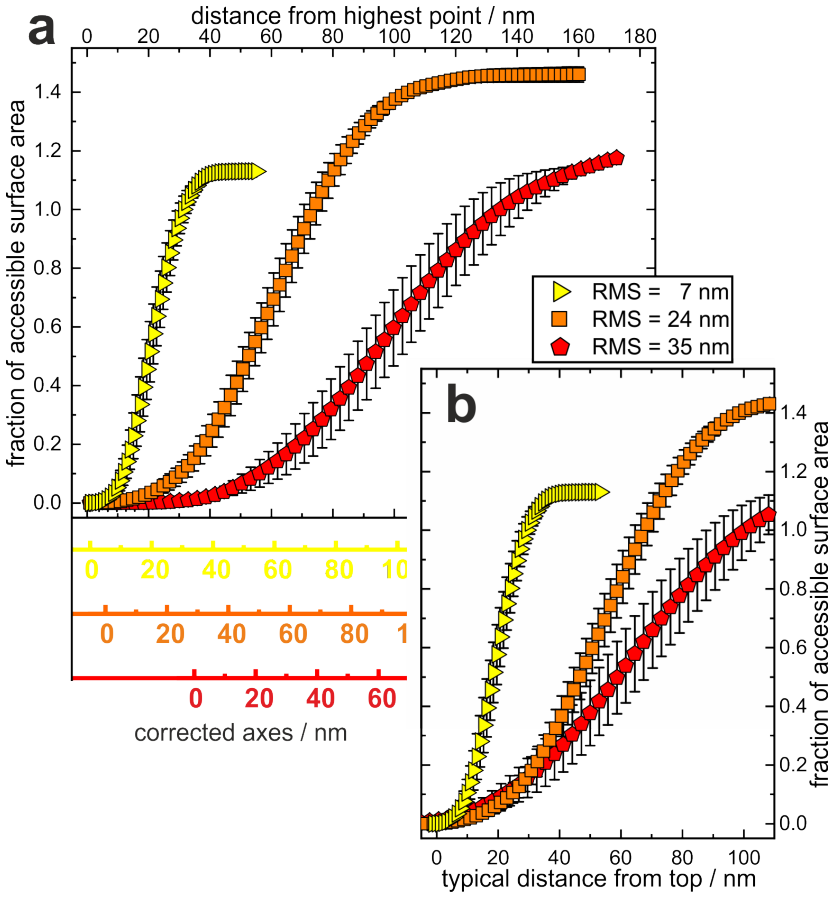

Fig. S8 Accessible fraction of surface area in dependence of the original and the corrected depth values from top of the surface (see text for details). In Fig. 4 c in the main manuscript, the axes are switched for illustrative purposes.

Adhesion of *Staphylococcus carnosus* to Nanostructured Silicon

Figure S9 shows the results of adhesion measurements of *Staphylococcus carnosus* (*S. carnosus*) on the nanostructured silicon surfaces: since this species is not clinical-relevant and experiments on a single-cell level are very time intensive, we did not reach the same large number of cells as for *S. aureus* that were used for the experiments in the manuscript, therefore the error bars are somewhat larger. Nevertheless, we see for *S. carnosus* the very same trend: since this species has a little shorter tether length of 43(2) nm (green rectangle in Fig. S9), also the mean adhesion forces are slightly smaller than for *S. aureus*, but they also fit the fraction of accessible surface area in a depth of 43 nm (vertical rectangles in Fig. S9).

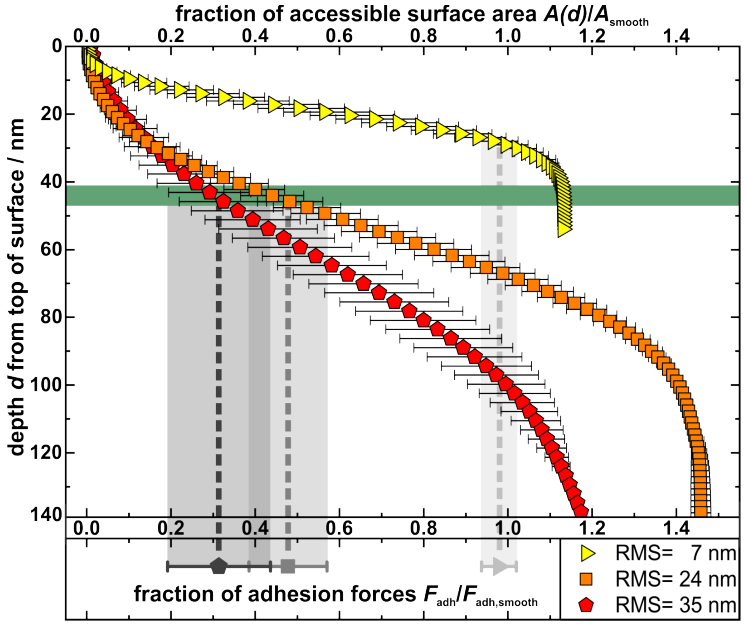

Fig. S9 Depth d from top of the surface and corresponding fraction of accessible surface area of all nanostructured substrates compared to the total surface area of a smooth substrate. The light-colored vertical rectangles show the relative decrease of adhesion forces on the nanostructured surfaces (The middle line of each rectangle indicates the mean value of adhesion forces and the width corresponds to the error of the mean.) The green horizontal rectangle indicates the mean tether length of the used *S. carnosus cells* which is 43(2) nm.

Adhesion of *Staphylococcus aureus* to Nanostructured PDMS

As a preliminary study of a different type of chemical homogenous surfaces, the hydrophobized silicon surfaces that were used for the experiments in the manuscript were filled with (liquid) non-crosslinked PDMS. After crosslinking (at 70 °C for 18 hours), the PDMS was gently peeled off (called mold casting). As it can be seen in the AFM images in Fig. S10 a, this procedure results in nanostructured surfaces. They were characterized by Minkowski functionals (see Fig. S10 b). Then, the adhesion forces of S. aureus cells to the nanostructured PDMS surfaces were measured as described in the manuscript. Results are shown in Fig. S10 c and confirm our results on nanostructured silicon surfaces: for the surface with the lowest and the medium RMS value, the average adhesion forces (having larger error bars) are again in good agreement with the accessible surface area in a depth of 50 nm. For the surface with the highest RMS value, we find slightly stronger adhesion than it would be expected by the total surface area. This cannot be studied in detail at this stage, but is very likely an effect of the higher elasticity of PDMS compared to the silicon surfaces, which leads to an enhanced contact area between cell and substrate[5,9,10]. Under this assumption, the direction of the shift in adhesion forces (forces higher than expected) can be explained qualitatively: since the cell is pressed onto each surface with the same force, the pressure is higher where the cell–surface contact is smaller, namely on the surface with the highest RMS value.

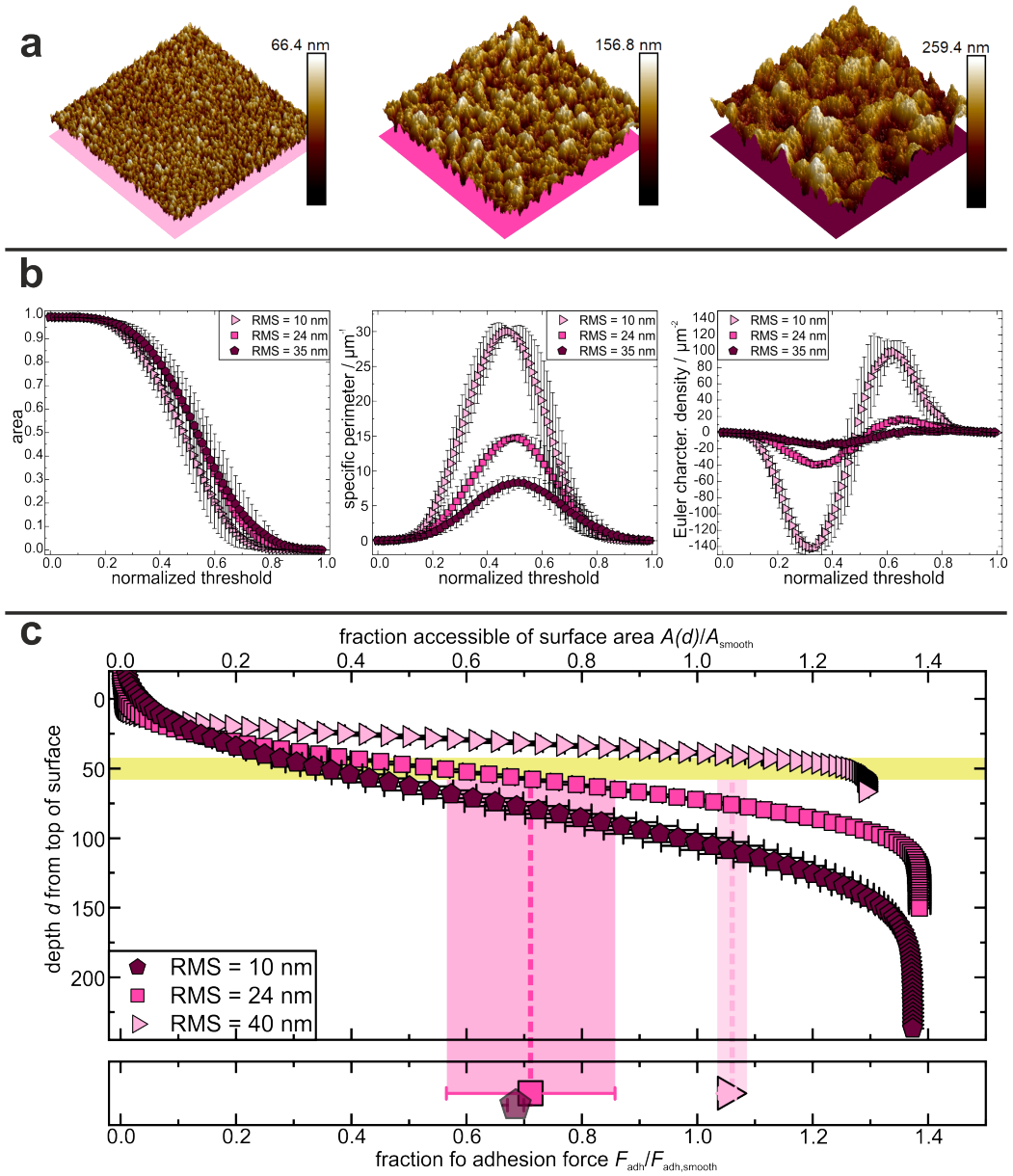

Fig. S10 a) AFM scans of nanostructured PDMS ($3 \times 3\,\mu m^2$), b) Normalized Minkowski functionals of nanostructured PDMS surfaces, c) Fraction of bacterial adhesion forces compared to fraction of accessible surface area in a depth of 50 nm.

References

1 P. Loskill, H. Hähl, T. Faidt, S. Grandthyll, F. Müller and K. Jacobs, *Adv. Colloid Interface Sci.*, 2012, **179**, 107–113.
2 P. Loskill, H. Hähl, N. Thewes, C. T. Kreis, M. Bischoff, M. Herrmann and K. Jacobs, *Langmuir*, 2012, **28**, 7242–7248.
3 M. Lessel, O. Bäumchen, M. Klos, H. Hähl, R. Fetzer, M. Paulus, R. Seemann and K. Jacobs, *Surf. Interface Anal.*, 2015, **47**, 557–564.
4 D. Quéré, *Physica A: Statistical Mechanics and its Applications*, 2002, **313**, 32–46.
5 A. L. Weisenhorn, M. Khorsandi, S. Kasas, V. Gotzos and H.-J. Butt, *Nanotechnology*, 1993, **4**, 106.
6 P. Loskill, P. M. Pereira, P. Jung, M. Bischoff, M. Herrmann, M. G. Pinho and K. Jacobs, *Biophys. J.*, 2014, **107**, 1082–1089.
7 S. Pogodin, J. Hasan, V. A. Baulin, H. K. Webb and V. K. Truong, *Biophys. J.*, 2013, **104**, 835–840.
8 C. Spengler, N. Thewes, P. Jung, M. Bischoff and K. Jacobs, *Nanoscale*, 2017, **9**, 10084–10093.
9 K. Johnson, *Tribology International*, 1998, **31**, 413–418.
10 B. N. Persson, O. Albohr, U. Tartaglino, A. Volokitin and E. Tosatti, *Journal of Physics: Condensed Matter*, 2004, **17**, R1.

III Influence of the surface hydrophobicity on bacterial adhesion

Authors: E. Maikranz,[1,*] C. Spengler,[2,*] N. Thewese,[2] A. Thewes,[1] **F. Nolle**,[2] P. Jung,[3] M. Bischoff,[3] L. Santen,[1] and K. Jacobs[2]

[1] Theoretical Physics, Saarland University, Center for Biophysics, 66123 Saarbrücken, Germany.
[2] Experimental Physics, Saarland University, Center for Biophysics, 66123 Saarbrücken, Germany.
[3] Institute of Medical Microbiology and Hygiene, Saarland University, Center for Biophysics, 66421 Homburg/Saar, Germany.
[*] These authors contributed equally to this work.

Reprinted with permission from *Nanoscale*, 2020, **12**, 19267.
https://doi.org/10.1039/d0nr03134h

Author contributions:
*E.M., A.T., L.S.: modeled experiments and designed simulations. C.S., N.T., **F.N.**, P.J., M.B., K.J.: designed experimental research. E.M. performed Monte Carlo simulations, **F.N.**, C.S., N.T.: performed single-cell force spectroscopy, E.M., C.S.: writing–original draft. All authors: writing–review and editing.*

Abstract – Bacterial adhesion to surfaces is a crucial step in initial biofilm formation. In a combined experimental and computational approach, we studied the adhesion of the pathogenic bacterium Staphylococcus aureus to hydrophilic and hydrophobic surfaces. We used atomic force microscopy-based single-cell force spectroscopy and Monte Carlo simulations to investigate the similarities and differences of adhesion to hydrophilic and hydrophobic surfaces. Our results reveal that binding to both types of surfaces is mediated by thermally fluctuating cell wall macromolecules that behave differently on each type of substrate: on hydrophobic surfaces, many macromolecules are involved in adhesion, yet only weakly tethered, leading to high variance between individual bacteria, but low variance between repetitions with the same bacterium. On hydrophilic surfaces, however, only few macromolecules tether strongly to the surface. Since during every repetition with the same bacterium different macromolecules bind, we observe a comparable variance between repetitions and different bacteria. We expect these findings to be of importance for the understanding of the adhesion behaviour of many bacterial species as well as other

microorganisms and even nanoparticles with soft, macromolecular coatings, used e.g. for biological diagnostics.

Nanoscale

PAPER

View Article Online
View Journal | View Issue

Cite this: *Nanoscale*, 2020, **12**, 19267

Different binding mechanisms of *Staphylococcus aureus* to hydrophobic and hydrophilic surfaces†

Erik Maikranz,‡[a] Christian Spengler, ‡[b] Nicolas Thewes,[b] Alexander Thewes,[a] Friederike Nolle,[b] Philipp Jung, [c] Markus Bischoff, [c] Ludger Santen *[a] and Karin Jacobs *[b]

Bacterial adhesion to surfaces is a crucial step in initial biofilm formation. In a combined experimental and computational approach, we studied the adhesion of the pathogenic bacterium *Staphylococcus aureus* to hydrophilic and hydrophobic surfaces. We used atomic force microscopy-based single-cell force spectroscopy and Monte Carlo simulations to investigate the similarities and differences of adhesion to hydrophilic and hydrophobic surfaces. Our results reveal that binding to both types of surfaces is mediated by thermally fluctuating cell wall macromolecules that behave differently on each type of substrate: on hydrophobic surfaces, many macromolecules are involved in adhesion, yet only weakly tethered, leading to high variance between individual bacteria, but low variance between repetitions with the same bacterium. On hydrophilic surfaces, however, only few macromolecules tether strongly to the surface. Since during every repetition with the same bacterium different macromolecules bind, we observe a comparable variance between repetitions and different bacteria. We expect these findings to be of importance for the understanding of the adhesion behaviour of many bacterial species as well as other microorganisms and even nanoparticles with soft, macromolecular coatings, used *e.g.* for biological diagnostics.

Received 21st April 2020,
Accepted 24th July 2020

DOI: 10.1039/d0nr03134h

rsc.li/nanoscale

Staphylococcus aureus (*S. aureus*) is an opportunistic pathogen associated with different community- and hospital-acquired infections.[1] One reason for its high pathogenicity is the cells' ability to adhere strongly to various surfaces, including natural and abiotic materials, such as implanted medical devices.[2–4] Subsequent to adhesion, the cells may proliferate and form mechanically and chemically robust biofilms.[5,6] Because of the latter, *S. aureus* is a major cause of implant-related infections with severe consequences for the patients' health.[7–11] Furthermore, since in biofilms the cells can be well-protected against environmental influences and have the ability to adhere to many different types of surfaces, they can spread quickly to formerly non-inhabited space, for example in clinical buildings.[12] Hence, understanding and controlling the adhesive behaviour of *S. aureus* is of fundamental importance for health care and engineering.[13,14]

The state-of-the-art method in quantitative bacterial adhesion research is atomic force microscopy (AFM)-based force spectroscopy with single bacterial probes (single-cell force spectroscopy, SCFS).[4,15–18] This method allows the investigation of many different mechanisms on a single-cell or even molecular level. For instance, it can be performed on bare abiotic surfaces, on conditioned surfaces or on natural or natural-like surfaces (*e.g.* hydroxyapatite) as well as with pretreated cells.[19–23] Using SCFS, a previous study demonstrated that bacterial adhesion to hydrophobic surfaces is governed by cell wall macromolecules tethering to the surface.[4] As a consequence, the adhesive strength of a single cell is determined by the number of contact-forming macromolecules and by the strength of each individual binding site. The composition of surface macromolecules, as well as important adhesion parameters, such as the bacterial contact area to solid surfaces, are highly cell-individual properties.[24] Thus, general statements concerning the adhesion of certain cell types can only be achieved with good statistics obtained from a sufficiently large number of cells and well-characterized sample surfaces. In addition, former studies have shown that the adhesive strength of several bacterial species strongly depends on surface

[a]*Theoretical Physics, Saarland University, Center for Biophysics, 66123 Saarbrücken, Germany. E-mail: l.santen@mx.uni-saarland.de*
[b]*Experimental Physics, Saarland University, Center for Biophysics, 66123 Saarbrücken, Germany. E-mail: k.jacobs@physik.uni-saarland.de*
[c]*Institute of Medical Microbiology and Hygiene, Saarland University, Center for Biophysics, 66421 Homburg/Saar, Germany*

†Electronic supplementary information (ESI) available. See DOI: 10.1039/D0NR03134H

‡These authors contributed equally to this work.

View Article Online

Paper Nanoscale

wettability.[25–27] Quantitative data is especially available by SCFS studies which demonstrated that adhesion of *Lactobacillus plantarum*,[28] *Streptococcus mutans*[29] and *S. aureus*[16,24] to hydrophobic surfaces is about one order of magnitude stronger than to hydrophilic surfaces.

In this paper, we present a detailed characterization of the adhesion of *S. aureus* cells to abiotic surfaces by evaluating differences in adhesion behaviour to very hydrophilic (5° water contact angle) and hydrophobic (111° water contact angle) Si wafer-based substrates. We performed SCFS experiments with *S. aureus* strain SA113 cells that are complemented by Monte Carlo simulations. Our study reveals that on hydrophobic surfaces, many macromolecules tether to the surface, while on hydrophilic surfaces, a potential barrier selects only a few tethering macromolecules. Since our model is based on unspecific binding of cell wall macromolecules, the results of this study may also be of relevance to understand the adhesive behaviour of many other bacteria and microorganisms, such as fungi, eukaryotic cells, or nanoparticles covered with soft, macromolecular coatings for applications like printable electronics,[30] biological diagnostics, optoelectronic devices, or energy' harvesting systems.[31] The colonisation of diverse and new habitats usually occurs in the presence of a liquid medium, making surface wettability a key parameter for understanding adhesion.

1. Materials and methods

1.1. Substrate preparation

Si wafers (Siltronic AG, Burghausen, Germany) are the basis of the hydrophilic as well as of the hydrophobic substrates used in this study. The Si substrates feature a native silicon oxide layer of 1.7(2) nm (the number in parentheses denotes the error of the last digit) and an RMS (root mean square) surface roughness of 0.09(2) nm.[32] Thoroughly cleaning the Si wafers results in a hydrophilic substrate with an advancing water contact angle of 5(2)°, a surface energy of 64(1) mJ m^{-2} and a zeta-potential of −104.4(1) mV at pH of 7.3.[32] The hydrophobic substrates are prepared by covering a Si wafer with a self-assembled monolayer of octadecyltrichlorosilane (OTS) according to a standard protocol.[33] The result is a CH_3-terminated substrate with an advancing (receding) water contact angle of 111(1)° (107(2)°), an RMS surface roughness of 0.17(3) nm, a surface energy of 24(1) mJ m^{-2} (ref. 33) and a zeta-potential of −80.0(1) mV.[32] The hydrophilic silicon wafers were cleaned as follows: the substrates were immersed for 30 min in fresh solution of H_2SO_4 (conc.)/H_2O_2 (30%) (1 : 1), then in boiling deionized water for 90 min, during which the water was changed at least four times. Afterwards, the surfaces were dried in a stream of ultrapure nitrogen. The hydrophobic surfaces were cleaned in an ultrasonic bath of ethanol and acetone subsequently for 5 min each. When changing the solvent and at the end of rinsing, the surfaces were dried in a stream of ultrapure nitrogen. For force spectroscopy experiments, substrates were immersed into phosphate-buffered saline (PBS, pH 7.3, ionic strength 0.1728 mol l^{-1} at 20 °C).

1.2. Bacteria

Adhesion studies were performed with *Staphylococcus aureus* strain SA113. This biofilm-positive laboratory strain is a common platform to study cell wall macromolecules of *S. aureus*.[34–37] All bacterial cultures were prepared the same way, starting the day before the force spectroscopy experiments: an overnight culture was prepared in 5 ml tryptic soy broth (TSB) medium and incubated at 37 °C and 150 rpm for 16 h. The next day, 40 µl of the overnight culture were transferred into 4 ml of fresh TSB medium and incubated for another 2.5 h to obtain exponential phase cells. Subsequently, 0.5 ml of this culture were washed three times, using 1 ml PBS each, to remove extracellular material.

1.3. Single-cell force spectroscopy

Single bacterial probes were prepared according to a standard protocol:[38] tipless cantilevers (MLCT-O, Bruker Nano GmbH, Berlin, Germany) were covered with a thin layer of polydopamine by polymerization of dopamine hydrochloride (99%, Sigma-Aldrich, St Louis, USA) in TRIS buffer (pH 4.8). Afterwards, single bacterial cells were attached to the polydopamine coated cantilever using a micromanipulator; care was taken to ensure that cells never dry out during probe preparation or force measurements. All cantilevers were calibrated before each measurement. Force spectroscopy measurements with single bacterial probes were conducted under ambient conditions in phosphate buffered saline (PBS, pH 7.3) using a Bioscope Catalyst (Bruker Nano GmbH, Berlin, Germany). We performed force–distance measurements with single bacterial cells of *S. aureus* SA113 on either a hydrophobic or a hydrophilic substrate. From force–distance curves, we cannot discern if bacteria are dead or alive. However, a previous study demonstrated that intentionally killed bacteria showed identical curves to bacteria that are alive and able to divide.[39] For the parameters of the curves, values that correspond to similar studies were chosen:[16,40–42] the ramp size was 800 nm, the force trigger (denoting the maximal force with which the cell is pressed onto the substrate) was 300 pN and retraction speed was 800 nm s^{-1}.

In total, we analysed 64 cells on hydrophobic surfaces and 52 cells on hydrophilic surfaces. On the tested hydrophobic surfaces, the surface delay time, *i.e.* the time between approach and retraction in which the cell is in contact to the substrate and the cantilever is not moved, had no big influence on the adhesive strength. Therefore all force–distance curves on hydrophobic surfaces were taken with a nominal surface delay of 0 s which corresponds to a 'real' contact time below 0.5 s.[16,40] On hydrophilic surfaces, however, the surface delay time is an important parameter whose influence should be checked, as follows. In general, values of a few seconds are a common choice to study the influence of surface delay time on bacterial adhesion processes.[18,28,41–43] Therefore, on the hydrophilic surface, 52 cells were probed with a surface delay time

of 5 s, and 19 cells were probed without additional surface delay time. For curves with surface delay time, the approach speed was set to 100 nm s^{-1} while it was 800 nm s^{-1} when no surface delay was applied. For all cells and delay times, 30 repeated force–distance curves have been analysed the following way: the retraction part of each force–distance curve was evaluated to characterise the strength of adhesion. Hence, the maximum force needed to detach an individual cell from the surface ('adhesion force') as well as the separation at which bacterium and surface lose contact ('rupture length') were determined. For the latter, the Matlab function *findchangepts* was used: the largest separation where the root mean square of the signal changed the first time significantly from the background noise was defined as the rupture length.

During approach, bacterial cells can be attracted to the surface at rather large separations due to individually tethering long macromolecules ('snap-in event').[4] We evaluated this mechanism on both surfaces with respect to its maximum attractive force ('snap-in force') and the separation at which the attraction starts ('snap-in separation'). To compute the latter, we used the same method as for computing the rupture length. While on hydrophobic surfaces, reliable approach curves could be measured, on hydrophilic surfaces, due to the use of a soft cantilever to record the expected lower adhesion forces, fewer reliable curves could be observed. The characteristics of retraction as well as approach curves were quantified by computing histograms and mean curves. The characteristics for the histograms where computed from the individual force separation curves and subsequently binned. The error bars in the histograms and the standard error of the mean are computed in the usual manner by dividing the estimated standard deviation by the square root of the number of curves.

Since the extracted adhesion forces for repeated measurements of the same cell on hydrophobic surfaces are strongly correlated, we estimated those errors not in the usual manner: since the number of independent events is given by the number of cells, we divided by the square root of the number of cells. For the computation of the mean curves, all individual curves where interpolated along a given grid of separation values, and subsequently the corresponding mean and standard deviation were computed point-wise.

1.4. Monte Carlo simulation

To simulate SCFS experiments, we modify a stochastic model introduced by Thewes *et al.*[4] The bacterium is considered to be a hard sphere decorated with soft macromolecules. The length fluctuations, as well as mechanical response to stretching of these macromolecules is modelled as worm-like chain (WLC) polymer, where the properties of each macromolecule are sampled from a given distribution. The interaction with the surface is mediated by a simple square potential with a given potential depth V and interaction range. However, before any macromolecule is able to bind to the surface, it needs to overcome a potential barrier of height H. This barrier is overcome with probability e^{-H}. This binding allows the molecules to pull on the bacterium. The pulling forces on the bacterium are balanced by the bending of the cantilever (modelled as the extension of a spring), and the bacterium is moved to equilibrium position between each step of the cantilever. For more information about the simulation procedure, used parameters and model details, see the ESI.†

2. Results and discussion

2.1. Experimental data

Adhesion to hydrophilic surfaces. When performing force–distance measurements on hydrophilic surfaces with 0 s surface delay time, in many individual curves, no significant adhesion of the cells to the surface can be observed. However, other studies showed that adhesion of microbial cells can change with the cell–surface contact time.[44] Therefore, in a first step, the influence of the surface delay time on the adhesion to hydrophilic surfaces was investigated. Fig. 1a, shows the mean retraction curves for all tested cells for 0 s (purple) and 5 s (blue) surface delay time as coloured lines (with standard deviations indicated by shaded areas).§ For both delay times, the recorded force of the retraction curve first decreases as the separation increases, then reaches a minimum and thereafter relaxes back to zero. For the longer delay time, the minimum is at higher negative forces and the relaxation ends at larger separation values. In addition, the standard deviation increases markedly with longer surface delay time.

Quantifying the retraction curves further, we computed the rupture length (indicating the point where the last macromolecule of the bacterium looses contact to the surface) and the adhesion force (maximal force between bacterium and surface) for every curve and computed corresponding histograms (see Fig. 1b and c). The adhesion forces for 0 s surface delay time have mostly values close to 0 pN, but reach values up to hundreds of pN.¶ For 5 s delay time, the adhesion forces have maximum occurrence at about 700 pN but reach values up to several nN. The rupture lengths vary in both cases from several tens of nm to a few hundred nm, whereby for longer surface delay time, larger values are observed more regularly.

Since adhesion is only rarely observed on hydrophilic surfaces without additional delay time and, if it is the case, the forces are rather small, we focus in the following on retraction curves with 5 s delay time. To gain deeper insight in the retraction characteristics of individual bacteria, we show in Fig. 2 mean retraction curves for some cells and mean rupture

§ Note that most of the positive parts of the shaded area (representing the standard deviation) are a consequence of the symmetrical display of the standard deviation. The measured values are – except for the positive part of the baseline noise – never positive and, therefore, not symmetrical around the mean value.

¶ Notably, depth and position of the minima of the mean curves do not match the corresponding mean values in the histograms because the force-separation curves are highly non-monotonic (see Fig. 5b). As a consequence, the minimum of the mean curve is in general not the same as the mean of the minima of each individual curve. In other words, the mean of the minima does not take into account the position of the minimum while the mean curve does.

View Article Online
Paper Nanoscale

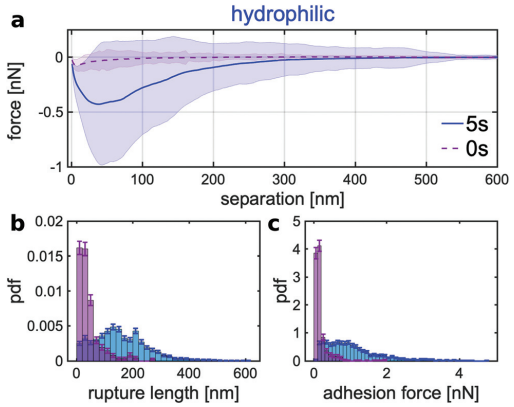

Fig. 1 (a) Mean SCFS retraction curves (calculated as described in section 1.3) with surface delay times of 0 s (purple, 19 cells) and 5 s (blue, 52 cells) on hydrophilic surface (shaded area is standard deviation). (b, c) Probability density histograms of rupture lengths and adhesion force extracted from single SCFS retraction curves with to (a) corresponding colours.

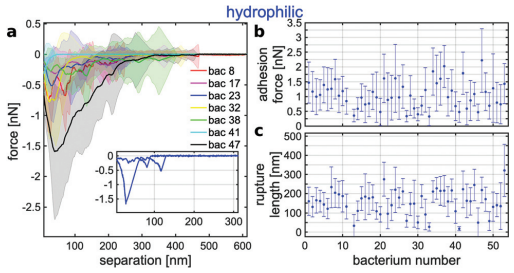

Fig. 2 (a) Mean SCFS retraction curves (calculated as described in section 1.3) of 7 exemplary individual bacteria on the hydrophilic surface for a surface delay time of 5 s (shaded area is standard deviation). The inset depicts two exemplary force–distance curves of cell no. 23, whose mean curve is shown in blue in the main diagram. (b, c) Mean adhesion forces and rupture lengths extracted from single SCFS retraction curves of 52 cells (error bars are standard deviation).

length and adhesion force for all cells. For every cell, the mean curve is different but their standard deviation markedly overlap (Fig. 2a). The reason for this can be seen in the inset, which shows two exemplary force-separation curves from two successive measurements with the same cell. Although, both curves have similar 'spiky' features, they are obviously very different from each other. This fact is also reflected in the mean adhesion forces and rupture lengths: the adhesion forces are all located in a range of about 0.1 to 1.7 nN with error bars (depicting the standard deviation) between 0.5 and 1 nN (Fig. 2b), while the rupture lengths vary around 150 nm and have error bars of more than 100 nm (Fig. 2c).

An in depth discussion follows in the next section in direct comparison to the results on hydrophobic surfaces.

Adhesion to hydrophobic surfaces. We analysed the adhesion of *S. aureus* to hydrophobic surfaces in the same manner as on hydrophilic substrates. In the case of hydrophobic surfaces, a surface delay time of 0 s is sufficient to observe strong adhesion for all tested cells (Fig. 3). Additional 5 s of surface delay time were tested for 6 of 64 cells, and it showed that the adhesion force was not strongly enhanced and the characteristics of the retraction curves did not markedly change (for data, see the ESI†). Therefore, force–distance curves on hydrophobic surfaces discussed in the following were recorded with 0 s surface delay time.

To analyse the adhesion on hydrophobic surfaces in detail, Fig. 3a depicts – analogously to the data on hydrophilic surfaces – the mean retraction curves of several single cells. Here, every single cell features 'cup-shaped' retraction curves with a well-defined minimum and only a very small standard deviation (note the different scale of the adhesion force in comparison to the hydrophilic case). The low variability for different curves from one and the same cell is explicitly shown in the inset, where two repetitive curves with almost identical shapes are depicted. Hence, the variability on hydrophobic surfaces is mainly given from cell to cell, while on hydrophilic surfaces, the cell-to-cell variance is comparable to the variability between repetitive curves. Further, the mean adhesion forces on hydrophobic surfaces (see Fig. 3b) range from 5 to 70 nN with most error bars in the order of a few nN. Therefore, the adhesion force on hydrophobic surfaces seems highly cell specific, while it is highly stochastic on hydrophilic surfaces. The rupture lengths, however, vary on hydrophobic surfaces from repetition to repetition with the same cell (see Fig. 3c) and show very similar performance in magnitude and variability to the behaviour on hydrophilic surfaces. This will be discussed later.

In order to compare the adhesion properties of a typical population of bacteria on hydrophilic and hydrophobic sur-

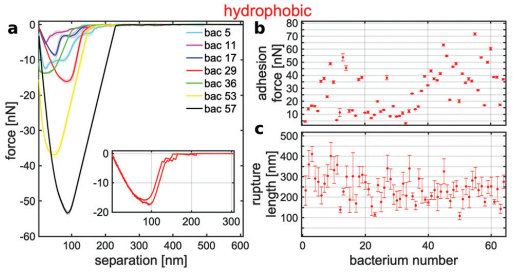

Fig. 3 (a) Mean SCFS retraction curves (calculated as described in section 1.3) of 7 exemplary bacteria on the hydrophobic surface for 0 s surface delay time (shaded area is standard deviation and very small). The inset depicts two exemplary force–distance curves of cell no. 29, whose mean curve is shown in red in the main diagram. (b, c) Mean adhesion forces and rupture lengths extracted from single SCFS retraction curves of 64 cells (error bars are standard deviation). Note the different scales in this figure and Fig. 2 for the adhesion forces, but identical scale for the rupture lengths.

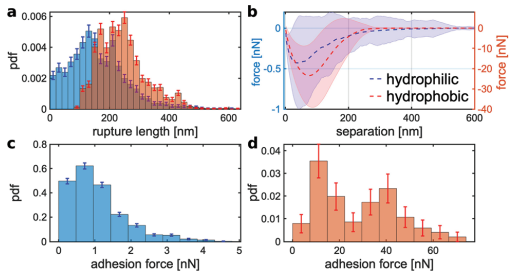

Fig. 4 (a, c, d) Probability density histograms of rupture lengths and adhesion force of each tested cell on hydrophilic (blue) and hydrophobic (red) surfaces (where histograms overlap, a mixed colour is displayed). (b) Corresponding mean retraction curve (shaded area is standard deviation) calculated from all tested cells calculated as described in section 1.3. (Note the different scales of the *y*-axes!)

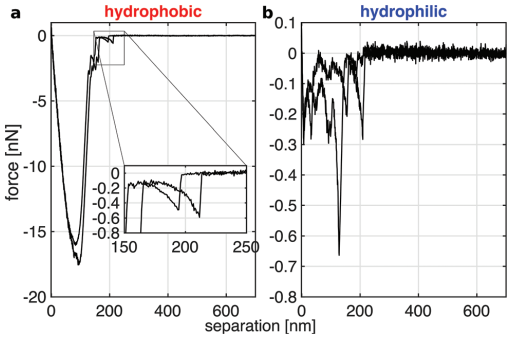

Fig. 5 Force-separation curves of two repeated SCFS experiments with one bacterium (per surface) on a hydrophobic (a) and a hydrophilic surface (b) to illustrate similarities and differences.

faces, we computed mean retraction curves and relevant histograms of all cells measured (see Fig. 4). Interestingly, for both surfaces, the mean retraction curves look very similar but feature completely different force scales (see Fig. 4b).‖ This also manifests in the adhesion force histograms: on hydrophilic surfaces, typical adhesion forces are hundreds of pN up to several nN (see Fig. 4c and d) while on hydrophobic surfaces, they are several tens of nN. Their mean values differ by a factor of 25 (1.1(0) nN *vs.* 28(2) nN).

As already mentioned before, the rupture lengths differ much less than the adhesion forces: although, in the rupture length histograms (Fig. 4a), a clear shift to higher rupture lengths on hydrophobic surfaces is observed, the mean rupture lengths differ only by a factor of about 1.5 (from 160(2) nm on hydrophilic surfaces, to 242(2) nm on hydrophobic surfaces). Especially, the tails in both histograms extend to remarkably high rupture lengths. Such high rupture lengths, with values even bigger than 400 nm, are quite notable for surfaces that are unconditioned with biological material. On such surfaces, cell wall macromolecules can just tether non-specifically to the surface. If we consider for proteins 0.36 nm length contribution per amino acid as usually done in single molecule force spectroscopy experiments,[42,45] these rupture lengths are comparable to the fully unfolded length of different *S. aureus* surface proteins, like Serine-aspartate repeat-containing protein C (SdrC, 360 nm[45]), clumping factor A (ClfA, 285 nm[46]), and *S.* aureus surface protein G (SasG, 505 nm[47]).** Forces to unfold proteins are typically 0.1–0.4 nN,[48–50] but are specific to the structure and the pulling speed. In the literature only values are provided for SasG whose E and G5 domains have unfolding forces of 0.25 nN and 0.42 nN, respectively,[50] but may depend on the Zn^{2+} concentration.[51] However, the large rupture lengths might also result from the tethering of other cell surface macromolecules like glycolipids (teichoic acids) or extracellular polysaccharides, such as poly-*N*-acetyl-D-glucosamine (PNAG). This could by analysed in future studies with specific knock-out mutants of *S. aureus* SA113.

When directly comparing typical retraction curves on hydrophilic and hydrophobic surfaces (Fig. 5a and b), it seems reasonable that single molecule tethering is involved on both types of abiotic surfaces. These show – besides the already mentioned fundamental differences in the curve shapes – also similar features. On hydrophilic surfaces, the retraction curves show several peaks, which resemble partial force stretch curves of worm-like chain polymers ('WLC-like peaks'), of varying magnitude (Fig. 5a and b). Such WLC behaviour is commonly observed in single force spectroscopy measurements for various proteins.[48–50] However, our experiments show most likely the stretching of several macromolecules at the same time, generating more complicated retraction curves. On hydrophobic surfaces, we also often observe single peaks at separations close to the rupture length. These show similar signatures as the retraction curves on hydrophilic surfaces resembling WLC behaviour (inset in Fig. 5a). This marks the adhesion process as a stochastic tethering of individual macromolecules to both surfaces.

Approach curves. In addition to the retraction curves, also the approach parts of force–distance curves can provide insights into the adhesion process. Therefore, all recorded approach curves were analysed in terms of the presence and characteristics of the so-called snap-in event, *i.e.* a sudden attraction of the cantilever towards the surface.[4] While this event is present in nearly all experiments on the hydrophobic surfaces, it is only rarely observed in curves on hydrophilic surfaces. For a quantitative analysis, only those curves that show a reliable snap-in were pooled and – analogously to the retraction curves – the ensemble properties were calculated (Fig. 6). Thereby, strong differences between curves on hydrophilic and hydrophobic surfaces are observed: the mean snap-in separ-

‖ That the standard deviation on hydrophilic surfaces seems to extend to higher separations as on the hydrophobic surfaces is just an optic effect of the strongly different force scales.

** Note that the fully unfolded length of the protein structure does not necessarily correspond to the rupture length; for details, see the ESI.†

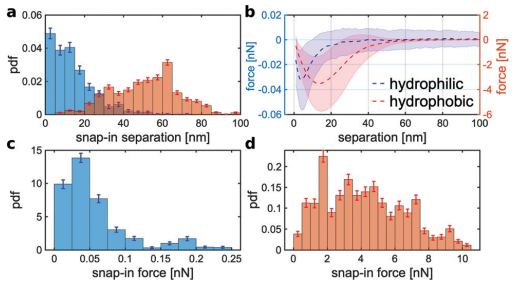

Fig. 6 (a, c, d) Probability density histograms of snap-in separation and snap-in force of each tested cell on hydrophilic (blue) and hydrophobic (red) surfaces (where histograms overlap, a mixed colour is displayed). (b) Corresponding mean approach curve (shaded area is standard deviation) calculated from all tested cells calculated as described in section 1.3.

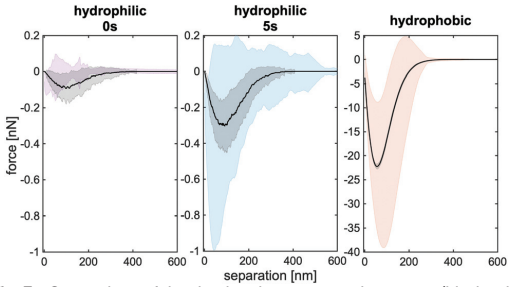

Fig. 7 Comparison of the simulated mean retraction curves (black, with standard deviation as shaded area) that match the experimental results (purple, blue, red). We used 17 k_BT (0 k_BT) for the potential barrier and 50 k_BT (20 k_BT) binding energy for hydrophilic (hydrophobic) surfaces. Note the different force scale of the right panel in comparison with the others and the remarkably small standard deviation.

ation (separation were the snap-in starts) on hydrophilic surfaces is 13.5(4) nm and thus approximately four times lower than on hydrophobic surfaces (51.9(4) nm). The mean snap-in force on hydrophilic surfaces is almost one order of magnitude weaker than it is on hydrophobic surfaces (0.06(1) nN *vs.* 4.2(1) nN). In order to display a snap-in event, rather fast binding of macromolecules is necessary. Therefore, the observation of a much weaker pronounced snap-in on hydrophilic surfaces nicely corroborates the strong surface delay time dependence that we observe on these substrates.

In summary, our experimental curves hint to stochastic binding of a rather low number of macromolecules on hydrophilic surfaces, leading to a strong surface delay time dependence and a high variance between individual curves that is comparable to the cell-to-cell variance. A low number of individual macromolecules exert forces in the low nN range and detach at separations varying from tens of nm to remarkably hundreds of nm. On hydrophobic surfaces in contrast, the retractions curves show very low variance between individual curves, adhesion forces of several tens of nN, and rupture lengths in the order of several 100 nm.

In a first step to validate whether these results can be generalized and do not only hold true for the tested strain of *S. aureus* SA113, we probed two more clinically relevant *S. aureus* strains, the USA300 CA-MRSA derivative JE2 and the HA-MRSA strain N315, with a smaller number of individuals. The results are given in the ESI† and support our conclusions stated above.

2.2. Monte Carlo simulations

To substantiate the conclusions and hypotheses drawn from the experiments, we performed Monte Carlo (MC) simulations of the bacterial adhesion process, in which the bacterium is modelled as a sphere decorated with thermally fluctuating macromolecules. These molecules bind individually to the surface after overcoming a potential barrier. Once bound to the surface, the potential depth quantifies their bonding strength. Further details and parameter discussion is provided in section 1.4 and the ESI†.

As can be seen in Fig. 7, our simulations are able to reproduce the experimental mean SCFS retraction curves on hydrophilic as well as on hydrophobic surfaces with biological reasonable parameters. For both surfaces, the parameters for the cell wall macromolecules were kept the same (see ESI†) and only the potential depth and barrier height were changed. The simulated mean retraction curve (black line) in Fig. 7 features the correct force scale as well as the right rupture lengths. In addition, the strong surface delay time dependence on hydrophilic surfaces can be reproduced (Fig. 7a and b). However, especially on hydrophobic surfaces, the standard deviation in the simulation is much lower than in the experiments meaning that the variability between individual cells is not represented in the simulations (Fig. 7c). This lack of diversity is the result of a fixed high number of macromolecules on the cell surface, that use the same simple force stretch model with identical binding energy. In order to increase the quantitative agreement, a more complete characterisation of the involved surface macromolecules would be necessary. This is, however, beyond the scope of this paper. In addition, the introduction of nano domains of proteins on the cell surface (that are for example suggested for Serine-aspartate repeat-containing protein G (SdrG) on *S. epidermis* and Collagen adhesin (Cna) protein on *S. aureus*) would increase the cell to cell variability in our model.[42,52]

Since the bacteria used are grown under the same conditions, cell-individual surface properties should be mainly responsible for the different adhesion characteristics. To this end we analysed the influence of the potential depth and barrier on individual and mean retraction curves of specific bacteria (Fig. 8). First we observe, for low potential barriers and sufficiently high potential depths, always cup-shaped retraction curves. All the repetitions with the same cell (blue, red, green line) show the same signature and, as expected, bigger potential depths increase the adhesion force. Second, if we increase the potential barrier, we observe a decrease in

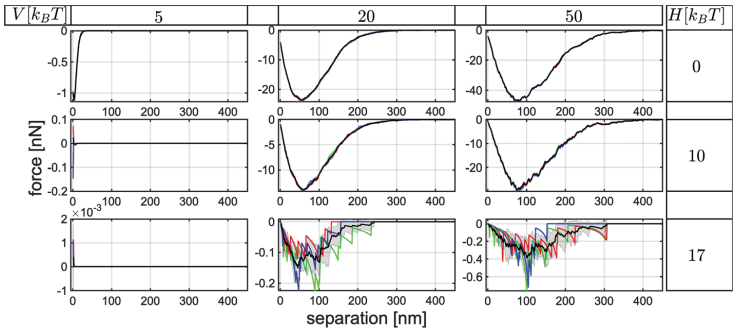

Fig. 8 Simulation results: single (coloured) and mean retraction curves (black) for different potential depth V and potential barriers H and fixed bacteria. Surface delay time is 5 s.

adhesion force and individual 'WLC-like peaks' which vary from repetition to repetition. The lack of variability in repetitions, for low potential barriers, matches the experimental behaviour on hydrophobic surfaces. The drop in adhesion force, the partial WLC behaviour and the strong increase in variability of repetitions matches the observed behaviour on hydrophilic surfaces.

To gain a deeper understanding in the change of adhesion behaviour with varying potential depth and barrier height, we counted the number of macromolecules that in fact bind to the surface and investigated how surface delay time affects this binding (Fig. 9). For low potential barriers, additional surface delay time does not lead to an considerable increase in bound macromolecules. Yet, for high barriers, a substantial increase is observed. This increase in attached molecules leads to an increase in adhesion force (for the corresponding mean retraction curves, see ESI†) which matches the experimental behaviour on hydrophilic surfaces. Furthermore, for low potential barriers, a substantial amount of available macromolecules binds without any delay time, rendering additional binding with more delay time negligible. This leads to only a weak dependence of the adhesion force on surface delay time, like we have observed in the experiments on hydrophobic surfaces. For higher barriers, only few macromolecules bind to the surface, corroborating the notion that indeed on hydrophilic surfaces few, and on hydrophobic surfaces many macromolecules are responsible for adhesion.

In summary, the simulations provide evidence that a large number of macromolecules bind to hydrophobic surfaces, while only a few macromolecules are stochastically selected to bind to hydrophilic surfaces. This leads to almost identical shapes of consecutive curves on hydrophobic surfaces and a high variability of consecutive curves on hydrophilic surfaces. Our model suggest that the reason for the different number of tethering molecules is that on hydrophobic surfaces, many weakly binding macromolecules can attach quickly without hindrances, while on hydrophilic surfaces, a potential barrier selects only few but strongly binding macromolecules.

Although the origin of the potential barrier is unclear, we propose that it stems from conformational changes of the

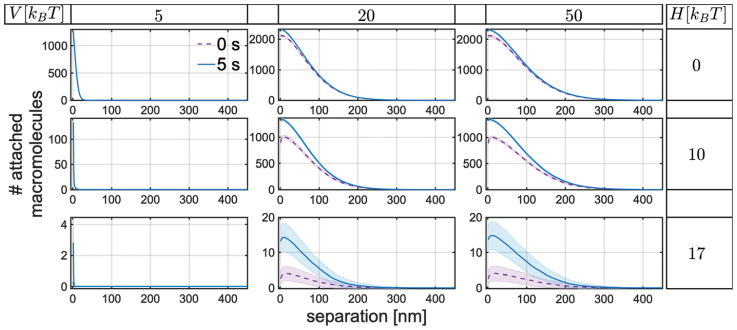

Fig. 9 Simulation results: ensemble mean of the number of attached macromolecules for different potential depth V and barriers H, extracted from the first 10 retractions of 20 simulated cells. Shaded area is standard deviation. While blue solid lines indicate 5 s of surface delay time, purple dashed lines indicate 0 s.

View Article Online
Paper Nanoscale

macromolecules and/or disturbances of the hydrogen bond network close to the surface. The latter seems reasonable because hydrophobic interactions are non-directional and fast while hydrogen-bonds are directional and need time to form. This depends, however, on the structure of the involved macromolecules and water network.

3. Conclusions

In conclusion, we have analysed the adhesion characteristics of a high number of force–distance curves of single *S. aureus* cells to hydrophilic and hydrophobic surfaces. The experimental data could be quantitatively reproduced by MC simulations of the adhesion process using reasonable parameters for the surface potential as well as for the involved macromolecules.

Together, our results can explain bacterial adhesion to abiotic surfaces: *S. aureus* cells adhere to hydrophobic surfaces by many weakly binding macromolecules, while they adhere to hydrophilic surfaces *via* few, but strongly binding macromolecules. Tethering of many macromolecules on hydrophobic surfaces leads to high adhesion forces and low variability repetitive SCFS retraction experiments with the same cell. In contrast, a potential barrier on hydrophilic surfaces selects only a few strongly binding macromolecules which leads to high variability between repetitive measurements. The origin of this barrier is an interesting subject for future research.

We expect that our results hold true also for other types of bacteria, especially Gram-positive bacteria where no additional diffusion dynamics of macromolecules in the membrane play a role. Therefore, they can have important implications for applications where bacterial adhesion is unwanted: the remarkable difference of binding strength for hydrophilic and hydrophobic surfaces could be used in order to reduce considerably the binding affinity of bacteria to surfaces. Moreover, our results can also help to predict the adhesive strength of bacteria to different types of smooth substrates of which only the surface energies are known. *Vice versa*, with the help of our results, single adhesion curves on chemically unknown (conditioned) surfaces may be sufficient to derive statements about the substrates' surface energies and/or involved interactions.

Conflicts of interest

There are no conflicts to declare.

Acknowledgements

The authors thank Dr. Thomas Faidt (Saarland University) for the artwork in the TOC graphic. This work was supported by the German Research Foundation (DFG) within the collaborative research centre SFB 1027 (Projects B1 and B2).

References

1 F. D. Lowy, *N. Engl. J. Med.*, 1998, **339**, 520–532.
2 R. Yongsunthon, V. G. Fowler, B. H. Lower, F. P. Vellano, E. Alexander, L. B. Reller, G. R. Corey and S. K. Lower, *Langmuir*, 2007, **23**, 2289–2292.
3 D. Linke and A. Goldman, *Bacterial Adhesion: Chemistry, Biology and Physics*, Springer Science & Business Media, 2011, vol. 715.
4 N. Thewes, A. Thewes, P. Loskill, H. Peisker, M. Bischoff, M. Herrmann, L. Santen and K. Jacobs, *Soft Matter*, 2015, **11**, 8913–8919.
5 L. Hall-Stoodley, J. W. Costerton and P. Stoodley, *Nat. Rev. Microbiol.*, 2004, **2**, 95.
6 H.-C. Flemming and J. Wingender, *Nat. Rev. Microbiol.*, 2010, **8**, 623.
7 F. Götz and G. Peters, *Infections Associated with Indwelling Medical Devices*, American Society of Microbiology, 3rd edn, 2000, pp. 55–88.
8 A. L. Chamis, G. E. Peterson, C. H. Cabell, G. R. Corey, R. A. Sorrentino, R. A. Greenfield, T. Ryan, L. B. Reller and V. G. Fowler Jr., *Circulation*, 2001, **104**, 1029–1033.
9 E. Mylonakis and S. B. Calderwood, *N. Engl. J. Med.*, 2001, **345**, 1318–1330.
10 M. A. Olsen, J. Mayfield, C. Lauryssen, L. B. Polish, M. Jones, J. Vest and V. J. Fraser, *J. Neurosurg. Spine*, 2003, **98**, 149–155.
11 R. O. Darouiche, *N. Engl. J. Med.*, 2004, **350**, 1422–1429.
12 S. Lax, N. Sangwan, D. Smith, P. Larsen, K. M. Handley, M. Richardson, K. Guyton, M. Krezalek, B. D. Shogan, J. Defazio, *et al.*, *Sci. Transl. Med.*, 2017, **9**, eaah6500.
13 C. R. Arciola, D. Campoccia, P. Speziale, L. Montanaro and J. W. Costerton, *Biomaterials*, 2012, **33**, 5967–5982.
14 M. Razavi, D. S. Shepard, J. A. Suaya and W. B. Stason, *PLoS One*, 2014, **9**, e110133.
15 S. Kang and M. Elimelech, *Langmuir*, 2009, **25**, 9656–9659.
16 N. Thewes, P. Loskill, P. Jung, H. Peisker, M. Bischoff, M. Herrmann and K. Jacobs, *Beilstein J. Nanotechnol.*, 2014, **5**, 1501–1512.
17 Y. F. Dufrêne, *Trends Microbiol.*, 2015, **23**, 376–382.
18 S. Aguayo, N. Donos, D. Spratt and L. Bozec, *Nanotechnology*, 2015, **26**, 062001.
19 G. Mitchell, C.-A. Lamontagne, E. Brouillette, G. Grondin, B. G. Talbot, M. Grandbois and F. Malouin, *Mol. Microbiol.*, 2008, **70**, 1540–1555.
20 E. S. Ovchinnikova, B. P. Krom, H. J. Busscher and H. C. van der Mei, *BMC Microbiol.*, 2012, **12**, 281.
21 P. Herman-Bausier, S. El-Kirat-Chatel, T. J. Foster, J. A. Geoghegan and Y. F. Dufrêne, *mBio*, 2015, **6**, e00413–e00415.
22 T. Vanzieleghem, P. Herman-Bausier, Y. F. Dufrene and J. Mahillon, *Langmuir*, 2015, **31**, 4713–4721.
23 C. Spengler, N. Thewes, F. Nolle, T. Faidt, N. Umanskaya, M. Hannig, M. Bischoff and K. Jacobs, *J. Mol. Recognit.*, 2017, **30**, e2615.
24 C. Spengler, N. Thewes, P. Jung, M. Bischoff and K. Jacobs, *Nanoscale*, 2017, **9**, 10084–10093.

25 C. Berne, C. K. Ellison, A. Ducret and Y. V. Brun, *Nat. Rev. Microbiol.*, 2018, **16**, 616–627.
26 F. Rupp, L. Liang, J. Geis-Gerstorfer, L. Scheideler and F. Hüttig, *Dent. Mater.*, 2018, **34**, 40–57.
27 Z. Wang, M. Elimelech and S. Lin, *Environ. Sci. Technol.*, 2016, **50**, 2132–2150.
28 A. Beaussart, S. El-Kirat-Chatel, P. Herman, D. Alsteens, J. Mahillon, P. Hols and Y. F. Dufrêne, *Biophys. J.*, 2013, **104**, 1886–1892.
29 R. M. A. Sullan, J. K. Li, P. J. Crowley, L. J. Brady and Y. F. Dufrêne, *ACS Nano*, 2015, **9**, 1448–1460.
30 B. Reiser, L. González-García, I. Kanelidis, J. Maurer and T. Kraus, *Chem. Sci.*, 2016, **7**, 4190–4196.
31 K. J. Si, Y. Chen, Q. Shi and W. Cheng, *Adv. Sci.*, 2018, **5**, 1700179.
32 M. Bellion, L. Santen, H. Mantz, H. Hähl, A. Quinn, A. Nagel, C. Gilow, C. Weitenberg, Y. Schmitt and K. Jacobs, *J. Phys.: Condens. Matter*, 2008, **20**, 404226.
33 M. Lessel, O. Bäumchen, M. Klos, H. Hähl, R. Fetzer, M. Paulus, R. Seemann and K. Jacobs, *Surf. Interface Anal.*, 2015, **47**, 557–564.
34 C. Weidenmaier, A. Peschel, Y.-Q. Xiong, S. A. Kristian, K. Dietz, M. R. Yeaman and A. S. Bayer, *J. Infect. Dis.*, 2005, **191**, 1771–1777.
35 I. Maxe, C. Rydén, T. Wadström and K. Rubin, *Infect. Immun.*, 1986, **54**, 695–704.
36 A. Peschel, M. Otto, R. W. Jack, H. Kalbacher, G. Jung and F. Götz, *J. Biol. Chem.*, 1999, **274**, 8405–8410.
37 S. Bur, K. T. Preissner, M. Herrmann and M. Bischoff, *J. Invest. Dermatol.*, 2013, **133**, 2004–2012.
38 N. Thewes, P. Loskill, C. Spengler, S. Hümbert, M. Bischoff and K. Jacobs, *Eur. Phys. J. E: Soft Matter Biol. Phys.*, 2015, **38**, 140.
39 C. Spengler, F. Nolle, J. Mischo, T. Faidt, S. Grandthyll, N. Thewes, M. Koch, F. Müller, M. Bischoff, M. A. Klatt, *et al.*, *Nanoscale*, 2019, **11**, 19713–19722.
40 A. Beaussart, P. Herman, S. El-Kirat-Chatel, P. N. Lipke, S. Kucharíková, P. Van Dijck and Y. F. Dufrêne, *Nanoscale*, 2013, **5**, 10894–10900.
41 G. Zeng, T. Müller and R. L. Meyer, *Langmuir*, 2014, **30**, 4019–4025.
42 P. Herman, S. El-Kirat-Chatel, A. Beaussart, J. A. Geoghegan, T. J. Foster and Y. F. Dufrêne, *Mol. Microbiol.*, 2014, **93**, 356–368.
43 P. Herman, S. El-Kirat-Chatel, A. Beaussart, J. A. Geoghegan, T. Vanzieleghem, T. J. Foster, P. Hols, J. Mahillon and Y. F. Dufrêne, *Langmuir*, 2013, **29**, 13018–13022.
44 H. C. van der Mei, M. Rustema-Abbing, J. de Vries and H. J. Busscher, *Appl. Environ. Microbiol.*, 2008, **74**, 5511–5515.
45 C. Feuillie, C. Formosa-Dague, L. M. C. Hays, O. Vervaeck, S. Derclaye, M. P. Brennan, T. J. Foster, J. A. Geoghegan and Y. F. Dufrêne, *Proc. Natl. Acad. Sci. U. S. A.*, 2017, **114**, 3738–3743.
46 P. Herman-Bausier, C. Labate, A. M. Towell, S. Derclaye, J. A. Geoghegan and Y. F. Dufrêne, *Proc. Natl. Acad. Sci. U. S. A.*, 2018, **115**, 5564–5569.
47 R. M. Corrigan, D. Rigby, P. Handley and T. J. Foster, *Microbiology*, 2007, **153**, 2435–2446.
48 M. Rief, M. Gautel, F. Oesterhelt, J. M. Fernandez and H. E. Gaub, *Science*, 1997, **276**, 1109–1112.
49 F. Oesterhelt, D. Oesterhelt, M. Pfeiffer, A. Engel, H. E. Gaub and D. J. Müller, *Science*, 2000, **288**, 143–146.
50 D. T. Gruszka, F. Whelan, O. E. Farrance, H. K. H. Fung, E. Paci, C. M. Jeffries, D. I. Svergun, C. Baldock, C. G. Baumann, D. J. Brockwell, J. R. Potts and J. Clarke, *Nat. Commun.*, 2015, **6**, 7271.
51 C. Formosa-Dague, P. Speziale, T. J. Foster, J. A. Geoghegan and Y. F. Dufrêne, *PNAS*, 2016, **113**, 410–415.
52 P. Herman-Bausier, C. Valotteau, G. Pietrocola, S. Rindi, D. Alsteens, T. J. Foster, P. Speziale and Y. F. Dufrêne, *mBio*, 2016, **7**, e01529–e01516.

Electronic Supplementary Material (ESI) for Nanoscale.

Journal Name

ARTICLE TYPE

Cite this: DOI: 00.0000/xxxxxxxxxx

Electronic Supplementary Information for 'Different binding mechanisms of *Staphylococcus aureus* to hydrophobic and hydrophilic surfaces'

Erik Maikranz[a,‡], Christian Spengler[b,‡], Nicolas Thewes[b], Alexander Thewes[a], Friederike Nolle[b], Philipp Jung[c], Markus Bischoff[c], Ludger Santen[a] and Karin Jacobs[b]

1 Influence of surface delay time on hydrophilic and hydrophobic surfaces

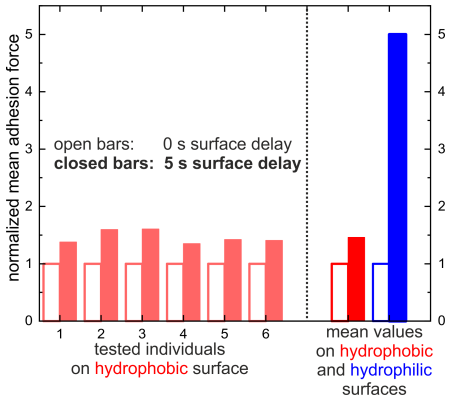

Fig. S1 Relative differences in mean adhesion forces for 6 individual cells on the hydrophobic surface compared to the more than one order of magnitude larger difference on the hydrophilic surface.

Figure S1 shows that for the tested cells on the hydrophobic surface, the increase in adhesion force was on average less than 50 %, while it increases more than 500 % in the hydrophilic case (see also Fig. 1 in the main text). Also, if we compare in how many cases a cell shows distinct adhesion to a surface (indicated by a detectable adhesion force in the retraction curve), this number is 100 % on the hydrophobic surfaces no matter what the surface delay time is. On hydrophilic surfaces, however, about 40 % of cells do not show adhesion for 0 s surface delay time while this value decreases to under 1 % after 5 s of surface delay.

[a]Theoretical Physics, Saarland University, Campus E2 6, D-66123 Saarbrücken, Germany
[b]Experimental Physics, Saarland University, Campus E2 9, D-66123 Saarbrücken, Germany
[c]Insitute of Medical Microbiology and Hygiene, Saarland University, D-66421 Homburg/Saar, Germany

2 Adhesion of *S. aureus* strains JE2 and N315 to hydrophilic and hydrophobic surfaces

Figure S2 shows the mean force-distance curves and the mean values of the adheion force and rupture lengths for 6 tested individuals each of the clinically relevant *S. aurues* strains, the USA300 CA-MRSA derivative JE2 and the HA-MRSA strain N315, on hydrophilic and hydrophobic surfaces, respectively. As described in the main text for strain SA113, for both strains here, the mean curves on hydrophilic surfaces reach lower forces and have a much larger standard deviation as the curves on hydrophobic surfaces. Although the number of tested individuals is not as large as for strain SA113, the probed cells nicely corroborate our finding discussed in the main text of the manuscript.

3 Model details

Our model extends the work of Thewes *et al.* [1] who described the bacterium as hard sphere decorated with macromolecules that is attached to a moving cantilever to simulate SCFS experiments. For computational purposes only the bottom part up to a certain height is covered by a fixed number of randomly distributed macromolecules. The length fluctuations, as well as mechanical responses to stretching of these macromolecules is modelled by Hooke's law where the stiffness of each macromolecule is drawn random from a distribution. The binding of individual molecules to the surface is modelled by a simple square potential with a given potential depth V and interaction range r. This binding allows the molecules to pull on the bacterium. The pulling forces on the bacterium are balanced by the bending of the cantilever (modelled as the extension of a spring), and the bacterium is moved to equilibrium position, between each step of the cantilever.

We modify this model by using worm-like chain (WLC) polymers with probabilistic parameters. The contour length L is drawn from a Weibull distribution while the Kuhn length B is sampled from a uniform distribution. To compute the response to stretching efficiently we use the well known approximation of the WLC model by Marko and Siggia [2]. For simplicity, we use

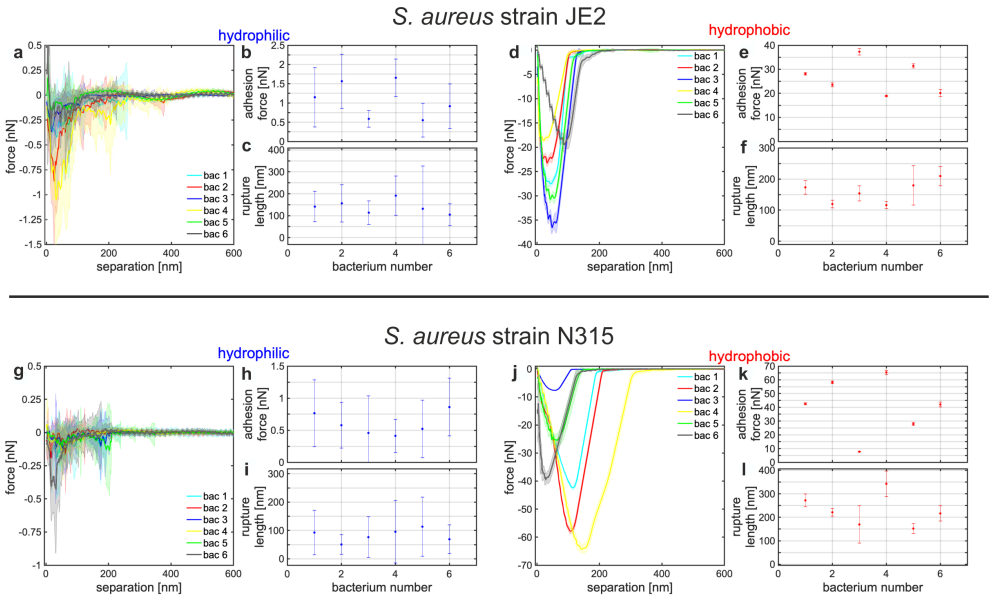

Fig. S2 (a,d,g,j) Mean SCFS retraction curves of 6 exemplary individual bacteria of each strain on hydrophilic (a,g) and hydrophobic surfaces (d,j) (shaded area is standard deviation). (b,c,e,f,h,i,k,l) Mean adhesion forces (b,e,h,k) and rupture lengths (c,f,i,l) extracted from single SCFS retraction curves of the cells (error bars are standard deviation).

the same energy for stretching and length fluctuations. To account for compression of the macromolecules, we introduce a rest length $l_0 = \sqrt{\frac{L \cdot B}{6}}$ below that the response is modelled as Hookean spring. Hence the energy E and force f of a macromolecule with stretch l are determined by

$$E(l) = k_B T \frac{L}{2B} \left(\frac{l - l_0}{L} \right)^2 \begin{cases} 2 + \frac{1}{1 - \frac{l - l_0}{L}} & , l_0 \leq l \\ 3 & , 0 \leq l \leq l_0 \end{cases}$$

$$f(l) = -\frac{k_B T}{2B} \begin{cases} 4\frac{l - l_0}{L} - 1 + \frac{1}{\left(1 - \frac{l - l_0}{L}\right)^2} & , l_0 \leq l \\ 6\frac{l - l_0}{L} & , 0 \leq l \leq l_0 \, . \end{cases}$$

Since the force model is non linear, we have to calculate the equilibrium position of the bacterium numerically, by simple bisectioning. Additional to changing the force response, we do not allow binding to the surface by mere proximity to the surface. If the macromolecule is in the range of the surface, it can bind with probability e^{-H}, where H represents a potential barrier. If the molecule is attached, it decreases it's energy by a binding energy V, and is able to pull on the bacterium.

The model parameters used, if not stated differently, are given in table S1. An overview of the simulation steps is given in Algorithm 1 SCFS-Simulation. In order to avoid artefacts from instantaneous cantilever steps, we subdivided each experimental cantilever step in hundred sub steps inside the simulation.

4 Parameter discussion

Kuhn lengths of proteins are typically in the range of $0.1 - 1$ nm[3–5] . As already mentioned in the main text, forces to unfold binding proteins are typically $0.1 - 0.4$ nN[5–7], and are structure and pulling speed-specific. The experimental estimation for the relevant protein length is difficult: While usually 0.36 nm per amino acid are used to estimate the length of a fully unfolded protein, some proteins detach before fully unfolding. We found that for relevant surface proteins of *Staphylococcus aureus* both behaviours are observed. ClfA for instance has a folded length of 25 nm and unfolds fully to a length of 285 nm before detaching[8] while Cna or SdrC do not unfold fully before detaching[9,10]. SasG is a well studied example which forms fibrils of 53 nm length while it is composed of several domains which, depending on the loading rate, can unfold independently to give a fully unfolded length of 505 nm[7,11,12]. In addition, the proteins are initially anchored in height of the membrane, but it's not clear if they stay or change their height within the membrane due to synthesis of new peptidoglycan. Therefore, it is not possible to deduce how far surface proteins protrude from the cell wall. Hence, rupture lengths do not need to correspond to the lengths of folded or even unfolded proteins. However, it is worth reminding that not just proteins might contribute to the adhesion but also teichionic acids or capsular polycarbonates. For these reasons, we will briefly discuss the influence of different length of macromolecules.

To vary the length of the involved macromolecules, we changed the scale parameter of the Weibull distribution (see Fig. S3, S4). Note that this does not only change the mean, but also the variance of the distribution. Interestingly, an increase in the scale parameter did not lead to a significant change in the initial part of the retraction curves. However, with increasing scale parameter, the minima of the retraction curves shift to higher separations while reaching bigger adhesion forces. Additionally, the rupture lengths increase substantially with increasing scale parameter. That behaviour is observed for all barrier heights, but for high barriers, is overshadowed by the stochastic response. The number of attached macromolecules (see Fig. S4) varies accordingly. This means that with a higher scale parameter more attached molecules are observed. However, for high barriers, the variance increases substantially, leading to overlapping curves. The increase of attached macromolecules with increasing scale parameter has its origin in the short interaction range of the surface. Just when macromolecules are long enough to get into the range of the surface potential, they are able to bind. If the cells have longer macromolecules, more of them can come into the range of the surface potential and can tether. If now more molecules of different lengths are bound to the surface, one would naively expect a change in the initial part of the retraction curve. However, as already mentioned, this is not observed, because the macromolecules show a non-linear WLC behaviour when stretched, and only contribute to the force when they are significantly extended in relation to their length. This lack of strong forces at small extensions is the reason why the initial part of the retraction curves shows no sensitivity to the changing scale parameter although more macromolecules bind to the surface. Because the macromolecules only contribute substantially to the force when they are strongly stretched, and because more and longer macromolecules bind, the adhesion force increases and shifts to higher distances. To conclude, if we compare two cells with longer and short macromolecules, the adhesion force of the cell with longer macromolecules increases and shifts to higher distances.

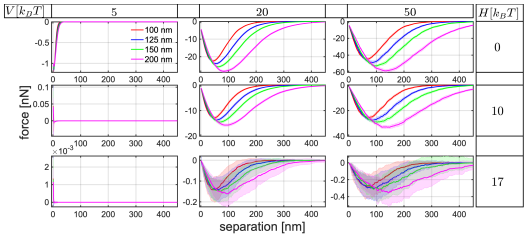

Fig. S3 Mean retraction curves for different potential depth V and barriers H, extracted from the first 10 retractions of 20 simulated cells with surface delay time of 5 s. Shaded area is standard deviation. Different colors correspond to scale parameters as indicated in the first panel.

5 Mean Retraction Plot with Delay Time Dependence

We discuss now the mean retraction curves for 5 s (blue) and 0 s (black) surface delay time belonging to figure 9 (see Fig. S5).

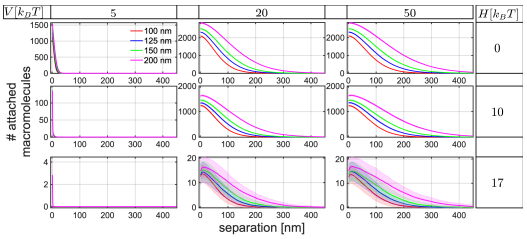

Fig. S4 Ensemble mean of the number of attached macromolecules for different potential depth V and barriers H, extracted from the first 10 retractions of 20 simulated cells with surface delay time of 5 s. Shaded area is standard deviation. Different colors correspond to scale parameters as indicated in the first panel.

The adhesion force, increases with increasing potential depth and drops for higher barriers. For low potential barriers, additional surface delay time increases the adhesion force only marginally. Yet, for high barriers, a substantial increase in adhesion force and stochasticity was observed. This conforms to the change in the number of involved macromolecules as discussed in the main text.

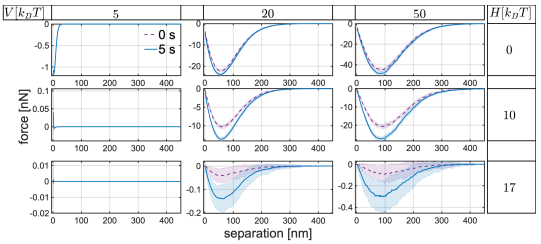

Fig. S5 Mean retraction curves for different potential depth V and barriers H, extracted from the first 10 retractions of 20 simulated cells. Shaded area is standard deviation. While blue solid lines indicate 5 s of surface delay time, purple dashed lines indicate 0 s.

Notes and references

1 N. Thewes, A. Thewes, P. Loskill, H. Peisker, M. Bischoff, M. Herrmann, L. Santen and K. Jacobs, *Soft Matter*, 2015, **11**, 8913–8919.

2 J. F. Marko and E. D. Siggia, *Macromolecules*, 1995, **28**, 8759–8770.

3 A. F. Oberhauser, P. E. Marszalek, H. P. Erickson and J. M. Fernandez, *Nature*, 1998, **393**, 181–185.

4 M. Rief, J. Pascual, M. Saraste and H. E. Gaub, *Journal of molecular biology*, 1999, **286**, 553–561.

5 F. Oesterhelt, D. Oesterhelt, M. Pfeiffer, A. Engel, H. E. Gaub and D. J. Müller, *Science (New York, N.Y.)*, 2000, **288**, 143–146.

6 M. Rief, M. Gautel, F. Oesterhelt, J. M. Fernandez and H. E. Gaub, *Science (New York, N.Y.)*, 1997, **276**, 1109–1112.

7 D. T. Gruszka, F. Whelan, O. E. Farrance, H. K. H. Fung, E. Paci, C. M. Jeffries, D. I. Svergun, C. Baldock, C. G. Bau-

Algorithm 1 SCFS-Simulation

procedure INITIALIZATION

procedure APPROACH
  while force trigger not reached & step possible **do**
    cantileverHeight ← cantileverHeight − stepSize
    procedure MAINUPDATES
    if wantToMeausure **then**
      procedure TAKE MEASUREMENT
    end
  end

procedure WAITING
  for given number of iterations **do**
    procedure MAINUPDATES
  end

procedure RETRACTION
  while inital cantilverHeight is not reached **do**
    cantileverHeight ← cantileverHeight + stepSize
    procedure MAINUPDATES
    if wantToMeausure **then**
      procedure TAKE MEASUREMENT
    end
  end

procedure MAINUPDATES
  for 200 iterations **do**
    for number of macromolecules **do**
      chose a random macromolecule & propose a random change in the stretch $l \mapsto l + U\Delta l$ where U is uniformly distributed in $[-1, 1]$
      if proposed length and distance to surface > 0 **then**
        accept l according to Metropolis algorithm
      end
      if macromolecule in range of surface potential **then**
        if macromolecule is attached **then**
          bind with probability e^{-H}
        else
          unbind with probability $e^{-(H-V)}$
        end
      else
        unbind
      end
    end
    update bacterium position by force balance of cantilever and all bound macromolecules via bisection and threshold 10^{-4} nm
  end

Table S1 Reference Parameters and Symbols

number of macromolecules N	5000
minimum macromolecule Kuhn-length	0.2 nm
maximum macromolecule Kuhn-length	1 nm
scale parameter for macromolecule length	125 nm
form parameter for macromolecule length	1.5 nm
radius of bacterium	500 nm
decorate area height (from bottom of bacterium)	50 nm
Spring constant of the cantilever	0.6 nN/nm
k_BT	4.1 pN nm
interaction range of surface potential r	2 nm
change of macromolecule length Δl	1 nm
macromolecule stretch	l [nm]
macromolecule Kuhn length	B [nm]
macromolecule contour length	L [nm]
macromolecule rest length	$l_0 = \sqrt{\frac{L_B}{6}}$ [nm]
potential barrier	$H[k_BT]$
potential depth	$V[k_BT]$

mann, D. J. Brockwell, J. R. Potts and J. Clarke, *Nature Communications*, 2015, **6**, 7271.

8 P. Herman-Bausier, C. Labate, A. M. Towell, S. Derclaye, J. A. Geoghegan and Y. F. Dufrêne, *Proceedings of the National Academy of Sciences of the United States of America*, 2018, **115**, 5564–5569.

9 P. Herman-Bausier, C. Valotteau, G. Pietrocola, S. Rindi, D. Alsteens, T. J. Foster, P. Speziale and Y. F. Dufrêne, *mBio*, 2016, **7**, year.

10 C. Feuillie, C. Formosa-Dague, L. M. C. Hays, O. Vervaeck, S. Derclaye, M. P. Brennan, T. J. Foster, J. A. Geoghegan and Y. F. Dufrêne, *Proceedings of the National Academy of Sciences of the United States of America*, 2017, **114**, 3738–3743.

11 R. M. Corrigan, D. Rigby, P. Handley and T. J. Foster, *Microbiology*, 2007, **153**, 2435–2446.

12 D. T. Gruszka, J. A. Wojdyla, R. J. Bingham, J. P. Turkenburg, I. W. Manfield, A. Steward, A. P. Leech, J. A. Geoghegan, T. J. Foster, J. Clarke and J. R. Potts, *Proceedings of the National Academy of Sciences*, 2012, **109**, E1011–E1018.

IV Influence of different macromolecules on bacterial adhesion

Authors: C. Spengler,[1,*] **F. Nolle**,[1,*] N. Thewes,[1] B. Wieland,[2] P. Jung,[2] M. Bischoff [2] and K. Jacobs [1,3]

[1] Experimental Physics and Center for Biophysics, Saarland University, 66123 Saarbrücken, Germany.
[2] Institute of Medical Microbiology and Hygiene, Saarland University, 66421 Homburg/Saar, Germany.
[3] Max Planck School Matter to Life, Jahnstraße 29, 69120 Heidelberg, Germany
[*] These authors contributed equally to this work.

*International Journal of Molecular Sciences, 2021, **22**, 11952*

https://doi.org/10.3390/ijms222111952

Author contributions:
C.S.: data curation, investigation, methodology, visualization, writing–original draft, and writing–review and editing. ***F.N.****: data curation, investigation, methodology, visualization, writing–original draft, and writing–review and editing. N.T.: data curation, investigation, methodology, and writing–review and editing. B.W.: investigation, and writing–review and editing. P.J.: methodology, and writing–review and editing. M.B.: data curation, conceptualization, methodology, supervision, and writing–review and editing. K.J.: conceptualization, methodology, supervision, and writing–review and editing. All authors have read and agreed to the published version of the manuscript.*

Abstract – The adhesion of *Staphylococcus aureus* to abiotic surfaces is crucial for establishing devicerelated infections. With a high number of single-cell force spectroscopy measurements with genetically modified *S. aureus* cells, this study provides insights into the adhesion process of the pathogen to abiotic surfaces of different wettability. Our results show that *S. aureus* utilizes different cell wall molecules and interaction mechanisms when binding to hydrophobic and hydrophilic surfaces. We found that covalently bound cell wall proteins strongly interact with hydrophobic substrates, while their contribution to the overall adhesion force is smaller on hydrophilic substrates. Teichoic acids promote adhesion to hydrophobic surfaces as well as to hydrophilic surfaces. This, however, is to a lesser extent. An interplay of electrostatic effects of charges and protein composition on bacterial surfaces is predominant on hydrophilic surfaces, while it is overshadowed on

hydrophobic surfaces by the influence of the high number of binding proteins. Our results can help to design new models of bacterial adhesion and may be used to interpret the adhesion of other microorganisms with similar surface properties.

International Journal of
Molecular Sciences

MDPI

Article

Using Knock-Out Mutants to Investigate the Adhesion of *Staphylococcus aureus* to Abiotic Surfaces

Christian Spengler [1,†], Friederike Nolle [1,†], Nicolas Thewes [1], Ben Wieland [2], Philipp Jung [2], Markus Bischoff [2] and Karin Jacobs [1,3,*]

[1] Experimental Physics and Center for Biophysics, Saarland University, 66123 Saarbrücken, Germany; c.spengler@physik.uni-saarland.de (C.S.); f.nolle@physik.uni-saarland.de (F.N.); nicolas.thewes@web.de (N.T.)
[2] Institute of Medical Microbiology and Hygiene and Center for Biophysics, Saarland University, 66421 Homburg, Germany; ben.wieland@uks.eu (B.W.); philipp.jung@uks.eu (P.J.); markus.bischoff@uks.eu (M.B.)
[3] Max Planck School Matter to Life, Jahnstraße 29, 69120 Heidelberg, Germany
* Correspondence: k.jacobs@physik.uni-saarland.de; Tel.: +49-(0)681-302-71777
† These authors contributed equally to this work.

Abstract: The adhesion of *Staphylococcus aureus* to abiotic surfaces is crucial for establishing device-related infections. With a high number of single-cell force spectroscopy measurements with genetically modified *S. aureus* cells, this study provides insights into the adhesion process of the pathogen to abiotic surfaces of different wettability. Our results show that *S. aureus* utilizes different cell wall molecules and interaction mechanisms when binding to hydrophobic and hydrophilic surfaces. We found that covalently bound cell wall proteins strongly interact with hydrophobic substrates, while their contribution to the overall adhesion force is smaller on hydrophilic substrates. Teichoic acids promote adhesion to hydrophobic surfaces as well as to hydrophilic surfaces. This, however, is to a lesser extent. An interplay of electrostatic effects of charges and protein composition on bacterial surfaces is predominant on hydrophilic surfaces, while it is overshadowed on hydrophobic surfaces by the influence of the high number of binding proteins. Our results can help to design new models of bacterial adhesion and may be used to interpret the adhesion of other microorganisms with similar surface properties.

Keywords: bacterial adhesion; single-cell force spectroscopy; *Staphylococcus aureus*; *Staphylococcus aureus* knock-out mutants; surface charge; hydrophobicity

Citation: Spengler, C.; Nolle, F.; Thewes, N.; Wieland, B.; Jung, P.; Bischoff, M.; Jacobs, K. Using Knock-Out Mutants to Investigate the Adhesion of *Staphylococcus aureus* to Abiotic Surfaces. *Int. J. Mol. Sci.* **2021**, *22*, 11952. https://doi.org/10.3390/ijms222111952

Academic Editors: Lúcia Chaves Simões and Manuel Simões

Received: 2 October 2021
Accepted: 30 October 2021
Published: 4 November 2021

1. Introduction

Staphylococcus aureus is an opportunistic pathogen associated with different community and hospital acquired infections [1]. One reason for its high infectivity is that the cells can attach to various surfaces to form multicellular aggregates embedded in an extracellular matrix, called biofilms, in which the cells are protected against many therapeutics and the human immune system [2–6]. Therefore, the adhesion of cells and biofilm formation can take place on biotic surfaces as well as on abiotic surfaces, such as implanted medical devices. Due to the latter, the organism is a major cause of implant-related infections with severe consequences for the patient's health [7–12]. Hence, understanding and controlling the adhesive behavior of *S. aureus* is of fundamental importance for health care and engineering [13,14].

The state-of-the-art method in quantitative bacterial adhesion research is AFM-based force spectroscopy with single bacterial probes ('single-cell force spectroscopy', SCFS) [15–20]. This method allows for the investigation of many different mechanisms on a single-cell or even molecular level. For instance, it can be performed on bare or conditioned surfaces, biotic or abiotic, as well as with pretreated cells [21–25].

Int. J. Mol. Sci. 2021, 22, 11952

As demonstrated by SCFS, bacterial adhesion to hydrophobic surfaces is governed by cell wall macromolecules that tether to the surface [6,26–28]. As a consequence, the adhesive strength of a single cell is determined by the number of contact-forming macromolecules and by the strength of each individual binding site, whereby one macromolecule could also have more than one of these binding sites. In other words, the adhesive energy is the integral of the negative part of a force–distance curve upon retraction. Of note, important adhesion parameters, such as the bacterial contact area to solid surfaces, highly depend on the individual cell [29] as well as on the position at the cell wall [30]. Thus, bacterial adhesion and its strength is—to a large extent—cell-individual and, therefore, general statements concerning the adhesion of certain cell types can only be derived with good statistics.

Macromolecules play a crucial role in adhesion to the natural environment and are important adhesion factors [31–33]. For instance, it was found that *S. aureus* cells lacking cell wall teichoic acids adhere more weakly to human endothelial [31] and epithelial cells [32] than wild-type bacteria and that surface anchored proteins are important for nasal colonization [33]. Other work demonstrated that individual adhesion factors such as fibronectin-binding protein A and clumping factor B are important for the ability of *S. aureus* to adhere to endothelial cells and to human-desquamated nasal epithelial cells, respectively [34,35].

Nevertheless, apart from the studies showing reduced adhesion of *S. aureus* cells lacking cell wall teichoic acids or the D-alanylation of lipoteichoic acids to polystyrene [36,37], no quantitative analysis of the impact of bacterial macromolecules on adhesion to abiotic surfaces has yet been performed at the single cell level. Therefore, it is still unclear which macromolecules of the bacterial cell wall are mainly responsible for adhesion to abiotic surfaces with highly different surface energies.

In this paper, we characterize the role of different types of surface macromolecules in the adhesion process of *S. aureus* cells to abiotic surfaces (i. e., substrates without any surface conditioning layer). Our research is based on SCFS of *S. aureus* SA113 knock-out mutant strains that exhibit changes in cell wall macromolecular properties. Their adhesion properties were investigated on hydrophilic and hydrophobic Si wafer-based substrates and compared with the corresponding data of the wild-type that was recently published [28].

Considering that the investigated groups of surface molecules are quite common in the microbial world and have several general properties (e. g., hydrophobic domains on proteins and sugar-containing backbone in teichoic acids), the outcome of this study may also be of relevance to understanding the adhesive behavior of many other bacterial species. Even for other microorganisms, such as fungi or unicellular parasites, our results may help elucidate the process of adhesion to abiotic surfaces and the role of the surface hydrophobicity of various substrates.

2. Results and Discussion

2.1. Comparing the Adhesion of Knock-Out Mutants to Hydrophobic and Hydrophilic Surfaces

To provoke highly different adhesion scenarios [28], we use two types of very smooth abiotic surfaces that we have characterized in detail: bare (hydrophilic) and silane-coated (hydrophobic) Si wafers. Adhesion studies were performed with the knock-out mutants of *Staphylococcus aureus* strain SA113. This biofilm-positive laboratory strain is a common platform to study cell wall macromolecules of *S. aureus* [31,38–40]. For an in-depth analysis of the cell wall macromolecular contribution to the staphylococcal adhesion process, mutants exhibiting the following changes in cell wall properties were used:

- SA113 Δ*srtA*: deficient in covalently bound cell wall proteins due to a deletion of the gene *srtA* encoding the enzyme sortase A that catalyzes the covalent linkage of proteins into the cell wall [33,41].

- SA113 Δ*tagO*: lacking the gene *tagO* encoding a glycosyltransferase that catalyzes the first committed step of wall teichoic acid (WTA) synthesis (but having lipoteichoic acids) [31].
- SA113 Δ*dltA*: lacking the gene *dltA* encoding the D-alanine-D-alanyl carrier protein ligase catalyzing the first step in the D-alanylation of lipoteichoic acids (LTAs). As a consequence, the wall and lipoteichoic acids of this mutant lack D-alanine, leading to an increased negative surface charge of the cell wall [39].

In order to analyze differences in the adhesion of SA113 knock-out mutants to hydrophobic compared with hydrophilic surfaces, exemplary force–distance curves and box plots of the mean adhesion forces as shown in Figure 1 were calculated: for the SA113 Δ*srtA* cells, the retraction curves on hydrophobic surfaces are cup-shaped with a rather homogeneous, small standard deviation. In contrast, on the hydrophilic surface, the curves feature several minima and have rather broad standard deviation. While the curves overlap less on the hydrophobic surface and have distinctly different minima, they show a large overlap with minima at rather similar values on the hydrophilic surface. This observation are confirmed by the box plots of the mean adhesion forces in Figure 1 b): in the hydrophobic case, they differ between 0 nN and 8 nN, while they are in the range between 0 nN and 2 nN in the hydrophilic case. The distributions of the adhesion forces on the hydrophilic and hydrophobic surfaces therefore also display a high level of significance.

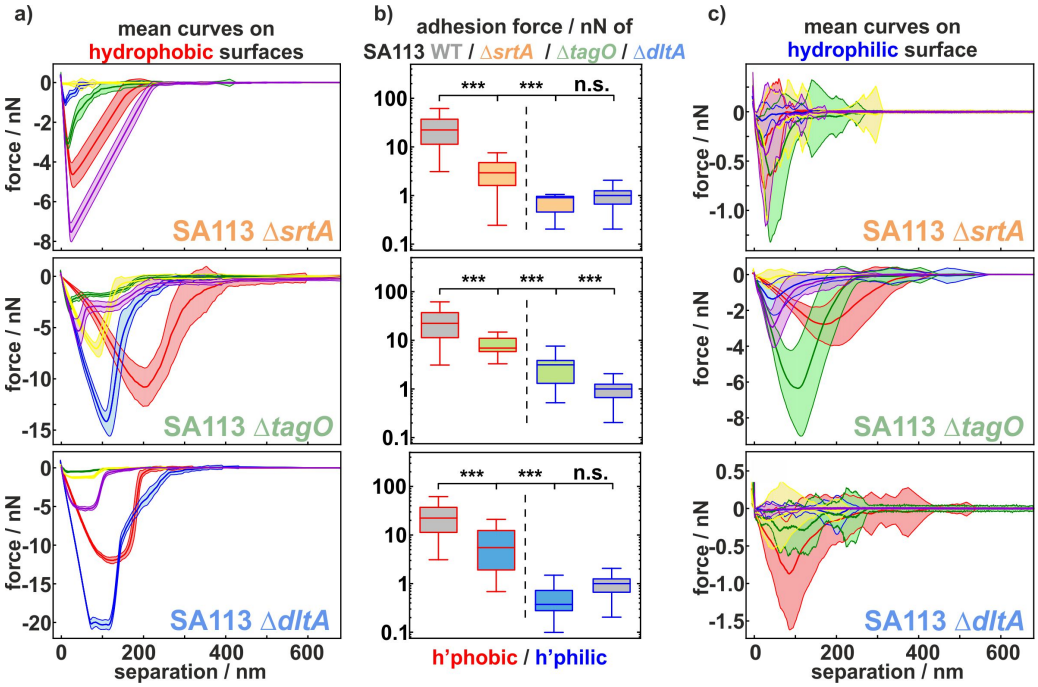

Figure 1. Adhesive strength of SA113 knock-out mutants to hydrophobic and hydrophilic surfaces. (**a**,**c**) For five individual mutant cells of each type, represented by five different colours, mean retraction parts of over 50 measured force–distance curves (with standard error as the shaded area) on both surfaces are shown. (**b**) In addition, box and whisker plots (min-to-max) of the adhesion force on hydrophobic and hydrophilic surfaces are shown for all tested mutant cells compared with the SA113 wild-type (WT) cells [28] (gray) in a logarithmic scale. Comparison between data sets was performed by ordinary one-way ANOVA and Dunnett's test for multiple comparison as well as an unpaired t-test for the pairwise comparison between the adhesion of the mutants to hydrophobic and hydrophilic surfaces: n.s., $p > 0.05$; ***, $p < 0.001$.

For SA113 Δ*tagO* cells, the situation is very different: The differences in curves shapes between hydrophobic and hydrophilic surfaces are much smaller, and the force scale differs by only a factor of two. Consequently, the differences in the distribution of the adhesion forces are quite small, though still significantly different.

This is contrasted by the adhesion of SA113 Δ*dltA* cells: Here, the curve shapes strongly differ between hydrophobic and hydrophilic surfaces and the force scale differs by more than one order of magnitude. The curves are cup-shaped on the hydrophobic surface with a very small, constant standard deviation, while the cells of the *dltA* deletion mutant display mostly irregular curve shapes with rather large standard deviations on the hydrophilic surfaces. However, the mean adhesion forces on the hydrophobic surface vary greatly between cells and are located between 1 nN and 22 nN, while all values on the hydrophilic surface are in the range of 0 nN to 3 nN. The difference between the distribution of adhesion on hydrophobic and hydrophilic surfaces is therefore also significant for this mutant strain.

Compared with the wild-type, all mutant strains show significantly lower adhesion forces on hydrophobic surfaces. In contrast, this is not the case on hydrophilic surfaces. Due to the generally low adhesion, no significant difference can be seen between the SA113 WT cells and the SA113 Δ*srtA* and SA113 Δ*dltA* cells. Only the SA113 Δ*tagO* cells show significantly higher adhesion forces on hydrophilic surfaces compared with the wild-type.

At this stage, several properties of the adhesion process can already be deduced: obviously, D-alanine residues of SA113 Δ*dltA* have a completely different influence on hydrophobic compared with hydrophilic surfaces. For cells without wall teichoic acids (SA113 Δ*tagO*), which type of substrate they adhere to is relatively unimportant. SA113 Δ*srtA* cells are somewhere between the other types. From the box and whisker plots, it can be stated that, for SA113 Δ*srtA* and SA113 Δ*dltA* cells, the number of adhesive molecules on the hydrophobic surface is much larger than on the hydrophilic surface. For SA113 Δ*tagO* cells, this difference seems quite small [28].

To analyze the adhesion behavior in more detail, several measures of the adhesion process of all mutant cells are compared with the measures of the wild-type from Reference [28]. The retraction part of each force–distance curve was evaluated in order to characterize the strength of adhesion. Hence, the maximum force between a surface and an individual cell ('adhesion force') was calculated. In addition, the 'rupture length' depicting the distance at which bacterium and surface lose contact was measured. Especially on hydrophobic surfaces, bacterial cells are also subject to a distinct attraction before reaching the surface, which is mediated by surface macromolecules ('snap-in event') [6]. We evaluated this mechanism with respect to the distance at which attraction started ('snap-in separation'), as detailed in the next sections. Moreover, all bacterial strains used were analyzed for their surface charge to enable a more precise interpretation of the adhesion data.

2.2. Comparing the Surface Charge of Knock-Out Mutants to the Parental Strain

For a better understanding of how the charge of the cell surface affects bacterial adhesion, all of the bacterial strains used in this work were examined for their surface charge (see Figure 2). It is immediately apparent that all of the bacterial strains used here have a positive binding affinity to cytochrome *c* and thus possess a negative surface charge. However, there are large differences in the percentage of binding affinity: while the SA113 Δ*srtA* cells have a similar surface charge to the parental strain, the two teichoic acid mutants show an increased binding affinity to cytochrome *c*. SA113 Δ*srtA* cells lack most of the cell-wall-anchored proteins of this species, so they most likely have a lower total protein density in their cell wall, although this does not seem to change the surface charge from that of the wild-type. On the contrary, teichoic acids are considered a major factor in the formation of the overall surface charge of bacterial cells [42]. Therefore, SA113 Δ*dltA* cells lacking the positively charged D-alanine groups linked to teichoic acids carry a higher negative surface charge than wild-type cells. However, it is unknown yet whether a lack of teichoic acids directly leads to a cell surface of lower negative charge or if this lack

provokes other charge-compensating effects. Notably, SA113 Δ*tagO* cells lacking the cell wall teichoic acids [31] also captured larger amounts of the cationic protein cytochrome *c* on their cell surface than SA113 wild-type (WT) cells, suggesting an increased negative surface charge, although a rather large inter-repeat variation was noticed with this mutant. This large variation in SA113 Δ*tagO* cells may also only be explained by the absence of teichoic acids, which account for up to 40% of the cell wall biomass. The lack of wall teichoic acids could leave space for additional proteins to bind to the peptidoglycan and/or adhere to the cell wall at sites usually occupied by teichoic acids, leading to greater variation in protein composition at the bacterial cell surface.

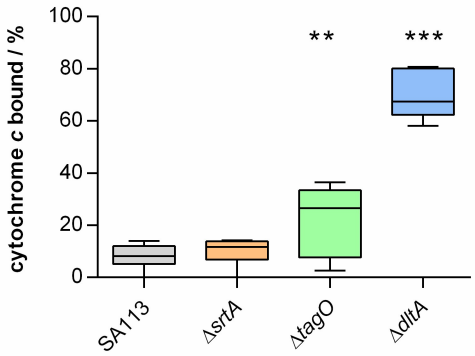

Figure 2. Surface charge of SA113 and its knock-out mutants. Binding capacities of the cationic protein cytochrome *c* by SA113 and its knock-out mutants. Data are presented as box and whisker plot (min-to-max) obtained from six to eight independent experiments. Comparison between data sets was conducted by ordinary one-way ANOVA and Dunnett's test for multiple comparison: **, $p < 0.01$; ***, $p < 0.001$.

2.3. Statistical Analysis of Mutants Adhesion to Hydrophobic Substrates

In line with our recent observations indicating a major impact of cell wall proteins on the adhesion force of *S. aureus* (wild-type, see gray bars in Figure 3) to hydrophobic surfaces [6,28], we observed markedly reduced adhesion forces of the SA113 Δ*srtA* mutant (see Figure 3a), which lacks the majority of covalently bound proteins on the bacterial cell wall. Interestingly, the adhesion strength of SA113 cells to the hydrophobic surface is also markedly affected, when the teichoic acid composition of the bacterial cell wall is altered. Therefore, both teichoic acid mutants (SA113 Δ*tagO* and SA113 Δ*dltA*) show slightly higher adhesion forces than the SA113 Δ*srtA* mutant with values around 10 nN.

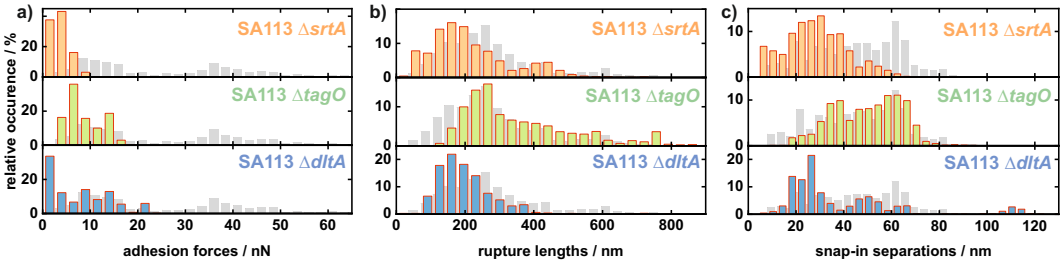

Figure 3. Histograms of all measured values of adhesion force (**a**), rupture length (**b**), and snap-in separation (**c**) of 18 single SA113 Δ*srtA*, 16 single SA113 Δ*tagO*, and 17 single SA113 Δ*dltA* cells on hydrophobic surfaces. Additionally, the corresponding values of the SA113 WT population are shown in gray [28].

Moreover, similar to the SA113 wild type, the histograms of the rupture lengths of all mutant cells show an extended rupture length range (see Figure 3b). For the SA113 Δ*srtA* and SA113 Δ*dltA* cells, most of the values are in the range of 100–200 nm and are thus smaller than the ones seen with SA113 WT cells (200–300 nm). In contrast, the majority of values for the SA113 Δ*tagO* cells are at slightly higher values of almost 300 nm. Regarding the maximum range of the measured distribution of rupture lengths, the highest values measured for SA113 Δ*srtA* (400–500 nm) and SA113 Δ*dltA* cells (approx. 400 nm) are smaller than for the wild type (approx. 650 nm). The SA113 Δ*tagO* cells exhibit the highest values here again, with another maximum at a rupture length of 750 nm. This means that the rupture lengths of SA113 Δ*srtA* and SA113 Δ*dltA* are slightly reduced compared with SA113 WT cells while SA113 Δ*tagO* cells display on average slightly increased rupture lengths.

Of note, all mutant cells show a distinct snap-in event in the approach part of their force–distance curves so that a snap-in separation was determined (see Figure 3c). For SA113 Δ*srtA* cells, the snap-in separations are in the range of 10–60 nm and are thus considerably smaller than the ones seen with SA113 WT cells. For SA113 Δ*tagO* cells, a distribution of snap-in separation very similar to that seen for cells of the parental strain can be observed. The histogram of snap-in separations of SA113 Δ*dltA* cells features several maxima: The first at around 25 nm and the second at around 50 nm are the most prominent, but even values as high as 110 nm, which is even higher than the values seen with SA113 WT cells, can be observed. The changed shape of the histogram indicates a strong effect due to the inactivation of *dltA*.

The most striking observation on the hydrophobic surface is the markedly reduced adhesive strength of all mutants compared with the wild-type cells. This suggests that covalently bound cell wall proteins as well as wall teichoic acids and the properties of D-alanine groups in teichoic acids, have a strong—direct or indirect—influence on the strength of adhesion to this type of surface.

Considering relevant forces, we can again state that electrostatic interactions seem to play a minor—or rather indirect—role in adhesion to hydrophobic surfaces that feature a negative surface potential [43]. This observation becomes particularly evident when analyzing the surface charge (see Figure 2) in comparison with the adhesion force of SA113 WT cells and the mutants. Although SA113 Δ*srtA* cells have a surface charge comparable with the wild-type, the adhesion is strongly reduced. Thus, charge effects cannot be responsible for the reduced adhesion on hydrophobic surfaces and the answer is rather found in the absence of most cell-wall-anchored proteins. Assuming that a lower protein density in the bacterial cell wall directly leads to a lower number of tethering macromolecules during the adhesion process, the lower adhesion strength of SA113 Δ*srtA* cells fits well with our hypothesis that proteins are a major factor affecting bacterial adhesion to hydrophobic surfaces [6,28].

However, looking at the two teichoic acid mutants, a putative role of bacterial cell surface charge in adhesion to hydrophobic surfaces becomes apparent.

The higher negative surface charge of SA113 Δ*dltA* and SA113 Δ*tagO* cells might account for the strongly reduced adhesion on hydrophobic surfaces [39]. However, SA113 Δ*tagO* cells do not show a large variation in adhesion strength, as is seen for the charge (see Figure 2), which would be anticipated if its adhesion were mainly influenced by surface charge. When compared, the two teichoic acid mutants also show no major differences in adhesion forces, but there are clear differences in cytochrome *c* binding affinity. This implies that electrostatic interaction does not dominate bacterial adhesion to hydrophobic surfaces but may play a role to some extent.

Very interestingly, no matter what type of surface macromolecules is knocked out, the adhesion capability is reduced to a quite large extent: the SA113 Δ*srtA* cells exhibit only one seventh to one eighth of the adhesion force of the SA113 WT cells, while both teichoic acid mutants exhibit only one third of the force of the wild-type cells (see Figure A1). A likely explanation for this observation is that the absence of a class of macromolecules

leave an altered environment for the remaining macromolecules (e.g., steric hindrance). Nevertheless, covalently bound surface proteins seem to have the biggest influence on adhesive strength [44–46].

It also cannot be excluded that the lack of cell wall teichoic acids or even of the alanine-groups of teichoic acids may change the protein composition of the cell wall and therefore alter the adhesion process. The translocation of proteins from their site of synthesis to the cell wall is a highly complex process involving many mechanisms and requires a specific interplay of charges, enzymes, and ions [47,48]. For example, cations, charge, and gradients in pH value inside the cell envelope influence protein folding, structure, and function [49]. Furthermore, the microenvironment of the cell wall is strongly influenced by the presence (or absence) of teichoic acids and, e. g., their D-alanine groups [42,50]. Moreover, it has been shown that D-alanylation directly influences protein expression [51–53].

After having elucidated the rather complex interplay of surface macromolecules defining adhesive strength on hydrophobic surfaces, we can now speculate about their influence on snap-in separations and rupture lengths. Most notably, the snap-in event is still observable for all mutants, whereas it it is no longer observed in SA113 WT cells in which the surface proteins have been degraded by proteases or cross-linked by glutaraldehyde [6]. Therefore, for all investigated cells, the number of surface factors can still be considered sufficient to induce this process. Additionally, the very reproducible and rather smooth shapes of the retraction curves for each individual cell (see Figure 1) supports the assumption of a rather high number of surface macromolecules participating in adhesion to hydrophobic surfaces [28].

The results of the SA113 Δ*srtA* cells show that sortase A-mediated covalently bound cell wall proteins have a stronger influence on the snap-in event, the first contact with the surface, than on the rupture length, denoting the last contact to the surface. This observation might be explained by the pure reduction in the density of surface proteins: The snap-in event occurs as soon as enough thermally fluctuating surface molecules reach the surface and bind to it. If the overall density is reduced—as it can be safely assumed for SA113 Δ*srtA* cells—this number is reached 'later', meaning at shorter distances to the surface, resulting in a decreased snap-in separation. The exact same reasoning holds true for the decreased rupture length: The cells lose contact at a distance where not enough proteins bind to the substrate anymore, which is probably earlier when the protein density on the bacterial cell surface is reduced than when, for fewer proteins, the force on each protein is increased, which can lead to an earlier (at smaller distance) detachment from the surface. However, the influence of covalently bound surface proteins on the rupture length is rather small. In other words, the strength of adhesion and snap-in separation on hydrophobic surfaces is largely determined by the presence of cell-wall-anchored proteins (CWAPs), but these are not necessarily the molecules that maintain final contact with the surface and thus determine the rupture length.

The slightly increased rupture lengths for SA113 Δ*tagO* cells may, without further experiments, only be explained by indirect secondary effects: For example, it is possible that at least some of the surface areas of the bacterial cell wall that are occupied by WTAs in wild-type cells are filled by more rather long CWAPs, resulting in some force–distance curves with an increased rupture length. This difference in protein composition may not have an influence on the snap-in separation because, in this case, a great number of surface proteins tether to the surface.

One bacterium out of the 17 SA113 Δ*dltA* cells shows significantly higher snap-in separation than the SA113 WT cells, with values around 110 nm. This outlier is suprising since electrostatic interactions between this mutant and the surface should generally be more repulsive than for the wild-type cells and should not lead to increased snap-in separations. However, if this outlier is to be explained, given that a SA113 Δ*dltA* mutant displays reduced activity of autolysins [54], which are known to smoothen the bacterial cell surface [55], it is conceivable that the higher roughness of the cell surface, coupled with some flexibility, could lead to more pronounced snap-in separations. Alternatively,

Int. J. Mol. Sci. **2021**, *22*, 11952

SA113 Δ*dltA* mutants may accumulate varying amounts of extracellular milieu-localized proteins on the cell surface, such as the extracellular adherence protein Eap, which is known to bind preferentially to (poly-) anionic molecules [56].

2.4. Statistical Analysis of Mutants Adhesion to Hydrophilic Substrates

The principal shape of the adhesion force histograms (see Figure 4a) of SA113 Δ*srtA* and SA113 Δ*dltA* cells are similar to each other and to the histograms of the wild-type cells: Most values are located at forces near 0 nN and a smooth decay of the distribution towards higher forces can be observed. Therefore, the values of SA113 Δ*srtA* cells (about 40% of the values are close to 0 nN and the distribution ends at around 4 nN) are almost the same as the values of the SA113 WT cells (about 25%, 4 nN). SA113 Δ*dltA* cells adhere slightly less strongly to the substrate: more values (about 60%) are located close to 0 nN and the decay of the distribution is steeper than for the wild-type. In contrast, SA113 Δ*tagO* cells adhere more strongly than SA113 WT cells and the adhesion forces display a very different distribution: They have a high number of values around 3 nN and maximal values going up to 12 nN (see Figure A2).

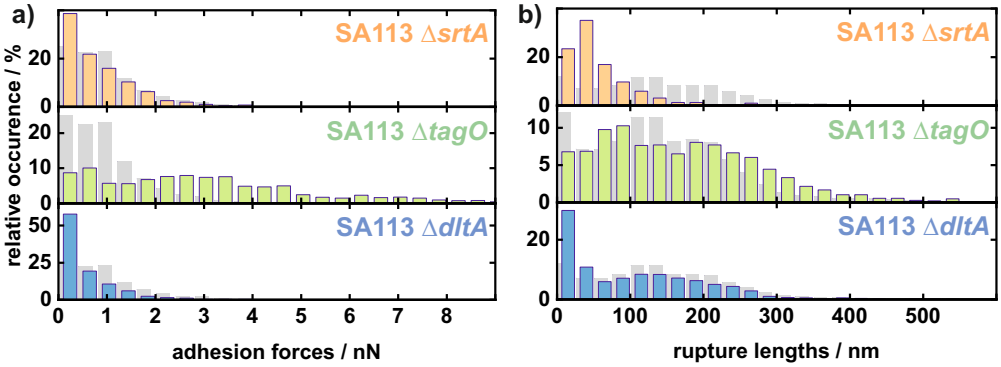

Figure 4. Histograms of all measured values of adhesion force (**a**) and rupture length (**b**) of 11 single SA113 Δ*srtA*, 15 single SA113 Δ*tagO*, and 18 single SA113 Δ*dltA* cells on hydrophilic surfaces. The corresponding values of an SA113 WT population are shown in gray [28].

As for the rupture lengths, the SA113 Δ*tagO* cells show slightly larger values (up to 600 nm) than the SA113 WT cells. However, the SA113 Δ*dltA* cells follow almost the same shape of distribution as the SA113 WT cells but tend to have smaller values with more than twice as many values at very low rupture lengths. The SA113 Δ*srtA* cells exhibit a distribution with a maximum below 50 nm, with occasionally higher maximal rupture lengths of about 400 nm but mainly up to 200 nm (see Figure 4b).

Adhesion forces are almost not affected by the absence of covalently bound surface proteins, whereas rupture lengths are markedly decreased. The latter implies that cell-wall-anchored proteins bind to hydrophilic surfaces and are on average longer or can be unfolded to a larger extent than other tethering macromolecules. The more minor effect of lacking covalently bound cell wall proteins on the adhesive strength to hydrophilic surfaces may be interpreted in the following way: either the covalently bound proteins have only a few hydrophilic residues (per protein or in total) able to interact with this type of surface (most likely through hydrogen bonds [28]), or there are—even without covalently bound proteins—so many surface molecules/proteins that they already occupy all possible binding sites in which the number may be limited due to interaction between different surface macromolecules. The mutant cells lacking wall teichoic acids (SA113 Δ*tagO*) show evidence for wall teichoic acids not contributing directly to the adhesion of *S. aureus* to abiotic hydrophilic substrates or at least their contribution is small compared with the adhesive strength exerted by other surface molecules. However, since we attribute

bacterial adhesion solely to the binding of cell wall macromolecules [16,28,57,58], the rising adhesive strength seen with SA113 Δ*tagO* cells may also be explained by a change in protein composition due to the absence of teichoic acids. Additional proteins important for adhesion to hydrophilic surfaces on the cell surface or a higher binding affinity of the remaining cell wall macromolecules could lead to this increased adhesion force. Both hypotheses are in line with the observation that *S. aureus tagO* mutants show a higher degree of cell aggregation [36], which might be caused by unusual protein–protein interactions that are in wild-type cells precluded by WTAs. On the other hand, for SA113 Δ*dltA* cells lacking D-alanine but not the total wall and lipoteichoic acids, a reduction in adhesion is observed compared with the wild-type. This is consistent with the results made with the SA113 Δ*dltA* cells on glass [37]. This could either indicate that teichoic acids play a minor role and that this was only overshadowed by the altered cell wall macromolecule composition in the SA113 Δ*tagO* cells. However, an equally likely reason could be a charge effect. The SA113 Δ*dltA* cells are distinctly more negatively charged compared with the wild-type as well as other mutants (see Figure 2). The reason for this could be that the formation of hydrogen bonds in particular, which seem to dominate adhesion to hydrophilic substrates [28], is influenced by altered electrostatic interactions on the bacterial cell surface induced by the *dltA* mutation. The dependence of the adhesion on the charge will be investigated in future measurements.

In contrast with SA113 Δ*srtA* cells, the rupture lengths of SA113 Δ*tagO* and SA113 Δ*dltA* cells were only slightly reduced, if at all. This suggests that most likely—as described above—the on average rather long covalently bound surface proteins contribute to the adhesion of teichoic acid mutants to hydrophilic substrates and seem to make the last contact to the surface. If teichoic acids themselves bind to the surface, they usually do not contribute markedly to the rupture lengths. This might be due to the natures of both macromolecules. Teichoic acids, being composed of glycerol phosphate or ribitol phosphate, and carbohydrates linked via phosphodiester bonds most likely do not form a complex tertiary structure that is usually seen with proteins. As a consequence, teichoic acids most likely exhibit only small stretching capabilities. Proteinaceous adhesion molecules, in contrast, are usually folded to yield a complex tertiary structure important to their functionality.

In summary, for all tested knock-out mutants of *S. aureus*, we found that the adhesive strength is reduced to a large extent (about an order of magnitude) on hydrophobic surfaces, no matter which specific type this might be (see Figure 3). The adhesion of *S.aureus*—at least on hydrophobic surfaces—is thus based on a very efficient interaction of the different types of surface macromolecules investigated. This result indicates that, for theoretical modelling, the description of a protein–protein interaction of the cell wall molecules is an important task, parallel to characterizing the tethering and the detaching phases.

All experimental results obtained from mutant cells can be explained by the hypothesis that the adhesion to hydrophobic surfaces is meditated by the hydrophobic interaction between the substrate and hydrophobic residues of a large number of surface macromolecules. On hydrophilic surfaces, however, we hypothesize that a quite small number of macromolecules tether to the surface, probably by formation of directional hydrogen bonds. Hence, bond formation is slower, as can be seen by the drastically enhanced adhesive strength when applying an additional surface contact time [28]. Due to the hypothetically small number of binding macromolecules, they exhibit, in total, rather low adhesion forces. This may also explain why electrostatic interactions seem to play a role in adhesion to hydrophilic surfaces, while this effect is not present or is suppressed by the high number of tethering proteins on non-wettable surfaces due to the hydrophobic interactions.

The experimental results of SA113 Δ*srtA* cells indicate that the presence of covalently bound cell wall proteins is more important for adhesion to hydrophobic surfaces than to hydrophilic surfaces, yet they are of great relevance to the final contact (rupture length) with both surfaces. Teichoic acids and their D-alanine residues seem to influence adhesion on hydrophilic surfaces rather indirectly. The results of these mutants tend to indicate the importance of the number of binding macromolecules as well as the charge of the bacterium

when adhering to hydrophilic surfaces. This effect may be caused by enhancing or reducing the probability of hydrogen bond formation. On hydrophobic surfaces, however, teichoic acids may contribute more directly through the tethering of hydrophobic D-alanine residues presented by teichoic acid regions that protrude from the cell wall.

Concerning adhesion-relevant surface proteins, we cannot state which proteins exactly contribute to which extent. Of note, different studies identified over 400 different proteins in or attached to the cell wall of *S. aureus* [59–64]. With the use of SA113 Δ*srtA* cells, we can at least state that LPXTG-anchored covalently bound proteins, although representing only a minor part of the cell wall proteome of this pathogen, have a major influence. However, other cell wall associated proteins (e. g., SERAMs, secretable expanded repertoire adhesive molecules), which might be quite high in number, likely contribute to the adhesion properties of *S. aureus* as well. Conversely, on hydrophilic surfaces, the absence of wall teichoic acids actually significantly increases adhesion, so that they probably do not play a major role in binding. This effect should be further investigated in future work. These are all crucial first steps towards understanding *S. aureus* adhesion at the macromolecule level.

3. Materials and Methods

3.1. Substrate Preparation

Si wafers (Siltronic AG, Burghausen, Germany) are the basis of the hydrophilic as well as the hydrophobic substrates used in this study. The Si substrates feature a native silicon oxide layer of 1.7(2) nm (the number in parentheses denotes the error of the last digit) and an RMS (root mean square) surface roughness of 0.09(2) nm [43]. Cleaning the Si wafers thoroughly results in a hydrophilic substrate with an advancing water contact angle of 5(2)°, a surface energy of 64(1) mJ/m^2, and a zeta-potential of $-104.4(1)$ mV at pH 7.3 [43]. The hydrophobic substrate is prepared by covering a Si wafer with a self-assembled monolayer of octadecyltrichlorosilane (OTS) according to a standard protocol [65]. The result is a CH_3-terminated substrate with an advancing (receding) water contact angle of 111(1)° (107(2)°), a surface energy of 24(1) mJ/m^2 [65], and a zeta-potential of $-80.0(1)$ mV [43]. For force spectroscopy experiments, the substrates were immersed into phosphate-buffered saline (PBS, pH 7.3, ionic strength 0.1728 mol/L at 20 °C).

3.2. Bacterial Strains and Growth Conditions

All bacterial cultures used were prepared in the same way, starting the day before the force spectroscopy experiments: One colony from a blood agar plate was placed into a 5 mL tryptic soy broth (TSB) medium and incubated at 37 °C and 150 rpm for 16 h. On the next day, 40 µL of the overnight culture were transferred into 4 mL of fresh TSB medium and incubated for another 2.5 h to obtain exponential phase cells. Subsequently, 0.5 mL of this culture was washed three times, using 1 mL PBS each, to remove extracellular material.

3.3. Cytochrome c Binding Assay

In order to characterize the surface charge of SA113 and its knock-outs, cytochrome *c* binding assays [66] were carried out. Bacterial cells were cultured to the exponential growth phase as outlined above. For the cytochrome *c* binding assays, bacterial cells from exponential growth phase cultures were collected by centrifugation, washed twice with morpholinepropanesulfonic acid (MOPS) buffer (20 mM, pH 7.0), and resuspended in the same buffer to an optical density at 600 nm (OD_{600}) of 7. The resulting cell suspension were incubated for 10 min at RT with 0.25 mg/mL cytochrome *c* (Merck, Darmstadt, Germany), the bacterial cells were subsequently removed by centrifugation, and the amount of cytochrome *c* that remained in the supernatant was quantitated photometrically at 530 nm using a standard curve as the reference.

3.4. Single-Cell Force Spectroscopy

Single bacterial probes were prepared according to a standard protocol [20]: Tipless cantilevers (MLCT-O, Bruker-Nano, Santa Barbara, USA) were covered with a thin layer

of polydopamine by polymerization of dopamine hydrochloride (99%, Sigma-Aldrich, St. Louis, MI, USA) in TRIS buffer (pH 8.4). Afterwards, single bacterial cells were attached to the polydopamine-coated cantilever using a micromanipulator; care was taken so that the cells never dry out during probe preparation or force measurements. The cantilevers were calibrated before each measurement.

Force spectroscopy measurements with single bacterial probes were conducted under ambient conditions in phosphate buffered saline (PBS, pH 7.3) using a Bioscope Catalyst and a Nanowizard 4 (Bruker Nano GmbH, Berlin, Germany). Force–distance curves were performed using parameter values that correspond to similar studies [16,67–69]: The ramp size was 800 nm, the force trigger (denoting the maximal force with which the cell is pressed onto the substrate) was 300 pN, and retraction speed was 800 nm/s. The approach speed was 800 nm/s for force–distance measurements without surface delay and 100 nm/s when a surface delay of 5 s was applied. Surface delay times of a few seconds are a common choice to study the influence of the contact time on bacterial adhesion processes [19,58,68–70]. Measurements without surface delay yield a contact time below 0.5 s [16,67].

Force–distance measurements with single, viable bacterial cells were performed on either a hydrophobic or a hydrophilic substrate. Thus, for each bacterial probe and parameter set, at least 50 force–distance curves were recorded.

4. Conclusions

We investigated the adhesion process of *S. aureus* to abiotic substrata by combining AFM-based single cell force spectroscopy with a set of isogenic knock-out mutants. As substrates, we used a smooth silicon wafer in its natural hydrophilic oxidized state as well as covered with a self-assembling monolayer of hydrophobic silanes. On both surfaces, bacterial adhesion can be described by the binding of thermally fluctuating bacterial cell wall macromolecules.

The experiments revealed that (i) the influence of bacterial cell wall macromolecules mediating adhesion differs depending on the substrate's hydrophobicity; (ii) on hydrophobic substrates, all tested knock-out mutants of *S. aureus* adhere about an order of magnitude less than the wild-type; (iii) covalently bound cell wall proteins largely contribute to the adhesion force on hydrophobic substrates but less on hydrophilic ones; (iv) on hydrophilic substrates, adhesion forces are influenced by the number of tethering molecules and by the cell surface charge; (v) teichoic acids seem to play a minor role for the adhesion on hydrophilic substrates; and (vi) on the hydrophobic substrates, wall teichoic acids seem to contribute directly and/or indirectly to the adhesion because of their hydrophobic residues.

In particular, the impact of electrostatic interactions through surface charges on hydrophilic substrates may be an important topic for material engineering and is of interest to future studies. With the experiments presented, it is not possible to determine which specific proteins are relevant for adhesion to abiotic surfaces and how numerous they are. This could be the subject of future studies using more sophisticated mutant cells, in which, for example, only one specific cell-wall-anchored/associated protein is knocked out, combined with qualitative simulations of the bacterial cell wall in different surface potentials.

Finally, the fundamental mechanisms of *S. aureus* adhesion to abiotic surfaces revealed in this study may be transferred to other bacterial species as microbial adhesion might generally rely on the binding of surface macromolecules. The challenge here is to design theoretical models and simulations that include the description of a protein–protein interaction of the different cell wall molecules. In addition to the characterization of the attachment and detachment phases, this is an important step towards a comprehensive biophysical understanding of biofilm formation.

Int. J. Mol. Sci. **2021**, *22*, 11952

Author Contributions: C.S.: data curation, investigation, methodology, visualization, writing—original draft, and writing—review and editing. F.N.: data curation, investigation, methodology, visualization, writing—original draft, and writing—review and editing. N.T.: data curation, investigation, methodology, and writing—review and editing. B.W.: investigation, and writing—review and editing. P.J.: methodology, and writing—review and editing. M.B.: data curation, conceptualization, methodology, supervision, and writing—review and editing. K.J.: conceptualization, methodology, supervision, and writing—review and editing. All authors have read and agreed to the published version of the manuscript.

Funding: The project was supported by the German Research Foundation (DFG) under the DFG project number 449375068 (Nanowizard) and in the framework of the collaborative research center SFB 1027, projects B1 and B2. C.S. and K.J. also acknowledge funding from the DFG project JA 905/6.

Acknowledgments: The authors thank Andreas Peschel from the Cellular and Molecular Microbiology Division, Interfaculty Institute of Microbiology and Infection Medicine at the University of Tübingen for providing the mutant cells.

Conflicts of Interest: The authors declare no conflict of interest.

Abbreviations

AFM	Atomic force microscopy
SCFS	Single-cell force spectroscopy
WTA	Wall teichoic acid
LTA	Lipoteichoic acid

Appendix A. Comparison of All Cells

Appendix A.1. Comparison of All Cells Measured on Hydrophobic Surfaces

For better comparability of the *S. aureus* mutants among each other, all adhesion forces of the mutant cells measured on OTS were plotted in one histogram. In addition, they were also compared with the measurements of the wild-type from Reference [28].

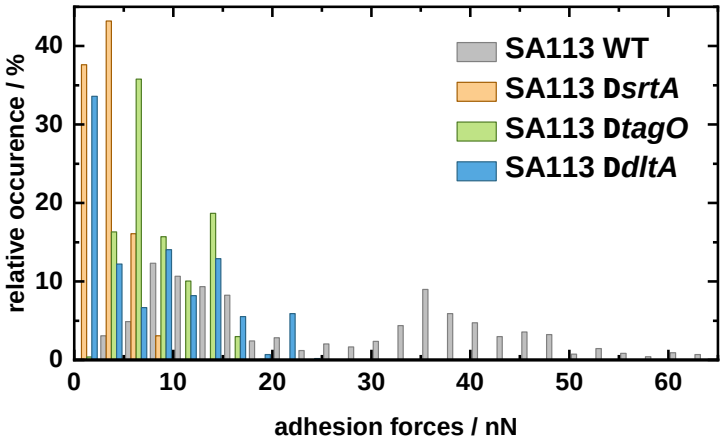

Figure A1. Overview histogram of all adhesion forces on OTS of 18 single SA113 Δ*srtA*, 16 single SA113 Δ*tagO*, and 17 single SA113 Δ*dltA* cells. Additionally, the corresponding values of the SA113 wild-type population are shown in gray [28].

Appendix A.2. Comparison of All Cells Measured on Hydrophilic Surfaces

For better comparability of the *S. aureus* mutants among each other, all adhesion forces of the mutant cells measured on native Si were plotted in one histogram. In addition, they were also compared with the measurements of the wild-type from Reference [28].

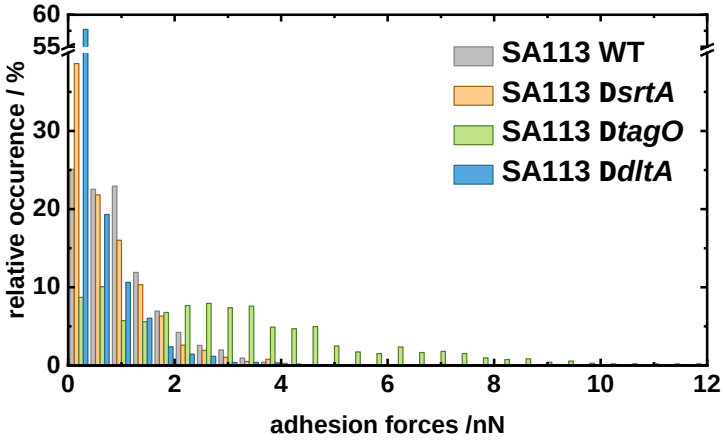

Figure A2. Overview histogram of all measured values of adhesion force of 11 single SA113 Δ*srtA*, 15 single SA113 Δ*tagO*, and 18 single SA113 Δ*dltA* cells on hydrophilic surfaces. The corresponding values of an SA113 wild-type population are shown in gray [28].

References

1. Lowy, F.D. *Staphylococcus aureus* Infections. *N. Engl. J. Med.* **1998**, *339*, 520–532. [CrossRef]
2. Hall-Stoodley, L.; Costerton, J.W.; Stoodley, P. Bacterial biofilms: From the Natural environment to infectious diseases. *Nat. Rev. Microbiol.* **2004**, *2*, 95–108. [CrossRef]
3. Flemming, H.C.; Wingender, J. The biofilm matrix. *Nat. Rev. Microbiol.* **2010**, *8*, 623–633. [CrossRef] [PubMed]
4. Yongsunthon, R.; Fowler, V.G.; Lower, B.H.; Vellano, F.P.; Alexander, E.; Reller, L.B.; Corey, G.R.; Lower, S.K. Correlation between Fundamental Binding Forces and Clinical Prognosis of *Staphylococcus aureus* Infections of Medical Implants. *Langmuir* **2007**, *23*, 2289–2292. [CrossRef]
5. Heilmann, C. Adhesion Mechanisms of Staphylococci. In *Advances in Experimental Medicine and Biology*; Springer: Dordrecht, The Netherlands, 2011; pp. 105–123. [CrossRef]
6. Thewes, N.; Thewes, A.; Loskill, P.; Peisker, H.; Bischoff, M.; Herrmann, M.; Santen, L.; Jacobs, K. Stochastic binding of *Staphylococcus aureus* to hydrophobic surfaces. *Soft Matter.* **2015**, *11*, 8913–8919. [CrossRef]
7. Gotz, F.; Peters, G. Colonization of Medical Devices by Coagulase-Negative Staphylococci. In *Infections Associated with Indwelling Medical Devices*; ASM Press: Washington, DC, USA, 2014; pp. 55–88. [CrossRef]
8. Christensen, G.D.; Baldassarri, L.; Simpson, W.A. Methods for studying microbial colonization of plastics. In *Methods in Enzymology*; Elsevier: Amsterdam, The Netherlands, 1995; pp. 477–500. [CrossRef]
9. Chamis, A.L.; Peterson, G.E.; Cabell, C.H.; Corey, G.R.; Sorrentino, R.A.; Greenfield, R.A.; Ryan, T.; Reller, L.B.; Fowler, V.G. *Staphylococcus aureus* Bacteremia in PatientsWith Permanent Pacemakers or Implantable Cardioverter-Defibrillators. *Circulation* **2001**, *104*, 1029–1033. [CrossRef]
10. Mylonakis, E.; Calderwood, S.B. Infective Endocarditis in Adults. *N. Engl. J. Med.* **2001**, *345*, 1318–1330. [CrossRef]
11. Olsen, M.A.; Mayfield, J.; Lauryssen, C.; Polish, L.B.; Jones, M.; Vest, J.; Fraser, V.J. Risk factors for surgical site infection in spinal surgery. *J. Neurosurg. Spine* **2003**, *98*, 149–155. [CrossRef]
12. Darouiche, R.O. Treatment of Infections Associated with Surgical Implants. *N. Engl. J. Med.* **2004**, *350*, 1422–1429. [CrossRef]
13. Arciola, C.R.; Campoccia, D.; Speziale, P.; Montanaro, L.; Costerton, J.W. Biofilm formation in Staphylococcus implant infections. A review of molecular mechanisms and implications for biofilm-resistant materials. *Biomaterials* **2012**, *33*, 5967–5982. [CrossRef] [PubMed]
14. Razavi, M.; Shepard, D.S.; Suaya, J.A.; Stason, W.B. Postoperative *Staphylococcus aureus* Infections in Medicare Beneficiaries. *PLoS ONE* **2014**, *9*, e110133. [CrossRef] [PubMed]
15. Kang, S.; Elimelech, M. Bioinspired Single Bacterial Cell Force Spectroscopy. *Langmuir* **2009**, *25*, 9656–9659. [CrossRef]
16. Thewes, N.; Loskill, P.; Jung, P.; Peisker, H.; Bischoff, M.; Herrmann, M.; Jacobs, K. Hydrophobic interaction governs unspecific adhesion of staphylococci: A single cell force spectroscopy study. *Beilstein J. Nanotechnol.* **2014**, *5*, 1501–1512. [CrossRef]
17. Dufrene, Y.F. Sticky microbes: Forces in microbial cell adhesion. *Trends Microbiol.* **2015**, *23*, 376–382. [CrossRef] [PubMed]
18. Sullan, R.M.A.; Li, J.K.; Crowley, P.J.; Brady, L.J.; Dufrene, Y.F. Binding Forces of Streptococcus mutans P1 Adhesin. *ACS Nano* **2015**, *9*, 1448–1460. [CrossRef] [PubMed]
19. Aguayo, S.; Donos, N.; Spratt, D.; Bozec, L. Single-bacterium nanomechanics in biomedicine: Unravelling the dynamics of bacterial cells. *Nanotechnology* **2015**, *26*, 062001. [CrossRef] [PubMed]

20. Thewes, N.; Loskill, P.; Spengler, C.; Humbert, S.; Bischoff, M.; Jacobs, K. A detailed guideline for the fabrication of single bacterial probes used for atomic force spectroscopy. *Eur. Phys. J. E* **2015**, *38*, 140. [CrossRef] [PubMed]
21. Mitchell, G.; Lamontagne, C.A.; Brouillette, E.; Grondin, G.; Talbot, B.G.; Grandbois, M.; Malouin, F. *Staphylococcus aureus* SigB activity promotes a strong fibronectin-bacterium interaction which may sustain host tissue colonization by small-colony variants isolated from cystic fibrosis patients. *Mol. Microbiol.* **2008**, *70*, 1540–1555. [CrossRef]
22. Ovchinnikova, E.S.; Krom, B.P.; Busscher, H.J.; van der Mei, H.C. Evaluation of adhesion forces of *Staphylococcus aureus* along the length of Candida albicanshyphae. *BMC Microbiol.* **2012**, *12*, 281. [CrossRef] [PubMed]
23. Herman-Bausier, P.; El-Kirat-Chatel, S.; Foster, T.J.; Geoghegan, J.A.; Dufrene, Y.F. *Staphylococcus aureus* Fibronectin-Binding Protein A Mediates Cell-Cell Adhesion through Low-Affinity Homophilic Bonds. m*Bio* **2015**, *6*, e00413-15. [CrossRef] [PubMed]
24. Vanzieleghem, T.; Herman-Bausier, P.; Dufrene, Y.F.; Mahillon, J. Staphylococcus epidermidis Affinity for Fibrinogen-Coated Surfaces Correlates with the Abundance of the SdrG Adhesin on the Cell Surface. *Langmuir* **2015**, *31*, 4713–4721. [CrossRef]
25. Spengler, C.; Thewes, N.; Nolle, F.; Faidt, T.; Umanskaya, N.; Hannig, M.; Bischoff, M.; Jacobs, K. Enhanced adhesion of Streptococcus mutansto hydroxyapatite after exposure to saliva. *J. Mol. Recognit.* **2017**, *30*, e2615. [CrossRef]
26. Viljoen, A.; Mignolet, J.; Viela, F.; Mathelie-Guinlet, M.; Dufrene, Y.F. How Microbes Use Force To Control Adhesion. *J. Bacteriol.* **2020**, *202*, e00125–20. [CrossRef] [PubMed]
27. Sjollema, J.; van der Mei, H.C.; Hall, C.L.; Peterson, B.W.; de Vries, J.; Song, L.; Jong, E.D.d.; Busscher, H.J.; Swartjes, J.J.T.M. Detachment and successive re-attachment of multiple, reversibly-binding tethers result in irreversible bacterial adhesion to surfaces. *Sci. Rep.* **2017**, *7*, 4369. [CrossRef] [PubMed]
28. Maikranz, E.; Spengler, C.; Thewes, N.; Thewes, A.; Nolle, F.; Jung, P.; Bischoff, M.; Santen, L.; Jacobs, K. Different binding mechanisms of *Staphylococcus aureus* to hydrophobic and hydrophilic surfaces. *Nanoscale* **2020**, *12*, 19267–19275. [CrossRef] [PubMed]
29. Spengler, C.; Thewes, N.; Jung, P.; Bischoff, M.; Jacobs, K. Determination of the nano-scaled contact area of staphylococcal cells. *Nanoscale* **2017**, *9*, 10084–10093. [CrossRef]
30. Spengler, C.; Glatz, B.A.; Maikranz, E.; Bischoff, M.; Klatt, M.A.; Santen, L.; Fery, A.; Jacobs, K. The adhesion capability of S. aureus cells is heterogeneously distributed over the cell envelope. *bioRxiv* **2021**. [CrossRef]
31. Weidenmaier, C.; Peschel, A.; Xiong, Y.Q.; Kristian, S.A.; Dietz, K.; Yeaman, M.R.; Bayer, A.S. Lack of Wall Teichoic Acids in *Staphylococcus aureus* Leads to Reduced Interactions with Endothelial Cells and to Attenuated Virulence in a Rabbit Model of Endocarditis. *J. Infect. Dis.* **2005**, *191*, 1771–1777. [CrossRef] [PubMed]
32. de Oliveira, L.M.F.; Steindorff, M.; Darisipudi, M.N.; Mrochen, D.M.; Trube, P.; Broker, B.M.; Bronstrup, M.; Tegge, W.; Holtfreter, S. Discovery of *Staphylococcus aureus* Adhesion Inhibitors by Automated Imaging and Their Characterization in a Mouse Model of Persistent Nasal Colonization. *Microorganisms* **2021**, *9*, 631. [CrossRef]
33. Weidenmaier, C.; Kokai-Kun, J.F.; Kulauzovic, E.; Kohler, T.; Thumm, G.; Stoll, H.; Gotz, F.; Peschel, A. Differential roles of sortase-anchored surface proteins and wall teichoic acid in *Staphylococcus aureus* nasal colonization. *Int. J. Med. Microbiol.* **2008**, *298*, 505–513. [CrossRef]
34. Kerdudou, S.; Laschke, M.W.; Sinha, B.; Preissner, K.T.; Menger, M.D.; Herrmann, M. Fibronectin binding proteins contribute to the adherence of *Staphylococcus aureus* to intact endothelium in vivo. *Thromb. Haemost.* **2006**, *96*, 183–189. [CrossRef] [PubMed]
35. Corrigan, R.M.; Miajlovic, H.; Foster, T.J. Surface proteins that promote adherence of *Staphylococcus aureus*to human desquamated nasal epithelial cells. *BMC Microbiol.* **2009**, *9*, 22. [CrossRef]
36. Vergara-Irigaray, M.; Maira-Litran, T.; Merino, N.; Pier, G.B.; Penades, J.R.; Lasa, I. Wall teichoic acids are dispensable for anchoring the PNAG exopolysaccharide to the *Staphylococcus aureus* cell surface. *Microbiology* **2008**, *154*, 865–877. [CrossRef]
37. Gross, M.; Cramton, S.E.; Gotz, F.; Peschel, A. Key role of teichoic acid net charge in *Staphylococcus aureus* colonization of artificial surfaces. *Infect. Immun.* **2001**, *69*, 3423. [CrossRef] [PubMed]
38. Maxe, I.; Ryden, C.; Wadstrom, T.; Rubin, K. Specific attachment of *Staphylococcus aureus* to immobilized fibronectin. *Infect. Immun.* **1986**, *54*, 695–704. [CrossRef] [PubMed]
39. Peschel, A.; Otto, M.; Jack, R.W.; Kalbacher, H.; Jung, G.; Gotz, F. Inactivation of the dlt Operon in *Staphylococcus aureus* Confers Sensitivity to Defensins, Protegrins, and Other Antimicrobial Peptides. *J. Biol. Chem.* **1999**, *274*, 8405–8410. [CrossRef]
40. Bur, S.; Preissner, K.T.; Herrmann, M.; Bischoff, M. The *Staphylococcus aureus* Extracellular Adherence Protein Promotes Bacterial Internalization by Keratinocytes Independent of Fibronectin-Binding Proteins. *J. Investig. Dermatol.* **2013**, *133*, 2004–2012. [CrossRef]
41. Dramsi, S.; Magnet, S.; Davison, S.; Arthur, M. Covalent attachment of proteins to peptidoglycan. *FEMS Microbiol. Rev.* **2008**, *32*, 307–320. [CrossRef] [PubMed]
42. Neuhaus, F.C.; Baddiley, J. A Continuum of Anionic Charge: Structures and Functions of d -Alanyl-Teichoic Acids in Gram-Positive Bacteria. *Microbiol. Mol. Biol. Rev.* **2003**, *67*, 686–723. [CrossRef]
43. Bellion, M.; Santen, L.; Mantz, H.; Hahl, H.; Quinn, A.; Nagel, A.; Gilow, C.; Weitenberg, C.; Schmitt, Y.; Jacobs, K. Protein adsorption on tailored substrates: Long-range forces and conformational changes. *J. Phys. Condens. Matter* **2008**, *20*, 404226. [CrossRef]
44. Schlag, M.; Biswas, R.; Krismer, B.; Kohler, T.; Zoll, S.; Yu, W.; Schwarz, H.; Peschel, A.; Gotz, F. Role of staphylococcal wall teichoic acid in targeting the major autolysin Atl. *Mol. Microbiol.* **2010**, *75*, 864–873. [CrossRef]

45. Becker, S.; Frankel, M.B.; Schneewind, O.; Missiakas, D. Release of protein A from the cell wall of *Staphylococcus aureus*. *Proc. Natl. Acad. Sci. USA* **2014**, *111*, 1574–1579. [CrossRef] [PubMed]
46. Bertsche, U.; Yang, S.J.; Kuehner, D.; Wanner, S.; Mishra, N.N.; Roth, T.; Nega, M.; Schneider, A.; Mayer, C.; Grau, T.; et al. Increased Cell Wall Teichoic Acid Production and D-alanylation Are Common Phenotypes among Daptomycin-Resistant Methicillin-Resistant *Staphylococcus aureus* (MRSA) Clinical Isolates. *PLoS ONE* **2013**, *8*, e67398. [CrossRef] [PubMed]
47. van Wely, K.H.; Swaving, J.; Freudl, R.; Driessen, A.J. Translocation of proteins across the cell envelope of Gram-positive bacteria. *FEMS Microbiol. Rev.* **2001**, *25*, 437–454. [CrossRef]
48. Sarvas, M.; Harwood, C.R.; Bron, S.; van Dijl, J.M. Post-translocational folding of secretory proteins in Gram-positive bacteria. *Biochim. Biophys. Acta (BBA) Mol. Cell Res.* **2004**, *1694*, 311–327. [CrossRef] [PubMed]
49. Forster, B.M.; Marquis, H. Protein transport across the cell wall of monoderm Gram-positive bacteria. *Mol. Microbiol.* **2012**, *84*, 405–413. [CrossRef]
50. Hyyrylainen, H.L.; Vitikainen, M.; Thwaite, J.; Wu, H.; Sarvas, M.; Harwood, C.R.; Kontinen, V.P.; Stephenson, K. D-Alanine substitution of teichoic acids as a modulator of protein folding and stability at the cytoplasmic membrane/cell wall interface of Bacillus subtilis. *J. Biol. Chem.* **2000**, *275*, 26696–26703. [CrossRef]
51. Nouaille, S.; Commissaire, J.; Gratadoux, J.J.; Ravn, P.; Bolotin, A.; Gruss, A.; Loir, Y.L.; Langella, P. Influence of Lipoteichoic Acid d -Alanylation on Protein Secretion in Lactococcus lactis as Revealed by Random Mutagenesis. *Appl. Environ. Microbiol.* **2004**, *70*, 1600–1607. [CrossRef] [PubMed]
52. Davis, E.; Kennedy, D.; Halperin, S.A.; Lee, S.F. Role of the Cell Wall Microenvironment in Expression of a Heterologous SpaP-S1 Fusion Protein by Streptococcus gordonii. *Appl. Environ. Microbiol.* **2011**, *77*, 1660–1666. [CrossRef]
53. Schneewind, O.; Missiakas, D. Lipoteichoic Acids, Phosphate-Containing Polymers in the Envelope of Gram-Positive Bacteria. *J. Bacteriol.* **2014**, *196*, 1133–1142. [CrossRef] [PubMed]
54. Peschel, A.; Vuong, C.; Otto, M.; Gotz, F. The d-Alanine Residues of *Staphylococcus aureus* Teichoic Acids Alter the Susceptibility to Vancomycin and the Activity of Autolytic Enzymes. *Antimicrob. Agents Chemother.* **2000**, *44*, 2845–2847. [CrossRef]
55. Biswas, R.; Voggu, L.; Simon, U.K.; Hentschel, P.; Thumm, G.; Gotz, F. Activity of the major staphylococcal autolysin Atl. *FEMS Microbiol. Lett.* **2006**, *259*, 260–268. [CrossRef]
56. Eisenbeis, J.; Saffarzadeh, M.; Peisker, H.; Jung, P.; Thewes, N.; Preissner, K.T.; Herrmann, M.; Molle, V.; Geisbrecht, B.V.; Jacobs, K.; et al. The *Staphylococcus aureus* Extracellular Adherence Protein Eap Is a DNA Binding Protein Capable of Blocking Neutrophil Extracellular Trap Formation. *Front. Cell. Infect. Microbiol.* **2018**, *8*, 235. [CrossRef]
57. Li, B.; Logan, B.E. Bacterial adhesion to glass and metal-oxide surfaces. *Colloids Surf. B Biointerfaces* **2004**, *36*, 81–90. [CrossRef]
58. Beaussart, A.; El-Kirat-Chatel, S.; Herman, P.; Alsteens, D.; Mahillon, J.; Hols, P.; Dufrene, Y.F. Single-Cell Force Spectroscopy of Probiotic Bacteria. *Biophys. J.* **2013**, *104*, 1886–1892. [CrossRef]
59. Glowalla, E.; Tosetti, B.; Kronke, M.; Krut, O. Proteomics-Based Identification of Anchorless Cell Wall Proteins as Vaccine Candidates against *Staphylococcus aureus*. *Infect. Immun.* **2009**, *77*, 2719–2729. [CrossRef] [PubMed]
60. Hempel, K.; Pane-Farre, J.; Otto, A.; Sievers, S.; Hecker, M.; Becher, D. Quantitative Cell Surface Proteome Profiling for SigBDependent Protein Expression in the Human Pathogen *Staphylococcus aureus* via Biotinylation Approach. *J. Proteome Res.* **2010**, *9*, 1579–1590. [CrossRef] [PubMed]
61. Solis, N.; Larsen, M.R.; Cordwell, S.J. Improved accuracy of cell surface shaving proteomics in *Staphylococcus aureus* using a false-positive control. *Proteomics* **2010**, *10*, 2037–2049. [CrossRef]
62. Ventura, C.L.; Malachowa, N.; Hammer, C.H.; Nardone, G.A.; Robinson, M.A.; Kobayashi, S.D.; DeLeo, F.R. Identification of a Novel *Staphylococcus aureus* Two-Component Leukotoxin Using Cell Surface Proteomics. *PLoS ONE* **2010**, *5*, e11634. [CrossRef]
63. Dreisbach, A.; Hempel, K.; Buist, G.; Hecker, M.; Becher, D.; van Dijl, J.M. Profiling the surfacome of *Staphylococcus aureus*. *Proteomics* **2010**, *10*, 3082–3096. [CrossRef] [PubMed]
64. Dreisbach, A.; van Dijl, J.M.; Buist, G. The cell surface proteome of *Staphylococcus aureus*. *Proteomics* **2011**, *11*, 3154–3168. [CrossRef]
65. Lessel, M.; Baumchen, O.; Klos, M.; Hahl, H.; Fetzer, R.; Paulus, M.; Seemann, R.; Jacobs, K. Self-assembled silane monolayers: An efficient step-by-step recipe for high-quality, low energy surfaces. *Surf. Interface Anal.* **2015**, *47*, 557–564. [CrossRef]
66. Hamilton, A.; Popham, D.L.; Carl, D.J.; Lauth, X.; Nizet, V.; Jones, A.L. Penicillin-Binding Protein 1a Promotes Resistance of Group B Streptococcus to Antimicrobial Peptides. *Infect. Immun.* **2006**, *74*, 6179–6187. [CrossRef] [PubMed]
67. Beaussart, A.; Herman, P.; El-Kirat-Chatel, S.; Lipke, P.N.; Kucharikova, S.; Dijck, P.V.; Dufrene, Y.F. Single-cell force spectroscopy of the medically important Staphylococcus epidermidis–Candida albicans interaction. *Nanoscale* **2013**, *5*, 10894. [CrossRef]
68. Zeng, G.; Muller, T.; Meyer, R.L. Single-Cell Force Spectroscopy of Bacteria Enabled by Naturally Derived Proteins. *Langmuir* **2014**, *30*, 4019–4025. [CrossRef] [PubMed]
69. Herman, P.; El-Kirat-Chatel, S.; Beaussart, A.; Geoghegan, J.A.; Foster, T.J.; Dufrene, Y.F. The binding force of the staphylococcal adhesin SdrG is remarkably strong. *Mol. Microbiol.* **2014**, *93*, 356–368. [CrossRef]
70. Herman, P.; El-Kirat-Chatel, S.; Beaussart, A.; Geoghegan, J.A.; Vanzieleghem, T.; Foster, T.J.; Hols, P.; Mahillon, J.; Dufrene, Y.F. Forces Driving the Attachment of Staphylococcus epidermidis to Fibrinogen-Coated Surfaces. *Langmuir* **2013**, *29*, 13018–13022. [CrossRef] [PubMed]

V *Staphylococcus aureus* adhesion on hydrophobin coatings: adhesion forces and the influence of surface charge

Authors: **F. Nolle**,[1,*] B. Wieland,[2,*] K. Kochems,[1] H. Heintz,[1] M. Lienemann,[3] P. Jung,[2] H. Hähl,[1] M. Bischoff,[2] and K. Jacobs[1,4]

[1] Experimental Physics and Center for Biophysics, Saarland University, 66123 Saarbrücken, Germany.
[2] Institute of Medical Microbiology and Hygiene, Saarland University, 66421 Homburg, Germany.
[3] VTT Technical Research Centre of Finland Ltd., Espoo 02150, Finland
[4] Max Planck School Matter to Life, Jahnstraße 29, 69120 Heidelberg, Germany
[*] These authors contributed equally to this work.

Author contributions:
*Experimental results were achieved and analyzed by **F. Nolle** (Hydrophobin surfaces, SCFM measurements), B. Wieland (SCFM measurements, SDS-PAGE), K. Kochems (Hydrophobin surfaces), H. Heintz (bacteria preparation), M. Lienemann (Hydrophobin purification). The methodology was developed by **F. Nolle**, B. Wieland, P. Jung, H. Hähl. Scientific work was directed by H. Hähl, M. Bischoff and K. Jacobs. The original draft was written by **F. Nolle** and B. Wieland. All authors haven reviewed and edited the manuscript.*

Abstract – *Staphylococcus aureus* (*S. aureus*) is one of the bacterial species that most frequently forms multilayered biofilms on implants. Such biofilms usually make a removal of the implant necessary in order to avoid sepsis or, in the worst case, even the death of the patient. To address the problem of unwanted biofilm formation, its first step, i.e. bacterial adhesion, must be understood and prevented. Thus, the development of adhesion-reducing surface coatings for implant materials is of utmost importance. In this work, we used single-cell force spectroscopy (SCFS) to analyze the adhesion of the biofilm-forming *S. aureus* strain SA113 on naive and protein-coated silicon surfaces (SiO_2). In addition to the SA113 wild type, we used the SA113 $\Delta dltA$ knock-out mutant to further investigate the effect of D-alanylation of lipoteichoic acids of the cell wall. In order to examine how the surface charge affects adhesion, we coated silanized SiO_2 surfaces with amphiphilic class II hydrophobins. The naturally occurring hydrophobin HFBI was used, as well as the HFBI variant D40Q/D43N, which is less negatively charged at physiological pH due to the exchange of two acidic aspartate residues. These two types of

hydrophobin-coated surfaces resemble each other in roughness and wettability but differ only in charge. By variation of the surfaces used, we show that the adhesion of *S. aureus* can be influenced by the charge of this type of surfaces. Therefore, in addition to hydrogen bonding, electrostatic interactions between the cell and the hydrophilic surface govern the adhesion on hydrophilic surfaces. However, the patchiness of macromolecules on the cell wall surface is crucial for the cell to form these interactions with the surface. In addition, we found that for both HFBI coatings the adhesion strength of *S. aureus* is reduced by nearly a factor of 30 compared to silanized SiO_2 surfaces. Therefore, hydrophobin coatings are of great interest for further use in the field of biomedical surface coating.

Staphylococcus aureus adhesion on hydrophobin coatings: adhesion forces and the influence of surface charge

Friederike Nolle,[†,‖] Ben Wieland,[‡,‖] Kirstin Kochems,[†] Hannah Heintz,[†] Michael Lienemann,[¶] Philipp Jung,[‡] Hendrik Hähl,[†] Markus Bischoff,[*,‡] and Karin Jacobs[*,†,§]

†*Experimental Physics, Saarland University, 66123 Saarbrücken, Germany*
‡*Insitute of Medical Microbiology and Hygiene, Saarland University, 66421 Homburg, Germany*
¶*VTT Technical Research Centre of Finland Ltd., Espoo 02150, Finland*
§*Max Planck School, Matter to Life, Jahnstraße 29, 69120 Heidelberg, Germany*
‖*These authors contributed equally to this work.*

E-mail: markus.bischoff@uks.eu; k.jacobs@physik.uni-saarland.de

Abstract

Staphylococcus aureus (*S. aureus*) is one of the bacterial species that most frequently forms multilayered biofilms on implants. Such biofilms usually make a removal of the implant necessary in order to avoid sepsis or, in the worst case, even the death of the patient. To address the problem of unwanted biofilm formation, its first step, i.e. bacterial adhesion, must be understood and prevented. Thus, the development of adhesion-reducing surface coatings for implant materials is of utmost importance. In this work, we used single-cell force spectroscopy (SCFS) to analyze the adhesion of the biofilm-forming *S. aureus* strain SA113 on naive and protein-coated silicon surfaces (SiO_2). In addition to the SA113 wild type, we used the SA113 $\Delta dltA$ knock-out mutant to further investigate the effect of D-alanylation of lipoteichoic acids of the cell wall. In order to examine how the surface charge affects adhesion, we coated silanized SiO_2 surfaces with amphiphilic class II hydrophobins. The naturally occurring hydrophobin HFBI was used, as well as the HFBI variant D40Q/D43N, which is less negatively charged at physiological pH due to the exchange of two acidic aspartate residues. These two types of hydrophobin-coated surfaces resemble each other in roughness and wettability but differ only in charge. By variation of the surfaces used, we show that the adhesion of *S. aureus* can be influenced by the charge of this type of surfaces. Therefore, in addition to hydrogen bonding, electrostatic interactions between the cell and the hydrophilic surface govern the adhesion on hydrophilic surfaces. However, the patchiness of macromolecules on the cell wall surface is crucial for the cell to form these interactions with the surface. In addition, we found that for both HFBI coatings the adhesion strength of *S. aureus* is reduced by nearly a factor of 30 compared to silanized SiO_2 surfaces. Therefore, hydrophobin coatings are of great interest for further use in the field of biomedical surface coating.

Keywords

HFBI; hydrophobins; surface coating; bacterial adhesion; single-cell force spectroscopy; *Staphylococcus aureus*; surface charge; hydrophobicity

Introduction

The ability of *Staphylococcus aureus* (*S. aureus*) to form biofilms on medical devices or to infect post-surgery wounds is well described[1–4]. *S. aureus*-related catheter and bloodstream infections can dramatically increase patient morbidity[5–8], mortality[9,10], and healthcare costs[11]. To address this burden, we must understand the crucial first steps of biofilm formation[12], including the initial adhesion. The state-of-the-art quantitative bacterial adhesion research method is based on atomic force microscopy (AFM), called single-cell force spectroscopy (SCFS). SCFS allows quantifying adhesion forces, adhesion energies, and rupture lengths of single bacterial cells with the substrate[13–20].

Besides studying the adhesion forces on abiotic and biotic surfaces, modifying or changing the surface is an excellent method to display antimicrobial properties[21]. Antimicrobial effects of naturally occurring surfaces have been described previously[22]; however, in medical applications, it is not always possible to change the material of these devices, such as catheters, because they need to keep a certain flexibility while inserted into the patient to not harm them during movement. To achieve antimicrobial effects on such surfaces, chemical coating or mechanical structuring is possible. Changing the surface roughness at nanoscopic scale step by step has proven to lower the adhesion[15] while, at the same time, creating rifts in the size of bacterial cells increases the adhesion[23,24]. Protein coatings are an alternative to structuring the surface for antimicrobial effects while keeping catheters biocompatible[18]. The coating process with proteins reduces the adhesion, while simultaneously changing the surface charge or energy[25–29]. Both characteristics are essential in *S. aureus* adhesion[16,30].

In this paper, we investigate the effect of surface charge on the adhesion of *S. aureus* SA113 and the general impact of coating silicon with amphiphilic HFBI proteins produced by *Trichoderma reesei*[31]. HFBI is a class II hydrophobin, creating stable interfacial protein monolayers[32,33], which can be used for surface coatings[34,35]. Beside the HFBI wild type, we use an HFBI mutant, in which two aspartic acid amino acids are changed to glutamine and asparagine, to change the surface charge[36]. In addition to changing the charge of the coated surface, we were also interested in the role of the charge of the bacterial cell wall. To study the influence of cell surface charge, we used the *S. aureus ΔdltA* mutant lacking D-alanylation of lipoteichoic acids of the cell wall. This bacterial mutant allowed us to understand the role of charge in cell wall-associated adhesion factors during adhesion.

Methods

Hydrophobin surface coating Class II hydrophobins, HFBI and HFBI D40Q/D43N, from the fungus *Trichoderma reesei* were prepared and purified at VTT (Espoo, Finland)[37]. The charge-based HFBI mutant HFBI D40Q/D43N was first reported by Lienemann *et al.*[36]. Silane-coated (octadecyltrichlorosilane, OTS)[38] Si wafers (Siltronic AG, Burghausen, Germany) were used as hydrophobic surfaces and served as the basis for the hydrophobin coatings. The coating was done by adding a 60 µL drop of a 10 mM sodium acetate solution containing hydrophobins at a concentration of 4 µM to one OTS surface and placing a second OTS surface on top. The setup was left for at least 30 min to allow the proteins to adsorb on the OTS surface. The entire setup was next placed in deionized water to remove non-adsorbed proteins. The surfaces were then dipped several times into deionized water to remove any protein aggregates on top of the monolayer film. Protein films were imaged using an atomic force microscope (FastScan Icon, Bruker, Santa Barbara, CA, USA) to verify complete protein coverage. Only the fully covered surfaces were afterwards used for bacterial adhesion measurements. An optical contact angle meter (OCA25, DataPhysics Instruments GmbH, Filderstadt, Germany) with a direct dosing system (ESr-M) was used to determine the water contact angle (WCA). Evaluation was performed with SCA20 dataphysics

software.

Bacterial strains and growth conditions To study bacterial adhesion, the biofilm-positive *Staphylococcus aureus* laboratory strain SA113 was utilized alongside the SA113 $\Delta dltA$ mutant[39], which was already used in a previous study[16]. Both strains were obtained from A. Peschel (University of Tübingen, Germany)[39,40].
The strains were grown on tryptic soy agar (TSA) plates with 5 % sheep blood (Becton Dickinson [BD], Heidelberg, Germany) and subsequently cultured in Tryptic Soy Broth (TSB, BD) in Erlenmeyer flasks at 37 °C and shaken at 150 rpm using a culture to flask volume of 1:10. The liquid cultures were inoculated the day before the experiment and incubated for 16 h. The next day, the overnight culture was diluted a hundredfold to inoculate a new liquid culture, which was then grown for 2.5 h at 37 °C and 150 rpm to obtain exponential growth phase cells. 1 ml of these cells was centrifuged for 3 min at 17,000 x g and were washed twice with phosphate-buffered saline (PBS, pH 7.4) to remove debris and extracellular material. Bacteria were then diluted 1:10 in PBS to prepare for single-cell force spectroscopy (SCFS).
Bacteria used for protein extraction were taken from the overnight culture and the bacterial cell number of the solution was adjusted to an optical density of 0.05 at 600 nm and subsequently multiplied again for 2.5 h at 37 °C while shaken at 225 RPM to obtain exponential growth phase cells.

Bacterial probes Tipless cantilevers (MLCT-O10-D, Bruker-Nano, Santa Barbara, USA) were covered with a thin layer of polydopamine by polymerization of dopamine hydrochloride (99 %, Sigma-Aldrich, St. Louis, MI, USA) in Tris buffer (pH 8.4). The cantilevers were dipped into the polydopamine solution for one hour before washed three times with water and dried under a flow bench. Next, a single bacterium was attached to a polydopamine-coated tipless AFM cantilever via a micromanipulator (Narishige Group, Tokyo, Japan). The preparation of the cantilevers and the immobilization of single bacterial cells were previously described by Thewes *et al.*[14]. Care was taken to ensure that the cells never dried out during probe preparation or force measurements. The cantilevers were calibrated before each measurement using the Sader method[41].

Single-cell force spectroscopy (SCFS) All force spectroscopy measurements with single bacterial probes were conducted under ambient conditions in PBS using a Nanowizard 4 (Bruker Nano GmbH, Berlin, Germany). Force–distance curves were performed using parameter values similar to a previous study by Spengler *et al.*[16]. The ramp size was set to 800 nm, the force trigger (denoting the maximal force with which the cell is pressed onto the substrate) was 300 pN, and the retraction speed was 800 nm/s with a surface delay of 5 s. This time delay was chosen, considering prior studies showing a correlation between cell adhesion strength and cell-surface contact time[30,42–46].
Force–distance measurements with single, viable bacterial cells were performed on either an HFBI- or an HFBI-D40Q/D43N-coated substrate. Thus, 64 force-distance curves were recorded for each bacterial probe and substrate in a 10 µm by 10 µm grid. Force-distance curves were analyzed by JPKSPM Data Processing software, Version 7.0.128. An adhesion curve was defined as a nonadhesion event at adhesion forces below 40 pN, as this could not be distinguished from the noise of the baseline.

Extraction of *S. aureus* proteins *S. aureus* SA113 and SA113 $\Delta dltA$ cells were grown as described above. After 2.5 h, the cells were harvested, and approximately 10 ml was centrifuged for 1 min at 10000 xg. The supernatant was discarded, and the pellet was resuspended in 160 µl PBS. 4 µg of lysostaphin, DNAse, and RNAse was added to the sample, respectively and incubated at 37 °C while lightly shaking until the solution was clear. The sample was centrifuged for 20 min at 10000 xg to separate the cytosolic and the cell wall fragment fractions. The supernatant was collected in a new

reaction tube, and the pellet was resuspended in 200 µl of PBS.
The bicinchoninic acid protein assay was used to determine the protein concentration of the cytosolic fraction. For the SDS-PAGE, 10 µg of cytosolic fraction or the corresponding volume for the cell wall fraction was loaded and seperated for about 3 h at 25 mA and 80 V in a 5 % stacking and 10 % separation polyacrylamide gel. Seperated protein bands were visualized by coomassie staining.

Results and Discussion

Characterization of HFBI wild type and HFBI D40Q/D43N coatings

To investigate the effect of surface charge on *S. aureus* adhesion, OTS-covered SiO_2 surfaces were used, which in turn were coated with wild-type HFBI and HFBI D40Q/D43N. Due to the coating, the wettability of the HFBI (WCA: 34±6°) and HFBI D40Q/D43N (WCA: 39±4°) surfaces are greatly reduced compared to the OTS surface (WCA: 111±2°), yet have a higher water contact angle than the uncoated SiO_2 (WCA: 5±2°) surface (see Table 1, WCA). A slightly increased roughness is measured on the HFBI- and HFBI-D40Q/D43N-coated surfaces (0.3–0.4 nm), nevertheless the samples have a root-mean-square roughness (RMSR) well below 1 nm (see Table 1, RMSR). The OTS is homogeneously covered by the hydrophobin coating and shows no structural differences between the HFBI and HFBI D40Q/D43N coatings in the range of bacterial size (see Fig. 1), so no major impact on bacterial adhesion due to the roughness is expected[15]. However, as published in Lienemann *et al.*[36], HFBI and HFBI D40Q/D43N have a crucial difference: The isoelectric point (IEP) is shifted (see Table 1, IEP). While the isoelectric point of HFBI is at pH 6.1, the isoelectric point of HFBI D40Q/D43N is at pH 7.0. Therefore, coating OTS with HFBI and HFBI D40Q/D43N, provides surfaces with similar wettability, roughness and chemistry, but differences in charge.

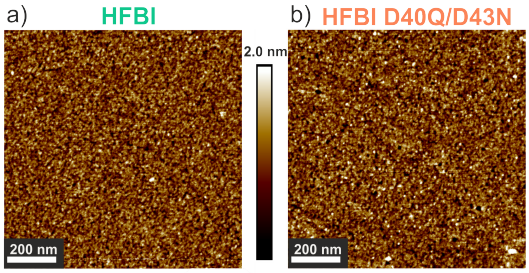

Figure 1: Images were captured using the off-resonance tapping mode PeakForce Tapping® (Bruker). AFM images (1 µm², 512x512 pixel) of HFBI (a) and HFBI D40Q/D43N (b) coatings.

Comparing the adhesion on bare SiO_2 to OTS- and HFBI-coated surfaces

It has already been reported that the adhesion of *S. aureus* to implant material is influenced by protein surface coatings[18,49,50]. First measurements of bacteria on hydrophobin-coated surfaces have shown reduced bacterial adhesion[51,52], effects on the adsorption of a second layer of proteins on the hydrophobin coating have also been reported[36,53,54]. It has been suggested that electrostatic interactions may play a key role in this adsorption[53]. To evaluate the detailed effect of HFBI coatings on *S. aureus* adhesion, adhesion was compared on silicon, on silane-coated silicon (OTS) and on hydrophobin HFBI-coated OTS surfaces. Adhesion measurements on SiO_2 and OTS have already been described in detail in Maikranz *et al.*[30].
On hydrophobic OTS surfaces, *S. aureus* cells exhibited by far the highest adhesion with a median adhesion force of 22±13 nN. In contrast, the adhesion force on hydrophilic SiO_2 and HFBI surfaces was in the pN to lower nN range (Fig. 2). By comparing the median adhesion forces on these two hydrophilic surfaces, however, a clear difference became apparent. While the median adhesion force on SiO_2 surfaces was still in the nN range (1.0±0.3 nN), the

Table 1: Surface properties (water contact angle, root-mean-square roughness) of HFBI coatings on OTS in comparison to bare SiO_2 and OTS-covered SiO_2[38,47,48]. The isoelectric points (IEP) for HFBI and HFBI D40Q/D43N proteins in solution are taken from Lienemann *et al.*[36], with the experimentally measured value and the theoretically determined value given in brackets.

Upper layer	WCA / °	RMSR / nm	IEP
Bare SiO_2	5±2[47]	0.14±0.02[38]	< 2[47]
OTS	111±2[38]	0.17±0.02[38]	≈ 3.0[47]
HFBI	34±6	0.33±0.04	6.1 (5.7)[36]
HFBI D40Q/D43N	39±4	0.38±0.07	7.0 (8.2)[36]

median adhesion force on HFBI surfaces was strongly reduced to 80±40 pN.

The increased adhesion on the OTS surfaces can be explained by the wettability of the surface (see Table 1, WCA). The shift in adhesion force of *S. aureus* on OTS (WCA: 111±2°) and SiO_2 (WCA: 5±2°) surfaces was described in previous studies[13,30,55] and could be explained by the number and strength of tethering macromolecules to the surface[30]. While many macromolecules can adhere weakly to the hydrophobic surfaces, only a few strong binding macromolecules can attach to the hydrophilic surfaces. Therefore, the difference between adhesion on the OTS- and HFBI-coated surfaces (WCA: 34±6°) can also be described by the effect of surface wettability. However, when comparing the adhesion on HFBI-coated surfaces with the adhesion on SiO_2 surfaces, it becomes clear that the wettability of the surfaces cannot explain the differences, as the measured water contact angle is higher on HFBI-coated surfaces (see Table 1, WCA). A possible explanation for the reduced adhesion on HFBI-coated surfaces compared to SiO_2 is the diminished surface area for the formation of hydrogen bonds. Coating the surface with HFBI protein creates a more chemically heterogeneous surface that may reduce the binding ability of bacterial macromolecules.

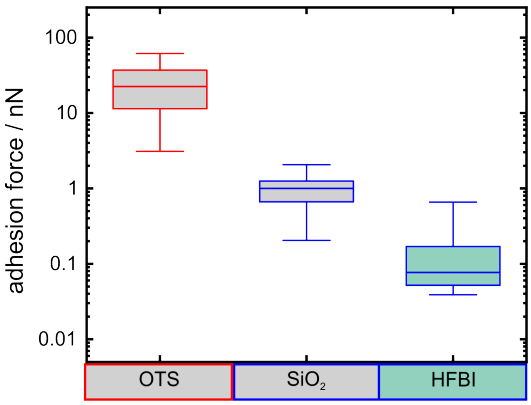

Figure 2: Min-to-max box plots of the adhesion force of *S. aureus* on OTS, SiO_2[30] and HFBI surfaces. Displaying the median adhesion force on these three different surfaces (OTS: 22±13 nN, SiO_2: 1.0±0.3 nN and HFBI: 80±40 pN). The border color of the box plots describes the hydrophobicity of the surface (red: hydrophobic, blue: hydrophilic).

Influence of the surface charge on the adhesion of *S. aureus*

To study the effect of the electrostatic interactions on the adhesion of *S. aureus*, SCFS measurements with immobilized cells on HFBI-coated surfaces were performed. In addition to HFBI, the HFBI variant D40Q/D43N with altered surface charge was employed (Table 1, IEP)[36]. Additional to *S. aureus* SA113, SA113 *ΔdltA* was used. The *ΔdltA* mutant lacks the gene *dltA* encoding the D-alanine-D-alanyl carrier protein ligase. This gene catalyzes the first step in the D-alanylation of lipoteichoic acids

(LTAs). Consequently, this mutant's wall- and lipoteichoic acids lack D-alanine, resulting in an increased negative surface charge of the cell wall[16,56].

SCFS data recorded with SA113 cells on a HFBI-D40Q/D43N-coated surface were analysed by normalising to the force of the same cell determined on a HFBI-coated surface (Fig. 3a). An increase in the mean adhesion force of SA113 on the HFBI D40Q/D43N surfaces is evident when compared to the more negatively charged HFBI surfaces (lower IEP). On average, there is a doubling of the adhesion force per bacterium on the HFBI D40Q/D43N surface, with the adhesion force of individual cells ranging from 50 to 330 %. Notably, in this series of experiments, 7 out of 9 SA113 cells tested displayed an increased adhesion to the HFBI D40Q/D43N surface. By displaying all measured adhesion values in a single histogram an increased probability for non-adhesion events on the HFBI surface becomes apparent. While the probability for non-adhesion on the HFBI D40Q/D43N surface is still about 10 %, it increases to about 40 % on the HFBI surface. After removing these non-adhesion events from the relative occurrence of the histogram, a slight shift in the adhesion force to higher values for the adhesion on HFBI D40Q/D43N compared to adhesion on HFBI is also evident.
Performing the same series of measurements with SA113 *ΔdltA* cells on HFBI and HFB D40Q/D43N led to an overall decrease in adhesion compared to SA113 (Fig. 3d), as already observed on SiO_2 surfaces in an earlier study[16]. Also unlike SA113, the majority of cells of the *ΔdltA* mutant displayed reduced adhesion forces on the HFBI-D40Q/D43N-covered surface (5 out of 9) when compared to HFBI-covered surfaces (Fig. 3c). However, the normalization of the adhesion forces did not show a clear trend between the adhesion force on HFBI and HFBI D40Q/D43N, with a normalized mean for the adhesion force on HFBI D40Q/D43N of 1.1 compared to the adhesion force on HFBI (Fig. 3c). The histogram of all adhesion forces measured with the SA113 mutant *ΔdltA* supports the statement of low impact of the surface to the adhesion of SA113 *ΔdltA*. Non-adhesion measurements are in the same order of magnitude (30–35 %) on both HFBI surfaces. A minimal shift of the measurable adhesion forces to higher values was seen on the HFBI D40Q/D43N surfaces, but marginal (Fig. 3d). The adhesion of all SA113 *ΔdltA* cells measured showed no significant difference in adhesion forces between the two surfaces tested ($p = 0.66$, unpaired t-test).
The measurements with SA113 clearly showed that electrostatic interactions play a role in the adhesion of *S. aureus* to hydrophilic surfaces. Thus, the charge of the surface can change the bacterial adhesion strength. Also, adhesion on HFBI surfaces is generally low and it is the high frequency of non-adhesion events that is of greater interest.
In contrast, the adhesion results of SA113 *ΔdltA* are not as easy to interpret. The decreased adhesion strength compared to the SA113 confirms the statement that the adhesion of this mutant is decisively influenced. The assumption that this is due to the higher surface charge of the bacterial cell cannot be confirmed unambiguously, since an increased effect of the charge of the adherent surface was absent. However, it could be possible that no effect on the adhesion is visible because of a already minimized adhesion. To understand the exact effects of such knock-out mutants, more detailed investigations of the indirect changes of the macromolecules in the cell wall are indispensable.

Protein extraction

Given the impact of DltA on autolysin activity[57], and the recent observations that D-alanylation of teichoic acids is important for the distribution of protein A on the cell surface of *S. aureus*[58], we wondered whether and how deletion of *dltA* might alter the cell wall composition. To get a first idea about this, we next determined the cell wall protein content by SDS-PAGE and coomassie staining. Figure S1 shows the coomassi stained SDS-PAGE gel of a single protein extraction experiment as an example. The extraction was performed three

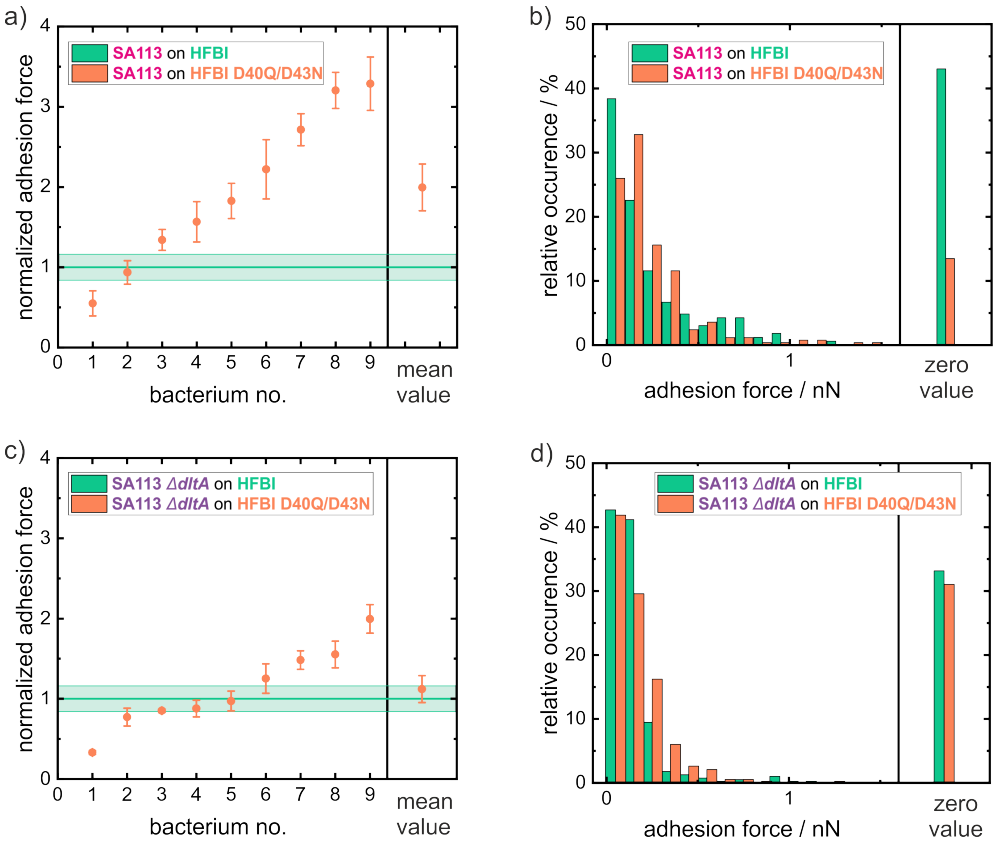

Figure 3: Adhesion forces of 9 *S. aureus* SA113 (a,b) and SA113 $\Delta dltA$ (c,d) cells on hydrophobin surfaces with different IEPs. (a,c) Mean adhesion forces of single *S. aureus* cells normalized to the adhesion value of each cell on the HFBI surfaces (HFBI: green line, HFBI D40Q/D43N: orange measurement points). Error bars depict the standard error of the mean. For better visualization, the measurements are sorted after increasing normalized adhesion force of the cell on HFBI D40Q/D43N surfaces. (b,d) Histograms of all adhesion force values measured for *S. aureus* cells. Display also the non-adhesion events (adhesion force $< 40\,\mathrm{pN}$) excluded from the main histogram.

times on different days to ensure authentic biological replica.
All the extractions have shown three prominent differences between SA113 and SA113 $\Delta dltA$, as seen in Figure 4. One band of about 70 kDa is found in higher quantities in the cell wall extracts of SA113 cells. In contrast, SA113 $\Delta dltA$ has a more prominent band at 40 kDa and 34 kDa, respectively.
A screening of available literature suggested that the protein with a mass around 40 kDa could be either the iron-regulated surface determinant protein A (IsdA, aka. FrpA, Seg7, StbA)[59], the extracellular matrix and plasma binding protein Emp, or the cell wall hydrolyase LytN. All three proteins are found in the secretome of *S. aureus*[60], display theoretical IEP values >10[61] and are associated with the cell envelope. The 70 kDa protein band identified in larger quantities in SA113 cell wall extracts might be IsdB, which displays an electronegative surface in the concave dumb-bell structure formed by its NEAT1-NEAT2 domains[62]. Lastly, the protein more expressed in the $\Delta dltA$ mutant at 34 kDa could be autolysin Sle1, a putative N-acetylmuramoyl-L-alanine amidase with a theoretical IEP of 9.9. It is important to note that the identifications made are purely speculative and based on a literature search. To ensure accurate identification of these proteins, further experimental work such as mass-spectrometry analysis must be conducted. Still nonetheless, all alterations in the composition of cell wall proteins displayed by the $\Delta dltA$ mutant have been highly reproducible.
Previous work has shown that the lack of DltA leads to a lower autolysin activity[63,64] because the highly charged teichoic acids are involved in the control of Atl activity. Atl is a major cell wall hydrolase in *S. aureus* and therefore an autolysin[65]. This reduced autolysin activity results in a different composition of the cell wall[57,66] and most likely influences the patchiness of the distribution of the cell wall-associated proteins[57]. These patches of adhesins are vital for strong adhesion, as shown by Spengler *et al.* using an SCFS approach combined with simulations[17]. It is feasable that the absence of LTA D-alanylation leads to a reduction in cell wall adhesins that are, however, more evenly distributed on the bacterial cell surface, which would be in line with our observations that the $\Delta dltA$ mutant displayed lower adhesion forces on the probed substrates (due to the reduced number of adhesins) and at the same time a smaller diversity in the adhesion forces recorded for each individual cell (due to a more even distribution of adhesins).

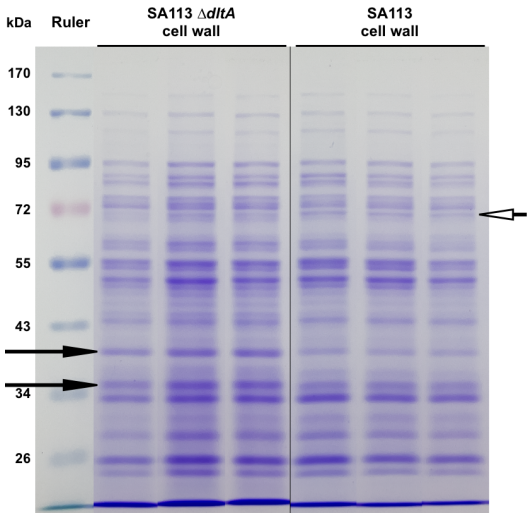

Figure 4: Comparison of all cell wall fractions of SA113 and SA113 $\Delta dltA$. The same amount of protein was loaded for each lane using the corresponding volumes of the cytosolic fractions. Around 70 kDa, 40 kDa, and 34 kDa a difference between SA113 and SA113 $\Delta dltA$ can be seen.

Conclusions

Our first SCFS measurements of bacterial adhesion on HFBI-coated surfaces show a significant reduction compared to naive silicon surfaces. The coating of hydrophobic surfaces with HFBI therefore provides a good alternative to already known protein coatings to reduce bacterial adhesion. Adhesion is greatly reduced even compared to hydrophilic surfaces, allowing a discussion of the forces involved. Thus, the adhesion to surfaces is determined by their wettability, their ability to form hydrogen bonds, and

their electrostatic interactions with the macromolecules of the bacterial cell wall. For the adhesion of *S. aureus* on hydrophilic HFBI surfaces, the electrostatic interactions are the dominant part. However, the composition of the cell wall macromolecules and their arrangement on the bacterial cell wall can shift the order of relevant binding forces. Therefore, the influence of HFBI surface charge on the adhesion of the *S. aureus* $\Delta dltA$ mutant is greatly reduced and the $\Delta dltA$ mutant exhibits generally decreased adhesion. The lowered autolysin actvity in $\Delta dltA$ cells and the resulting change in adhesion molecules distribution of the cell wall might explain this behaviour. Therefore the distribution of adhesins in patches seems to be advantageous enabling the cell to adhere effectively to a surface.

In continuing research, it would be of great biomedical interest to further develop the hydrophobin coatings into antibacterial coatings. Hydrophobin fusion proteins, which are designed to have an antibacterial effect, could not only prevent adhesion but also kill the adherent bacterial cells. Hydrophobin fusion proteins could already be produced with enzymatic activity and surfaces could be coated[67,68]. Also, a deeper understanding of the patchiness of bacterial cell wall macromolecules and the influence of this patchiness on the relevant adhesion forces is important for the understanding of bacterial adhesion.

Author Contributions

Experimental results were achieved and analyzed by F. Nolle (Hydrophobin surfaces, SCFM measurements), B. Wieland (SCFM measurements, SDS-PAGE), K. Kochems (Hydrophobin surfaces), H. Heintz (bacteria preparation), M. Lienemann (Hydrophobin purification). The methodology was developed by F. Nolle, B. Wieland, P. Jung, H. Hähl. Scientific work was directed by H. Hähl, M. Bischoff and K. Jacobs. The original draft was written by F. Nolle and B. Wieland. All authors haven reviewed and edited the manuscript.

Acknowledgement We thank Andreas Peschel (Cellular and Molecular Microbiology Division, Interfaculty Institute of Microbiology and Infection Medicine, University of Tübingen) for the provision of the *S. aureus* mutant strains. This research was supported by the German Research Foundation (SFB 1027 B1 and B2, and large instrument funding under grant number INST 256/542-1 FUGG, project number 449375068). Karin Jacobs acknowledges funding by the German Federal Ministry of Education and Research (BMBF) by the Max Planck School Matter to Life.

Supporting Information

The protein content of the cell wall and cytosol of SA113 and SA113 $\Delta dltA$ cells was extracted as described in "*Extraction of* S. aureus *proteins*". The protein concentration of the cytosolic fraction was determined using the bicinchoninic acid protein assay. A single SDS-PAGE experiment is shown in Fig. S1, where 10 µg of cytosolic fraction or the corresponding volume for the cell wall fraction was loaded and separated for about 3 h at 25 mA and 80 V in a 5 % stacking and 10 % separation polyacrylamide gel.

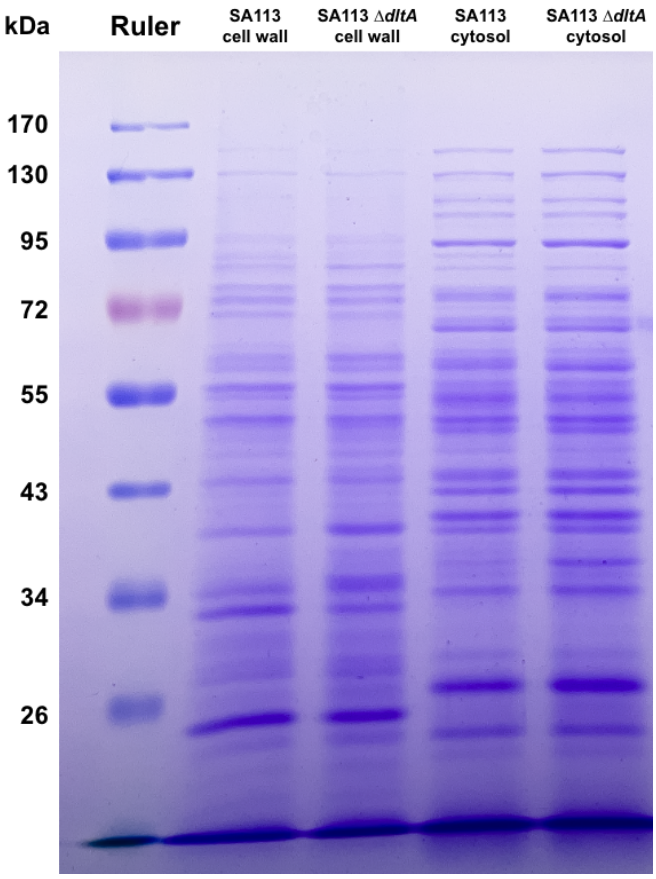

Figure S1: SDS-PAGE of the cell wall and cytosloic fraction of *S. aureus* SA113 and SA113 $\Delta dltA$. 10 µg of each cytosolic fraction was loaded onto the gel, and the corresponding volume for the cell wall fraction was used to load proportional amounts of proteins. Around 70 kDa, 40 kDa and 34 kDa, a difference between the cell wall of the wild type and the mutant can be seen.

References

(1) Oliveira, W.; Silva, P.; Silva, R.; Silva, G.; Machado, G.; Coelho, L.; Correia, M. *Staphylococcus aureus* and *Staphylococcus epidermidis* infections on implants. *Journal of Hospital Infection* **2018**, *98*, 111–117.

(2) Lowy, F. D. *Staphylococcus Aureus* Infections. *N Engl J Med* **1998**, *339*, 520–532.

(3) Yongsunthon, R.; Fowler, V. G.; Lower, B. H.; Vellano, F. P.; Alexander, E.; Reller, L. B.; Corey, G. R.; Lower, S. K. Correlation between Fundamental Binding Forces and Clinical Prognosis of *Staphylococcus Aureus* Infections of Medical Implants. *Langmuir* **2007**, *23*, 2289–2292.

(4) Heilmann, C. In *Bacterial Adhesion*; Linke, D., Goldman, A., Eds.; Springer Netherlands: Dordrecht, 2011; Vol. 715; pp 105–123.

(5) Gosbell, I. B. Diagnosis and Management of Catheter-Related Bloodstream Infections Due to *Staphylococcus Aureus*. *Intern Med J* **2005**, *35*, S45–S62.

(6) Austin, E. D.; Sullivan, S. B.; Whittier, S.; Lowy, F. D.; Uhlemann, A.-C. Peripheral Intravenous Catheter Placement Is an Underrecognized Source of *Staphylococcus Aureus* Bloodstream Infection. *Open Forum Infectious Diseases* **2016**, *3*, ofw072.

(7) Corey, G. R. *Staphylococcus Aureus* Bloodstream Infections: Definitions and Treatment. *CLIN INFECT DIS* **2009**, *48*, S254–S259.

(8) Kimmig, A.; Hagel, S.; Weis, S.; Bahrs, C.; Löffler, B.; Pletz, M. W. Management of *Staphylococcus Aureus* Bloodstream Infections. *Front. Med.* **2021**, *7*, 616524.

(9) Nambiar, K. et al. Survival Following *Staphylococcus Aureus* Bloodstream Infection: A Prospective Multinational Cohort Study Assessing the Impact of Place of Care. *Journal of Infection* **2018**, *77*, 516–525.

(10) Thwaites, G. E. et al. Adjunctive Rifampicin for *Staphylococcus Aureus* Bacteraemia (ARREST): A Multicentre, Randomised, Double-Blind, Placebo-Controlled Trial. *The Lancet* **2018**, *391*, 668–678.

(11) Kilic, M.; Yuzkat, N.; Soyalp, C.; Gulhas, N. Cost Analysis on Intensive Care Unit Costs Based on the Length of Stay. *Turk J Anaesthesiol Reanim* **2019**, *47*, 142–145.

(12) Moormeier, D. E.; Bayles, K. W. *Staphylococcus aureus* Biofilm: A Complex Developmental Organism. *Molecular Microbiology* **2017**, *104*, 365–376.

(13) Thewes, N.; Loskill, P.; Jung, P.; Peisker, H.; Bischoff, M.; Herrmann, M.; Jacobs, K. Hydrophobic Interaction Governs Unspecific Adhesion of Staphylococci: A Single Cell Force Spectroscopy Study. *Beilstein J. Nanotechnol.* **2014**, *5*, 1501–1512.

(14) Thewes, N.; Loskill, P.; Spengler, C.; Hümbert, S.; Bischoff, M.; Jacobs, K. A Detailed Guideline for the Fabrication of Single Bacterial Probes Used for Atomic Force Spectroscopy. *Eur. Phys. J. E* **2015**, *38*, 140.

(15) Spengler, C.; Nolle, F.; Mischo, J.; Faidt, T.; Grandthyll, S.; Thewes, N.; Koch, M.; Müller, F.; Bischoff, M.; Klatt, M. A.; Jacobs, K. Strength of Bacterial Adhesion on Nanostructured Surfaces Quantified by Substrate Morphometry. *Nanoscale* **2019**, *11*, 19713–19722.

(16) Spengler, C.; Nolle, F.; Thewes, N.; Wieland, B.; Jung, P.; Bischoff, M.; Jacobs, K. Using Knock-Out Mutants to Investigate the Adhesion of *Staphylococcus Aureus* to Abiotic Surfaces. *IJMS* **2021**, *22*, 11952.

(17) Spengler, C.; Maikranz, E.; Glatz, B.; Klatt, M. A.; Heintz, H.; Bischoff, M.; Santen, L.; Fery, A.; Jacobs, K. The Adhesion Capability of *Staphylococcus Aureus* Cells Is Heterogeneously Distributed over the Cell Envelope. 2023.

(18) Gunaratnam, G.; Spengler, C.; Trautmann, S.; Jung, P.; Mischo, J.; Wieland, B.; Metz, C.; Becker, S. L.; Hannig, M.; Jacobs, K.; Bischoff, M. Human Blood Plasma Factors Affect the Adhesion Kinetics of *Staphylococcus Aureus* to Central Venous Catheters. *Sci Rep* **2020**, *10*, 20992.

(19) Kang, S.; Elimelech, M. Bioinspired Single Bacterial Cell Force Spectroscopy. *Langmuir* **2009**, *25*, 9656–9659.

(20) Dufrêne, Y. F. Sticky Microbes: Forces in Microbial Cell Adhesion. *Trends in Microbiology* **2015**, *23*, 376–382.

(21) Harris, L. G.; Richards, R. G. *Staphylococcus aureus* adhesion to different treated titanium surfaces. *Journal of Materials Science: Materials in Medicine* **2004**, *15*, 311–314.

(22) Sun, D.; Babar Shahzad, M.; Li, M.; Wang, G.; Xu, D. Antimicrobial Materials with Medical Applications. *Materials Technology* **2015**, *30*, B90–B95.

(23) Kleine, D.; Chodorski, J.; Mitra, S.; Schlegel, C.; Huttenlochner, K.; Müller-Renno, C.; Mukherjee, J.; Ziegler, C.; Ulber, R. Monitoring of Biofilms Grown on Differentially Structured Metallic Surfaces Using Confocal Laser Scanning Microscopy. *Eng. Life Sci.* **2019**, elsc.201800176.

(24) Huttenlochner, K.; Davoudi, N.; Schlegel, C.; Bohley, M.; Müller-Renno, C.; Aurich, J. C.; Ulber, R.; Ziegler, C. *Paracoccus Seriniphilus* Adhered on Surfaces: Resistance of a Seawater Bacterium against Shear Forces under the Influence of Roughness, Surface Energy, and Zeta Potential of the Surfaces. *Biointerphases* **2018**, *13*, 051003.

(25) Khateb, H.; Sørensen, R. S.; Cramer, K.; Eklund, A. S.; Kjems, J.; Meyer, R. L.; Jungmann, R.; Sutherland, D. S. The Role of Nanoscale Distribution of Fibronectin in the Adhesion of *Staphylococcus Aureus* Studied by Protein Patterning and DNA-PAINT. *ACS Nano* **2022**, *16*, 10392–10403.

(26) Xu, L.-C.; Siedlecki, C. A. Protein Adsorption, Platelet Adhesion, and Bacterial Adhesion to Polyethylene-Glycol-Textured Polyurethane Biomaterial Surfaces: BIOLOGICAL RESPONSES TO PEG-TEXTURED BIOMATERIAL SURFACES. *J. Biomed. Mater. Res.* **2017**, *105*, 668–678.

(27) Lorenzetti, M.; Dogša, I.; Stošicki, T.; Stopar, D.; Kalin, M.; Kobe, S.; Novak, S. The Influence of Surface Modification on Bacterial Adhesion to Titanium-Based Substrates. *ACS Appl. Mater. Interfaces* **2015**, *7*, 1644–1651.

(28) Zhang, F.; Zhang, Z.; Zhu, X.; Kang, E.-T.; Neoh, K.-G. Silk-Functionalized Titanium Surfaces for Enhancing Osteoblast Functions and Reducing Bacterial Adhesion. *Biomaterials* **2008**, *29*, 4751–4759.

(29) Filipović, U.; Dahmane, R. G.; Ghannouchi, S.; Zore, A.; Bohinc, K. Bacterial Adhesion on Orthopedic Implants. *Advances in Colloid and Interface Science* **2020**, *283*, 102228.

(30) Maikranz, E.; Spengler, C.; Thewes, N.; Thewes, A.; Nolle, F.; Jung, P.; Bischoff, M.; Santen, L.; Jacobs, K. Different Binding Mechanisms of *Staphylococcus Aureus* to Hydrophobic and Hydrophilic Surfaces. *Nanoscale* **2020**, *12*, 19267–19275.

(31) Linder, M. B.; Szilvay, G. R.; Nakari-Setälä, T.; Penttilä, M. E. Hydrophobins: the protein-amphiphiles of filamentous

fungi. *FEMS Microbiology Reviews* **2005**, *29*, 877–896.

(32) Szilvay, G. R.; Paananen, A.; Laurikainen, K.; Vuorimaa, E.; Lemmetyinen, H.; Peltonen, J.; Linder, M. B. Self-Assembled Hydrophobin Protein Films at the Air-Water Interface: Structural Analysis and Molecular Engineering. *Biochemistry* **2007**, *46*, 2345–2354.

(33) Yamasaki, R.; Takatsuji, Y.; Asakawa, H.; Fukuma, T.; Haruyama, T. Flattened-Top Domical Water Drops Formed through Self-Organization of Hydrophobin Membranes: A Structural and Mechanistic Study Using Atomic Force Microscopy. *ACS Nano* **2016**, *10*, 81–87.

(34) Wösten, H. A. B.; Scholtmeijer, K. Applications of hydrophobins: current state and perspectives. *Applied Microbiology and Biotechnology* **2015**, *99*, 1587–1597.

(35) Hektor, H. J.; Scholtmeijer, K. Hydrophobins: proteins with potential. *Current Opinion in Biotechnology* **2005**, *16*, 434–439.

(36) Lienemann, M.; Grunér, M. S.; Paananen, A.; Siika-aho, M.; Linder, M. B. Charge-Based Engineering of Hydrophobin HFBI: Effect on Interfacial Assembly and Interactions. *Biomacromolecules* **2015**, *16*, 1283–1292.

(37) Paananen, A.; Vuorimaa, E.; Torkkeli, M.; Penttilä, M.; Kauranen, M.; Ikkala, O.; Lemmetyinen, H.; Serimaa, R.; Linder, M. B. Structural Hierarchy in Molecular Films of Two Class II Hydrophobins. *Biochemistry* **2003**, *42*, 5253–5258.

(38) Lessel, M.; Bäumchen, O.; Klos, M.; Hähl, H.; Fetzer, R.; Paulus, M.; Seemann, R.; Jacobs, K. Self-assembled Silane Monolayers: An Efficient Step-by-step Recipe for High-quality, Low Energy Surfaces. *Surf. Interface Anal.* **2015**, *47*, 557–564.

(39) Peschel, A.; Otto, M.; Jack, R. W.; Kalbacher, H.; Jung, G.; Götz, F. Inactivation of the Dlt Operon in *Staphylococcus Aureus* Confers Sensitivity to Defensins, Protegrins, and Other Antimicrobial Peptides. *Journal of Biological Chemistry* **1999**, *274*, 8405–8410.

(40) Iordanescu, S.; Surdeanu, M. Two Restriction and Modification Systems in *Staphylococcus Aureus* NCTC8325. *Journal of General Microbiology* **1976**, *96*, 277–281.

(41) Sader, J. E.; Chon, J. W. M.; Mulvaney, P. Calibration of Rectangular Atomic Force Microscope Cantilevers. *Review of Scientific Instruments* **1999**, *70*, 3967–3969.

(42) Van Der Mei, H. C.; Rustema-Abbing, M.; De Vries, J.; Busscher, H. J. Bond Strengthening in Oral Bacterial Adhesion to Salivary Conditioning Films. *Appl Environ Microbiol* **2008**, *74*, 5511–5515.

(43) Beaussart, A.; El-Kirat-Chatel, S.; Herman, P.; Alsteens, D.; Mahillon, J.; Hols, P.; Dufrêne, Y. F. Single-Cell Force Spectroscopy of Probiotic Bacteria. *Biophysical Journal* **2013**, *104*, 1886–1892.

(44) Herman, P.; El-Kirat-Chatel, S.; Beaussart, A.; Geoghegan, J. A.; Vanzieleghem, T.; Foster, T. J.; Hols, P.; Mahillon, J.; Dufrêne, Y. F. Forces Driving the Attachment of *Staphylococcus Epidermidis* to Fibrinogen-Coated Surfaces. *Langmuir* **2013**, *29*, 13018–13022.

(45) Herman, P.; El-Kirat-Chatel, S.; Beaussart, A.; Geoghegan, J. A.; Foster, T. J.; Dufrêne, Y. F. The Binding Force of the Staphylococcal Adhesin SdrG Is Remarkably Strong: Binding Strength of the Staphylococcal Adhesin SdrG. *Molecular Microbiology* **2014**, *93*, 356–368.

(46) Zeng, G.; Müller, T.; Meyer, R. L. Single-Cell Force Spectroscopy of Bacteria Enabled by Naturally Derived Proteins. *Langmuir* **2014**, *30*, 4019–4025.

(47) Bellion, M.; Santen, L.; Mantz, H.; Hähl, H.; Quinn, A.; Nagel, A.; Gilow, C.; Weitenberg, C.; Schmitt, Y.; Jacobs, K. Protein Adsorption on Tailored Substrates: Long-Range Forces and Conformational Changes. *J. Phys.: Condens. Matter* **2008**, *20*, 404226.

(48) Trevino, K. J.; Shearer, J. C.; Tompkins, B. D.; Fisher, E. R. Comparing Isoelectric Point and Surface Composition of Plasma Modified Native and Deposited SiO_2 Films Using Contact Angle Titrations and X-ray Photoelectron Spectroscopy. *Plasma Processes and Polymers* **2011**, *8*, 951–964.

(49) Paulsson, M.; Kober, M.; Freij-Larsson, C.; Stollenwerk, M.; Wesslén, B.; Ljungh, Å. Adhesion of *Staphylococci* to Chemically Modified and Native Polymers, and the Influence of Preadsorbed Fibronectin, Vitronectin and Fibrinogen. *Biomaterials* **1993**, *14*, 845–853.

(50) Kinnari, T. J.; Peltonen, L. I.; Kuusela, P.; Kivilahti, J.; Könönen, M.; Jero, J. Bacterial Adherence to Titanium Surface Coated with Human Serum Albumin. *Otology & Neurotology* **2005**, *26*, 380–384.

(51) Devine, R.; Singha, P.; Handa, H. Versatile biomimetic medical device surface: hydrophobin coated, nitric oxide-releasing polymer for antimicrobial and hemocompatible applications. *Biomaterials Science* **2019**, *7*, 3438–3449.

(52) Sorrentino, I.; Gargano, M.; Ricciardelli, A.; Parrilli, E.; Buonocore, C.; de Pascale, D.; Giardina, P.; Piscitelli, A. Development of anti-bacterial surfaces using a hydrophobin chimeric protein. *International Journal of Biological Macromolecules* **2020**, *164*, 2293–2300.

(53) Wang, Z.; Lienemann, M.; Qiau, M.; Linder, M. B. Mechanisms of Protein Adhesion on Surface Films of Hydrophobin. *Langmuir* **2010**, *26*, 8491–8496.

(54) Von Vacano, B.; Xu, R.; Hirth, S.; Herzenstiel, I.; Rückel, M.; Subkowski, T.; Baus, U. Hydrophobin Can Prevent Secondary Protein Adsorption on Hydrophobic Substrates without Exchange. *Anal Bioanal Chem* **2011**, *400*, 2031–2040.

(55) Spengler, C.; Thewes, N.; Jung, P.; Bischoff, M.; Jacobs, K. Determination of the Nano-Scaled Contact Area of Staphylococcal Cells. *Nanoscale* **2017**, *9*, 10084–10093.

(56) Neuhaus, F. C.; Baddiley, J. A Continuum of Anionic Charge: Structures and Functions of D -Alanyl-Teichoic Acids in Gram-Positive Bacteria. *Microbiol Mol Biol Rev* **2003**, *67*, 686–723.

(57) Leonard, A. C.; Goncheva, M. I.; Gilbert, S. E.; Shareefdeen, H.; Petrie, L. E.; Thompson, L. K.; Khursigara, C. M.; Heinrichs, D. E.; Cox, G. Autolysin-Mediated Peptidoglycan Hydrolysis Is Required for the Surface Display of *Staphylococcus Aureus* Cell Wall-Anchored Proteins. *Proc. Natl. Acad. Sci. U.S.A.* **2023**, *120*, e2301414120.

(58) Zhang, R.; Shebes, M. A.; Kho, K.; Scaffidi, S. J.; Meredith, T. C.; Yu, W. Spatial Regulation of Protein A in *Staphylococcus Aureus*. *Molecular Microbiology* **2021**, *116*, 589–605.

(59) Morrissey, J. A.; Cockayne, A.; Hammacott, J.; Bishop, K.; Denman-Johnson, A.; Hill, P. J.; Williams, P. Conservation, Surface Exposure, and In Vivo Expression of the Frp Family of Iron-Regulated Cell Wall Proteins in *Staphylococcus Aureus*. *Infect Immun* **2002**, *70*, 2399–2407.

(60) Busche, T.; Hillion, M.; Van Loi, V.; Berg, D.; Walther, B.; Semmler, T.; Strommenger, B.; Witte, W.; Cuny, C.; Mellmann, A.; Holmes, M. A.; Kalinowski, J.; Adrian, L.; Bernhardt, J.; Antelmann, H. Comparative Secretome Analyses of Human and Zoonotic Staphylo-

coccus Aureus Isolates CC8, CC22, and CC398. *Molecular & Cellular Proteomics* **2018**, *17*, 2412–2433.

(61) Fuchs, S.; Mehlan, H.; Bernhardt, J.; Hennig, A.; Michalik, S.; Surmann, K.; Pané-Farré, J.; Giese, A.; Weiss, S.; Backert, L.; Herbig, A.; Nieselt, K.; Hecker, M.; Völker, U.; Mäder, U. *Aureo*Wiki - The Repository of the *Staphylococcus Aureus* Research and Annotation Community. *International Journal of Medical Microbiology* **2018**, *308*, 558–568.

(62) Alfeo, M. J.; Pagotto, A.; Barbieri, G.; Foster, T. J.; Vanhoorelbeke, K.; De Filippis, V.; Speziale, P.; Pietrocola, G. *Staphylococcus aureus* Iron-Regulated Surface Determinant B (IsdB) Protein Interacts with von Willebrand Factor and Promotes Adherence to Endothelial Cells. *Sci Rep* **2021**, *11*, 22799.

(63) Peschel, A.; Vuong, C.; Otto, M.; Götz, F. The D -Alanine Residues of *Staphylococcus Aureus* Teichoic Acids Alter the Susceptibility to Vancomycin and the Activity of Autolytic Enzymes. *Antimicrob Agents Chemother* **2000**, *44*, 2845–2847.

(64) Cafiso, V.; Bertuccio, T.; Purrello, S.; Campanile, F.; Mammina, C.; Sartor, A.; Raglio, A.; Stefani, S. *dltA* Overexpression: A Strain-Independent Keystone of Daptomycin Resistance in Methicillin-Resistant *Staphylococcus Aureus*. *International Journal of Antimicrobial Agents* **2014**, *43*, 26–31.

(65) Foster, S. J. Molecular Characterization and Functional Analysis of the Major Autolysin of *Staphylococcus Aureus* 8325/4. *J Bacteriol* **1995**, *177*, 5723–5725.

(66) Houston, P.; Rowe, S. E.; Pozzi, C.; Waters, E. M.; O'Gara, J. P. Essential Role for the Major Autolysin in the Fibronectin-Binding Protein-Mediated *Staphylococcus Aureus* Biofilm Phenotype. *Infect Immun* **2011**, *79*, 1153–1165.

(67) Joensuu, J. J.; Conley, A. J.; Lienemann, M.; Brandle, J. E.; Linder, M. B.; Menassa, R. Hydrophobin Fusions for High-Level Transient Protein Expression and Purification in *Nicotiana Benthamiana*. *Plant Physiology* **2010**, *152*, 622–633.

(68) Takatsuji, Y.; Yamasaki, R.; Iwanaga, A.; Lienemann, M.; Linder, M. B.; Haruyama, T. Solid-Support Immobilization of a "Swing" Fusion Protein for Enhanced Glucose Oxidase Catalytic Activity. *Colloids and Surfaces B: Biointerfaces* **2013**, *112*, 186–191.

Danksagung

An dieser Stelle möchte ich mich bei allen bedanken, die mich auf dem Weg meiner Doktorarbeit begleitet haben; sei es durch fachliche oder manchmal auch moralische Unterstützung.

Mein besonderer Dank gilt Frau Prof. Dr. Karin Jacobs, die es mir ermöglicht hat, in ihrer Arbeitsgruppe zu promovieren und die mir stets zur Seite stand. Immer die Zukunft der eigenen Leute im Blick und dabei ein Höchstmaß an Unterstützung, das man wirklich nicht von jedem erwarten kann. Ich finde es wirklich toll, ein Teil der Arbeitsgruppe von Frau Prof. Dr. Karin Jacobs zu sein.

Ebenso herzlich möchte ich mich bei Herrn Prof. Dr. Markus Bischoff bedanken. Neben der Übernahme des Zweitgutachtens war er immer ansprechbar, wenn es um Fragen zur bakteriellen Adhäsion ging. Aber auch in allen anderen Themenbereichen dieser Dissertation war er immer offen für eine angenehme und hilfreiche Diskussion.

Bevor ich mich bei allen anderen Gruppenmitgliedern und Kooperationspartnern bedanke, möchte ich mich noch bei zwei Personen ganz besonders bedanken: Bei meinem Betreuer/Büronachbarn Dr. Hendrik Hähl, der mich gerade im Bereich der Hydrophobine maximal unterstützt hat. Die fachlichen Diskussionen mit ihm haben mich so manches Mal dann weitergebracht, wenn es einmal nicht so lief, wie es sollte. Bei PD Dr. Frank Müller möchte ich mich vor allem für die Möglichkeit bedanken, Lehrerfahrung zu sammeln, Vorlesungen zu halten und auch als Beisitzer bei Prüfungen dabei zu sein. Das hat mir immer Spaß gemacht und mir Erfahrungen vermittelt, die ich sonst nicht bekommen hätte.

Am liebsten würde ich die Liste meiner Helfer und Unterstützer Person für Person durchgehen, aber ich glaube, dann würde die Arbeit noch einige Seiten länger. Ich möchte mich daher bei allen ehemaligen und aktuellen Mitgliedern der AG Jacobs bedanken, die mich auf meinem Weg begleitet haben. Mein Dank gilt Judith Rech, Monika Schuck und Candida Andreas-Cuva, bei denen ich immer große Unterstützung in allen administrativen Fragen oder bei Fragen zu jeweiligen Bestellungen fand. Ebenso möchte ich mich bei meiner lieben Freundin und Kollegin Hannah Heintz bedanken, die immer ein offenes Ohr für mich hatte. Besonders bedanken möchte ich mich auch bei Kirstin Kochems, die mir vor allem am Ende meiner Doktorarbeit sehr geholfen hat. Dr. Christian Spengler und Dr. Nicolas Thewes möchte ich für die bisherige Zusammenarbeit danken, die es mir ermöglicht hat, meine Promotion so weit voranzutreiben. Dr. Thomas Faidt und Dr. Anne Holtsch danke ich für die grafische Unterstützung. Mats Stauske und Chloé Bûcheron danke ich für ihre, wenn auch leider nur kurze, Unterstützung im Bereich der Hydrophobine. Jens Neurohr, Khalil Remini, Samer Alokaidi, Dr. Martin Brinkmann und Johannes Mischo, auch euch ein herzliches Dankeschön für die netten Gespräche in der Mit-

tagspause, die gerade im Endspurt zu meiner geliebten „Durchschnauf-Pause“ geworden ist.

Mein Dank gilt auch allen Kooperationspartnern. Herrn Prof. Dr. Ralf Seemann und Jean-Baptiste Fleury für die Einführung und Unterstützung im Bereich der Mikrofluidik. Danke für die vielen hilfreichen Diskussionen. Auch dem Rest der Arbeitsgruppe möchte ich für die angenehme Arbeitsatmosphäre danken. Ich möchte mich auch bei der Arbeitsgruppe von Herrn Prof. Markus Bischoff bedanken. Insbesondere bei Ben Wieland, der mit mir das Hydrophobin-/Bakterien-Projekt durchgeführt hat. Leonhard Starke und Herrn Prof. Dr. Jochen Hub möchte ich für die enge Zusammenarbeit im Projekt „Wasserpermeabilität von Hydrophobindoppelschichten“ danken. Dr. Erik Maikranz und Herrn Prof. Dr. Ludger Santen danke ich für die Durchführung der bakteriellen Adhäsionssimulationen und die Unterstützung bei meiner Doktorarbeit. Danke an Carsten Baltes und danke an Frau Prof. Dr. Franziska Lautenschläger für die sehr angenehme und thematisch spannende Zusammenarbeit auf dem Gebiet der humanen Zelladhäsion. Bedanken möchte ich mich auch bei unseren finnischen Kooperationspartnern: Dinara Bozzhigitova, Dr. Michael Lienemann und Dr. Arja Paananen. Die Zeit in Finnland war zwar kurz, aber sehr spannend und lehrreich. Ich hoffe, dass aus dieser Zusammenarbeit noch viele interessante Projekte entstehen werden.

Last but not least möchte ich mich bei meiner ganzen Familie und allen meinen Freunden für ihre Unterstützung bedanken. Dabei geht ein besonderer Dank an zwei Personen.

Papa: Danke für all deine Unterstützung, gerade in der Zeit, als es nicht so einfach war. Ohne dich hätte ich es nicht geschafft.

Jaesang Lee Danke für alles: Du bist mir eine große Stütze und mein Rückhalt geworden, ich weiß gar nicht wie oft du mich aufgefangen hast.

Danke euch ALLEN!

Friederike